

Multivalent Heparin Binding and Sensing

Stephen Marriott Bromfield

PhD

University of York

Chemistry

September 2014

Abstract

Heparin therapy involves the clinical use of heparin as an anti-coagulant, for example, during surgery. At the conclusion of treatment, systemic heparin levels must be quantified to allow accurate dosing of a heparin antidote. This thesis details work towards a better sensing methodology and an improved antidote.

A synthetically-simple arginine-functionalized dye – Mallard Blue (MalB) – was synthesised and shown able to detect heparin across a clinically relevant concentration range in biological media such as human serum. The heparin binding of MalB is selective over structurally related glycosaminoglycans and is highly tolerant of electrolytic competition. Indeed, the performance of MalB is comparable with the best heparin sensors currently known and makes it the new best-in-class thionine dye.

Mallard Blue was developed into a straightforward competition assay able to report on the relative heparin binding efficiencies of candidate molecules in competitive media, including human serum. Using this assay in conjunction with molecular dynamics modelling techniques, fundamental insights into the binding of poly(amidoamine) (PAMAM) dendrimers to heparin were gained. Interestingly, the medium sized (G2-G4) dendrimers achieved the most charge-efficient heparin binding. Comparisons against derivatives modified with poly(phenylenevinylene) cores revealed native PAMAMs to be exponents of adaptive multivalency, in contrast to the more rigid derivatives' shape-persistent multivalency.

The performance of self-assembled multivalent (SAMul) heparin binder $C_{22}G1DAPMA$ was studied in different biological media and shown to be more charge-efficient than the currently used heparin antidote under competitive conditions. Also, $C_{22}G1DAPMA$ was able to reverse anti-coagulation in heparinized human plasma and degrade on a clinically interesting timescale. Structural modifications afforded two new families of SAMul binders, which unveiled fundamental differences in the chiral preferences of heparin and DNA, along with probing the effects of nanoscale morphology on heparin binding ability and aggregate-stability in serum.

Table of Contents

Abstract	2
Table of Contents	3
List of Figures	6
List of Tables	16
List of Schemes	19
List of Equations	20
Acknowledgements	22
Declaration	23
1 Introduction	24
1.1 From Multivalency to Self-Assembling Multivalency (SAMul) . 24	
<i>1.1.1 Multivalency</i>	24
<i>1.1.2 Self-Assembly</i>	33
<i>1.1.3 Self-Assembling Multivalency (SAMul)</i>	35
1.2 Heparin Therapy	42
<i>1.2.1 Heparin: the anti-coagulant of choice</i>	42
<i>1.2.2 Heparin Rescue</i>	45
1.3 Heparin Sensing	47
<i>1.3.1 Monitoring heparin levels</i>	47
<i>1.3.2 Electrochemical sensing</i>	49
<i>1.3.3 Colorimetric sensing</i>	49
<i>1.3.4 Solid/nanoparticle supported sensing</i>	57
1.4 Heparin Binding	59
<i>1.4.1 Enzymatic, protein-based and polymeric systems</i>	59
<i>1.4.2 Small molecules</i>	61
<i>1.4.3 Self-assembling systems</i>	64
1.5 Project Aims	65
<i>1.5.1 Heparin sensing</i>	66
<i>1.5.2 Heparin binding</i>	66
2 Chapter 2 – A Simple Robust Heparin Sensor	69
2.1 Introduction	69
2.2 Considering Commercial Options	70
2.3 A New Dye is Born	76

2.4	Mallard Blue: Initial Studies	78
2.5	Mallard Blue: Establishing Clinical Relevance	83
2.6	Mallard Blue: Further Studies	87
2.7	Conclusions & Future Work.....	90
3	Insights into Heparin Binding	93
3.1	Introduction.....	93
3.2	Mallard Blue Heparin Binding Competition Assay	97
3.2.1	<i>Electrolytically Competitive Conditions</i>	<i>97</i>
3.2.2	<i>Clinically Relevant Conditions</i>	<i>99</i>
3.3	Studying Generational Effects in PAMAM Dendrimers	101
3.3.1	<i>PAMAM Dendrimers</i>	<i>101</i>
3.3.2	<i>Heparin Binding in Competitive Conditions</i>	<i>102</i>
3.3.3	<i>Heparin Binding in Clinically Relevant Conditions</i>	<i>107</i>
3.3.4	<i>Summary</i>	<i>108</i>
3.4	Studying Effects of Rigidity and Flexibility with Transgeden Dendrimers	109
3.4.1	<i>Transgeden (TGD) Dendrimers</i>	<i>109</i>
3.4.2	<i>Heparin Binding Studies in Competitive Conditions</i>	<i>111</i>
3.5	Modified Transgeden Dendrimers	118
3.6	Conclusion and Future Work.....	120
4	Self-Assembling Multivalent Heparin Binders I: DAPMA-containing system	123
4.1	Introduction.....	123
4.1.1	<i>Background.....</i>	<i>123</i>
4.1.2	<i>Preliminary Work²¹¹</i>	<i>125</i>
4.2	Effects of Different Media on Heparin Binding.....	127
4.2.1	<i>Heparin Binding in Competitive Conditions</i>	<i>127</i>
4.2.2	<i>Heparin Binding in Clinically Relevant Conditions</i>	<i>134</i>
4.2.3	<i>Degradation Studies.....</i>	<i>138</i>
4.3	Conclusions and Future Work	143
5	Self-Assembling Multivalent Heparin Binders II: Lysine-containing systems	145
5.1	Introduction.....	145
5.2	Generation 1 Systems	147
5.2.1	<i>Synthesis of C₂₂G1LLys and C₂₂G1DLys</i>	<i>147</i>
5.2.2	<i>Self-Assembly Studies</i>	<i>152</i>
5.2.3	<i>Heparin Binding in Competitive Conditions</i>	<i>157</i>

5.2.4	<i>Heparin Binding in Clinically Relevant Conditions</i>	160
5.2.5	<i>Degradation</i>	162
5.2.6	<i>DNA Binding</i>	169
5.3	Generation 2 Systems	176
5.3.1	<i>Synthesis of C₂₂G₂LLys and C₂₂G₂DLys</i>	176
5.3.2	<i>Self-Assembly Studies</i>	179
5.3.3	<i>Heparin Binding in Competitive Conditions</i>	183
5.3.4	<i>Degradation</i>	186
5.3.5	<i>DNA Binding</i>	189
5.4	Conclusions and Future Work	191
5.4.1	<i>Conclusions</i>	191
5.4.2	<i>Future Work</i>	192
6	Hydrophobically-Enhanced Self-Assembling Heparin Binders	194
6.1	Introduction	194
6.2	Generation 1 (G1) Systems	196
6.2.1	<i>Lysine-containing system (G1)</i>	196
6.2.2	<i>Ornithine-containing systems</i>	208
6.3	Generation 2 (G2) Lysine-containing System	216
6.3.1	<i>Synthesis of (C₁₂)₂LAspLLys(LLys)₂ and (C₁₂)₂DAspDLys(DLys)₂</i>	217
6.3.2	<i>Self-Assembly Studies</i>	218
6.3.3	<i>Heparin Binding in Competitive Conditions</i>	220
6.3.4	<i>Heparin Binding in Clinically Relevant Conditions</i>	222
6.4	Conclusions and Future Work	223
7	Experimental	226
7.1	Synthetic Materials and Methods	226
7.2	Assay Materials and Methods	261
	Abbreviations	266
	References	268

List of Figures

Figure 1.1 – Schematic cartoon of (a) a virus binding to cell surface and (b) a dendritic polymer binding to DNA.	25
Figure 1.2 – Schematic representations of allosteric, chelate and interannular cooperativity.....	27
Figure 1.3 – Example of interannular cooperativity from the work of Shinkai and co-workers. ¹⁴	28
Figure 1.4 – Schematic cartoon of stepwise dissociation of a multivalent binder in the absence and presence of a competitor.	30
Figure 1.5 – Schematic depiction of trivalent vancomycin host-guest complex (top) along with comparison of monomeric vancomycin binding to D-Ala-D-Lys (bottom left) and mutated D-Ala-lactate (bottom right).	31
Figure 1.6 – Trivalent pseudorotaxanes from the group of Stoddart. Figure adapted from reference ³²	32
Figure 1.7 – Exquisite ligand preorganization gives Anderson’s porphyrin wheel well optimized multivalent interactions. Figure adapted from reference ³⁷	33
Figure 1.8 – The work of Israelachvili allowed aggregate morphology in aqueous solution to be predicted as a function of critical packing parameter.....	35
Figure 1.9 – The hydrophobically modified sialic acid derivative from the group of Whitesides was one of the earliest examples of self-assembled multivalency (SAMul). ⁴⁷	36
Figure 1.10 – Cartoon of Ravoo and co-workers’ cyclodextrin vesicles (large grey structure) decorated with adamantane-maltose ligands (red and orange) for Con A binding (green). Image reproduced from reference ⁴⁹	37
Figure 1.11 – Amphiphilic galactosamine-conjugate from the group of Bertozzi self-assembled along CNTs to achieve high-affinity lectin binding. ⁵¹	37
Figure 1.12 – Self-assembling multivalent mannose-functionalised lectin-binding discotic molecules from Brunsveld and co-workers. Figure adapted from reference ⁵²	38

Figure 1.13 – Integrin binding systems from the work of Smith and co-workers. ⁵⁶	40
Figure 1.14 – Example spermine-containing DNA binding systems from the groups of (a) Cheng, ⁶⁴ (b) Ravoo ⁶⁶ and (c) Smith. ⁶⁵	41
Figure 1.15 – An example heparin polysaccharide (top) along with the predominant disaccharide repeat unit (bottom left) and the specific pentasaccharide sequence required to confer anticoagulant activity (bottom right).	42
Figure 1.16 – Schematic representation of the blood coagulation cascade.	44
Figure 1.17 – An example protamine structure (a) with the prevalent arginine residues depicted as wedges, adapted from reference ¹⁰¹ and (b) a molecular dynamic modelling snapshot of protamine, taken from reference ¹⁰²	45
Figure 1.18 – Schematic representation of heparin binding to Yang’s quaternary amine functionalized membrane. ¹³⁵	49
Figure 1.19 – Anslyn’s heparin sensors operating (a) in an indicator displacement regime ¹⁴⁴ and (b) using a single molecule fluorescent sensor. ¹⁴⁵ These structures are also shown in Figure 3.2.	51
Figure 1.20 – Fluorescent sugar-containing heparin sensors from the groups of (a) Chen ¹⁴⁷ and (b) Bhosale. ¹⁴⁸	52
Figure 1.21 – A polyfluorene heparin sensing derivative from Liu and co-workers. ¹⁵⁴	53
Figure 1.22 – A perylene diimide sensor structure from Krämer and co-workers. ¹⁵⁸	54
Figure 1.23 – Heparin orange and heparin blue, discovered <i>via</i> a diversity-oriented library approach in the group of Chang. ¹⁶⁰	55
Figure 1.24 – Two-component heparin sensor from Zhang and co-workers. ¹⁶¹	56
Figure 1.25 – Selective ratiometric sensors: (a) phosphorescent conjugated polyelectrolyte structure from Zhao, Liu and Huang ¹⁶⁷ and (b) peptide structure from Lee. ¹⁶⁸	57
Figure 1.26 – Graphene-AuNPs sensing system from Chen and co-workers. Figure adapted from reference ¹⁷²	58

Figure 1.27 – Cationic heparin binding polymers: (a) Quaternary ammonium-based cationic polymer polybrene and (b) an arginine functionalised PAH. ¹⁹¹	61
Figure 1.28 – Delparantag is a lysine-containing penta-cationic heparin binder.....	62
Figure 1.29 – Calix[8]arene from Cunsolo and co-workers with structure (left) enabling chelate effect to be maximized through adoption of ‘octopus-like’ conformation (right, space-filled species represents calix[8]arene, stick model represents heparin). Figure adapted from ²⁰⁰	63
Figure 1.30 – An octa-cationic arginine-containing foldamer from DeGrado and co-workers. ²⁰²	63
Figure 1.31 – Surfen, one of the smallest synthetic heparin binders to be examined as a potential heparin rescue agent. ²⁰⁵	64
Figure 1.32 – A self-assembling heparin-binding lipopeptide from Stupp and co-workers. ²⁰⁷	64
Figure 1.33 – Self-assembling heparin binding compound subjected to preliminary testing by Smith and co-workers. ²¹¹ This Figure is also shown as Figure 4.2.....	65
Figure 1.34 – Cartoon showing the concept of self-assembled multivalency (SAMul) in for heparin effective heparin binding	67
Figure 2.1 – A selection of dyes from the thionine family.	71
Figure 2.2 – UV-vis absorbance spectra of thionine acetate (16 μ M) in salt (150 mM) and buffer (1 mM Tris HCl) in presence (grey) and absence (solid black) of heparin. Thionine acetate (16 μ M) in the presence of heparin with no NaCl present is included for comparison (dashed black).....	73
Figure 2.3 – UV-vis absorbance spectra of methyl green (30 μ M) in salt (150 mM) and buffer (1 mM Tris HCl) in presence (grey) and absence (solid black) of heparin. Methyl green (30 μ M) in the presence of heparin with no NaCl present is included for comparison (dashed black).....	74
Figure 2.4 – UV-vis absorbance spectra of alcian blue (38 μ M) in salt (150 mM) and buffer (1 mM Tris HCl) in presence (grey) and absence (black) of heparin. Inset: structure of alcian blue.....	76

Figure 2.5 – UV-vis absorbance spectrum of MalB (25 μM) in salt (150 mM) and Tris HCl (1 mM) in the presence (grey) and absence (black) of heparin. Inset: Picture showing colour of MalB to <i>Mallard</i>	79
Figure 2.6 – Binding curves resulting from titration of heparin into a solution of methylene blue (10 μM , left) or Mallard blue (25 μM , right) in the absence (top) or presence (bottom) of 150 mM NaCl.	80
Figure 2.7 – Extent to which increasing concentrations of Buffer/Electrolyte disrupt MalB-heparin interaction.	82
Figure 2.8 – Equilibrated MD snapshot of MalB-heparin interactions. Heparin is represented as purple (D-glucosamine) and green (L-iduronic acid) space-filling spheres, while MalB is shown as pink stick model.....	83
Figure 2.9 – Three structurally related GAGs: heparin, hyaluronic acid (HA) and chondroitin sulfate (CS).	84
Figure 2.10 – Normalised response of MalB to glycosaminoglycans HA, CS and heparin.....	85
Figure 2.11 – Mallard Blue response to heparin delivered in 100% human serum (solid circles) or 100% horse serum (open triangles) within a clinically relevant range.	86
Figure 2.12 – Mallard Blue (solid circles) and Azure A (open squares) response to heparin delivered in 100% human serum within a clinically relevant range.	87
Figure 2.13 – Stability traces of MalB in the presence of light or dark under either air or nitrogen.	88
Figure 2.14 – Time-lapse photographs showing development of MalB colour over time at room temperature.	89
Figure 2.15 – UV-visible absorbance spectra for MalB in water as concentration increases. Inset: Plot of absorbance at λ_{max} between 0 – 500 μM	90
Figure 3.1 – Cartoon concept of an indicator displacement assay (IDA).	95

Figure 3.2 – Anslyn’s heparin sensing systems: (a) tri-boronic acid receptor and pyrocatechol violet indicator; ¹⁴⁴ (b) modified fluorophore-containing receptor. ¹⁴⁵ These structures are also shown in Figure 1.19.	96
Figure 3.3 – UV-visible absorbance spectra for MalB (25 μ M) in the absence and presence of heparin (27 μ M), and following the subsequent addition protamine in the presence of NaCl (150 mM) and Tris HCl (10 mM).	97
Figure 3.4 – Heparin binding curve for protamine, with the point of 50% dye displacement indicated.	98
Figure 3.5 – Heparin binding curves for protamine obtained from MalB assay with heparin delivered in 10% and 100% human serum.	100
Figure 3.6 – Structure of G2-PAMAM with the generation levels G0 – G2 shown. The higher generations result from larger iterations of the dendritic structure.	101
Figure 3.7 – Equilibrated MD snapshots of heparin binding to selected PAMAM dendrimers and protamine. Binders are represented as blue stick models while heparin is shown as red and orange space-filling structures.	107
Figure 3.8 – Structure of Transgeden (TGD) dendrimers showing the PPV core unit and G1-G3 PAMAM surface groups.	110
Figure 3.9 – Heparin binding curve comparisons for TGD (closed shapes) and PAMAM (open shapes) dendrimers at G1 (top left), G2 (top right) and G3 (bottom) from MalB assay in buffer and salt.	112
Figure 3.10 – MD simulations for TGD (top) and PAMAM (bottom) binding heparin at a charge excess of 0.4 across generations 1, 2 and 3 (left-to-right).	115
Figure 3.11 – Snapshots of the mesoscale simulations between dendrimers and heparin at CE = 0.1 for TGD (top) and PAMAM (bottom) at G1 (left), G2 (middle) and G3 (right) in each case.	116
Figure 3.12 – Heparin titration curves for TGD dendrimers (G1-G3) in 150 mM NaCl and 10 mM Tris HCl, probed by fluorescence of PPV-core.	117
Figure 3.13 – Heparin binding curves for TGD-dendrimers containing differing numbers of surface amines.	119

Figure 4.1 – An amphiphilic integrin binder from Smith and co-workers. ⁵⁶	125
Figure 4.2 – Structure of heparin binder C ₂₂ G1DAPMA along with cartoon representation of self-assembly. This Figure is also shown as Figure 1.33.	125
Figure 4.3 – TEM images of C ₂₂ G1DAPMA in absence (left, scale bar: 100 nm) and presence (right, scale bar: 50 nm) of heparin.	126
Figure 4.4 – Mesoscale (top) and atomistic (bottom) representations of C ₂₂ G1DAPMA in the presence (left) and absence (right) of 150 mM NaCl.	130
Figure 4.5 – Atomistic models of self-assembled C ₂₂ G1DAPMA (top) or protamine (bottom) binding heparin in absence (left) and presence (right) of 150 mM NaCl.	132
Figure 4.6 – Heparin binding curves for PG1DAPMA, C ₂₂ G1DAPMA and protamine from MalB heparin binding assay.	134
Figure 4.7 – Measured absorbance for heparin delivered into solution of C ₂₂ G1DAPMA at a (+ : -) = 0.67 in 0 – 10 % human serum.	136
Figure 4.8 – Fluorescence intensity of NR in PBS buffer over time in the presence of C ₂₂ G1DAPMA in the absence (solid circles) and presence (open circles) of heparin.	139
Figure 4.9 – Mass spectrometric degradation assay: observed species (top) after 0 hours (middle) and 24 hours (bottom) incubation at 37 °C.	142
Figure 5.1 – Target molecules C ₂₂ G1LLys, C ₂₂ G1DLys.	147
Figure 5.2 – The three distinct components of G1 target molecules C ₂₂ G1LLys and C ₂₂ G1DLys, where ‘PG’ represents a protecting group.	147
Figure 5.3 – Circular dichroism spectra of target molecules C ₂₂ G1LLys and C ₂₂ G1DLys (10 mM in methanol) indicating opposing chirality.	152
Figure 5.4 – Chemical structure of hydrophobic dye probe, Nile Red (NR)	153
Figure 5.5 – Nile Red encapsulation curves for C ₂₂ G1LLys and C ₂₂ G1DLys.	153
Figure 5.6 – TEM image of 200 μM C ₂₂ G1LLys (scale bar: 50 nm).	155
Figure 5.7 – TEM image of 200 μM C ₂₂ G1LLys in the presence of heparin (scale bar: 100 nm).	155

Figure 5.8 – TEM image of 200 μ M C ₂₂ G1DLys (scale bar: 50 nm).	156
Figure 5.9 – TEM image of 200 μ M C ₂₂ G1DLys in the presence of heparin (scale bar: 100 nm).	156
Figure 5.10 – Heparin binding curves for PG1LLys, C ₂₂ G1LLys and C ₂₂ G1DLys.....	158
Figure 5.11 – Heparin binding curves for C ₂₂ G1DLys obtained from MalB assay carried out (i) in salt and buffer (black) and (ii) with heparin delivered in 100% human serum (grey).	161
Figure 5.12 – Time resolved degradation curve of C ₂₂ G1DLys. Discontinuities are indicated where the sample was vigorously shaken to simulate blood-flow shear forces.	163
Figure 5.13 – Mass spectrometric degradation assay: observed species (top) after 0 hours (middle) and 24 hours (bottom) incubation at 37 °C.	166
Figure 5.14 – ¹ H and ¹³ C NMR spectra for C ₂₂ G1DLys before (left) and after (right) refrigeration under an inert atmosphere for 18 months.....	168
Figure 5.15 – Heparin binding curves for C ₂₂ G1LLys and C ₂₂ G1DLys obtained using the MalB assay in buffer and salt initially following synthesis (black) and after 18 months of storage (grey).	169
Figure 5.16 – Segment of DNA showing the 2-deoxyribose sugar-phosphate backbone and the hydrogen bonding interactions between the labelled nucleobases.	170
Figure 5.17 – An example PNA strand containing a lysine functionalised region; a so-called ‘chiral box’. ³⁴⁸	171
Figure 5.18 – Chemical structure of fluorescent dye ethidium bromide.....	172
Figure 5.19 – DNA binding curves from EthBr assay for PG1LLys, C ₂₂ G1LLys and C ₂₂ G1DLys.	173
Figure 5.20 – Nile red encapsulation curve for C ₂₂ G1DLys in the presence of DNA.	174
Figure 5.21 – G2 target molecules C ₂₂ G2LLys and C ₂₂ G2DLys.....	176

Figure 5.22 – Circular dichroism spectra of target molecules C ₂₂ G2LLys and C ₂₂ G2DLys indicating opposing chirality.	179
Figure 5.23 – Nile Red encapsulation curves for C ₂₂ G2LLys and C ₂₂ G2DLys.....	180
Figure 5.24 – TEM image of 125 μM C ₂₂ G2LLys (scale bar: 50 nm).....	181
Figure 5.25 – TEM image of 125 μM C ₂₂ G2LLys in the presence of heparin (scale bar: 50 nm).	182
Figure 5.26 – TEM image of 125 μM C ₂₂ G2LLys (scale bar: 50 nm).....	182
Figure 5.27 – TEM image of 125 μM C ₂₂ G2LLys in the presence of heparin (scale bar: 100 nm).	183
Figure 5.28 – Heparin binding curves for PG2LLys, C ₂₂ G2LLys and C ₂₂ G2DLys obtained from MalB assay.	184
Figure 5.29 – Time resolved degradation curve for C ₂₂ G2DLys. Discontinuities are indicated where the sample was vigorously shaken to simulate blood-flow shear forces.	186
Figure 5.30 – Mass spectrometric degradation assay: observed species (top) after 0 hours (middle) and 24 hours (bottom) incubation at 37 °C.	188
Figure 5.31 – DNA binding curves from EthBr assay for PG1LLys, C ₂₂ G1LLys and C ₂₂ G1DLys.	190
Figure 6.1 – Twin-tailed G1 target molecules (C ₁₂) ₂ LAspLLys and (C ₁₂) ₂ DAspDLys.	195
Figure 6.2 – The three component pieces of G1 target molecules (C ₁₂) ₂ LAspLLys and (C ₁₂) ₂ DAspDLys.	196
Figure 6.3 – Circular dichroism data at different stages during the preparation of (C ₁₂) ₂ LAspLLys (solid lines) and (C ₁₂) ₂ DAspDLys (dashed lines) measured at 10 mM in methanol.....	198
Figure 6.4 – Nile Red encapsulation curve for (C ₁₂) ₂ DAspDLys.	198
Figure 6.5 – TEM images of 100 μM (C ₁₂) ₂ DAspDLys (scale bars: 100 nm (left), 50 nm (right)).	199

Figure 6.6 – TEM image of 100 μM $(\text{C}_{12})_2\text{DAspDLys}$ in the presence of heparin (scale bars: 200 nm (left), 100 nm (right)).	200
Figure 6.7 – Heparin binding curves for $(\text{C}_{12})_2\text{LAspLLys}$ and $(\text{C}_{12})_2\text{DAspDLys}$ obtained from MalB assay in 150 mM NaCl and 10 mM Tris HCl.	203
Figure 6.8 – Comparison of the relative proximity of the hydrophobic units (blue squares) and chiral region (red circles) of $(\text{C}_{12})_2\text{AspLys}$ and $\text{C}_{22}\text{G1Lys}$ systems.	204
Figure 6.9 – DNA binding curves for $(\text{C}_{12})_2\text{LAspLLys}$ and $(\text{C}_{12})_2\text{DAspDLys}$ obtained from EthBr displacement assay.	207
Figure 6.10 – Ornithine-containing twin-tailed target molecules $(\text{C}_{12})_2\text{LAspLOrn}$ and $(\text{C}_{12})_2\text{DAspDOrn}$.	208
Figure 6.11 – Circular dichroism spectra for $(\text{C}_{12})_2\text{LAspLOrn}$ and $(\text{C}_{12})_2\text{DAspDOrn}$.	209
Figure 6.12 – Nile Red encapsulation data for $(\text{C}_{12})_2\text{LAspLOrn}$ and $(\text{C}_{12})_2\text{DAspDOrn}$.	210
Figure 6.13 – TEM images of 100 μM $(\text{C}_{12})_2\text{LAspLOrn}$ (scale bars: 500 nm (left), 100 nm (right)).	210
Figure 6.14 – TEM images of 100 μM $(\text{C}_{12})_2\text{LAspLOrn}$ in the presence of heparin (scale bars: 100 nm (both images)).	211
Figure 6.15 – TEM images of 100 μM $(\text{C}_{12})_2\text{LAspLOrn}$ (scale bars: 500 nm (left), 100 nm (right)).	211
Figure 6.16 – TEM image of 100 μM $(\text{C}_{12})_2\text{DAspDOrn}$ in the presence of heparin (scale bar: 100 nm (left), 50 nm (right)).	211
Figure 6.17 – Heparin binding curves for $(\text{C}_{12})_2\text{LAspLOrn}$ and $(\text{C}_{12})_2\text{DAspDOrn}$ obtained from MalB assay.	213
Figure 6.18 – DNA binding curves for $(\text{C}_{12})_2\text{LAspLOrn}$ and $(\text{C}_{12})_2\text{DAspDOrn}$ obtained from EthBr assay.	215
Figure 6.19 – Two G2 aspartic acid-lysine target molecules $(\text{C}_{12})_2\text{LAspLLys}(\text{LLys})_2$ and $(\text{C}_{12})_2\text{DAspDLys}(\text{DLys})_2$.	216

Figure 6.20 – Nile Red encapsulation curve for $(C_{12})_2DAspDLys(DLys)_2$	218
Figure 6.21 – TEM images of $(C_{12})_2DAspDLys(DLys)_2$ alone (scale bars: 50 nm (left), 200 nm (right)).	219
Figure 6.22 – TEM images of $(C_{12})_2DAspDLys(DLys)_2$ in the presence of heparin (scale bars: 100 nm (left), 50 nm (right)).	219
Figure 6.23 – Heparin binding curves for $(C_{12})_2LAspLLys(LLys)_2$ and $(C_{12})_2DAspDLys(DLys)_2$ from MalB assay in buffer and salt.	221

List of Tables

Table 3.1 – Heparin binding data for protamine, calculated from MalB assay.....	98
Table 3.2 – Heparin binding data for protamine from MalB assay with heparin delivered in 10 and 100% human serum.	100
Table 3.3 – Heparin binding data for PAMAM dendrimers tested in MalB assay in buffer and salt. Protamine data included for comparison.	103
Table 3.4 – MD simulation data for PAMAM dendrimers interacting with heparin. Protamine data included for comparison. Q_{tot} : number of binder charges; Q_{eff} : number of interacting charges; $\Delta G_{\text{bindeff}}$: effective free energy of binding; $\Delta G_{\text{bindeff}}/Q_{\text{eff}}$: effective-charge-normalised free energy of binding.	105
Table 3.5 – Heparin binding data for G2-PAMAM with heparin delivered in 100% serum.	108
Table 3.6 – Heparin binding data from MalB assay in buffer and salt for G1-G3 TGD dendritic systems, along with G1-G3 PAMAM data for comparison.....	111
Table 3.7 – MD simulation binding parameters at a charge excess of 0.4. Q_{tot} : number of binder charges; Q_{eff} : number of interacting charges; $\Delta G_{\text{bindeff}}$: effective free energy of binding; $\Delta G_{\text{bindeff}}/Q_{\text{tot}}$: charge-normalised free energy of binding; $\Delta G_{\text{bindeff}}/Q_{\text{eff}}$: effective-charge-normalised free energy of binding.	114
Table 3.8 – Heparin binding data for the TGD-G1 derivatives with different numbers of surface charges.	119
Table 4.1 – Heparin binding data for C ₂₂ G1DAPMA and protamine in the absence and presence of salt. Assay conditions: [a] 10 μM MB, 178 μM heparin, 1 mM Tris HCl. [b] 25 μM MalB, 27 μM heparin, 150 mM NaCl, 10 mM Tris HCl.	128
Table 4.2 – Experimental solution-phase diameters of C ₂₂ G1DAPMA aggregates, as measured by DLS.	131
Table 4.3 – Modelling interpretations of effective charges per binder (Q_{eff}), effective free binding energy ($\Delta G_{\text{bindeff}}$) and effective charge-normalised free energy of binding ($\Delta G_{\text{bindeff}}/Q_{\text{eff}}$) for C ₂₂ G1DAPMA and protamine.	132

Table 4.4 – DLS sizes observed for C ₂₂ G1DAPMA in the absence and presence of different amounts of heparin.	133
Table 4.5 – Heparin binding data from MalB assay with heparin delivered in 100% human serum.	135
Table 4.6 – DLS sizes observed for C ₂₂ G1DAPMA-heparin aggregates in the absence and presence of albumin (1 mg mL ⁻¹) over time.	137
Table 4.7 – Plasma clotting data for C ₂₂ G1DAPMA in aPTT and PT assays.	138
Table 5.1 – Nile Red encapsulation assay data for PG1LLys, C ₂₂ G1LLys and C ₂₂ G1DLys.	153
Table 5.2 – DLS data for C ₂₂ G1LLys and C ₂₂ G1DLys under different electrolytic conditions.	157
Table 5.3 – Heparin binding data from MalB assay for PG1LLys, C ₂₂ G1LLys and C ₂₂ G1DLys.	158
Table 5.4 – Heparin binding data for C ₂₂ G1DLys obtained from MalB assay carried out in salt and buffer, and with heparin delivered in 100% human serum.	160
Table 5.5 – Plasma clotting data for C ₂₂ G1DLys in PT assay.	162
Table 5.6 – Plasma clotting data for C ₂₂ G1DLys in PT assay before and after degradation.	167
Table 5.7 – DNA binding data from EthBr assay for PG1LLys, C ₂₂ G1LLys and C ₂₂ G1DLys. *EC ₅₀ and CE ₅₀ are coincidentally numerically equivalent.	173
Table 5.8 – Nile Red encapsulation assay data for PG2LLys, C ₂₂ G2LLys and C ₂₂ G2DLys.	179
Table 5.9 – Heparin binding data for PG2LLys, C ₂₂ G2LLys and C ₂₂ G2DLys obtained from MalB assay.	184
Table 5.10 – DNA binding data from EthBr assay for PG2LLys, C ₂₂ G2LLys and C ₂₂ G2DLys.	189

Table 6.1 – Dynamic Light Scattering (DLS) data for $(C_{12})_2LAspLLys$ and $(C_{12})_2DAspDLys$ in 10 mM Tris HCl in the absence and presence of 150 mM NaCl...	201
Table 6.2 – Heparin binding data for $(C_{12})_2LAspLLys$ and $(C_{12})_2DAspDLys$ obtained from MalB assay in 150 mM NaCl and 10 mM Tris HCl.	202
Table 6.3 – Heparin binding data for $(C_{12})_2DAspDLys$ with heparin delivered in 100% human serum.	205
Table 6.4 – Plasma clotting data for $(C_{12})_2DAspDLys$ from PT and aPTT assays.	206
Table 6.5 – DNA binding data for $(C_{12})_2LAspLLys$ and $(C_{12})_2DAspDLys$ obtained in EthBr displacement assay.	206
Table 6.6 – Heparin binding data for $(C_{12})_2LAspLOrn$ and $(C_{12})_2DAspDOrn$ obtained from MalB assay.	212
Table 6.7 – Heparin binding data for $(C_{12})_2DAspDOrn$ with heparin delivered in 100% human serum.	214
Table 6.8 – DNA binding data for $(C_{12})_2LAspLOrn$ and $(C_{12})_2DAspDOrn$ obtained from EthBr assay.	214
Table 6.9 – Heparin binding data for $(C_{12})_2LAspLLys(LLys)_2$ and $(C_{12})_2DAspDLys(DLys)_2$ from MalB assay in buffer and salt.	220
Table 6.10 – Heparin binding data for $(C_{12})_2DAspDLys(DLys)_2$ from MalB assay with heparin delivered in 100% human serum.....	222

List of Schemes

Scheme 2.1 – Molecular rearrangement of coloured methyl green to colourless carbinol.	75
Scheme 2.2 – Synthesis of Mallard Blue 2.2. Although commercial, conditions for preparation of Arg(Boc) ₃ also shown.....	78
Scheme 4.1 – Preparation of negative control molecule PG1DAPMA.....	133
Scheme 5.1 – Synthesis of alkyl hydrophobic tail unit.	148
Scheme 5.2 – Preparation of LLys(Boc) ₂ or DLys(Boc) ₂	148
Scheme 5.3 – Synthetic scheme for preparation of G1 linker unit. ³²⁵	150
Scheme 5.4 – Synthetic scheme showing connection of the component parts to generate PG1LLys, C ₂₂ G1LLys and C ₂₂ G1DLys.	151
Scheme 5.5 – Synthetic scheme showing preparation of G2-linker. ^{325,357}	177
Scheme 5.6 – Synthetic scheme for production of target molecules PG2LLys, C ₂₂ G2LLys and C ₂₂ G2DLys.	178
Scheme 6.1 – Preparation of G1 target molecules (C ₁₂) ₂ LAspLLys and (C ₁₂) ₂ DAspDLys.	197
Scheme 6.2 – Preparation of modified twin-tailed SAMul systems (C ₁₂) ₂ LAspLOrn and (C ₁₂) ₂ DAspDOrn.	209
Scheme 6.3 – Preparation of (C ₁₂) ₂ LAspLLys(LLys) ₂ and (C ₁₂) ₂ DAspDLys(DLys) ₂	217

List of Equations

Equation 1.1 – Calculation of Whitesides and co-workers’ multivalency enhancement factor, β26

Dedication

This thesis is written in loving memory of my late father.

Acknowledgements

I must begin by thanking Professor David Smith, my supervisor, for his unwavering enthusiasm for all things heparin, his many great scientific ideas and, importantly, for giving me the opportunity and freedom to grow as a research scientist during the past 4 years. I must also acknowledge our international flavour of collaborators including Professor Sabrina Pricl (Italy), Dr Marcelo Calderon (Germany), Professor Julián Rodríguez-López (Spain) and Professor Jeremy Turnbull (Liverpool), without whom this research project would not have been as fruitful.

I have been fortunate enough to work within a team containing some hugely talented people. In particular I must thank Anna Barnard for helping me get to grips with the world of heparin (and Athens), Will Edwards for being my partner in crime (and the sports discussion) and Ching Wan Chan for being my personal NMR putter-on-ner. I have also been lucky enough to supervise many undergraduate students, with Ellis Wilde deserving a special mention for her superb ability to unearth new literature, her excellent abilities as a research chemist and for bringing the perfect amount of crazy (and cake) to this project.

I am also grateful for the technical support received from Karl Heaton and Helen Robinson (MS), Heather Fish (NMR), Andrew Leech (CD), Meg Stark (TEM) and Scott Guimond (Clotting), who together provided the foundations on which this research is built.

On a personal level, I am deeply indebted to Kate Horner for supporting me and distracting me so steadfastly despite everything our lives threw at us (supermarkets never will be the same), Lizzie Smith for our many cathartic pub teas (usual table) and Maurice Waddle for offering such valuable advice and joining me on our voyage into the antithetical world of Monday Night Darts (it's definitely a sausage and chips situation).

Lastly, but most importantly, knowing that I have had the support of my Mum whatever happened has given me great security. I can only hope that the achievements in this volume would have made Dad proud.

Declaration

I declare that the work presented within this thesis is entirely my own, except where otherwise acknowledged. Aspects of this work have been published in the following journal articles: *J. Am. Chem. Soc.*, 2013, **135**, 2911-2914; *Chem. Commun.*, 2013, **49**, 4830-4832; *Chem. Soc. Rev.*, 2013, **42**, 9184-9195; *Chem. Sci.*, 2014, **5**, 1484-1492 and *Chem-Eur. J.*, 2014, **20**, 9666-9674. This work has not been submitted in part or fully for examination towards any other degrees or qualifications.

Stephen Marriott Bromfield

1 Introduction

1.1 From Multivalency to Self-Assembling Multivalency (SAMul)

1.1.1 Multivalency

1.1.1.1 Concept

Velcro is arguably the most widely acknowledged exponent of multivalency. Through establishment of many individually weak interactions between hooks on one side of the material and loops on the other, two physically distinct materials can be reversibly attached to each other. Within this macroscale analogy, the individual hook-loop interactions can be thought of as a monovalent interaction between a binding ligand and a complementary receptor site. In isolation, each single, reversible, interaction would be unable to meaningfully adhere the materials together, but when many of these interactions combine together, the resulting overall binding can be rather powerful.

1.1.1.2 Terminology and Thermodynamics

The concept of multivalency is widely applied across a range of scientific disciplines although only macromolecular chemists tend to employ the term ‘multivalency.’¹ Inorganic chemists refer to the same phenomenon as the ‘chelate effect,’ often with respect to the binding of multidentate ligands within the coordination sphere of a metal centre;^{2,3} while biologists tend to discuss ‘polyvalent’ interactions such as those of a virus with a cell surface.⁴ For the purposes of our discussion, the term multivalency will be taken to mean the simultaneous interaction of multiple binding groups on one species with complementary species on another, often to achieve high-affinity binding.

Defining multivalent interactions on the molecular level must be done with care. For example, a multivalent host – that is one with two or more binding sites – interacting with two or more monomeric guest molecules does not constitute a multivalent interaction as each individual guest only forms a single interaction with the host. As soon as the guest becomes divalent (or larger), the interactions can be classed as multivalent, so long as multiple binding groups on the guest interact with different receptor groups on the same host molecule. When all of the receptor and/or binding

sites are chemically identical, the species can be categorised as homomultivalent, while when the interacting groups vary, it is said to be heteromultivalent.

As we shall see in the next section, multivalent binding can be utilised across a variety of biological and chemical systems. Archetypal examples can be found in the adhesion of a virus to the exterior of a cell wall or the interaction of a dendritic polymer with DNA, as represented schematically in Figure 1.1.

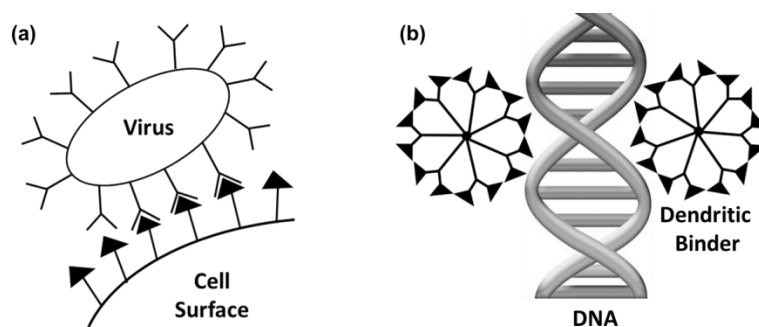


Figure 1.1 – Schematic cartoon of (a) a virus binding to cell surface and (b) a dendritic polymer binding to DNA.

1.1.1.3 Thermodynamics

As with all host-guest interactions, binding or association constants, K , can be calculated for multivalent interactions, although not without some fundamental considerations. Firstly, association constants for monovalent systems refer exclusively to the formation of a single interaction between two physically distinct species, while for multivalent binding it is not so simple. In changing from ‘fully unbound’ to ‘fully bound,’ a multivalent binder will necessarily form several interactions with its host. Despite much explanation in the literature, the misconception that a multivalent system must form multiple interactions which individually should have a higher association constant than the monovalent system remains.⁵ In fact, the individual interactions of a successful multivalent system should bind to the host collectively in a superior manner to the monovalent system. That is to say that the overall binding constant for a multivalent interaction, K^{multi} , referred to as the ‘avidity’ of the system, should be superior to the binding constant of the monovalent system, K^{mono} .

Whitesides and co-workers were the first to attempt to quantify the superiority (or otherwise) of multivalent systems with respect to their monovalent counterparts.⁴ To do this, they calculated a so-called ‘enhancement factor’, β , which was simply a ratio of the

avidity of the multivalent system to the association constant of the monovalent system when each system was interacting with a multivalent host, Equation 1.1. This subsequently enabled multivalent systems to be categorized as either cooperative (synergistic, $\beta > 1$), non-cooperative (additive, $\beta = 1$) or negatively cooperative (interfering, $\beta < 1$).⁴ The simplicity of this calculation does however limit the information which can be derived from it; for example, it is not possible to deconvolute the effect of the number of charges on a multivalent binder – referred to as symmetry effects – from the associated cooperativity.⁶ As such, β can become a useful parameter for the comparison of multivalent systems where the exact valence of the binder is unknown.

$$\beta = \frac{K^{multi}}{K^{mono}}$$

Equation 1.1 – Calculation of Whitesides and co-workers’ multivalency enhancement factor, β .

Accurately assigning cooperativity is tricky as the binding of a second (or subsequent) ligand group of an already partially-bound multivalent guest to the host is fundamentally different to the establishment of a new interaction between the host and a separate guest molecule. Indeed, the first interaction serves to ‘tether’ together the host and guest allowing subsequent interaction to be viewed as intramolecular, rather than intermolecular, binding events.⁷ This tethering also positions the ligand groups of the partially-bound system closer to the host further increasing the statistical likelihood of a complementary binding interaction forming, and ultimately leading to cooperativity.⁸ This dichotomy of the first and subsequent binding interactions must be taken into account for multivalent interactions and, as exemplified by Ercolani in 2011, the inter- and intramolecular processes should be considered independently in order to meaningfully assess cooperativity.⁹ Ercolani suggested that many systems had incorrectly been designated as cooperative or non-cooperative based solely on the consideration of Whitesides and co-workers enhancement factor, β .⁹

There have been several attempts to formalize and delineate different cooperativity regimes. In 2008, Whitty defined allosteric and chelate/configurational regimes as the ‘two faces’ of cooperativity.¹⁰ Whitty suggested that within an allosteric system, the binding of one ligand to a receptor site altered the affinity of a separate ligand for a

different binding site, while chelate or configurational cooperativity arose from the intramolecular nature of all but the first binding interactions within a multivalent system. In 2009, Hunter and Anderson¹¹ reaffirmed Whitty's observations in their candidly titled essay "What is cooperativity?" before Ercolani again went further and rigorously reasoned that a third type of cooperativity regime required defining. Ercolani's formalised definitions of allosteric, chelate and interannular cooperativity are depicted in Figure 1.2 and discussed below.⁹

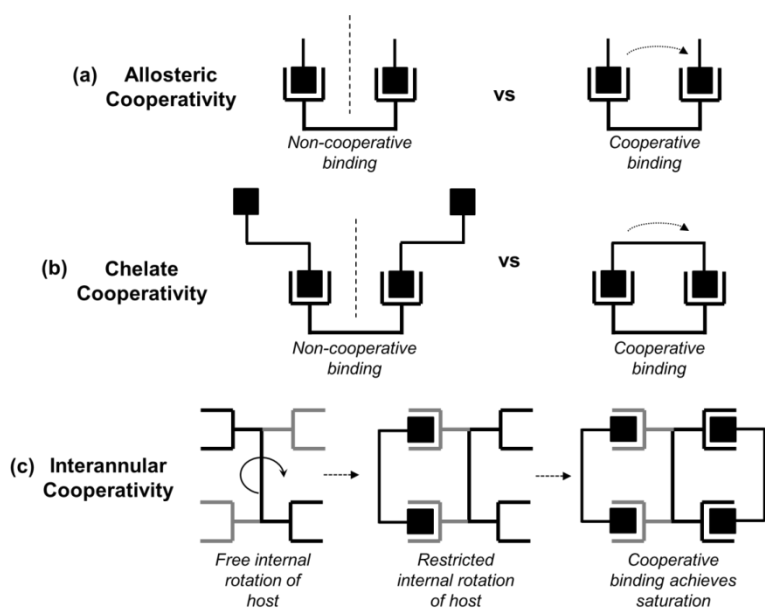


Figure 1.2 – Schematic representations of allosteric, chelate and interannular cooperativity.

The definition of allosteric cooperativity, which is the best understood of the three categories, did not greatly change. Specifically, allosteric cooperativity was said to pertain to two (or more) intermolecular binding sites influencing the behaviour of each other. The most widely recognized example of this is the mechanism of oxygen binding to haemoglobin, where binding of the first oxygen molecule induces a conformational change promoting the binding of three further oxygen species.^{12,13} Chelate cooperativity, meanwhile, is the most recognizable multivalent effect and was formalized as arising from the establishment of one or more intramolecular binding interaction.⁵ Chelate cooperativity is represented on the right-side of the middle row in Figure 1.2.

The final regime was defined by Ercolani as interannular cooperativity, which can be viewed as a subset of chelate cooperativity as it also arises from the interplay of

intramolecular binding interactions.⁹ The differentiator between chelate and interannular cooperativity is the multiplicity of the interactions involved, and it is well explained by an instructive example from the work of Shinkai and co-workers.¹⁴ In particular, the team led by Shinkai created a system containing two porphyrin ‘wheels’ each decorated with pyridinyl binding sites which were able to rotate relative to each other around a cerium ‘axle.’ When both ‘wheels’ simultaneously established interactions with a dicarboxylic acid guest molecule, the wheels became locked in place relative to each other, facilitating the binding of subsequent guest molecules, Figure 1.3.¹⁴

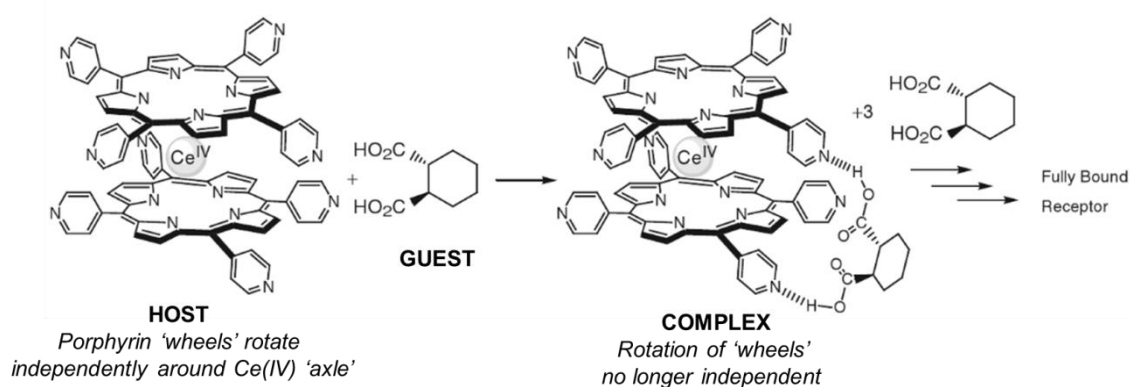


Figure 1.3 – Example of interannular cooperativity from the work of Shinkai and co-workers.¹⁴

Much like monovalent interactions, the free energy of multivalent interactions, ΔG^{multi} , can be calculated. It remains difficult to quantify the individual interactions between a host and a guest, and rather easier to focus on comparisons of the free energies of the fully bound and fully unbound states. As with all free energies, ΔG^{multi} is composed of enthalpic and entropic factors. Of these, it is the entropic component which courts most literature discussion.

It is widely acknowledged that the entropy change upon binding, ΔS^{bind} , has translational, rotational and conformational components, in addition to less well understood contributions from the associated/surrounding solvent(s).¹⁵ The reduction in conformational entropy associated with the formation of the first binding interaction between the multivalent host and the guest is most often considered, although there are contradictory models for determining the significance and/or magnitude of these interactions.¹⁵ For example, Jencks¹⁶ suggested a maximum loss of entropy of localization for an unrestrained rotor of $1.4 \text{ kcal mol}^{-1}$ while Whitesides and co-workers

suggested a much smaller value,¹⁷ although not without attracting criticism from other authors in the process.¹⁸ Overall, the widespread consensus seems to be that entropic factors are not as influential as has been previously thought in the past, with Huskens and Reinhoudt going so far as to suggest that in certain situations “entropic concerns should not be taken too seriously”⁷ however, in reality, the traditional view of multivalent interactions being governed by entropy remains.^{15,17}

The enthalpic component of the free energy of binding, ΔH^{bind} , is also difficult to quantify for multivalent interactions, either by experimental or theoretical methods.⁴ The biggest challenge is to deconvolute the effects of the linker group which connects the multiple ligand groups together from the binding groups, as the linker may itself interact somewhat with the host. The geometry and rigidity of the linker can also affect the relative enthalpy of interactions as, unless ligand pre-organization is highly complementary with the host, the distortion required to establish interaction is likely to lead to so-called enthalpically diminished binding.

As informative as these thermodynamic parameters can be, a more widely used concept is that of effective molarity (or effective concentration), EM (or C_{eff}), which serves to quantify the amount of ligand sites in close proximity to the host. In multivalent systems, once the first ligand group has bound, the effective concentration of ligand groups proximal to the host is increased due to the aforementioned ‘tethering’ of the binder to the host: indeed the subsequent interactions are intramolecular rather than intermolecular. The advantages associated with this increased EM have been demonstrated to be mostly entropic and can be utilised to afford exceptionally high local concentrations of ligand groups.^{16,19} The EM parameter has also been used to measure the affinity enhancement associated with the use of multivalent interactions.^{20,21}

One of the key factors influencing the enhanced binding of multivalent systems over their monovalent counterparts is their significantly different dissociation kinetics. By their very nature, the dissociation of a monovalent host from a guest molecule requires only a single interaction to be broken. In a multivalent system, multiple interactions need to be broken for host-guest dissociation back to two physically discrete species. This rate is determined by the concentration of the host-guest complex in which the two species are held together by only a single interaction (i.e. all other interactions have broken). As discussed above, it is common for partially-bound multivalent guests to re-

bind to the host due to the increased effective concentration, C_{eff} , of ligand groups proximal to the host, and for this reason the concentration of this monovalently bound species is often very low. This phenomenon is a key reason why multivalent interactions are so robust.

Dissociation of a multivalent complex can be promoted through introduction of a species which will compete for binding to the host. This competitor can be monovalent or multivalent and can establish its own interactions with the host as the original multivalent guest begins to dissociate, thereby preventing multivalent re-binding. This leads to a step-wise dissociation process in the manner depicted in Figure 1.4.

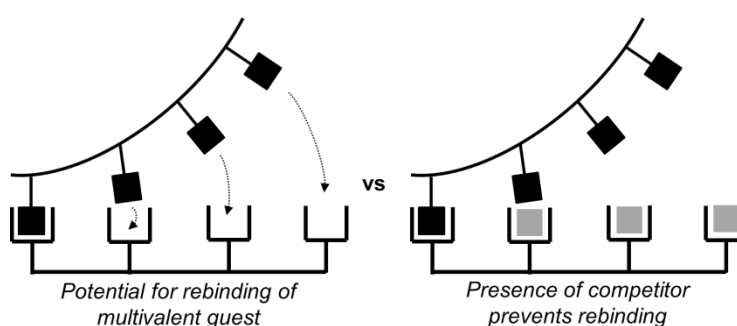


Figure 1.4 – Schematic cartoon of stepwise dissociation of a multivalent binder in the absence and presence of a competitor.

1.1.1.4 Multivalency in Action

Many varieties of multivalent binding arrays, ranging from systems targeted specifically for biological applications to templates to assist in covalent synthesis, have been studied by supramolecular chemists. For example, a programme of work in the group of Whitesides examined the multivalent interactions of the important antibiotic drug vancomycin through comparison against synthetically modified derivatives.²²⁻²⁶ ‘Native’ vancomycin interacts most favourably with a D-Ala-D-Ala host through the formation of five non-covalent interactions, however vancomycin-resistance can be increased when the host is mutated to D-Ala-lactate, as one of the hydrogen bonding opportunities is lost, Figure 1.5.²² In reality, the multivalency of the system still enables vancomycin to bind to D-Ala-lactate, albeit at reduced affinity.²² Whitesides and co-workers then developed a vancomycin dimer and trimer which were shown to exhibit significantly enhanced binding to dimeric^{23,24} and trimeric hosts.^{25,26} Indeed, binding of the trivalent guest to the trivalent host occurred with an association constant ten orders

of magnitude higher than the native monomeric derivatives, producing one of the strongest non-covalent interactions between small molecules ever known.^{25,26}

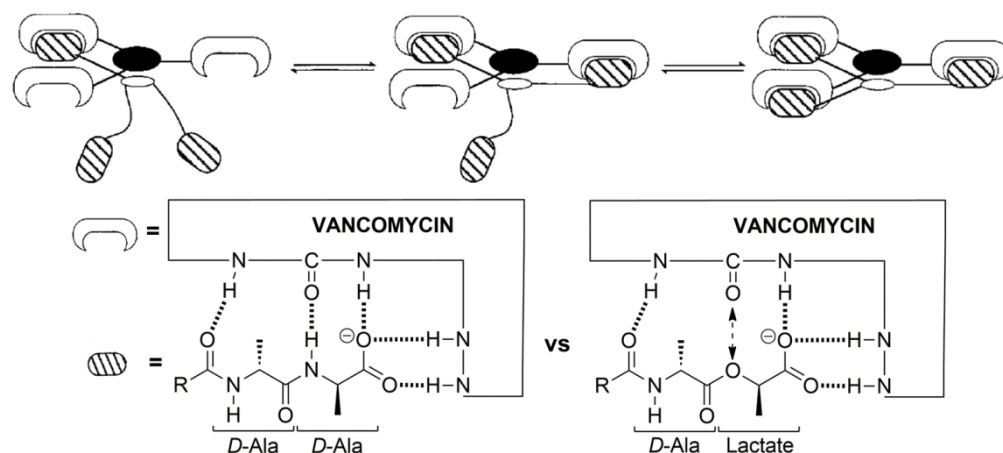


Figure 1.5 – Schematic depiction of trivalent vancomycin host-guest complex (top) along with comparison of monomeric vancomycin binding to D-Ala-D-Lys (bottom left) and mutated D-Ala-lactate (bottom right).

Pseudorotaxanes are supramolecular constructs formed when alkyl threads possessing dialkylammonium ions, $R_2-NH_2^+$, interpenetrate the macrocyclic interior of crown ether structures.²⁷ Dibenzo[24]crown-8 (DB24C8) is a much studied host in this context and, in work somewhat analogous to the vancomycin example above, the cooperativity of binding between multiple DB24C8 species and a multivalent guest, either in linear²⁸ or branched²⁹ form, has been studied. Fusions of three DB24C8 hosts around a triphenylene core by Stoddart and co-workers generated a multivalent system in which complexation of the alkylammonium guests within the crown ether hosts was enhanced by the favourable stacking of aromatic rings on the host and the guest, Figure 1.6.³⁰ Pseudorotaxanes such as this can also be ‘switchable’ owing to the pH controllability of the dialkylammonium species, and this makes them of wide interest in the design of molecular machines.³¹

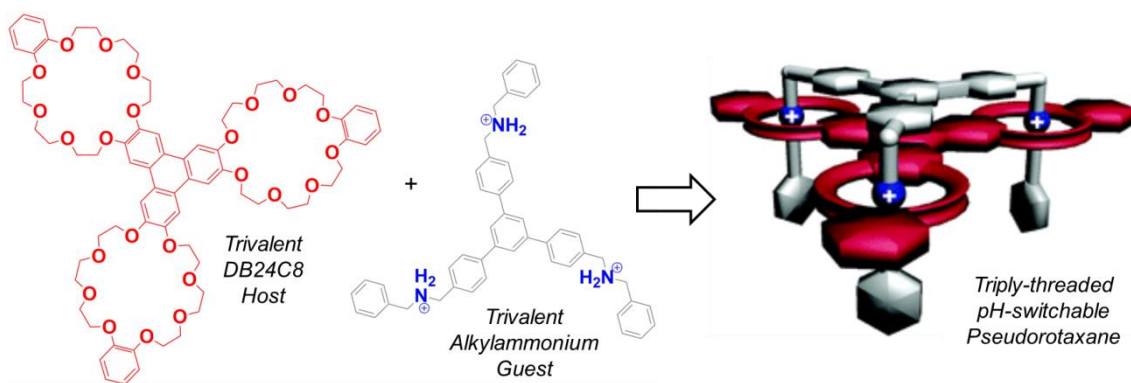


Figure 1.6 – Trivalent pseudorotaxanes from the group of Stoddart. Figure adapted from reference ³².

Other pseudorotaxane species were used in a series of works from the groups of Hunter³³ and Schalley³⁴ to demonstrate the acute sensitivity of the multivalent interactions to the length of the spacer unit between alkylammonium groups. Indeed, lengthening the linker unit by only one additional methylene group from the optimum length was enough to transform binding from positively cooperative into a non-cooperative regime.³⁵

Although host-guest complementarity is often very sensitive to small structural alterations, careful molecular design can reward the chemist with remarkable positive cooperativity. A notable example of this is found in the porphyrin wheels of Anderson and co-workers which showcase almost perfect host-guest preorganization and, somewhat assisted by the rigidity of the systems, form superb multivalent interactions, Figure 1.7.³⁶

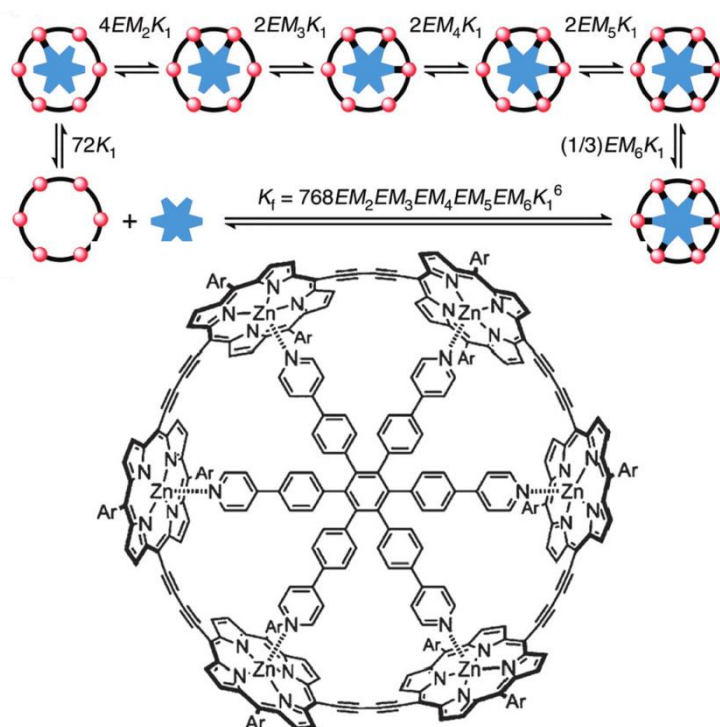


Figure 1.7 – Exquisite ligand preorganization gives Anderson’s porphyrin wheel well optimized multivalent interactions. Figure adapted from reference ³⁷.

1.1.2 Self-Assembly

Molecular self-assembly, as defined by Whitesides in the early 1990s, is the spontaneous association of molecules under equilibrium conditions into stable, structurally well-defined aggregates held together by non-covalent bonds.³⁸ Such self-assembly is ubiquitous in nature, with the tobacco mosaic virus, which is able to spontaneously arrange several thousand amino acid based subunits into a complementary helical sheath able to surround single RNA strands, providing a notable example.^{39,40} Molecular self-assembly also provides a useful tool for chemists designing systems for operation on the nanoscale.^{38,41} Indeed, production of relatively small molecular building blocks endowed with the ability to self-assemble and generate nanosized objects is often a far more attractive proposition than the synthesis of covalent structures of the same size.⁴²

The most widely used approach to this type of self-assembly involves the synthesis of amphiphilic molecules able to organize and assemble themselves in aqueous solution in processes driven by the hydrophobic effect.⁴³ As the concentration of monomer

molecules in solution increases, the non-polar regions within their structures tend to aggregate together, thereby excluding water molecules 'frozen' around their surface from the aggregate interior. The entropy increase associated with the liberation of these water molecules into solution is widely thought to outweigh the decrease in entropy associated with the aggregation of the non-polar components.⁴³ The aggregation of amphiphilic monomers in this way is completely reversible and, as we shall see, the type of aggregates which form are dependent on several factors such as concentration and monomer geometry.⁴⁴ The aggregates which do form often have dimensions on the nanometer scale and so their study has many connections with colloid science; a long-standing research area recognized by Nobel prizes as early as the 1920s.

In 1976, Israelachvili *et al.* published a seminal discussion of the effects of monomer geometry and degree of hydrophobicity upon the subsequent mode of self-assembly.⁴⁵ A critical packing parameter was defined, which allowed the morphology of an aggregate to be predicted based on the relative volumes of the hydrophobic and hydrophilic groups within the structure. As shown in Figure 1.8, when the monomer hydrophilic group is much larger than the hydrophobe, a spherical micelle displaying the polar groups at the surface is favoured. As the volume of the hydrophobic group is increased with respect to the hydrophilic surface group, cylindrical morphologies become more favourable as a means of minimising unfavourable interactions with the aqueous solvents. When the hydrophobicity continues to increase, often through the introduction of a second aliphatic tail, vesicles or liposomes become the optimum mode of self-assembly. When the head and tail groups are of comparable size-in-space, planar bilayer structures form, while when the hydrophobe is significantly larger than the tail group, inverted micelles form with the non-polar groups expressed at the surface and the hydrophilic groups internalised.

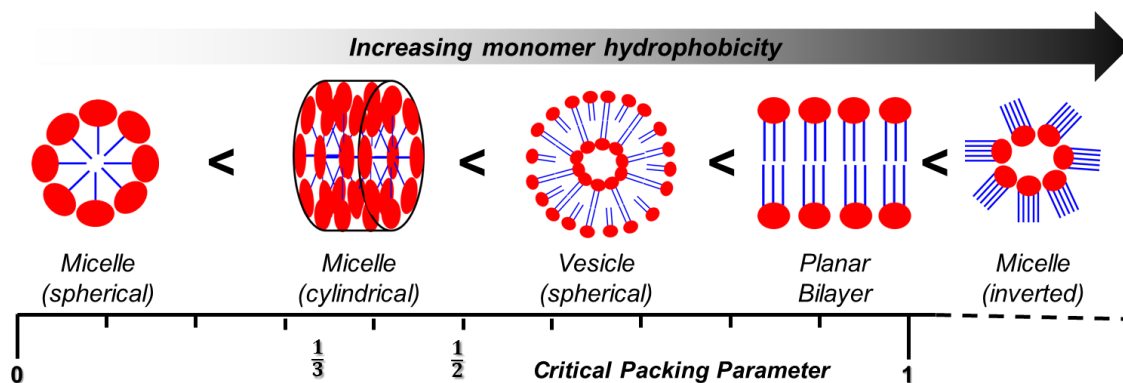


Figure 1.8 – The work of Israelachvili allowed aggregate morphology in aqueous solution to be predicted as a function of critical packing parameter.

1.1.3 Self-Assembling Multivalency (SAMul)

With the potential of multivalent binding and power of molecular self-assembly established, it is not surprising that chemists have combined these two concepts in order to generate nanoscale binding arrays for interaction with large biomolecules through so-called ‘self-assembling multivalency’ or ‘SAMul’. As we shall see, this is often achieved through the use of polar binding groups conjugated to an apolar hydrophobe to generate amphiphilic species with the ability to self-assemble in aqueous conditions. This approach carries many advantages over covalent synthesis for the generation of nanoscale ligands arrays.

For example, self-assembling monomers are individually more synthetically tractable than larger covalent arrays, and their subsequent assembly to generate the nanosystem is spontaneous (under appropriate conditions). The simplified synthetic access additionally makes structural modifications of the monomer units relatively straightforward, introducing the potential for the polar binding groups to be tuned/alterd to allow different targets to be bound by structurally related monomers. Alteration of the apolar hydrophobe also allows for the morphology of the resulting nanostructure to be easily altered. These smaller monomer building blocks are typically more ‘drug-like’ than their larger covalent counterparts, which can increase the likelihood of promising candidates receiving clinical approval.

The SAMul binding approach also makes creation of mixed binding systems straightforward, as different monomer units can be co-assembled into a single

nanostructure leading to synergistic effects, which can be relatively difficult to achieve using covalent methodology. A further key advantage of SAMul binding is the reversibility of the nanosystem assembly event, which allows multivalency to be switched-off in a controllable way. As well as ‘switching-off’ binding events, this disassembly minimizes the persistence of the binding ligand array which, in turn, can reduce toxicity of biologically relevant SAMul systems.

Given these multiple advantages, the employment of self-assembled multivalent (SAMul) techniques is becoming more widely applied and the area was reviewed recently by Barnard and Smith.⁴⁶ In the following sub-sections some of the key SAMul systems are discussed; selected examples have been chosen which fall into the categories of sugar arrays, DNA binding arrays and ligand arrays targeting other species.

1.1.3.1 SAMul saccharide arrays

One of the first examples of self-assembling multivalency came from the group of Whitesides, who developed an amphiphilic system to bind the protein hemagglutinin, Figure 1.9.⁴⁷ They conjugated a sialic acid residue onto a lipid chain to promote the self-assembly event, which increased the binding by a factor of around 100,000 over the monovalent analogue.⁴⁷

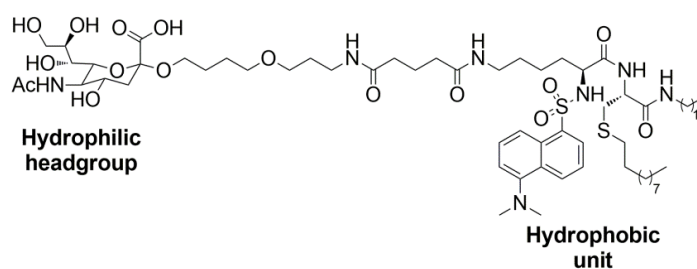


Figure 1.9 – The hydrophobically modified sialic acid derivative from the group of Whitesides was one of the earliest examples of self-assembled multivalency (SAMul).⁴⁷

Since this early work, many systems have been developed to express sugar residues on the exterior of self-assembled nanosystems in order to bind lectin targets such as concanavalin A (Con A). For example, Ravoo and co-workers decorated cyclodextrin vesicular structures with maltose and other sugar residues through coupling of the sugars with adamantane groups, which could then become encapsulated within the CD-cavities.⁴⁸ This created a sugar ligand array which exhibited considerably higher-affinity

for targets than the monomeric non-assembled sugars. Interestingly, within this ternary complex, the multivalent binding to Con A templates a further organization event for multiple CD vesicles, Figure 1.10.⁴⁹

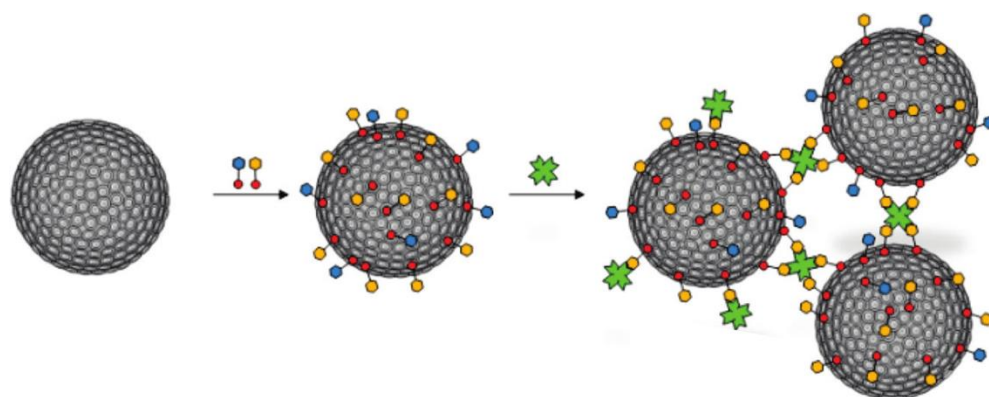


Figure 1.10 – Cartoon of Ravoo and co-workers’ cyclodextrin vesicles (large grey structure) decorated with adamantane-maltose ligands (red and orange) for Con A binding (green). Image reproduced from reference ⁴⁹.

In a similar manner, Kim and co-workers decorated the surface of cucurbit[6]uril vesicles with mannose groups although, rather than adamantane groups, the sugar residue was conjugated to a cationic spermine group as polyamines are more readily encapsulated by cucurbiturils.⁵⁰ Carbon nanotubes (CNTs) have also been employed as ‘templates’ by Bertozzi and co-workers, who functionalised an α -*N*-galactose-amine residue with an aliphatic tail such that the sugar could be ‘self-assembled’ along the CNT surface in order to promote enhanced-affinity binding to cell surface lectins, Figure 1.11.⁵¹

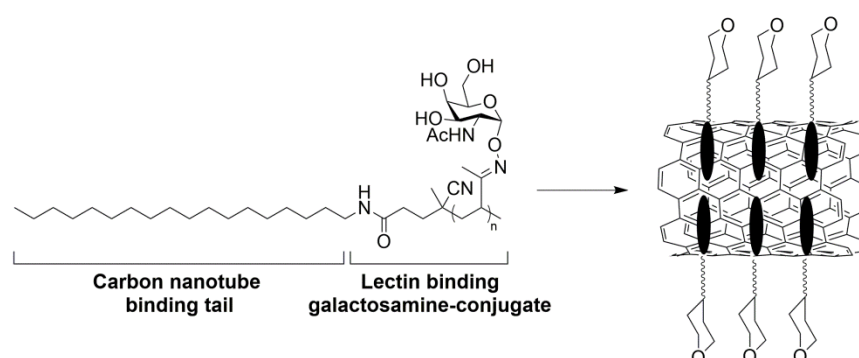


Figure 1.11 – Amphiphilic galactosamine-conjugate from the group of Bertozzi self-assembled along CNTs to achieve high-affinity lectin binding.⁵¹

Of the SAMul examples presented so far, many require some form of template such as a cyclodextrin vesicle or CNT around which the multivalent ligand array can be constructed. Work from the group of Brunsveld adopts a different approach by programming monomers with the ability to self-assemble with each other rather than with a unifying template to generate a nanoscale ligand array for effective target binding. A particular speciality of the Brunsveld group is the production of photoactive discotic molecules containing C_3 -symmetric aromatic cores consisting of three 2,2'-bipyridine-3,3'-diamine molecules connected to a central benzene-1,3,5-tricarbonyl unit.⁵² These units, being planar and aromatic, are readily able to self-assemble into columnar stacks.^{53,54} The density of ligands at the assembly surface can be easily tuned using this approach by carefully controlling the ratio of mono-, di- and/or tri-functionalised discotics present within a 'mixed' columnar stack. When the core is functionalized with water-solubilizing glycol, and suitable binding groups such as mannose are attached, the resulting columnar stacks become able to bind targets such as Con A with enhanced affinity over the non-assembled discotics. Brunsveld and co-workers have adapted this approach to generate SAMul binders able to interact with targets such as Con A and other lectins, *E. coli* and streptavidin, demonstrating the tunability of the SAMul approach, Figure 1.12.^{52,55}

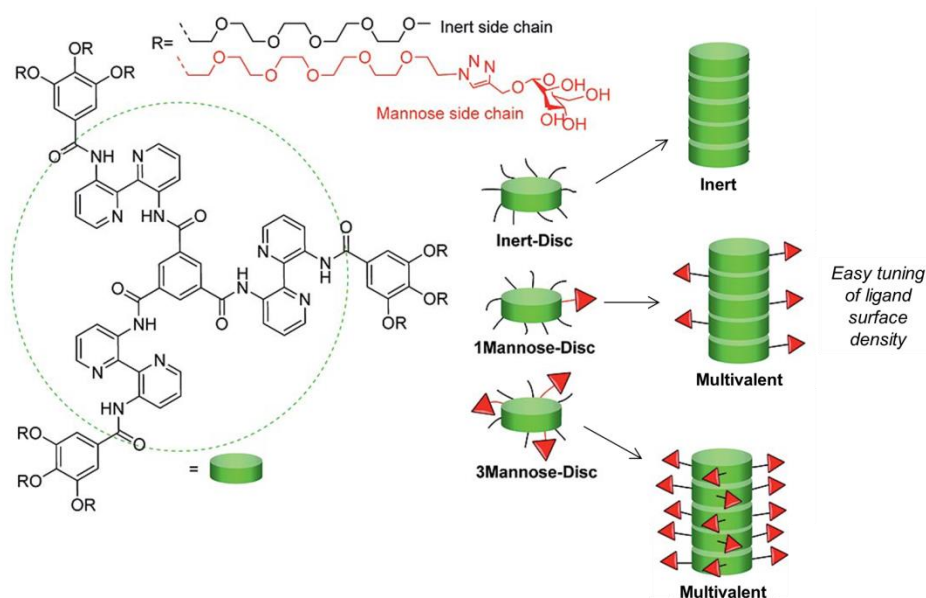


Figure 1.12 – Self-assembling multivalent mannose-functionalised lectin-binding discotic molecules from Brunsveld and co-workers. Figure adapted from reference ⁵².

One of the most interesting observations from the work of Brunsveld and co-workers was that increasing the number of binding groups displayed along each stack did not necessarily correlate with increased target binding. Indeed, in the case of their mannose-functionalized SAMul discotics, tri-functionalization of each monomer disc offered no valency-corrected binding enhancement over the mono-functionalised derivative.⁵² As we shall see later in this thesis, the concept of ‘more is not always better’ is a key feature of many multivalent binding phenomena.^{56,57}

1.1.3.2 *Binding other targets*

All of the examples presented above employ sugar units as the ligand groups, which lead primarily to lectin-type species being targeted for binding. Several other groups have developed SAMul binding approaches targeting different species. For example, work in the group of Urbach employed cucurbit[8]uril to host self-assembly events between scaffolds decorated with methyl viologen, and tryptophan groups,⁵⁸ while Merckx and co-workers developed self-assembling collagen binding micelles.⁵⁹ The groups of Williams and Hunter, meanwhile, developed a cholesterol-dansylamine amphiphile in which the hydrophobic cholesterol became embedded along membrane-water interfaces generating a multivalent display of Cu(II)-binding dansyl ligand groups.⁶⁰ This work provided a notable example of a SAMul approach being used to bind a smaller target species, Cu(II), rather than a large biomolecule.

Work from the group of Smith and co-workers employed a similar amphiphilic design consisting of a hydrocarbon aliphatic tail connected to a hydrophilic Arg-Gly-Asp (RGD) ligand group.⁵⁶ This ligand group was selected to endow the system with integrin binding ability and the study directly compared the performance of this self-assembling monomer against a non-assembling analogue and a larger non-assembling ‘multivalent’ binder, Figure 1.13. The results showed both the larger system and the self-assembling analogue exhibited similarly enhanced binding over the non-assembling monomer due to the multivalency of binding, however the achievement of this enhancement by the self-assembling system required much less effort during the synthetic preparation of the compounds.⁵⁶

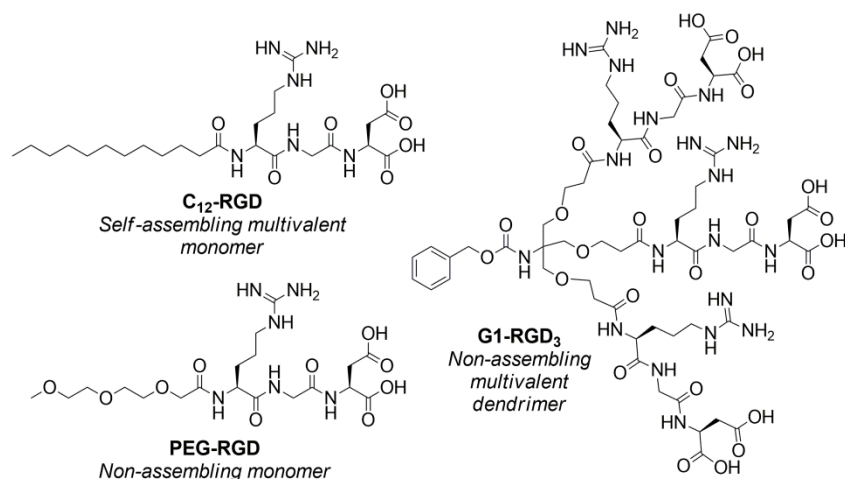


Figure 1.13 – Integrin binding systems from the work of Smith and co-workers.⁵⁶

Smith and co-workers then continued this fundamental study by modifying the hydrophobic component of the monomers to alter the self-assembled morphologies of the nanosystems.⁶¹ Spherical and cylindrical micelles along with rod-like vesicles were examined, and a spherical micellar RGD array was shown to be the optimum architecture for solution-phase integrin binding.⁶¹ This work demonstrated that the display of multivalent binding ligands holds significant influence over integrin binding ability.

1.1.3.3 SAMul approaches to DNA binding

DNA has been targeted by several research groups employing self-assembled binding technologies, demonstrating wide awareness of the potential of a SAMul approach to medicinal treatments of genetic diseases⁶² and even cancer.⁶³

The naturally occurring DNA-binding ligand spermine is amongst the most often utilised surface groups in SAMul systems and featured in notable work from both the groups of Cheng⁶⁴ of Smith.⁶⁵ The approach of Cheng and co-workers directly functionalized spermine with two oleyl hydrophobes, while Smith and co-workers adopted a similar methodology to that used in their integrin binding work by decorating the surface of a low-generation amphiphilic dendron with spermine. Other workers, such as the team led by Ravoo, developed switchable SAMul DNA binders by functionalizing spermine with an azobenzene moiety able to become encapsulated within cyclodextrins at the surface of CD-vesicles.⁶⁶ Example compounds from these approaches are shown in Figure 1.14.

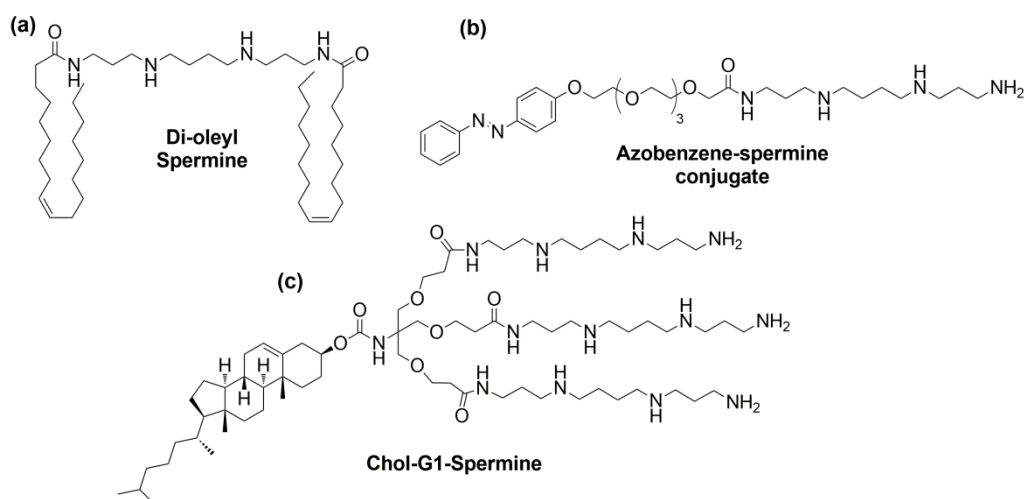


Figure 1.14 – Example spermine-containing DNA binding systems from the groups of (a) Cheng,⁶⁴ (b) Ravoo⁶⁶ and (c) Smith.⁶⁵

The team of Smith and co-workers went on to rigorously investigate their systems through structural modifications at the monomer surface,⁶⁷ within the dendritic branching scaffolds^{68,69} and of the hydrophobe,⁷⁰ as well as examining the effects of co-assembling PEG-additives into the self-assembled nanostructures.⁷¹ Overall, their most optimized potential gene delivery agent contained a DAPMA binding group, a degradable polyester scaffold and a reducible disulfide-containing cholesterol hydrophobe, all of which enabled the system to controllably release its DNA payload before itself degrading into small species with low individual DNA binding affinity.⁷⁰ Other workers have developed related systems targeted at binding siRNA, with the work of Haag, Smith and co-workers⁷² in particular showing good *in vitro* activity and significant promise by provoking no inflammatory response during *in vivo* testing.⁷³

As emphasized by the numerous works discussed in this section, the approach of self-assembled multivalency is receiving ever more attention in the development of novel high-affinity binding systems for a wide variety of molecular targets. From a biological and medicinal standpoint, SAMul approaches present real pharmacological advantages with the smaller monomer structures more easily finding regulatory approval and it is believed by some authors that this approach may eventually lead to ‘undruggable’ conditions becoming treatable through the use of these ‘middle weight’ drugs.⁷⁴

1.2 Heparin Therapy

1.2.1 Heparin: the anti-coagulant of choice

Heparin is most widely known as an anti-coagulant drug and finds applications, for example, during major surgical procedures to prevent blood clots from forming.⁷⁵ Ironically, heparin was discovered by Jay McLean in 1916 during his studies of cephalin, a suspected clotting accelerant.^{76,77} In the two decades following discovery, methods were developed for the effective extraction and purification of heparin and by 1935 pure samples were being used for anti-coagulation in clinical settings, although a reasonable understanding of the mechanism by which anti-coagulation was being achieved was not forthcoming until the early 1970s.^{78,79}

Heparin is a member of the glycosaminoglycan (GAG) family of linear polysaccharides and has a molecular weight range between 2500 – 25000 Da.⁸⁰ Structurally, heparin consists primarily of 1–4 linked uronic acid and glucosamine subunits, Figure 1.15, and the varying degrees of sulfation along these sugar components makes heparin the most complex member of the GAG family.⁸¹ The high levels of sulfation also lead heparin to be the most charge dense polyanion naturally occurring in biological systems, although the absolute biological roles of heparin remain a matter of discussion.⁸²⁻⁸⁴ Heparin is naturally biosynthesised as a proteoglycan and expressed in connective-tissue-type mast cells with pharmaceutical heparin tending to be purified from bovine or porcine mucosal tissue.^{75,80}

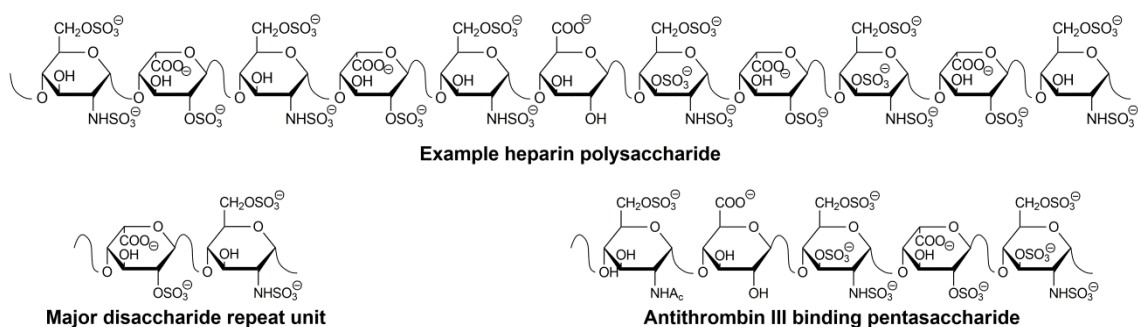


Figure 1.15 – An example heparin polysaccharide (top) along with the predominant disaccharide repeat unit (bottom left) and the specific pentasaccharide sequence required to confer anticoagulant activity (bottom right).

Given the highly polydisperse nature of heparin, it is typically fractionated into narrower molecular weight ranges before clinical application. Low molecular weight heparin (LMWH) consists of polysaccharides with M_r s typically between 4000 – 6000 Da while unfractionated heparin, as the name suggests, encompasses the whole M_r range and tends to have an average M_r of *ca.* 15000 Da.⁸⁵ Of the two, the less-polydisperse LMWH is preferred for use in most types of general and orthopaedic surgeries, where it is introduced either intravenously or through subcutaneous injection, as it offers a more appealing pharmacokinetic profile.⁸⁶ Typically, LMWH is metabolised with a half-life anywhere between 3 – 6 hours, whereas the larger UFH is removed much more rapidly in *ca.* 30 minutes.⁷⁵

Metabolism of heparins tends to occur through two pathways: saturable binding to receptors on endothelial cells and macrophages or renally through the kidneys, although several factors including the degree of sulfation influence the overall rate of heparin metabolism.^{86,87} Further complications in accurately predicting the dose-response of heparin include the amount of plasma-protein binding (PPB) in which heparin becomes involved. LMWH has a more predictable dose-response than UFH as it participates in much less PPB.⁸⁶ Indeed, greater predictability underpins the preference of LMWH for most applications. Extracorporeal procedures such as cardiopulmonary bypass circuits or haemodialysis provide notable exceptions, where the faster metabolism of UFH is highly attractive. Here, the use of UFH allows the anticoagulant effect to be removed more quickly, in some instances without the introduction of a rescue agent.⁸⁸

The blood coagulation cascade *in vivo* is far from straightforward, although it can be simplified into two distinct pathways, Figure 1.16. The ‘intrinsic’ pathway originates from a surface contact trauma event while the ‘extrinsic’ pathway originates from tissue damage.^{89,90} Both pathways involve a plethora of clotting factors, distinguished by roman numerals, becoming activated or deactivated through interaction or reaction with each other, before converging and sharing the final few steps of the cascade to ultimately generate a fibrin-reinforced clot.⁹¹ At the convergence of this ‘common’ pathway sits Factor-Xa, which plays a key role catalysing the production of thrombin, the species responsible for catalysing the production of the insoluble fibrin fibre and the final clot. It is the ability of heparin to directly inhibit the catalytic activity of thrombin, thereby retarding the production of fibrin, which primarily confers the anti-coagulant activity.^{86,92}

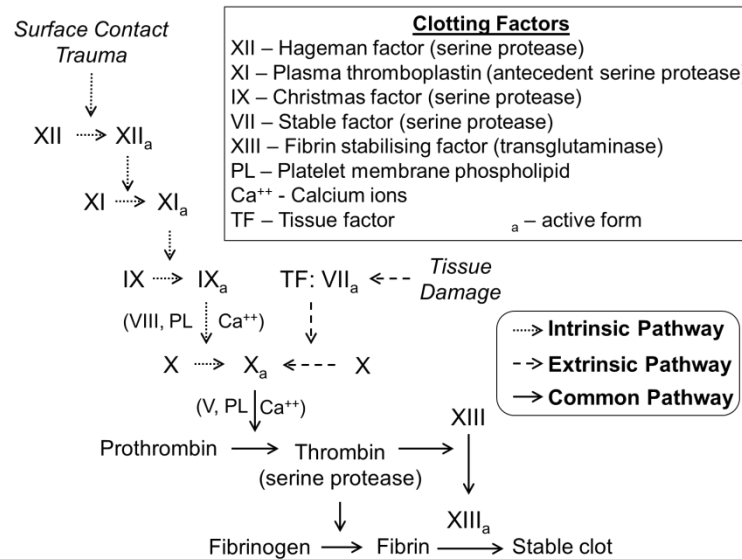


Figure 1.16 – Schematic representation of the blood coagulation cascade.

In order to effectively inhibit thrombin, a specific pentasaccharide sugar sequence within heparin forms a ternary complex with thrombin and the naturally occurring thrombin inhibitor, antithrombin III (ATIII). The presence of heparin accelerates the natural inhibition of thrombin by ATIII by several orders of magnitude.⁹³ Despite these impressive credentials, the requirement of the specific pentasaccharide sequence shown in Figure 1.15 renders larger amounts of every heparin dose inactive as an anticoagulant as the structural variability of heparin leads to only 15–25% of all LMWH and 30–40% of UFH being composed of this specific pentasaccharide sequence, or so-called High Affinity Material (HAM).⁹⁴ It is for this reason that, within clinical settings, heparin amounts are discussed in terms of anticoagulant activity, measured in terms of ‘international units’, rather than in terms of mass.

It is not uncommon for drugs to be standardised in terms of activity and the definition of the heparin unit has evolved since its implementation by Howell in the 1920s.^{78,95} This so-called ‘Howell unit’ was first defined as the amount of heparin required to prevent one millilitre of cat’s blood coagulating at 0°C.^{78,95} Following this, the first of many international standards of heparin was established in 1943 before being superseded 16 years later.^{96,97} In its current, and sixth, manifestation, the international heparin standard (IHS) is calibrated by using all current major assay methods to determine the amount of heparin required to cause one millilitre of sheep plasma to half-clot when held for one hour at 37°C.⁹⁴ Most often, assays such as the activated partial thromboplastin time

(aPTT) technique⁹⁸ and anti-factor Xa assay⁹⁹ are used for these purposes.⁹² These procedures will be discussed in more detail in the Heparin Sensing section below.

Commercially, heparin is also sold in terms of activity rather than mass, and so each individual batch is tested post-extraction and assigned an activity. It is possible therefore to purchase, for example, 100 KIU (that is 100,000 IU) of heparin with a designated activity of 185 IU mg⁻¹.

1.2.2 Heparin Rescue

At the conclusion of a procedure in which heparin has been used, there is usually an immediate need to neutralise the anti-coagulant effects and allow the patient to return to homeostasis. To do this, a so-called ‘heparin rescue’ agent is often introduced into the patient. Currently, protamine sulfate – an arginine rich shellfish protein of ill-defined structure – is the only licensed heparin rescue agent available in the clinic, although its use is not without consequence.¹⁰⁰ Structurally, the protamine protein strand is composed of approximately 70% arginine amino acids which confer highly cationic character and promote electrostatically driven heparin binding, Figure 1.17.¹⁰¹

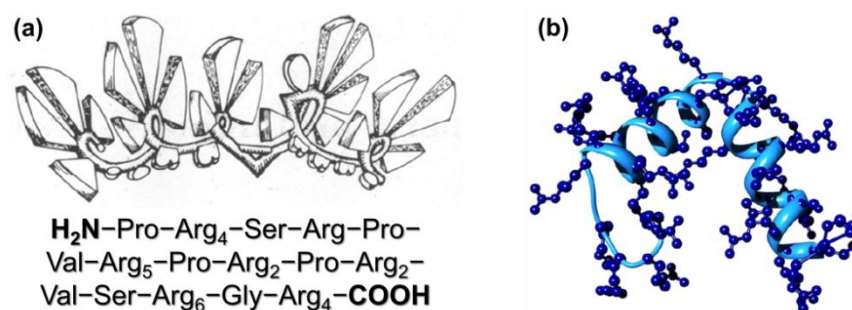


Figure 1.17 – An example protamine structure (a) with the prevalent arginine residues depicted as wedges, adapted from reference¹⁰¹ and (b) a molecular dynamic modelling snapshot of protamine, taken from reference¹⁰².

Much like UFH, protamine itself is usually introduced intravenously to the patient and once there, it is relatively short-lived with an *in vivo* half-life of less than 10 minutes.^{103,104} This transient presence can cause problems with the use of protamine, particularly given the previously mentioned tendency of heparin to bind to plasma proteins (PPB).¹⁰⁵ Often by the time such PPB-heparins are released back into the systemic blood flow, any free protamine may have already been metabolized away. This

can lead to the phenomenon of ‘heparin rebound’ where the now-released heparin causes a second anti-coagulant event.^{106,107} Such rebound is widely regarded as an associated risk of protamine use and some authors recommend a second, smaller, dose of protamine should be administered to avoid it, although interestingly other authors go so far as to regard heparin rebound as “much ado about nothing.”^{108,109}

A further major problem associated with the clinical use of protamine is the toxicity risk presented to a significant number of patients, and it is this which prevents a larger dose of protamine being administered in the first place to negate heparin rebound. Adverse reactions are known in up to 10% of protamine-treated patients, with up to 2.6% of cardiac surgeries experiencing significant respiratory complications and/or hemodynamic instability when protamine is used.¹¹⁰⁻¹¹² Nybo and Madsen have systematically reviewed the serious allergic reactions to protamine and demonstrated that factors as diverse as allergy to fish and whether a patient is infertile or has previously had a vasectomy can impact on the likelihood of an allergic response.¹¹³ Kimmel and co-workers added to this discussion by suggesting that such allergic reactions are often under-reported and so these statistics may actually provide an underestimate of the true hazards associated with protamine.¹¹⁴

A further limitation to the clinical usefulness of protamine is its inability to fully neutralise LMWH.¹¹⁵ This intermittent effectiveness has been investigated by Chan and co-workers who found that resistance to protamine came primarily from very low molecular weight heparin chains, which possess lower-than-normal levels of sulfation.¹¹⁶ LMWH contains a higher proportion of these shorter, less anionic polysaccharides than UFH and this accounts for the decreased effectiveness of protamine in the neutralization of LMWH.

Given the many problems associated with protamine, it is perhaps surprising that it still finds such prevalent use. In reality, the situation was aptly surmised by Stafford-Smith and co-workers in 2005: “in the absence of a safer replacement, undesirable effects [are] outweighed by its utility as the only available heparin-reversal agent.”¹¹⁰ As we shall see in the Heparin Binding section below, there has been much research undertaken in the search for an equally effective but less risky method for heparin reversal.

1.3 Heparin Sensing

1.3.1 Monitoring heparin levels

1.3.1.1 During surgery

Throughout a procedure in which heparin is administered, there are two periods of time during which it is critical to monitor the anti-coagulation level of the patient. Firstly, whilst the procedure is in progress, suitable heparin levels must be maintained to ensure that clotting does not begin prematurely and hinder the surgical team. To do this, a range of so-called ‘clotting time assays’ are widely applied in the clinic.¹¹⁷ As the name suggests, these record the time taken for samples of the patient’s blood to clot.¹¹⁸ Put simply, a longer clotting time indicates higher levels of anti-coagulation and a higher level of active heparin.

There are many different clotting time assays capable of monitoring the anti-coagulancy of a clinical sample and there is much literature discussion and comparison of their relative effectiveness and reliabilities.^{117,119,120} Two of the most widely used clotting time assays are the activated partial thromboplastin time (aPTT assay)⁹⁸ and the anti-Xa assay.¹²¹ The aPTT technique specifically monitors clotting time *via* the ‘intrinsic’ clotting pathway, while the anti-Xa technique relies on the formation of a ternary complex between a known excess of Factor-Xa, ATIII and heparin. Following the introduction of a chromogenic mimic of the natural Xa substrate, the amount of non-complexed Xa can be detected in order to indirectly calculate the amount of heparin present.⁹⁹

The reliability of each of these assays has been questioned by several authors. For example, Rosenberg and co-workers¹²¹ pointed to limitations of the aPTT approach due to intra- and inter-patient variability while the teams led by Ignjatovic⁹⁹ and Raymond¹²² shared the view that particular care must be taken to select the most appropriate technique for the procedure being undertaken. It is widely accepted however that the various clotting time techniques do afford reasonably accurate measures of the anti-coagulancy of a sample and, therefore, the levels of active heparin.^{118,120}

1.3.1.2 *At the conclusion of surgery*

At the conclusion of a procedure in which heparin has been used, the focus of the clinicians immediately switches from needing to know how much active heparin is present (i.e. the level of anti-coagulancy) to how much total heparin polysaccharide is present (i.e. irrelevant of anti-coagulant activity). The indiscriminate binding of protamine to heparin, regardless of the polysaccharide's activity, is the underlying reason for this change in viewpoint. The aforementioned risks associated with incorrect protamine dosing further emphasizes the importance of accurately quantifying the amount of heparin remaining in the patient.¹²³ It is perhaps surprising therefore that in the clinic, residual heparin levels are still determined through clotting time based techniques such as aPTT or anti-Xa measurements.

As discussed in the previous section, these techniques can each provide a good measure of the anti-coagulant activity of heparin within a given sample.¹²⁴ It is not straightforward however to determine the global load of polysaccharide from these values as the proportion of active heparin present in any given dose varies from batch to batch. Consequently, there is a real need for an alternative methodology whereby the total load of heparin polysaccharide present systemically within the patient can be accurately and rapidly determined.

As we shall see in the sub-sections which follow, there have been a variety of approaches to this problem, often from supramolecular chemists specializing in controlling non-covalent interactions between different molecular species. It must be remembered however that developing a system to interact with, or sense, heparin within the regime described here requires the non-covalent interactions to be established selectively with heparin within a complex biological medium such as serum, plasma or even whole blood. This challenge is far from trivial.

The detection and quantification of polysaccharides in aqueous media is an important task in many medicinal and industrial contexts.¹²⁵ As such, there is an impressive body of literature on sugar sensing, with much focus falling on the utilization of boronic acid moieties.^{126,127} Boronic acids are particularly effective as sugar or diol targeting species, where interactions result in the reversible formation of boronate esters.¹²⁸ When suitable chromogenic or fluorescent groups are appended onto them, the establishment of these interactions can facilitate a sensing event, which in turn can be tuned through molecular

design to respond preferentially to specific targets such as, for example, glucose¹²⁹ or fructose.¹³⁰⁻¹³² As we shall see below, boronic acid derivatives were also amongst the first synthetic systems to be investigated for heparin sensing.

1.3.2 Electrochemical sensing

Several researchers have developed systems able to exhibit a potentiometric response upon heparin binding.^{133,134} Such systems were designed such that binding occurred with all regions of the polysaccharide regardless of anti-coagulant activity, and so the measurements could be taken as representative of the global amount of heparin within a given sample. As an example, Yang and co-workers developed a system incorporating cationic units into PVC membranes and films and, impressively, were able to obtain a quantitative heparin binding response even when using relatively non-functional quaternary ammonium groups as the cationic species within the membrane, Figure 1.18.¹³⁵ Optimization of this system can be achieved by altering the cationic polymer within the membrane, and most impressively, sensing in this manner can operate within full human blood. A limitation of this methodology, however, is the irreversibility of heparin binding to the membranes, as this necessitated a rinsing step between sensing events; something of a detraction for clinicians. Nonetheless, numerous groups have investigated this approach, with detection limits in some cases reported to be as low as 0.005 IU mL^{-1} .¹³⁶⁻¹³⁸

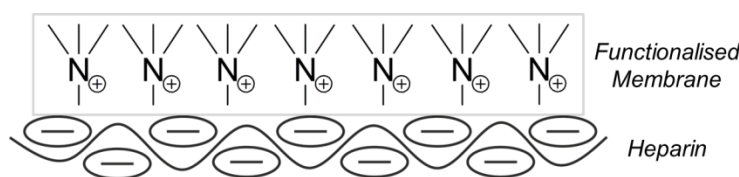


Figure 1.18 – Schematic representation of heparin binding to Yang’s quaternary amine functionalized membrane.¹³⁵

1.3.3 Colorimetric sensing

By far the most prevalent approaches to developing heparin sensors are those targeting spectrophotometric or fluorescent dye systems, primarily due to their potential for a simple read-out. As we shall see in some of the following examples, it is possible to develop systems which can in some cases respond to heparin in preference to other anionic species.

Early fluorescence-based approaches monitored the inhibition activity of heparin when binding to a fluorescent thrombin substrate.^{139,140} This is an example of an indirect approach to heparin quantification as only non-heparin-bound thrombin reacted with the substrate to generate the fluorescent response. Although this approach was relatively fast in the clinic, with the requisite filtration and measurement of the resulting plasma sample taking only 5 minutes, it has not widely been employed due to problems maintaining and reliably calibrating the instruments.¹²⁰

1.3.3.1 Switch-off sensors

It is preferable for heparin detection to be direct, and for that reason much attention has focused on indicator dye systems capable of exhibiting significant switch-on or switch-off response upon direct interaction with the heparin polysaccharide. In the same way as the binding of protamine to heparin, direct detection in this manner can quantify the total amount of heparin present, rather than only the anti-coagulant active portion.

Commercial thionine-derived dyes were amongst the first to be investigated for this purpose, although not without problems.^{141,142} In particular, although Azure A, a simple commercial cationic dye, was purported to be able to monitor heparin levels in plasma,¹⁴¹ it was also known to be acutely sensitive to many of the electrolytes present in biological samples.¹⁴³ These issues are examined in detail in Chapter 2.

Given the general unreliability of commercial systems, as typified by the Azure A example, interest was fuelled in the design and development of bespoke synthetic systems. Landmark work came in 2002 from the laboratory of Anslyn and co-workers who synthesised a tris-boronic acid species able to indicate indirectly through displacement of a pyrocatechol violet indicator dye.¹⁴⁴ In order to allow for direct heparin response, the system was elegantly modified to incorporate the fluorophore into the binding site, Figure 1.19.¹⁴⁵ This allowed for an association constant of $1.4 \times 10^8 \text{ M}^{-1}$ to be determined in 10 mM HEPES buffered at pH 7.4, and also for binding to be observed in human serum. Upon binding to heparin within Anslyn's system, the associated spectroscopic signal exhibits a decrease in intensity. This type of system can be categorized as a switch-off sensor.

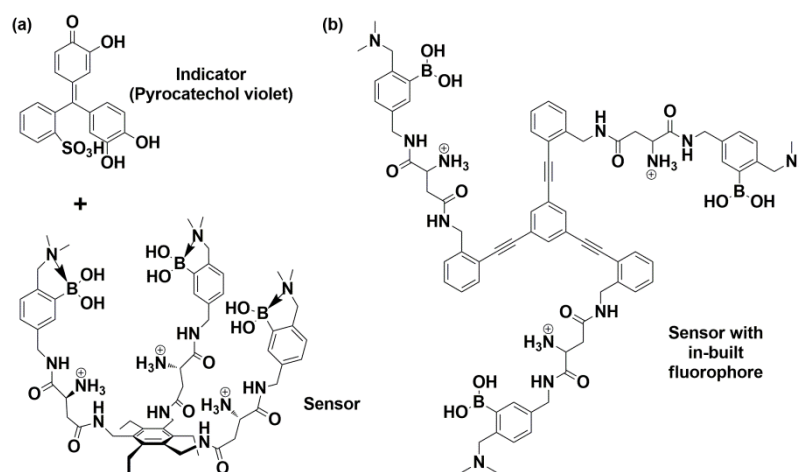


Figure 1.19 – Anslyn’s heparin sensors operating (a) in an indicator displacement regime¹⁴⁴ and (b) using a single molecule fluorescent sensor.¹⁴⁵ These structures are also shown in Figure 3.2.

Many switch-off sensors have been developed, with a notable example within the last decade coming from the work of Egawa and co-workers. Their strategically sage approach involved the functionalization of protamine with fluorescent fluorescein moieties which, upon binding heparin, became located within the Förster distance required for self-quenching, leading to the ‘switch-off’ of the observed signal.¹⁴⁶ Clearly, the key advantage of this approach is that the heparin binding array is protamine itself and so the reported binding for each sample of heparin should be indicative of precisely what protamine will be able to bind to.

Other fluorescent switch-off sensors came from the group of Chen and co-workers who created an array of cationic sugars by appending them onto a conjugated polymer scaffold, Figure 1.20.¹⁴⁷ The fluorescence of this scaffold became quenched when the cationic groups bound to heparin as it led to aggregation of the scaffold units. A similar approach from Bhosale and co-workers functionalized a kanamycin A derivative with a pyrene moiety, which became quenched as the sugars bound to heparin.¹⁴⁸ Although effective, this system only responded at relatively high concentrations of heparin.

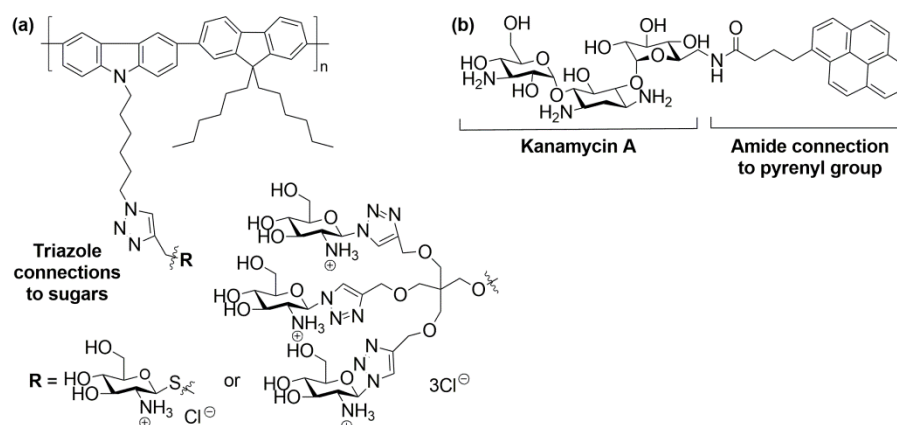


Figure 1.20 – Fluorescent sugar-containing heparin sensors from the groups of (a) Chen¹⁴⁷ and (b) Bhosale.¹⁴⁸

A particularly interesting switch-off sensor came from the work of Schrader and co-workers, who designed a multi-binding methacrylamide polymer which, clearly inspired by the landmark work of Anslyn,¹⁴⁵ was decorated with *o*-aminomethylphenyl-boronate derivatives, along with fluorescent dansyl groups.¹⁴⁹ Most impressively, even in the absence of any charge, near micromolar heparin binding was observed in the presence of 25 mM HEPES buffer. In this system, the interactions were not strictly non-covalent as covalent boronate-esters form between the polymer and heparin, but these bonds were fully reversible, as demonstrated by their cleavage upon the addition of protamine.

1.3.3.2 Switch-on sensors

As insightful as the plethora of switch-off sensors can be, switch-on sensors carry the advantage of even easier detection, as the spectroscopic signal increases from zero upon heparin binding. Often, the signal switch-on is the result of a triggered aggregation event. An example from Zhang, Zhu and co-workers involved the use of an ammonium functionalized silole species which aggregated in the presence of heparin leading to a switch-on response.¹⁵⁰ The system was shown to be effective in the presence of sulfate rich HEPES buffer and also in horse serum although there was a need to manually subtract the signals from the fluorescence of serum itself. In a related, albeit more synthetically complex, example from Wang and co-workers, a pyrene functionalized quinine exhibited switch-on fluorescence in the presence of heparin due to the formation of an excimer complex between two molecules of dye and the heparin biopolymer.¹⁵¹ Selectivity for heparin over other GAGs was demonstrated for this example and

rationalised by Wang and co-workers to be due to structural compatibility between heparin and the indicator dye.

Selective heparin binding was also achieved by Liu and co-workers who developed a range of versatile conjugated polyelectrolyte structures appended onto a polyfluorene backbone, Figure 1.21.¹⁵²⁻¹⁵⁴ Their system was able to respond to heparin either in a switch-on, direct colorimetric or ratiometric fashion as a result of aggregation. Indeed, the colour change upon heparin binding in 2 mM PBS was so vivid that it could be observed by the naked eye, and was easily differentiable from binding to other GAGs such as hyaluronic acid. Other examples of this type of aggregation-induced fluorescence can be found in the work of Wang and co-workers, who developed similar cationic conjugated polyfluorene systems to Liu.¹⁵⁵ Král and co-workers, meanwhile, focussed on the development of polymethinium salts which exhibited selective heparin binding at the more acidic pH of 5.53 in 1 mM phosphate although it was not clear whether the same results could be reproduced under more biologically relevant conditions.¹⁵⁶

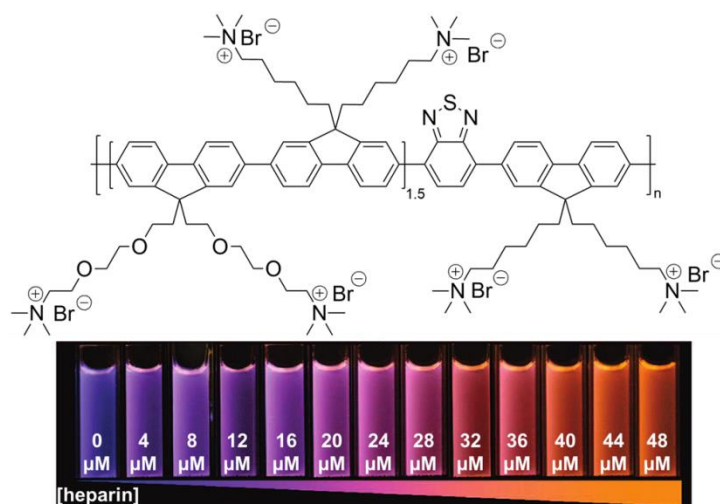


Figure 1.21 – A polyfluorene heparin sensing derivative from Liu and co-workers.¹⁵⁴

One of the main limitations of developing fluorescent sensors which are able to sense heparin in biological conditions such as serum is the problem of serum auto-fluorescence. Specifically, the hydrophobic regions of serum tend to exhibit fluorescence following excitation with short wavelengths of light and, at concentrations as low as *ca.* 5% serum, this effect becomes sufficient to render any sensing response meaningless. In order to overcome this, there have been several efforts to develop

sensors which fluoresce at longer wavelengths. A particularly eye-catching attempt at this came from Nitz and co-workers with a system based around the polyelectrolyte effect.¹⁵⁷ They developed a cationic sensor which had its fluorescence quenched by chloride counter ions meaning that a switch-on response was observed upon binding to heparin, as this caused chloride anions to be expelled from the binding ensemble. Disappointingly though, the system was too insensitive to detect heparin at clinically relevant concentration levels. A more promising longer-wavelength fluorescent sensor came from Krämer and co-workers who synthesised a perylene diimide species, Figure 1.22, which fluoresced at 615 nm following excitation at 485 nm and was able to achieve meaningful detection of LMWH in up to 20 vol% of serum and/or plasma.¹⁵⁸

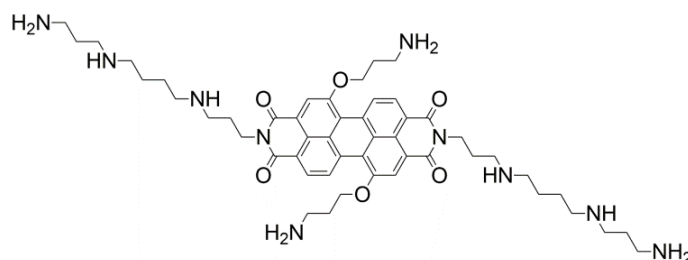


Figure 1.22 – A perylene diimide sensor structure from Krämer and co-workers.¹⁵⁸

Other researchers have employed different methods for working around serum auto-fluorescence. For example, Yam and Yeung developed an alkynylplatinum(II) complex which emitted in the near infra-red (NIR) region upon binding to heparin.¹⁵⁹ Their system also gave useful circular dichroism signals; the magnitude of which allowed differentiation between UFH, LMWH and other GAGs such as chondroitin sulfate.

Arguably the most promising, and fundamentally impressive, switch-on fluorescent sensor to date came from the work of Chang and co-workers, who employed a high-throughput diversity-oriented fluorescent library approach (DOFLA) in their search for an effective sensor.¹⁶⁰ This approach is significantly different to the previous examples presented above, which generally originated from some modicum of semi-rational design. Chang's DOFLA approach was able to screen a large number of molecules and identified two particularly promising functionalized benzimidazolium dyes, named heparin orange and heparin blue after their respective colours, Figure 1.23. These dyes were able to respond significantly to clinically relevant concentrations of heparin, even in the presence of 20% human plasma. Moreover, these sensors are only dicationic at

physiological pHs which further suggests that the DOFLA approach identified well optimized structures.

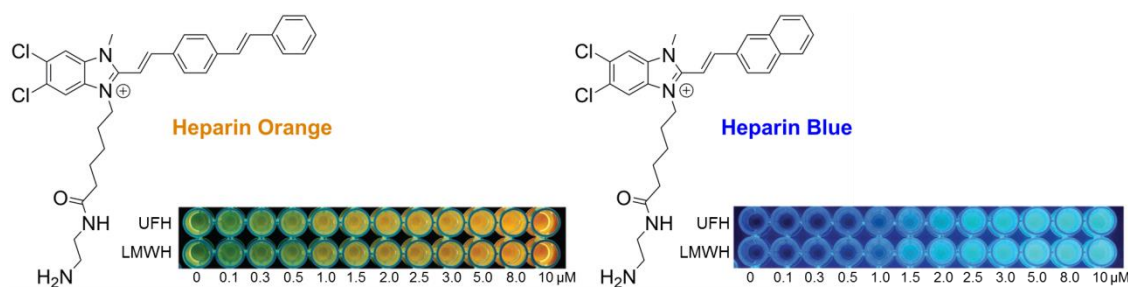


Figure 1.23 – Heparin orange and heparin blue, discovered *via* a diversity-oriented library approach in the group of Chang.¹⁶⁰

1.3.3.3 Ratiometric sensors

In addition to the work involving single sensor dyes presented above, there is a growing interest in sensing systems involving more than one indicator dye. This approach usually takes the form of ratiometric sensing, which involves monitoring spectroscopic changes at two wavelengths to provide internal calibration of the system: a key advantage over a single dye approach.

The team lead by Zhang adopted this methodology and their two component binding ensemble provides an excellent recent example of ratiometric heparin sensing.¹⁶¹ The ensembles consisted of an alkyl-ammonium functionalised anthracene derivative which exhibited a decrease upon binding to heparin as a result of aggregation-caused quenching (ACQ), and an alkyl-ammonium tetraphenylethene (TPE) species which exhibited enhanced fluorescence upon binding due to aggregation-induced emission (AIE), Figure 1.24. The unusual phenomenon of AIE is widely thought to be associated with the enhanced conjugation which results from the coplanarisation of photoluminescent groups, such as TPE, upon intermolecular assembly.^{162,163} Consequently, when both components in Zhang's system bind to heparin, in a 10 : 11 ratio, monitoring the relative ratio of their fluorescence intensities affords ratiometric data. Although more robust than some single-dye approaches, correction factors still needed to be introduced when heparin sensing was carried out in serum.

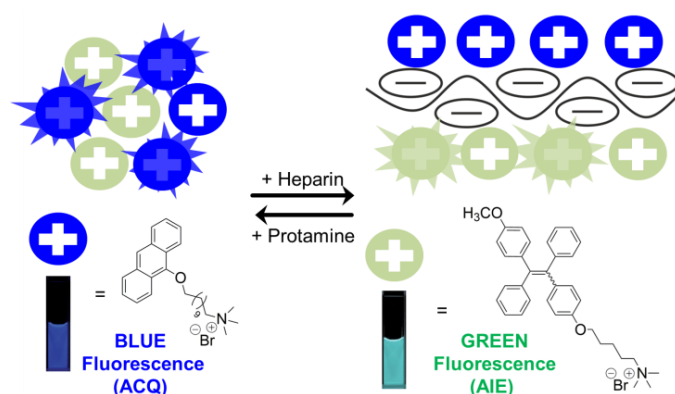


Figure 1.24 – Two-component heparin sensor from Zhang and co-workers.¹⁶¹

Similar AIE approaches have recently been adopted by other researchers such as Tang, Liu and co-workers who developed a fluorene-based system which adopted a propeller-like conformation to exhibit a fluorescence enhancement upon interaction with heparin.¹⁶⁴ A particularly selective AIE-based heparin sensor has also recently been forthcoming from Tong and co-workers, which in addition to high selectivity, exhibited acute sensitivity with a heparin detection limit of 57.6 ng mL^{-1} .¹⁶⁵

Krämer and co-workers, meanwhile, built on their earlier approach of using long wavelength fluorescent dyes by developing a pair of cationic ruthenium complexes in which, upon co-assembling on heparin, the proximity of the second complex quenched the fluorescence of the first leading to a detectable optical output at 630 nm.¹⁶⁶ Although this system was able to detect heparin within a clinically useful concentration range in the presence of serum, the system was not selective for heparin and so responded somewhat to the presence of other GAGs.

Other recent attempts to work around serum-autofluorescence from Zhao, Liu and Huang employed a phosphorescent conjugated polyelectrolyte (PCPE) containing an Ir(III) complex which was able to selectively respond to heparin in a ratiometric manner both in aqueous solution and in the presence of serum, Figure 1.25a.¹⁶⁷ Most impressively, this system was able to respond to heavily diluted samples of heparinized human blood. In separate work, the fluorescently-labelled peptide of Lee and co-workers was not tested directly in human blood, although it did offer remarkable sensitivity, in the picomolar (pM) range, in aqueous solutions across a range of pHs and also in samples containing 5% serum or plasma, Figure 1.25b.¹⁶⁸

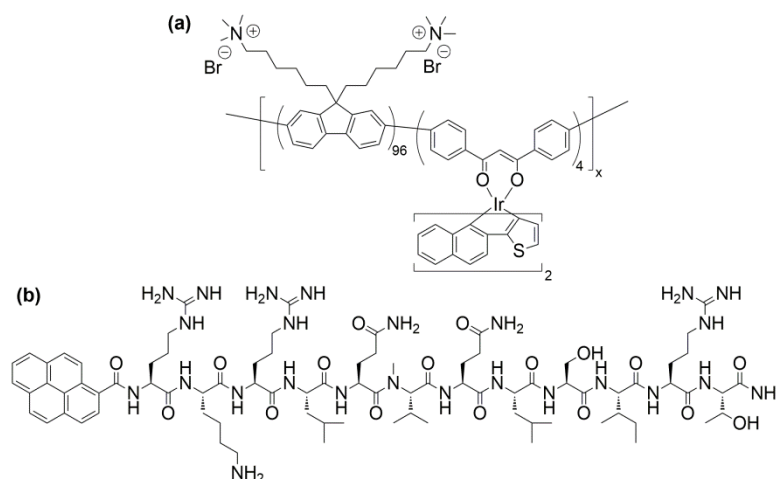


Figure 1.25 – Selective ratiometric sensors: (a) phosphorescent conjugated polyelectrolyte structure from Zhao, Liu and Huang¹⁶⁷ and (b) peptide structure from Lee.¹⁶⁸

1.3.4 Solid/nanoparticle supported sensing

All of the heparin sensors presented so far operate within the homogeneous solution phase, however there are a growing number of heterogeneous and/or nanoparticle approaches to heparin sensing. For example, the aforementioned sensors developed by Krämer and co-workers have been immobilised on SiO₂ beads in an attempt to increase the commercial appeal of the system.¹⁶⁶ Disappointingly, this modification retarded the heparin on-rate, decreasing the efficacy of the system and meaning further development is still required if such a system is to become commercialised. This gives a suitable reminder that molecular-scale chemical considerations are not the only drivers which must be addressed in the search for viable heparin sensing systems.

The group of Martínez-Mañez, Marcos and co-workers functionalised silica nanoparticles with both thiols and cationic amines to generate a sensing system in which a fluorescent squaraine dye was perturbed in the absence of heparin due to the nucleophilic attack of the surface thiols.¹⁶⁹ In the presence of heparin, the surface amines interacted with the polysaccharide causing it to wrap around the NPs and prevent the thiol-induced perturbation of the squaraine, thereby leading to the detection event. Unfortunately, the poor solubility of the NPs within this system necessitated operation in the clinically unappealing presence of 45% DMSO and 10% CH₃CN.

Gold nanoparticles (AuNPs) have been investigated in heparin, and indeed protamine, sensing situations by several groups trying to utilise the distance-dependant optical properties of the AuNPs.¹⁷⁰ For example, Li and Cao functionalized AuNPs with cationic cysteamine groups and were able to observe an absorbance change at 670 nm as the AuNPs aggregated along the heparin chain.¹⁷¹ This system was demonstrated to be operable in the presence of 1% human serum with a detection limit of $0.1 \mu\text{g mL}^{-1}$. Another well thought out method involving AuNPs came from the work of Chen and co-workers, who monitored the change in surface plasmon resonance signals as AuNPs aggregated on a graphene oxide (GO) surface, Figure 1.26.^{172,173} In this example, the AuNPs were capped with anionic citrate groups and protamine was used to bridge between the GO and the AuNPs, assisting their aggregation along the surface. Upon the addition of heparin, protamine was sequestered from this bridging role by forming preferential electrostatic interactions with the polysaccharide, and the AuNPs thereby deaggregated away from the GO surface. The resulting ‘blue-to-red’ colour shift indicated the extent of de-aggregation, which in turn corresponded directly to the amount of heparin present. Remarkably for such a complex-sounding methodology, heparin could be quantified down to $1.0 \mu\text{g mL}^{-1}$ at pH 7.4, and also in fetal bovine serum.

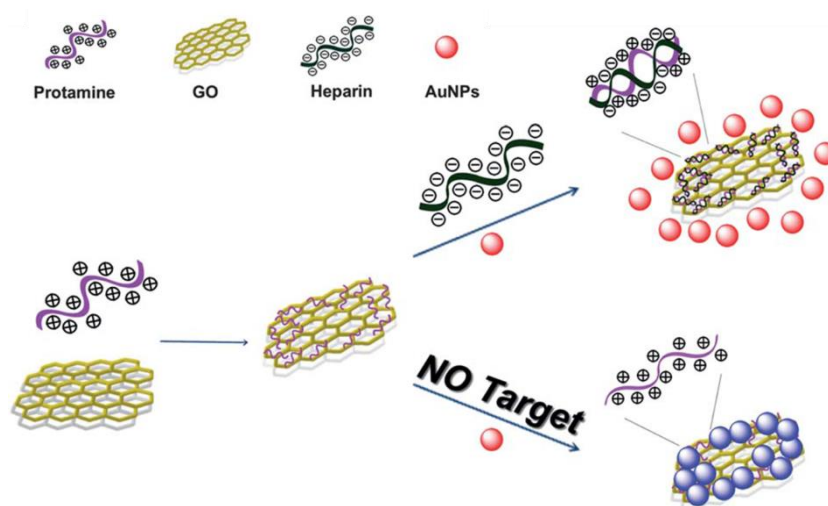


Figure 1.26 – Graphene-AuNPs sensing system from Chen and co-workers. Figure adapted from reference ¹⁷².

As we have seen throughout this section, there have been a variety of promising approaches to developing a novel heparin sensing system able to accurately determine the residual systemic amount of heparin in a biological sample, however to date none of

these approaches have reached the clinic. Our attempts to address this problem are detailed in Chapter 2. The next section considers some of the landmark efforts to address the problem of heparin reversal *in vivo*, through the search for an alternative to the current heparin rescue agent, protamine.

1.4 Heparin Binding

The focus on developing novel heparin binding systems with the potential to replace the clinical use of protamine has understandably centered on cationic systems. Indeed, protamine itself uses multiple arginine and lysine cationic amino acids to establish favourable electrostatic and hydrogen bonding interactions with the anionic heparin biopolymer. In order to have clinical potential, synthetic protamine alternatives must readily bind heparin in competitive biological media and, crucially, possess more appealing toxicity profiles than protamine. Much like heparin sensing, heparin binding has attracted a significant amount of attention although, as yet, no fully-functional protamine replacement has been found. In the following sub-sections, some of the landmark work in the area will be discussed.

1.4.1 Enzymatic, protein-based and polymeric systems

Given that protamine is itself a protein, there have been several attempts to apply other protein-based or enzymatic systems in its place. An early enzymatic approach involved the use of *heparinase I* enzymes to cleave glycosidic bonds between heparin saccharides effectively fragmenting the biopolymer into smaller units and removing its anti-coagulant properties. Although somewhat effective, the use of *heparinase I* in trials was associated with a higher likelihood of a patient requiring a blood transfusion than when treated with protamine.^{174,175}

Lactoferrin is an iron binding protein released from neutrophils, which is thought to play an active role in heparin control owing to having superior binding ability to protamine *in vitro*.¹⁷⁶ As such, there has been some focus on promoting the natural release of *lactoferrin* at inflamed sites post-surgery in order to study the effects on heparin. Bacteriophage Q β is a large icosahedral RNA virus containing 180 copies of a 14.1 kDa coat protein, which has a high tolerance to genetic insertions and/or point mutations.¹⁷⁷ This has enabled it to be established as a multivalent platform for heparin

binding following the insertion of multiple arginine groups.¹⁷⁸ Although this approach did generate some systems with superior neutralisation effects than protamine in clotting assays, their time-consuming preparation is a significant detraction, as is the current absence of toxicology studies.

Unsurprisingly, several researchers have focussed on producing smaller shorter-chain peptide structures. For example, Yang and co-workers developed a range of low-molecular-weight-protamine (LMWP) systems by digesting native protamine strands with *thermolysin*.¹⁷⁹ This technique produced arginine rich peptide sequences such as VSRRRRRRGGRRRR which could effectively neutralise heparin *in vivo* whilst provoking less immunogenicity than native protamine, although the complex digestion step again restricted genuine clinical interest.¹⁸⁰⁻¹⁸² A similar study by Wakefield and co-workers observed that a range of cationic peptides were significantly less toxic than protamine, although they also suggested that treatment with these peptides resulted in incomplete reversal of heparin.¹⁸³ A further range of synthetic peptides has been developed from residues 27–38 of human serum amyloid P.¹⁸⁴ Despite not possessing a high density cluster of basic amino acids, this specific sequence still demonstrated the ability to bind heparin at micromolar levels. The inactivity of a sequence scrambled version of this peptide suggested that the binding mode of residues 27–38 is fundamentally optimised in some way, although further studies are required to better understand this.¹⁸⁴

Some of the earliest work in the area came in 1958, when the synthetic polymer polybrene – hexadimethrine bromide, Figure 1.27a – was examined as a protamine alternative.¹⁸⁵⁻¹⁸⁷ Polybrene has a much simpler cationic polymer structure than protamine and was tested *in vivo*, where it showed promise but ultimately was only around 70% as effective as protamine.¹⁸⁸ Interestingly, development of this system appeared to halt and it seems likely that toxicity problems hindered its progress. Toxicity of cationic synthetic polymers can however be tempered by careful design of the polymeric backbone. For example, dextran and hydroxypropylcellulose polymers have been functionalised with cationic groups and shown to have relatively good biocompatibility, with heparin binding affinity increasing with degree of cationic decoration.^{189,190} A further advantage of such sugar-based systems is their wide commercial availability.

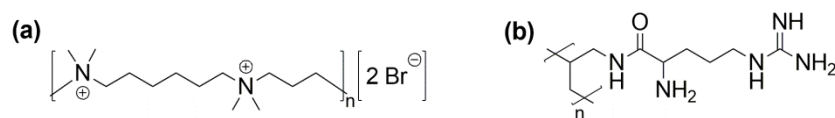


Figure 1.27 – Cationic heparin binding polymers: (a) Quaternary ammonium-based cationic polymer polybrene and (b) an arginine functionalised PAH.¹⁹¹

Recently, Szczubiałka, Nowakowska and co-workers reported the preparation and rigorous preliminary testing of an arginine functionalised poly(allylamine hydrochloride) (PAH) polymer, Figure 1.27b.¹⁹¹ Impressively, across a variety of solution phase and biological assays including *in vitro* plasma clotting (aPTT) and *in vivo* coagulation studies in rats, the heparin neutralisation performance of the polymers was shown to be similar or superior to protamine. Initially, the argininylated structures also appeared to be non-toxic to cells although, as acknowledged by the authors, more systematic pharmacokinetic and toxicity studies are still required for this promising candidate.

A different family of cationic polymers are the commercially available poly(amidoamine) (PAMAM) dendrimers, and these well-defined species have been examined for their heparin binding ability.¹⁹² Xu, Cheng and co-workers observed some insightful generational effects, where the most highly charged dendrimer was not necessarily the best heparin binder. The binding of PAMAM dendrimers to LMWH has also been studied in rats, although in this example no reversal of anti-coagulation was observed.^{193,194} Instead, it was suggested that the PAMAM dendrimers may be used in this setting to enhance the absorption and assist delivery of the LMWH, hinting at the potential for use as deep vein thrombosis prevention agents. Indeed, this is an example of how heparin binders could be developed into delivery vehicles rather than rescue agents. Our own studies involving PAMAM (and related) dendritic systems are presented in Chapter 3.

1.4.2 Small molecules

Despite heparin being a large somewhat polydisperse polysaccharide, there are several examples of heparin neutralization being attempted using more traditional well-defined ‘drug-like’ small molecules. One of the earliest small molecules to be considered as a potential heparin rescue agent was known heparin sensor methylene blue, although, presumably owing to its monocationic nature, it was shown to be ineffective.^{186,195}

An important ‘small molecule’ system emerged in the form of Delparantag, a pentacationic species derived from alternating aromatic and lysine amino acid units, Figure 1.28.^{196,197} The lysine side-chains confer heparin binding ability while the aromatic units confer some rigidity to the species. Impressively, an *in vivo* clinical trial in six male humans, along with animal studies, suggested Delparantag was as effective as protamine at neutralizing heparin without creating complications such as a heparin rebound effect. Following Phase II clinical trials, considerations of the suitability of Delparantag in different clinical situations continue.¹⁹⁸

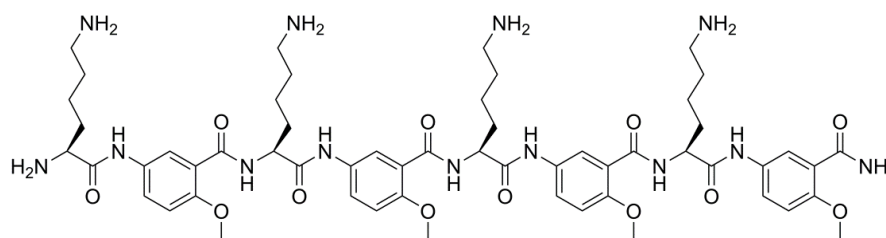


Figure 1.28 – Delparantag is a lysine-containing penta-cationic heparin binder.

Eye-catching work from the group of Cunsolo and co-workers developed polycationic calix[8]arenes and demonstrated their ability to neutralise heparin in blood. *In vitro* studies showed that neutralization was faster and more efficient than protamine, although hemolysis did occur at high calix[8]arene concentrations.^{199,200} On the molecular level, it was proposed that the flexibility of the scaffold maximized heparin binding as the cationic groups had some freedom to optimize their individual interactions with the biopolymer. Indeed, an ‘octopus-like’ chelate effect was observed computationally, Figure 1.29. Follow-up work from the same group then immobilized these structures onto a polymer matrix to yield a filter-like structure which may have potential for the ‘clean-up’ of a patients’ bloodstream following a procedure such as coronary bypass.²⁰¹ It can be envisaged that the blood could be passed through the filter-like structure, thereby avoiding the need to directly introduce antidote molecules directly into the bloodstream.

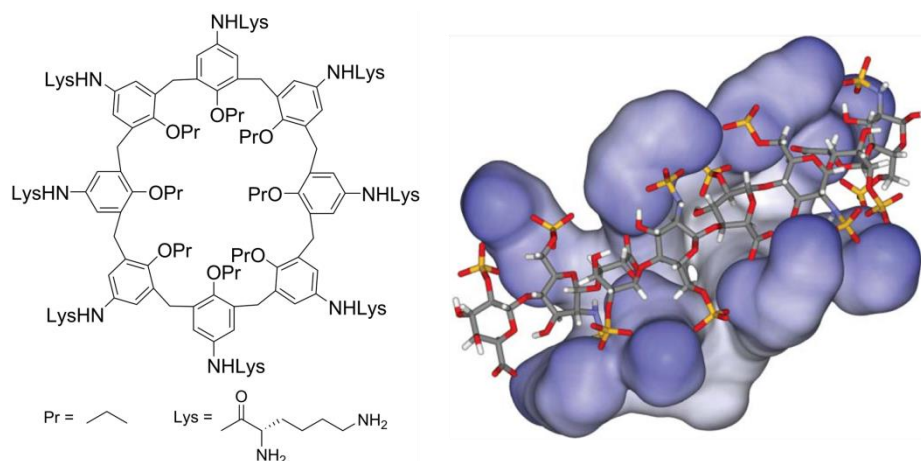


Figure 1.29 – Calix[8]arene from Cunsolo and co-workers with structure (left) enabling chelate effect to be maximized through adoption of ‘octopus-like’ conformation (right, space-filled species represents calix[8]arene, stick model represents heparin). Figure adapted from ²⁰⁰.

Foldamers are small peptide-protein mimics which establish well-defined conformations. The group of DeGrado and co-workers established an octa-cationic arylamide-derived foldamer decorated with amine and/or guanidinium groups which exhibited heparin antagonism *in vitro*, Figure 1.30.^{202,203} Their controlled structure-activity studies demonstrated that guanidinium cations enhanced the heparin binding of the system 2.5-fold over simple amines. Recently published follow-up studies demonstrated further activity of these systems against ATIII in Factor-Xa type heparin binding assays, and the systems were also shown to be sufficiently versatile to neutralise fondaparinux (a synthetic analogue of the specific pentasaccharide sequence which confers heparin anti-coagulant behaviour).²⁰⁴

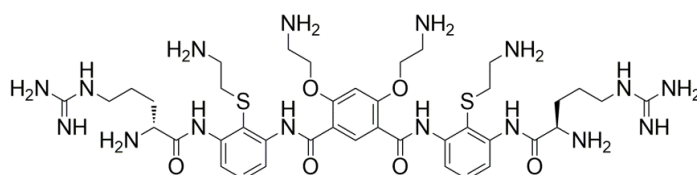


Figure 1.30 – An octa-cationic arginine-containing foldamer from DeGrado and co-workers.²⁰²

As a final example, surfen – bis-2-methyl-4-amino-quinolyl-6-carbamide, Figure 1.31 – was investigated as a heparin binder by Esko and co-workers in 2008.²⁰⁵ It was demonstrated that protonation of the quinoline rings was sufficient to confer heparin binding activity, despite the low molecular charge. Surfen had first been studied by

Hunter and Hill in 1961, who suggested that the small amount of charge per molecule made heparin-reversal performance inferior to protamine.²⁰⁶ This lower potency ultimately leads to unacceptably high IC₅₀ values and so further investigation of surfen has been halted.

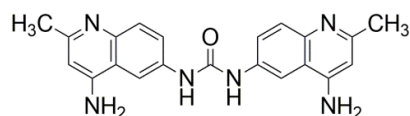


Figure 1.31 – Surfen, one of the smallest synthetic heparin binders to be examined as a potential heparin rescue agent.²⁰⁵

1.4.3 Self-assembling systems

Given the many advantages of creating large multivalent ligand arrays from smaller, more synthetically tractable and biologically compatible building blocks, it is perhaps surprising that there are so few examples of self-assembling multivalent (SAMul) approaches to heparin binding. The maiden example came from Stupp and co-workers in 2006 with a complex lipopeptide capable of self-assembling into heparin binding cylindrical micellar nanostructures, Figure 1.32.²⁰⁷⁻²⁰⁹ Structurally, a known heparin binding sequence consisting of three lysine and one arginine group was installed within the hydrophilic region of the self-assembling lipopeptide, while an *n*-alkyl chain conferred amphiphilicity.²¹⁰ In the presence of heparin, the individual self-assembled nanofibres were able to nucleate a further assembly event to form gel-based materials.²⁰⁹ Stupp and co-workers then demonstrated that the heparin within these gels was able to stimulate the formation of new blood vessels (angiogenesis), opening up further biomedical interest. Subsequent studies additionally showed that by co-assembling a fluorescently-labelled lipopeptide into the system, fluorescein-tagged heparin could be detected through a FRET mechanism.²⁰⁸

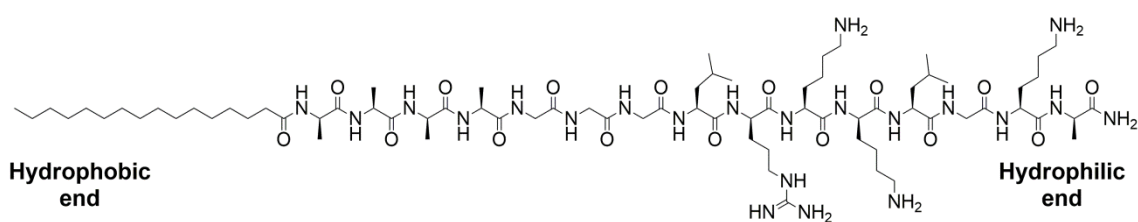


Figure 1.32 – A self-assembling heparin-binding lipopeptide from Stupp and co-workers.²⁰⁷

Other noteworthy approaches to self-assembling heparin binders came from Smith and co-workers in 2011, who adapted a low generation analogue of a known DNA binding SAMul dendron and demonstrated its potential for binding to the heparin biopolymer, Figure 1.33.²¹¹ An attractive feature of this approach is the relative synthetic accessibility of the molecular building block. The initial work from the group of Smith established that the amphiphile self-assembled to afford nanoscale micellar structures which appeared to bind heparin due to the multivalent cationic ligand array displayed at the assembly surface. There were some limitations to this initial work and these are discussed in more detail in Chapter 4.

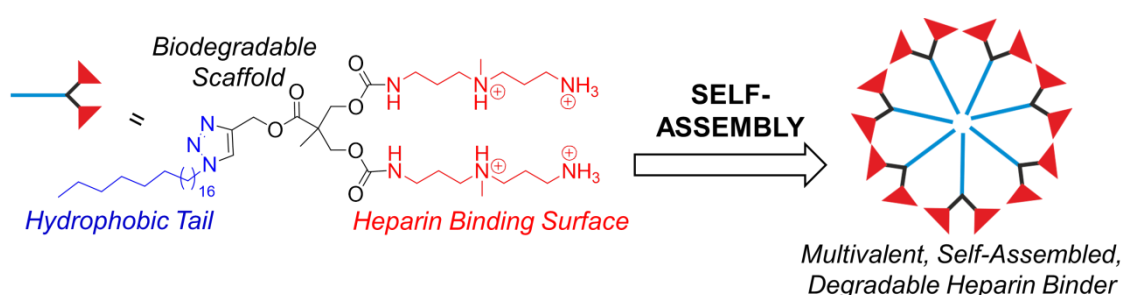


Figure 1.33 – Self-assembling heparin binding compound subjected to preliminary testing by Smith and co-workers.²¹¹ This Figure is also shown as Figure 4.2.

1.5 Project Aims

The overarching theme of this project is heparin therapy, the clinical use of heparin as an anti-coagulant during surgery or other medical procedures. In particular, the focus falls on two distinct areas: (i) heparin sensing, and the need for a more effective and/or reliable methodology for quantifying the amount of heparin remaining within a patient during, and at the conclusion of, treatment; and (ii) heparin binding, and the need for a better heparin rescue agent capable of neutralizing the anti-coagulant effect of heparin at the conclusion of surgery, without presenting risks such as those associated with the clinical use of protamine. By considering these two clinical problems from a supramolecular chemistry perspective, it was hoped that fundamental insights into heparin binding and sensing might be revealed, which, in turn, may be able to inform future developments in the area.

1.5.1 Heparin sensing

The heparin sensing arm of this project adopted the goal of identifying a more suitable methodology for the determination of the overall residual load of heparin – that is the complete biopolymer, regardless of anti-coagulant activity – remaining systemically within a patient at the conclusion of surgery. Building on the many promising examples presented earlier, a colorimetric sensing regime was targeted. It was hoped that this would offer significant advantages over clotting based techniques, which are based exclusively on heparin activity, by binding indiscriminately to heparin in a manner more simulative of protamine binding characteristics.

In order to maximize the clinical appeal of a potential heparin sensing system, commercial indicator dyes were considered first to examine whether any ‘off-the-shelf’ species would be suitable for such heparin sensing applications. Should an already-commercial option not be forthcoming, the intention was to design a bespoke heparin sensor with a major focus on synthetic simplicity. Indeed, one of the drawbacks of even the most promising colorimetric systems discussed previously is their often unattractive, multi-step syntheses. The ease of uptake for a potential end-user remained a consideration throughout the study of our sensing systems.

It is worth noting that from a supramolecular chemistry perspective, developing and testing such a colorimetric heparin sensor is far from trivial. Establishing selective supramolecular interactions with any target (but in our case heparin) within highly competitive media such as high buffer and/or salt concentrations, or biological media such as human serum or plasma, is a great challenge. Also, any output signal from the sensor must remain quantitative, unperturbed and easy-to-calibrate within such media.

1.5.2 Heparin binding

The heparin binding part of the project aimed, ultimately, to advance the understanding of the potential for self-assembling multivalent (SAMul) systems to be applied in heparin rescue treatments. To do this, initially, a range of well-defined cationic species such as commercial PAMAM dendrimers were studied for their relative heparin binding properties. This study hoped to give insights into some fundamental binding preferences of heparin.

Subsequently, the project moved on to consider, initially through further investigation of the previously reported SAMul heparin binder from within the Smith group, the potential of a SAMul approach for heparin binding in competitive conditions.²¹¹ The SAMul-heparin-binding concept is cartooned in Figure 1.34.

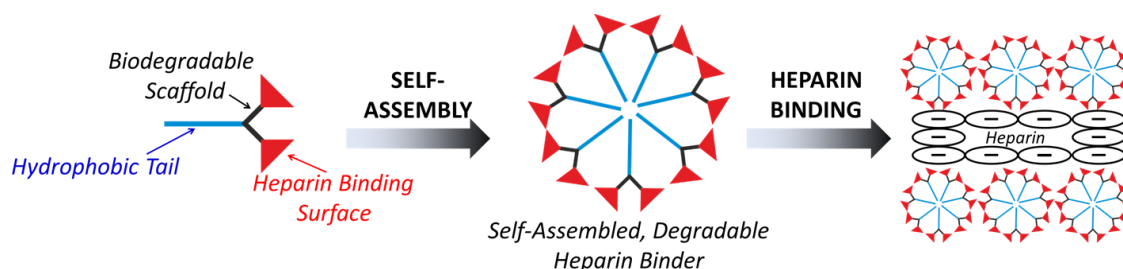


Figure 1.34 – Cartoon showing the concept of self-assembled multivalency (SAMul) in for heparin effective heparin binding.

In particular, there was to be a focus on examining the effects of electrolytic competition and biological conditions upon the heparin binding performance, and more fundamentally, the properties of such self-assembled nanosystems. Meaningfully probing heparin binding under such conditions may require the careful development of a sufficiently robust assay technique, as this was a limitation previously acknowledged by Smith and co-workers in their preliminary studies.²¹¹ Further insights into the physical and theoretical properties of our SAMul systems were to be targeted through collaborations with the laboratories of Dr Marcelo Calderon at Freie Universität Berlin, Germany and Professor Sabrina Pricl at University of Trieste, Italy. It was intended that Dr Calderon would provide solution phase insights through dynamic light scattering techniques which would be ideal for comparison against our own microscopy imaging and the computational molecular dynamic modelling approaches employed by Professor Pricl.

Once some understanding of the SAMul systems had been gained, it was intended to evolve the approach by re-designing the monomer unit(s) in response to these observations. It was hoped that promising candidates would be subjected to clinically relevant plasma clotting assays through collaboration with Professor Jeremy Turnbull at University of Liverpool, UK. This application-driven design, test, review, modify approach was intended to permit progress towards a clinically relevant understanding of

the real-world requirements of SAMul systems, and allow a meaningful assessment of the potential of SAMul approaches for use in heparin rescue treatments.

2 Chapter 2 – A Simple Robust Heparin Sensor

2.1 Introduction

At the conclusion of a surgical procedure involving the use of heparin as an anti-coagulant drug, there is an immediate need to reverse the effect and allow clotting to begin.²¹² This heparin reversal is achieved through introduction of the only licenced heparin reversal agent: protamine. Due to the toxicity risks associated with the clinical use of protamine, dosing is crucial in order to minimise the risk to patients. In order to dose protamine appropriately, the amount of heparin remaining in the patient at the end of surgery must be accurately quantified.

While a surgical procedure is in progress, the level of heparin in the patient must be closely monitored in order to maintain sufficient levels of anti-coagulation. Clotting time assays such aPTT or anti-Xa techniques can be particularly effective in this role; giving a good measure of the active heparin levels in a blood sample, from an anti-coagulation viewpoint.^{117,118} Currently, at the conclusion of surgery, these same techniques are employed to calculate the amount of residual heparin remaining in the patient. The use of clotting time based techniques at this stage of the process is not ideal.¹²² Rather than determining the amount of heparin remaining in the patient from an anti-coagulancy viewpoint, it would be more informative to quantify the amount of global heparin remaining in the patient, irrespective of its activity. Protamine, the heparin antidote, is unable to differentiate between active and inactive regions of heparin when neutralising the anti-coagulant effects and so a measure of total amount of heparin in the patient may help with more accurate dosing.²¹³

Colorimetric sensors have great potential for quantifying the global amount of heparin in a sample.²¹² Colorimetric detection involves an indicator dye exhibiting a change in photospectroscopic or fluorescent signal intensity upon interaction – usually, but not exclusively, in a non-covalent manner – with heparin. This type of measurement is able to give a direct read-out of heparin levels by simple comparison to known standards. A key advantage of a colorimetric approach to heparin monitoring is the ability of the dye to bind to / interact with all of the heparin chains indiscriminately, regardless of whether they contain the correct sequence of sugars to confer anti-coagulant activity. This leads to quantification of the total amount of heparin – not just the amount of active heparin –

which in turn should allow for more accurate protamine dosing and, ultimately, improved clinical outcomes.

A sensor dye capable of detecting heparin in a clinically relevant situation has many key challenges to overcome. Firstly, the sensor must be able to establish interactions with heparin. Most widely, heparin sensors contain cationic functional groups which can establish electrostatic interactions with the anionic sulfate and carboxylate groups on the heparin biopolymer. Secondly, the sensor must exhibit a quantifiable spectroscopic change upon establishing these interactions with heparin either in the form of an increase (switch-on sensing) or decrease (switch-off sensing) in signal intensity. Thirdly, for the sensor to be of potential clinical relevance, it must be able to exhibit this response to heparin when heparin is present at clinically relevant concentration levels, and, most challengingly, in an electrolytically competitive media such as human plasma.

To date, a wide variety of spectrophotometric and fluorescent heparin sensors have been investigated, with some demonstrating a particularly impressive ability to detect and quantify heparin levels in complex biological media such as human plasma.^{158,160} An important factor for any potential heparin sensor wishing to find application at the point-of-care in the clinic is synthetic accessibility. Understandably, this is not always maintained as a high priority during the development of candidate sensors and so promising molecules can often be accompanied by unwieldy synthetic baggage. Indeed, one of the significant detractors of many of these systems is the complex, multi-step, syntheses required in their creation. As a consequence of this, the Smith group became interested in the challenge of identifying a synthetically-simple, or ideally already commercial, sensor dye able to detect/respond to heparin in a clinically relevant sample.

2.2 Considering Commercial Options

Our search for an accessible heparin sensor began by considering commercially available species, starting with the thionine family of dyes. Thionine consists of a heteroaromatic phenothiazine-like core functionalised with two pendant amines. Thionine is the parent member of a family of dye analogues, each of which contains the same aromatic core functionalised to differing degrees by methylation of pendant

amines. At one extreme is the tetra-methylated analogue methylene blue, while at the other is non-methylated thionine, see Figure 2.1.

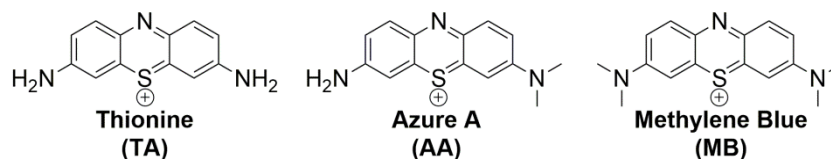


Figure 2.1 – A selection of dyes from the thionine family.

Thionine dyes have been known and studied from as early as 1884²¹⁴ and have been used commercially throughout the twentieth century. In the early-to-mid part of the century, commercial samples were routinely of unreliable purity²¹⁵ and much effort had to be put into purifying them.²¹⁶⁻²¹⁸ Thionine dyes can be readily protonated to give cationic species, and consequently have previously been investigated in systems to bind biological polyanions such as DNA.²¹⁹

Methylene blue (MB) has been investigated as a heparin reversal agent in its own right in several studies, although dosing was found to be unreliable,²²⁰ there were toxicity problems²²¹⁻²²³ and, most potently, it was widely shown to be ineffective.^{186,195} A straightforward explanation of MBs inability to neutralize heparin in these clinical studies lies with its mono-cationic nature.

The spectrophotometric study of the heparin binding site by Liu and co-workers showed that increasing the amount of competitive electrolytes in the test system interfered with the MB-heparin interaction, and so the spectroscopic response was reduced.¹⁴² These observations marry-up well with the observations of Smith and co-workers, who found the MB-heparin interaction was no longer spectroscopically evident even in the presence of relatively low concentrations of NaCl.²¹¹ Similarly, the acute sensitivity of di-methylated thionine analogue Azure A (AA) to increasing electrolyte concentrations has also been well documented.¹⁴³

Given this electrolytic sensitivity, reports from the teams of Klein¹⁴¹ and Yang²²⁴ utilising mono-cationic Azure A for heparin quantification in samples of human plasma are somewhat surprising. Human plasma contains a plethora of charged electrolytes and so it would be reasonable to expect the AA-heparin interactions to be disrupted. One of the limitations in the works of Klein and Yang is the absence of attempts to control the pH in their systems. Thionine derivatives, including Azure A, are known to exhibit

perturbed spectrophotometric responses under different pH regimes, and it seems likely that in changing the relative concentrations of heparin or protamine during their assays, Klein and Yang may have unwittingly also altered the pH of the system.²²⁵⁻²²⁷ This change may account for their observed spectrophotometric responses.

Thionine – often referred to as Lauth’s violet in honour of pioneering French dye chemist Charles Lauth – is the only member of the dye family in which neither of the pendant amines is decorated with methyl groups. The absence of methyl groups allows native thionine to carry two positive charges at biologically relevant pHs (e.g. pH 7). For this reason, the ability of thionine to spectrophotometrically respond to heparin in the presence of 5 mM KCl in the work of Baumgärtel and co-workers can begin to be understood.²²⁸ Their work charted the change in UV-vis spectra as different amounts of thionine were added to samples of heparin. It was suggested that the spectroscopic signal was independent of the proportion of heparin covered by dye; that is to say an ‘all-or-none’ binding model was declared valid. One self-acknowledged limitation of their study was the use of a relatively high concentration of thionine (200 μ M). They were concerned that the previously studied phenomenon of thionine aggregation may have played a role in their results.²²⁹ The response of thionine to heparin in the presence of some competitive electrolyte showed promise, although the tolerance to more biologically relevant electrolytes (e.g. NaCl) was not studied. This was taken as the starting point for our investigations.

The ultimate goal of this work was to identify a heparin sensor able to spectroscopically respond to heparin in biologically relevant media such as human serum/plasma. For initial screening, it was decided to test candidate sensors in 150 mM NaCl. This concentration of electrolyte was chosen to somewhat mimic the electrolyte concentration present in human plasma, which are known to be 150 mM Na^+ , 110 mM Cl^- and HCO_3^- .²³⁰ A propensity to operate within this regime would indicate a potential for heparin binding, and therefore spectroscopic response, in the even more competitive conditions presented by human serum. These ‘intermediate’ salt-containing conditions also allow sub-standard dyes to be dis-regarded without consumption of the more expensive serum. In order to minimise any pH changes, all test solutions were buffered at pH 7 using Tris HCl.

Thionine was optimised at a concentration of 16 μM , which gave a satisfactory absorbance of *ca.* 1 at 595 nm. This concentration additionally ensured thionine was operating below previously observed critical aggregation concentrations.²²⁹ As shown in Figure 2.2, in the absence of salt, a strong ‘switch-off’ response is seen upon introduction of heparin to a cuvette containing thionine and buffer. Disappointingly, the same response was not observed upon addition of heparin to a cuvette additionally containing 150 mM NaCl. This suggests that the doubly-charged thionine is unable to out-compete the mono-cationic sodium at the heparin surface although this is perhaps not surprising as in total there is only 0.2% as much cationic charge in the solution from thionine (32 μM) as there is from Na^+ (150 mM). Using a higher concentration of dyestuff, in the manner of Baumgärtel and co-workers may help to overcome this however a significant increase may lead to absorbance intensity becoming above detectable levels.

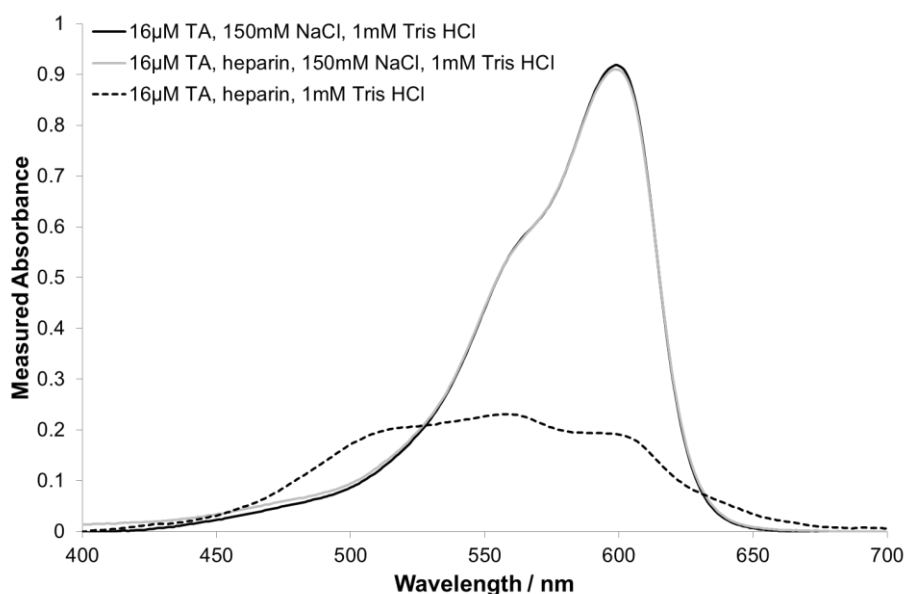


Figure 2.2 – UV-vis absorbance spectra of thionine acetate (16 μM) in salt (150 mM) and buffer (1 mM Tris HCl) in presence (grey) and absence (solid black) of heparin. Thionine acetate (16 μM) in the presence of heparin with no NaCl present is included for comparison (dashed black).

Following the failure of dicationic thionine to bind heparin in biologically relevant concentrations of salt, a second cheap commercially available dicationic indicator dye was studied. Methyl green (MG) is a triphenylmethane-derivative, Scheme 2.1, and presents a different charge profile to heparin than the smaller thionine molecule.

Delocalisation of the second cationic charge across two aromatic rings allows MG to present a reasonably charge diffuse binding patch to heparin when compared directly to thionine. MG has previously been shown to spectroscopically respond upon interaction with either DNA²³¹ or heparin²³² through a decrease in absorbance intensity at 640 nm. In particular, Scott showed MG was able to retain interaction with polyanions such as DNA/RNA/heparin in the presence of electrolytic species (e.g. sodium acetate).²³² This led us to examine MG for spectroscopic response in biologically relevant salt concentrations.

In our studies, an optimised MG concentration of 30 μM exhibited a switch-off response upon introduction of heparin in the presence of 150 mM NaCl although the decrease in signal intensity ($\sim 17\%$) was significantly less than in the absence of salt ($\sim 32\%$), Figure 2.3. This perturbation suggests that although more robust than thionine, MG is not able to fully out-compete sodium cations for binding to heparin.

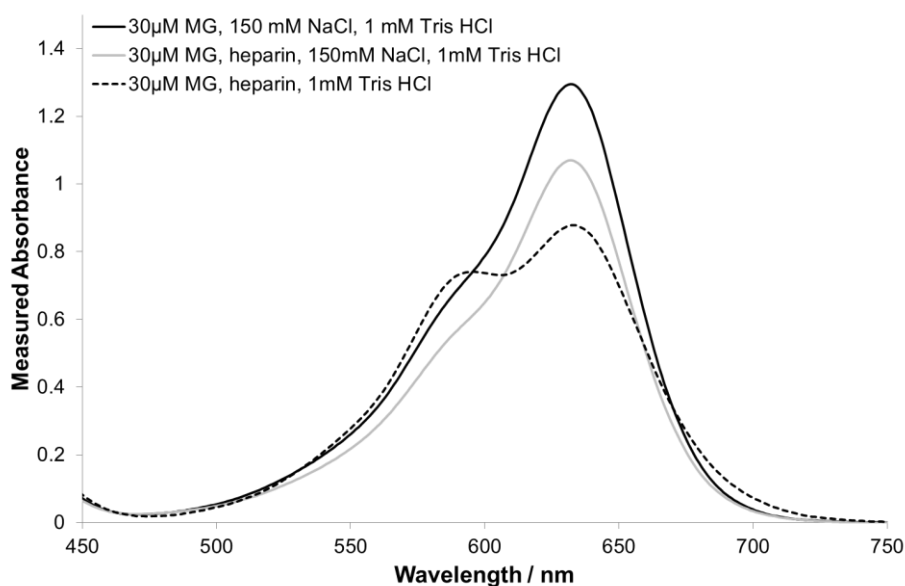
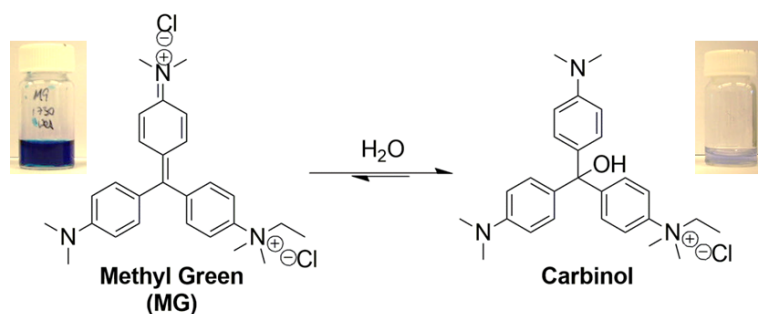


Figure 2.3 – UV-vis absorbance spectra of methyl green (30 μM) in salt (150 mM) and buffer (1 mM Tris HCl) in presence (grey) and absence (solid black) of heparin. Methyl green (30 μM) in the presence of heparin with no NaCl present is included for comparison (dashed black).



Scheme 2.1 – Molecular rearrangement of coloured methyl green to colourless carbinol.

A further detraction presented by MG is the practical limitation of bleaching. MG bleaching occurs through incorporation of a hydroxyl group at the centre of the molecule. Following molecular re-arrangement, the colourless species carbinol is generated. This process has been well studied, for example, by the work of Nir, Margulies and co-workers³² and Hahn³⁰ who collectively demonstrated that dilution and pH were important factors. In particular, Hahn suggested carbinol would be rapidly generated at pH values above 5. Our work, which is buffered at pH 7 by 1 mM Tris HCl, served to confirm this observation as the absorbance signal intensity at 640 nm fell by ~25% in only 90 minutes upon standing. In line with Hahn's observations, a control solution buffered at pH 3 retained full colour intensity over a 7 day period.

With MG dismissed, Alcian blue (AB) was identified as a more highly charged commercial heparin binding system. Alcian blue, Figure 2.4, is an aromatic copper complex possessing 4 positive charges which has been widely studied as a histological heparin stain.²³³ Despite prevalent histological use, influential biochemist J. E. Scott suggested true understanding and investigation of AB was often controversially hindered by “commercial secrecy and entrepreneurial dishonesty.”²³⁴ Whiteman has previously shown AB to be capable of interacting with many glycosaminoglycans in biological fluids such as urine, presumably due to guanidinium-like functionalities which decorate its surface.²³⁵ The electrolyte tolerance of AB is also known to be high with the aforementioned Scott and co-worker Willet reporting that AB is able to retain interaction with heparin up to NaCl concentrations of 900 mM. More recently, Bjornsson employed AB in spectrophotometric studies, where response was observed in the presence of sulfated GAGs such as chondroitin-4-sulfate.^{236,237}

In our studies, an optimised solution of 38 μ M AB in 150 mM NaCl and 1 mM Tris HCl exhibited an absorbance maximum at 618 nm, however upon addition of heparin,

no change in absorbance intensity was observed, Figure 2.4. Several of the aforementioned studies left AB-heparin mixtures over an extended time period to ensure complexation had reached its maximum. Our solution was allowed to stand for 5 hours, after which there was still no absorbance change. Instead, a precipitate was clearly visible in the cuvette. Bjornsson, in the second part of his 1993 study, relied upon the precipitation of AB-GAG complexes for quantification.²³⁷ It had been hoped that the non-acidic buffered pH in our system would circumvent this precipitation event, however this was not the case. As a result of this undesired precipitation and absence of spectroscopic change, AB was dis-regarded for further investigation.

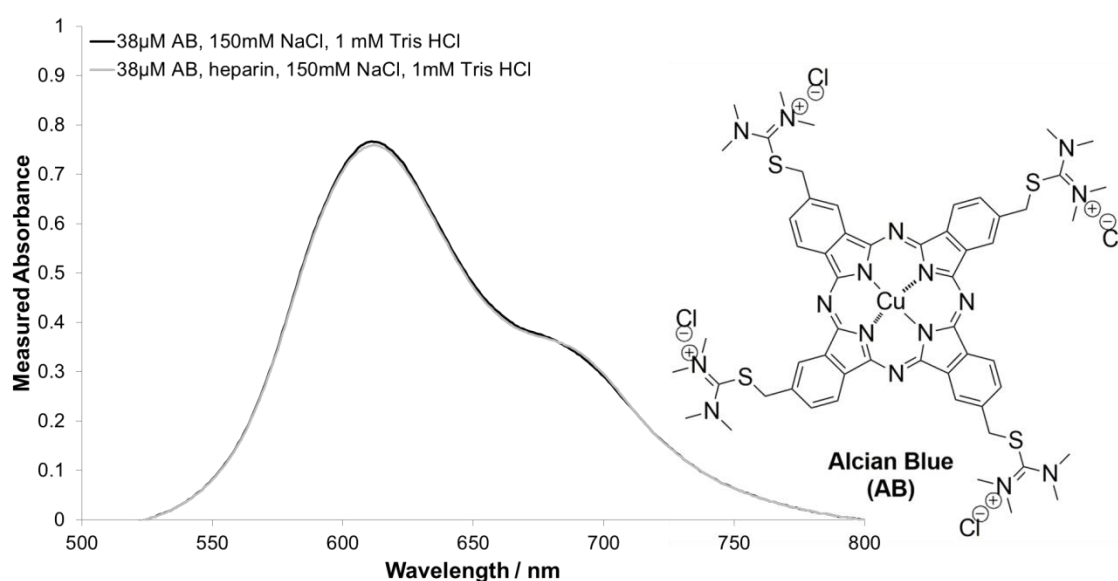


Figure 2.4 – UV-vis absorbance spectra of alcian blue (38 μM) in salt (150 mM) and buffer (1 mM Tris HCl) in presence (grey) and absence (black) of heparin. Inset: structure of alcian blue.

2.3 A New Dye is Born

With an effective, affordable commercial heparin sensor not forthcoming, attention turned instead to designing a synthetically straightforward dye. Any successful heparin sensor requires two key components: (i) chromophoric or fluorogenic character and (ii) heparin binding groups. In sourcing a chromophoric core, inspiration was sought from the previously discussed thionine family of dyes. In particular, thionine itself was considered an attractive building block due to its possession of two aniline-like

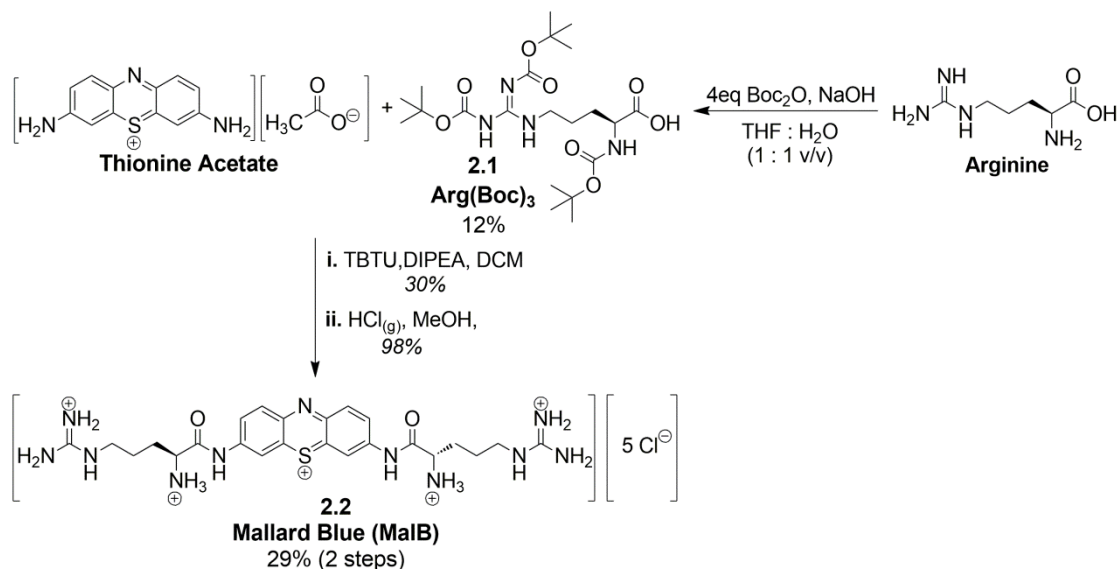
nucleophilic functional handles, which had previously been functionalised by Barton and co-workers.²³⁸

The search for a suitable heparin binding motif began by considering the way in which proteins interact with heparin. Most prolifically, the amino acid arginine is used to achieve high-affinity heparin binding, with the guanidinium group thought to play a key role in establishing electrostatic interactions with the sulfate groups along the polysaccharide chain.^{82,239} Arginine is the key heparin binding component of the clinically used reversal agent protamine, with arginine making up around 70% of the sequence.^{100,179} It was envisaged that a straightforward peptide coupling reaction involving the nucleophilic amines on thionine and the carboxylic acid on arginine should allow the chromogenic core to be functionalised with two arginine residues. It was hoped that, if successful, this new member of the thionine family may have greatly enhanced heparin binding ability, and may be robust enough to remain bound to heparin in the presence of competitive electrolytes such as salt.

In order to maintain regioselectivity during synthesis and minimise the potential for arginine polymerisation, the pendant primary α -amine and both amine components of the guanidinium group required protection. It is relatively unusual to tri-protect arginine; however with previous functionalization of thionine proceeding in relatively low yields, it seemed prudent to increase the odds in our favour as much as possible.²⁴⁰ Tri-Boc-protected arginine, Arg(Boc)₃, was identified as a suitable reagent because it is commercially available and all of the amine groups are protected with the same acid-labile *tert*-butoxycarbonyl (Boc) protecting group.

Although available commercially, Arg(Boc)₃ can be readily prepared on a multi-gram scale by heating arginine with an excess of di-*tert*-butyl dicarbonate in the presence of sodium hydroxide. The relatively low yield of *ca.* 10% can be accounted for by the well-known difficulty of installing the second protecting group on the guanidinium moiety.²⁴¹ As shown in Scheme 2.2, once in hand, two equivalents of Arg(Boc)₃ were readily appended onto thionine acetate in a TBTU-mediated peptide coupling reaction to afford the fully protected dye molecule, after purification by silica flash column chromatography. The yield of 30% is respectable as, although low, it is an improvement on the 9% yield observed by Barton and co-workers for functionalization of a thionine

core.²³⁸ A final global Boc deprotection using HCl gas in methanol afforded the new dye 2.2 in a near quantitative yield.



Scheme 2.2 – Synthesis of Mallard Blue 2.2. Although commercial, conditions for preparation of Arg(Boc)₃ also shown.

The preparation of this modified thionine derivative in two synthetically straightforward steps from commercial starting materials is highly attractive, and appears reliable enough to withstand scale-up.

2.4 Mallard Blue: Initial Studies

With new dye 2.2 in hand, it was examined by UV-visible spectroscopy. As shown in Figure 2.5, dye 2.2 is blue in appearance and has a strong absorbance band at 615 nm. The blue colour of the dye is remarkably similar in appearance to the livery of the world-record-holding A4 steam locomotive *Mallard 4468*, which is housed at the National Railway Museum in York. For that reason, the new dye 2.2 was christened Mallard Blue (MalB).

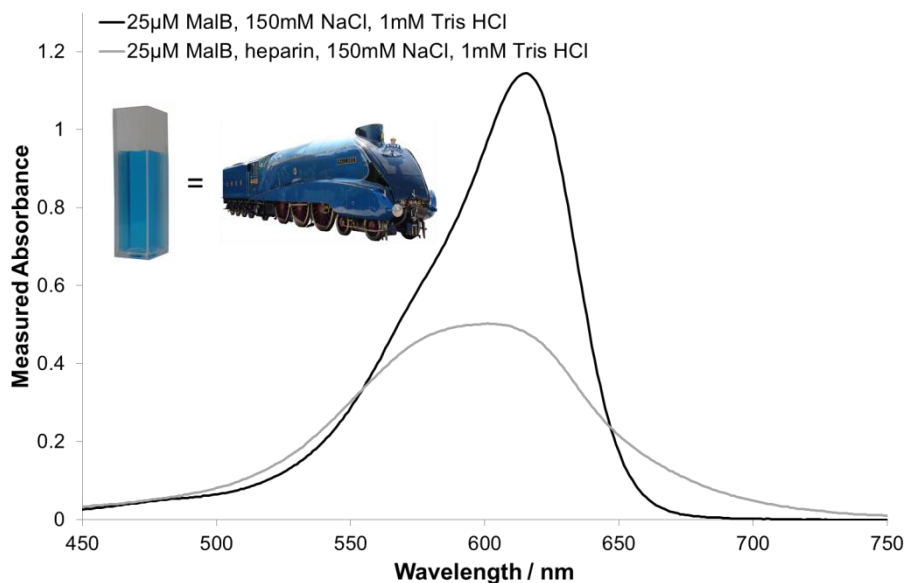


Figure 2.5 – UV-vis absorbance spectrum of MalB (25 μM) in salt (150 mM) and Tris HCl (1 mM) in the presence (grey) and absence (black) of heparin. Inset: Picture showing colour similarity of MalB and *Mallard*.

Mallard Blue was first tested in the manner previously applied to thionine, methyl green and alcian blue. Pleasingly, upon introduction of heparin to a solution of MalB (25 μM) in the presence of 150 mM NaCl, a strong spectroscopic response was observed, Figure 2.5. This response is significant when compared against the previously tested dyes. The 58% switch-off in signal intensity indicates that the introduction of the arginine groups has dramatically increased the ability of our thionine derivative to out-compete sodium cations at the heparin surface when compared directly to native thionine. Following this qualitative promise, a titration experiment was set up in order to probe this response more quantitatively.

An optimised MalB concentration of 25 μM was titrated with second portion of the same dye solution which had additionally been endowed with heparin. The titration was repeated in the absence and presence of 150 mM NaCl, and all solutions were buffered at pH 7 using 1 mM Tris HCl. In order to provide a performance comparison against an unmodified member of the thionine family, methylene blue (MB) was subjected to the same heparin titration in the absence/presence of 150 mM NaCl. A MB concentration of 10 μM was chosen in line with previous studies by Smith and co-workers.²¹¹ The resulting titration curves are shown in Figure 2.6.

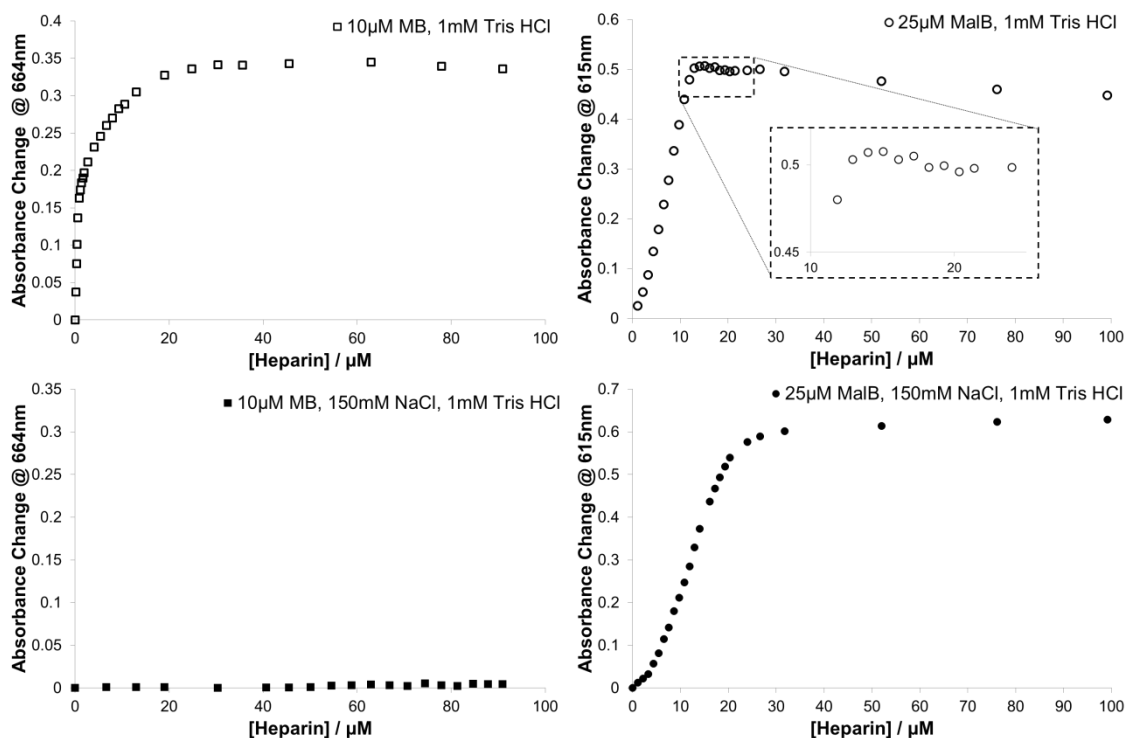


Figure 2.6 – Binding curves resulting from titration of heparin into a solution of methylene blue (10 μM , left) or Mallard blue (25 μM , right) in the absence (top) or presence (bottom) of 150 mM NaCl.

Before discussing the binding curves, it is worth re-emphasising that the ‘concentrations’ of heparin plotted in Figure 2.6 do not refer to the global concentration of heparin polysaccharide but rather to the concentration of the predominant disaccharide repeat unit (M_r : 665.40 g mol^{-1}). For both dyes, binding to heparin results in a decrease in spectroscopic signal intensity, however for visual appeal, the magnitude of spectroscopic change at λ_{max} is plotted in the binding curves.

In the absence of salt, the binding curve for MB indicates the dye is fully bound to heparin at concentrations above *ca.* 22 μM , indicated by the plateau region. The requirement for so much heparin may be a consequence of electrolytic competition from the Tris HCl buffer for interaction with MB. This hypothesis may be supported by the observation of no MB-heparin interaction at all in the presence of 150 mM NaCl.

In the absence of salt, 25 μM MalB appears to be fully bound to 13 μM heparin, while in the presence of 150 mM NaCl, the value increases to *ca.* 27 μM . Without salt present, the MalB-heparin binding curve does not plateau in a traditional manner. As further heparin is added beyond 13 μM , the absorbance change value begins to decrease again

suggesting a reduction in the total amount of heparin-bound MalB. As more heparin is added beyond the point of initial saturation, new interactions may form between this ‘new’ heparin and molecules of MalB which were already interacting with the heparin present. This disruption may lead to the overall MalB-heparin interactions being reduced as multiple heparin chains compete for binding to MalB, giving rise to the apparent regression of saturation observed. When salt is present, however, the disruptive effect of further heparin addition is not seen. This suggests that the sodium cations are able to ‘screen’ newly-added heparin preventing it from disrupting already-established MalB-heparin interactions. Consequently, in the presence of salt, the binding curve exhibits a traditional plateau region.

Close inspection of the MalB-heparin binding curves reveals a slightly sigmoidal line shape. This may be a consequence of the polydisperse nature of heparin, which is likely to dictate a different binding mode for different regions of the heparin chain with specific regions exhibiting preferential interactions. For MB, this sigmoidal character is less evident. This is likely to be a consequence of MB interacting in a monovalent manner with individual anionic charges on heparin rather than a larger region containing several anionic charges, as is the case with MalB.

The significant binding of MalB to heparin in the presence of 150 mM NaCl and 1 mM Tris HCl suggested that the MalB-heparin interaction is tolerant of electrolytic competition. To that end, an experiment was set up to determine the effect of further increasing concentrations of NaCl and Tris HCl buffer on the spectroscopic response of MalB. An optimised solution of heparin-saturated MalB (25 μ M MalB, 27 μ M heparin) was separately titrated with increasing amounts of NaCl or Tris HCl up to a final electrolyte concentration of 1 M. The disruptive effect on the MalB-heparin interaction is plotted in Figure 2.7, where disruption is normalised between the absorbance intensity at 615 nm of a solution of MalB alone and when saturated with heparin.

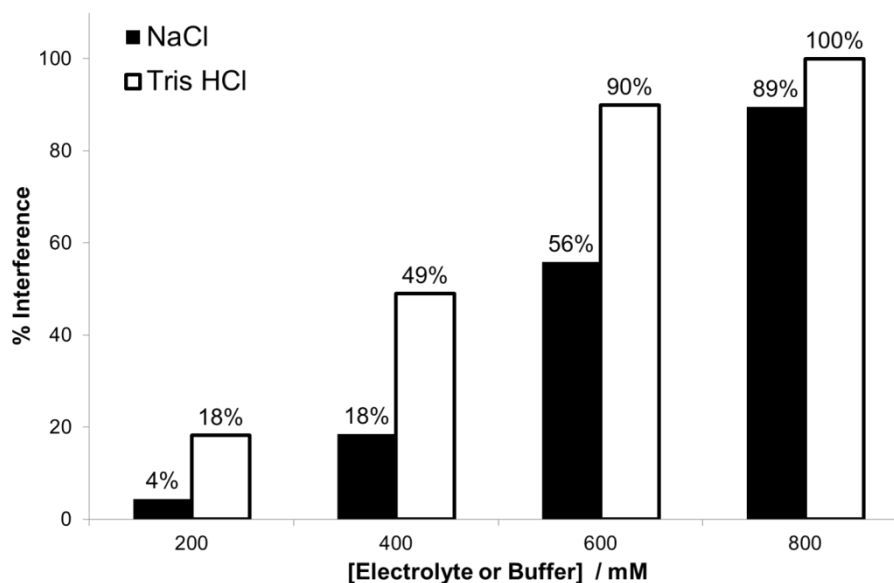


Figure 2.7 – Extent to which increasing concentrations of Buffer/Electrolyte disrupt MalB-heparin interaction.

The tolerance of the MalB-heparin interaction in the presence of increasing concentrations of electrolyte is impressive. As electrolytic competition increases though, so too does the disruption of the MalB-heparin interaction. Tris HCl causes more perturbation than NaCl, although spectroscopic responses are still detectable up to 600 mM and 800 mM respectively. Perhaps most impressive is the minimal disruption caused by the presence of 400 mM NaCl. In this particular scenario, sodium cations are present in a 1600-fold excess to MalB itself, yet MalB is still able to bind to heparin preferentially. The performance of MalB under these conditions is far superior to those previously reported for unmodified thionine dyes, further emphasising the performance enhancement resulting from functionalisation with arginine.¹⁴³

With the MalB-heparin interaction appearing to be so robust, our collaborators led by Professor Sabrina Pricl at University of Trieste, Italy studied the MalB-heparin interaction using molecular dynamics (MD) modelling. Their experiments represented heparin as a repeating sequence of the predominant disaccharide and allowed an optimised binding trajectory to be visualised, Figure 2.8. The observed binding mode suggests that two MalB molecules interact with a tetra-saccharide segment of the heparin chain, in complete agreement with our observed binding stoichiometry. Unsurprisingly, the interaction is dominated by electrostatics. In particular, the guanidinium groups play a key anchoring role with the arginine α -amines

supplementing the interaction and the cationic charge on the phenothiazine-like ring angling towards the polysaccharide. It appears that the crescent shaped geometry of MalB is particularly well-suited for interaction with heparin.²⁴²

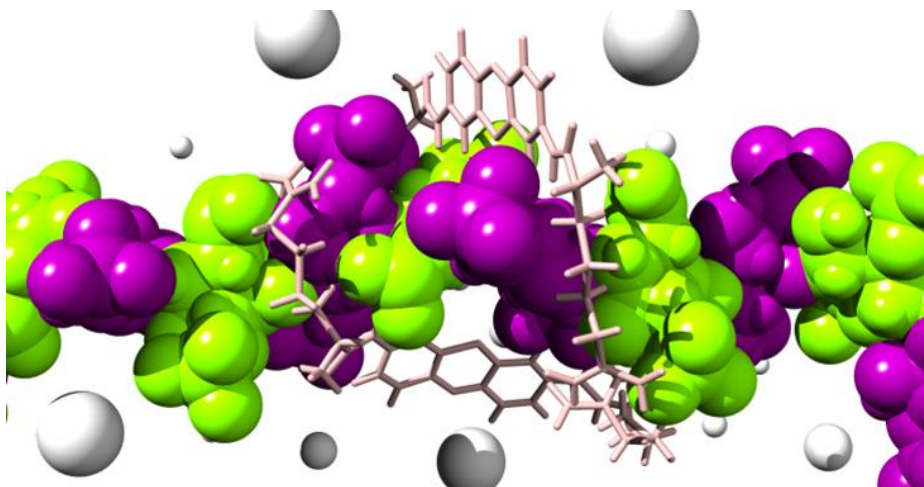


Figure 2.8 – Equilibrated MD snapshot of MalB-heparin interactions. Heparin is represented as purple (D-glucosamine) and green (L-iduronic acid) space-filling spheres, while MalB is shown as pink stick model.

So far, Mallard Blue had demonstrated an impressive tolerance to electrolytic competition and appeared to be well-suited for establishing robust non-covalent interactions with heparin. The next stage was to challenge the heparin binding ability of MalB in more biologically relevant situations.

2.5 Mallard Blue: Establishing Clinical Relevance

One of the biggest challenges facing any heparin sensor with clinical potential is selectivity. As previously discussed, biological media is a complex mixture of electrolytes and serum/albumin proteins.²³⁰ In addition to establishing interactions within this electrolytically rich media, an effective heparin sensor must be able to bind heparin selectively over structurally similar glycosaminoglycans (GAGs). In total, there are six structurally related GAGs: heparin, heparan sulfate (HS), dermatan sulfate (DS), chondroitin sulfate (CS), keratan sulfate (KS) and hyaluronic acid (HA).⁸¹ Influential work from the group of Ansyln in 2005 demonstrated a heparin sensor with selectivity over HA and CS, and so these were selected for benchmarking the performance of MalB, Figure 2.9.¹⁴⁵

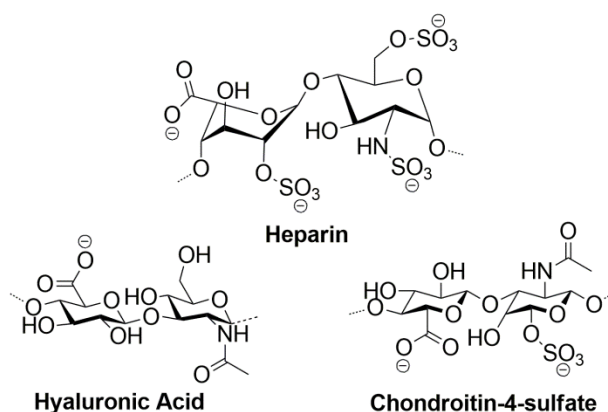


Figure 2.9 – Three structurally related GAGs: heparin, hyaluronic acid (HA) and chondroitin sulfate (CS).

In turn, each GAG was titrated into a solution of MalB (25 μ M) endowed with NaCl (150 mM) and buffered at pH 7 with Tris HCl (10 mM). The resulting absorbance intensity at 615 nm was plotted against increasing GAG concentration, Figure 2.10. The polydisperse nature of the GAGs along with the differing degrees of variability along the polysaccharide chains make defining absolute concentration values difficult. For that reason, in line with the earlier comments about heparin, the concentration values in Figure 2.10 refer to the concentration of the most common disaccharide repeat unit rather than the global concentration of polysaccharide.

It can be clearly seen that neither HA nor CS produce a large spectroscopic response from MalB when compared to heparin. Of the two, MalB interacts more significantly with CS. This is most likely due to the repeating disaccharide of CS possessing one more sulfate group than HA and consequently presenting more anionic character to MalB for binding. Whilst effective binding constants could be calculated from the data in Figure 2.10, it was reasoned that any values would remain somewhat ambiguous due to the variability in polydispersity and/or polysaccharide structures from batch to batch of each GAG. The data show that MalB is able to match the selective heparin binding performance of Anslyn's benchmark work.

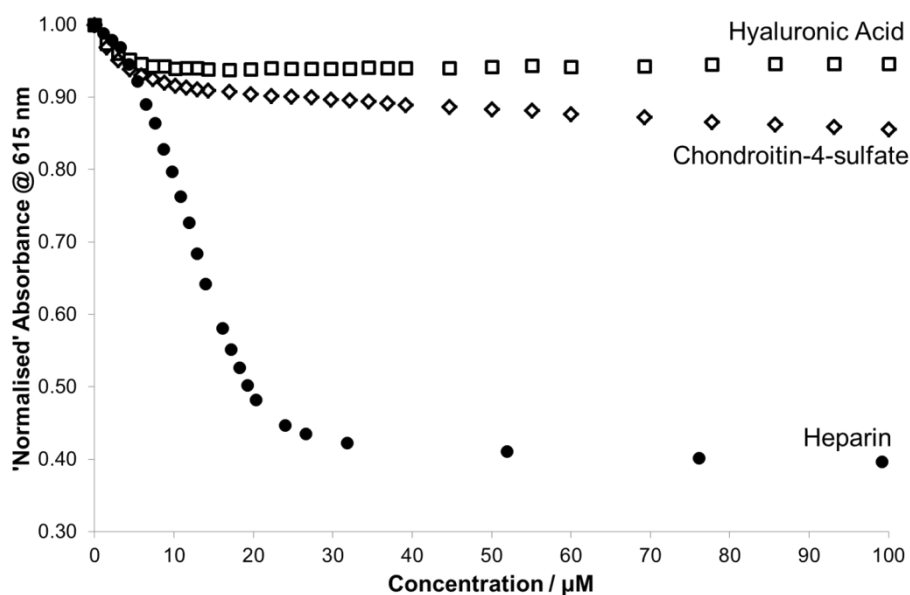


Figure 2.10 – Normalised response of MalB to glycosaminoglycans HA, CS and heparin.

With heparin selectivity over other GAGs in the presence of biological concentrations of NaCl demonstrated, the next challenge was for MalB to respond to heparin in a clinically relevant sample. Human serum is a real biological fluid containing all of the proteins (except those involved in blood clotting), antibodies, antigens, hormones and other exogenous and endogenous species naturally present in blood. The combination of these species with the electrolytes mentioned previously makes selective binding in serum particularly challenging. Taking further inspiration from the work of Ansyln,¹⁴⁵ an experiment was set up in which samples of 100% human serum were endowed with a concentration of heparin. Aliquots (0.5 mL) of this solution were then introduced to a cuvette containing MalB (1.5 mL, 25 μM) buffered at pH 7 with Tris HCl (20 mM). The absorbance intensity at 615 nm could then be recorded and plotted in response to different concentrations of heparin.

In the clinic, surgical teams dose heparin in terms of anticoagulant activity – measured in international units per millilitre of blood (IU mL^{-1}) – rather than in terms of raw amount. The clinically relevant range for cardiovascular surgery routinely lies within the range 2 – 8 IU mL^{-1} .^{243,244} It was therefore decided to probe the ability of MalB to detect heparin in the concentration range 0 – 10 IU mL^{-1} . The resulting heparin detection curve is plotted in Figure 2.11.

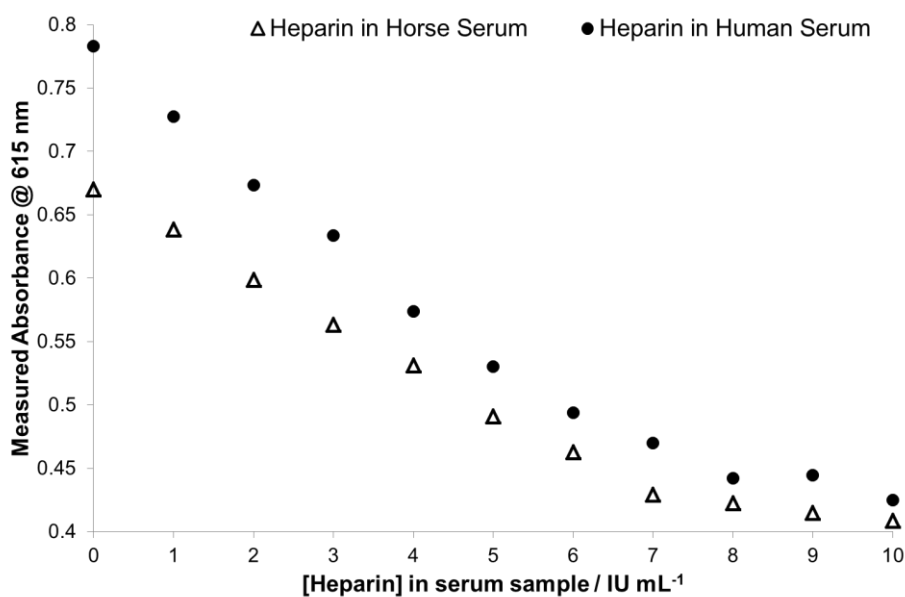


Figure 2.11 – Mallard Blue response to heparin delivered in 100% human serum (solid circles) or 100% horse serum (open triangles) within a clinically relevant range.

This experiment is an excellent mimic of the clinical setting, where a blood sample from a patient could easily be filtered using a cellulose filter such as those present in the blood electrolyte monitors carried by paramedics, thereby removing the blood cells and affording a relatively colourless sample of heparin-containing human plasma.²⁴⁵ Titration of this sample into a pre-prepared Mallard Blue solution in the clinic would be exactly analogous to the titration carried out here. Our choice of serum rather than plasma was expected to have no material bearing on the experiment as serum is simply plasma with some of the clotting factors (e.g. fibrinogen) removed.

Impressively, Mallard Blue showed a significant spectroscopic response upon addition of heparin in 100% human serum. Heparin can be clearly detected down to concentrations as low as 1 IU mL⁻¹. From these results, it can be envisaged that this assay could readily be adapted to operate with different concentrations of heparin, through increasing/decreasing amounts of MalB or by diluting the serum sample during pre-treatment. A comparable detection range was additionally observed in horse serum, further demonstrating the robustness of MalB for heparin detection.

In addition to matching the performance of Ansyln's landmark work, MalB also offers the advantage of greater synthetic accessibility. At this stage, the opportunity was taken to re-examine the previously reported work of Klein and co-workers who detected heparin across the same concentration range as us 'in plasma' using commercial

thionine derivative Azure A.¹⁴¹ For direct comparison against MalB, AA was examined under the same conditions of our assay. Specifically, heparin-containing serum samples were titrated into a solution of AA (25 μM) which was buffered at pH 7 with Tris HCl (20 mM). As shown in Figure 2.12, under these conditions, AA was unable to respond at all to the addition of heparin. Interestingly, and further in contrast to the observations of Klein and co-workers,¹⁴¹ even when the buffering was removed, there was still no observable spectroscopic change from AA upon heparin-in-serum titration, regardless of the wavelength chosen for monitoring.

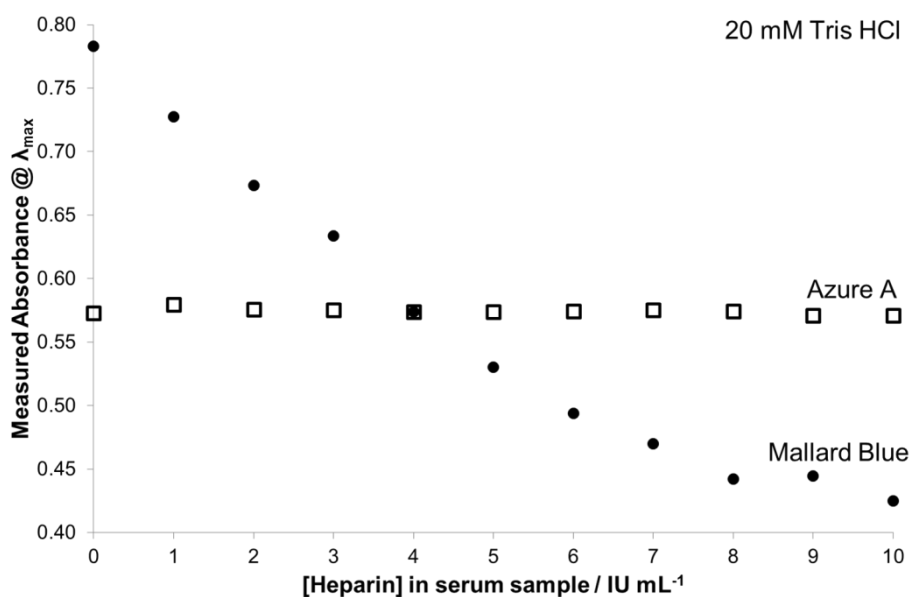


Figure 2.12 – Mallard Blue (solid circles) and Azure A (open squares) response to heparin delivered in 100% human serum within a clinically relevant range.

The data in Figure 2.12 clearly indicate that heparin detection by MalB occurs within a clinically relevant range and that the performance is significantly better than other thionine dyes such as Azure A. The performance benefit of introducing arginine groups into the thionine system is clear to see. This simple synthetic modification not only makes Mallard Blue the best-in-class for this dye family but also makes the dye an attractive proposition to non-synthetic chemists.²⁴⁶

2.6 Mallard Blue: Further Studies

In order for Mallard Blue to be used clinically, it would be desirable to incorporate it into an ‘assay kit’ such as those routinely used in biological protein binding studies, for

example. Such kits are routinely prepared some time (e.g. weeks) in advance of their use to allow for shipping, storage etc. so it was decided to scope out the potential of MalB. A crucial property which MalB must exhibit therefore is stability. Two options were considered for how such an assay kit may operate: (i) the MalB solution would be provided pre-dissolved in buffer at the correct concentration, or (ii) the MalB would be supplied as solid to be dissolved in appropriate amounts of buffered solution (which would be supplied separately).

In order to probe the stability of MalB in solution – to simulate delivery option (i) – a solution of MalB (25 μM) was made up in the related conditions of 150 mM NaCl and 10 mM Tris HCl and left to stand in either light or dark and under either an air or nitrogen atmosphere. Stability was probed by monitoring the absorbance intensity at 615 nm every 24 hours, and is plotted in Figure 2.13.

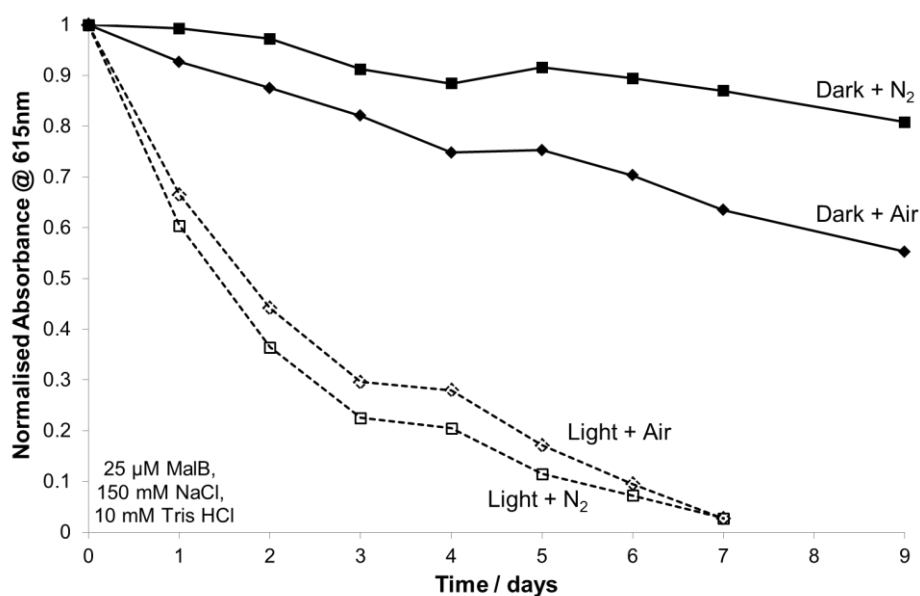


Figure 2.13 – Stability traces of MalB in the presence of light or dark under either air or nitrogen.

When exposed to light, MalB de-colours rather quickly with a half-life of approximately 30 hours regardless of the atmosphere of storage. Thionine dyes are known to be susceptible to photo-bleaching, and the phenomenon has been studied previously.^{247,248} The tri-cyclic ring of methylene blue, for example, can be reduced through introduction of a proton to generate the colourless *leuco* species, although oxidative bleaching of thionines is also known.²⁴⁹⁻²⁵¹ For MalB, it seems likely that in the presence of light, a proton could transfer from either of the arginine amine or guanidinium groups onto the

thiazine nitrogen atom causing the photoreductive bleaching to occur in a similar manner to that observed for thionines by Usui and Koizumi.²⁵² In darkness, the half-life of MalB is considerably extended to >9 days, with the solution stored under an inert nitrogen atmosphere least affected by bleaching. Clearly, it is not ideal for potential development into an assay kit device if MalB solutions require long-term storage in darkness under an inert atmosphere.

The possibility of providing a solid sample of MalB ready for dissolution in buffer shortly before use was probed next, to simulate delivery option (ii). This approach was also found to have problems associated with it. Most notably, when solid MalB is dissolved in aqueous buffer, the solution is not immediately blue. At room temperature (*ca.* 20°C), the blue colouration actually develops rather slowly: over a period of approximately 96 hours, as shown in Figure 2.14. This slow colour development is assigned to the slow de-aggregation kinetics of the dye system or, more specifically, the un-stacking of the tri-cyclic aromatic cores.

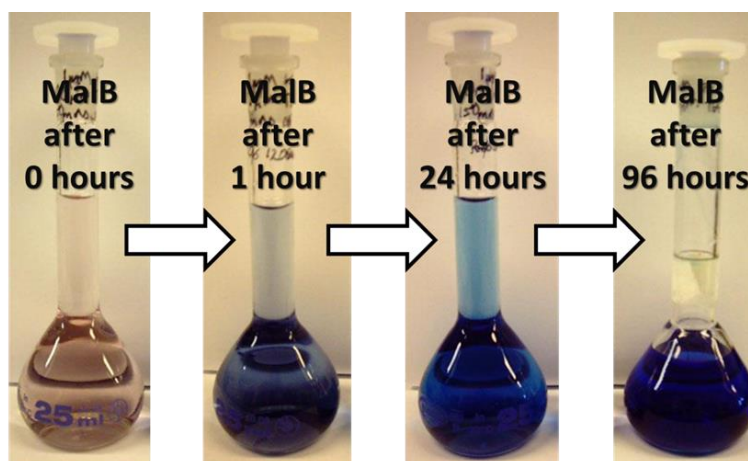


Figure 2.14 – Time-lapse photographs showing development of MalB colour over time at room temperature.

Aggregation of thionine based dyes is well known and has been widely studied.^{253,254} In general, as concentration of the dye increases, so does the propensity for π - π intermolecular interactions between the aromatic cores and dye-stacking. Thionine aggregation has been studied previously by Mackay and co-workers who showed that aggregation of the dye enhanced its water solubility compared to theoretical solubility predictions.²²⁹ An often-employed way of monitoring dye aggregation is by monitoring the UV/visible absorbance maxima for a dye (λ_{max}) as concentration changes;

aggregation causes λ_{\max} to be shifted. For our system, titrating increasing amounts of de-aggregated MalB into a cuvette of water, up to a final concentration of 500 μM , resulted in the absorbance spectra shown in Figure 2.15. A linear increase in absorbance intensity was observed as concentration increased but, importantly, there was no change in λ_{\max} . This suggests that MalB aggregation is not playing a role at the concentrations used in any of the heparin detection assays carried out in our studies. The critical aggregation concentration of MalB was not determined as the CAC of native thionine is known to be in the millimolar concentration range and so such experiments would be compound expensive.²²⁹

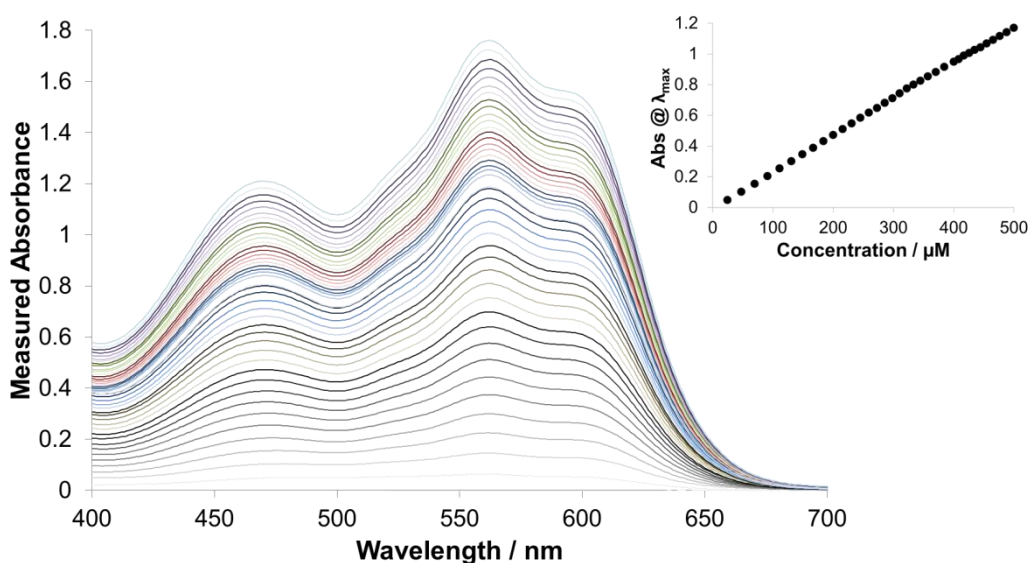


Figure 2.15 – UV-visible absorbance spectra for MalB in water as concentration increases. Inset: Plot of absorbance at λ_{\max} between 0 – 500 μM .

The MalB de-aggregation event upon dissolution can be accelerated by incubating the MalB solution for *ca.* 24 hours at 50°C. Although effective, the requirement of such preparation is not appealing from the perspective of designing an ‘assay kit.’ Nonetheless, the stability, preparation and storage studies have all served to inform the current use of MalB, where all solutions are incubated for 24 hours at 50°C before use, and stored in the dark.

2.7 Conclusions & Future Work

A selection of commercial cationic indicator dyes were examined and shown to be unable to reliably respond to heparin in the presence of competitive electrolytes such as

150 mM NaCl. Taking inspiration from the commercial thionine family of dyes, a novel heparin sensor was synthesised in two straightforward steps through coupling of two arginine residues onto a thionine core. The new dye, named Mallard Blue, was not only shown capable of responding to heparin in the presence of 150 mM NaCl – something none of the commercial thionines can do – but also of doing so selectively over structurally related glycosaminoglycans such as chondroitin sulfate and hyaluronic acid.

Mallard Blue was shown to be capable of responding to heparin delivered in 100% human serum. This impressive performance matches landmark work in the heparin sensing field and shows real clinical promise as the assay was carried out in a manner which directly simulated the clinical setting. Crucially, heparin detection occurred within a clinically relevant heparin concentration range. Through direct comparison against Azure A, MalB was also shown to be the new best-in-class for the thionine family of dyes.

The incorporation of MalB into a chemically applicable heparin-sensing assay kit was considered. The MalB de-aggregation event upon dissolution was identified as a limiting factor and shown to take around 96 hours at room temperature or 24 hours at 50°C. Concentration dependant aggregation of MalB in aqueous solution was shown spectrophotometrically not to occur below 500 µM.

A time-resolved stability study of MalB revealed a gradual bleaching event which occurred in the presence of light and was assigned to a slow photo-reduction of the phenothiazine-like ring structure. This photo-degradation was significantly retarded upon storing MalB in darkness.

Future work in this area could focus on increasing the commercial viability and appeal of the sample preparation post-synthesis. This may include enhancing the photo-stability of the dye solution or re-designing the system to reduce sample preparation time (eg. by removing the necessity for incubation). These improvements are likely to involve modification of the chromophoric dye core. A sensible, and convenient, starting point may be the use of a close structural analogue of thionine such as proflavine. Proflavine offers a slightly different heteroaromatic dye core which may have different susceptibility to the reductive processes identified as the cause of MalB bleaching. Much like thionine, proflavine also offers two aniline-like functional handles although it is noteworthy that previous work from Smith and co-workers focussed on non-covalent

interactions between these groups and carboxylic acids, rather than direct reaction between them.^{255,256} This may suggest that the different dye core affects the reactivity of the pendant amines. Other functionalisable chromogenic or fluorescent dye cores such as, for example, fluorescein could also be considered.

3 Insights into Heparin Binding

3.1 Introduction

Given the well-documented toxicity problems associated with the clinical use of protamine for heparin neutralization, there is a growing interest in the development of novel chemical agents which are able to provide the same neutralization role in the absence of the associated side-effects.²¹² During the development of such systems, there is a key requirement to probe the performance ability of the candidate molecules. Often, researchers choose to move quickly to clinically relevant heparin neutralization assays to assess potential efficacy. Techniques such as the anti-factor Xa assay, which directly measures the inhibition of clotting Factor-Xa in the presence of heparin, or other direct ‘clotting-time’ measurements such as the activated partial thromboplastin time (aPTT assay) or prothrombin time (PT assay) are often employed for this purpose. Indeed, as examples, early developmental studies of foldamer systems in the work of DeGrado and co-workers²⁰² focused on anti-factor Xa results for compound comparisons, while *ex vivo* clotting studies were heavily relied upon alongside animal testing work during the development of delparantag.¹⁹⁷

Although such clotting based assays are well accepted for providing measures of anticoagulancy, and therefore provide some measure of the potential clinical effectiveness of the candidate being tested, the results can mask more fundamental performance information.^{118,257} Such clotting-based techniques typically operate in genuine biological media such as human plasma, which is a highly competitive mixture of serum and albumin proteins, electrolytes, antibodies, antigens and hormones, along with other exogenous and endogenous species naturally present in blood. Successful heparin neutralization in this medium therefore indicates the ability of a binder molecule to selectively form interactions with heparin in preference to the many other aforementioned components. Conversely, in the event of a candidate molecule failing to neutralise anticoagulation, it can be difficult to de-convolute the reason for failure in terms of, for example, an inability to bind heparin, or a preferential ability to bind some other biological species in plasma (i.e. off-target binding). Consequently, most studies additionally employ a complementary assay technique to interrogate heparin binding ability.

An early report on the development of calix[8]arenes for heparin neutralisation from the group of Cunsolo²⁰⁰ provides a typical example of the use of a variety of heparin binding assays. Initially, Cunsolo and co-workers probed heparin binding performance using a fluorescence-based indicator displacement assay in the presence of low concentrations of buffer. Subsequently, NMR titration experiments were carried out to validate the indicator displacement results and further interrogate the binding under more competitive conditions containing 150 mM NaCl. Comparison of the data from these studies gave insight to heparin binding performance.²⁰⁰ Interestingly, further developments in the aforementioned work of DeGrado and co-workers developing foldamer systems employed isothermal titration calorimetry (ITC) to probe heparin binding in 150 mM NaCl as a complementary technique to the anti-Xa data reported previously.²⁰⁴ Indeed, these two examples appear representative of researchers' desires to probe heparin binding in electrolytically competitive conditions alongside the more clinically-relevant plasma clotting assays.

Although NMR titration experiments and ITC investigations are well-suited to studying heparin binding, it can be argued that they are not ideal for initial screening of novel heparin binding systems at the early stages of development. Each technique is relatively compound intensive and may present unattractively high associated costs. It is perhaps not surprising therefore that a variety of other techniques such as affinity co-electrophoresis²⁵⁸ and competitive inhibition assays²⁵⁹ have emerged as alternative approaches. A particularly eye-catching recent approach involved the employment of turbidimetric screening by Koide and co-workers, where the ability of heparin to inhibit the spontaneous formation of insoluble fibrils by collagen was the key tool in probing a candidate's heparin binding ability.²⁶⁰ Upon introduction of an effective heparin binder, collagen fibril formation was no longer inhibited and the associated turbidity increase could be used to quantify the relative heparin binding ability of the candidate compound. This approach was also shown to be well suited to high-throughput screening methods.²⁶⁰

Building on our interest in heparin sensing systems, we became interested in simple spectroscopic screening methods able to quickly determine the relative heparin binding ability of a range of candidate systems under electrolytically competitive, or even biologically relevant, conditions. Indicator displacement assays (IDA) were identified as well-suited for this type of monitoring owing to their requirement of a relatively small

amount of compound and straightforward titration-based methodology.^{261,262} Indeed, the development of chemical bioprobes is an ever-expanding field, and is readily applicable to this type of heparin binder screening.²⁶³ For a successful heparin binding IDA, a spectroscopically active dye must exhibit a characteristic signal change when displaced into free solution by the formation of preferable binder-heparin complexes. The IDA concept is shown in cartoon form in Figure 3.1.

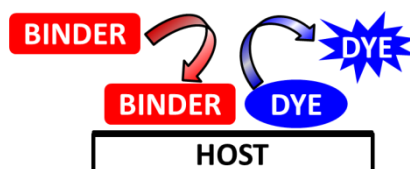


Figure 3.1 – Cartoon concept of an indicator displacement assay (IDA).

Of the many heparin sensors presented in the previous Chapter, several have explicitly been shown to be suitable for application in an IDA regime. The commercial thionine dyes azure A¹⁴³ and methylene blue¹⁴² are both operable within such systems, although their monocationic nature has limited their widespread use due to their intolerance of high levels of competitive electrolytes.^{143,211} The landmark tris-boronic acid scaffold from Ansyn and co-workers was amongst the first synthetic systems to be developed into an IDA system although the sensor initially required the presence of pyrocatechol violet as the indicator dye.¹⁴⁴ The system was then elegantly modified to embed the fluorophore into the host structure. Addition of protamine to a complex of this modified sensor and heparin was shown to ‘strip’ heparin out of the scaffold binding site, leading to the re-establishment of the initial fluorescent signal, Figure 3.2.¹⁴⁵ Other works, for example from the groups of Nitz¹⁵⁷ and Chang,¹⁶⁰ also demonstrated the reversibility of sensor-heparin interactions by introduction of protamine and displacement of the sensor dye, although neither group appeared to capitalise on the potential insight which could be gained from displacement assays utilizing their robust fluorescent sensors.

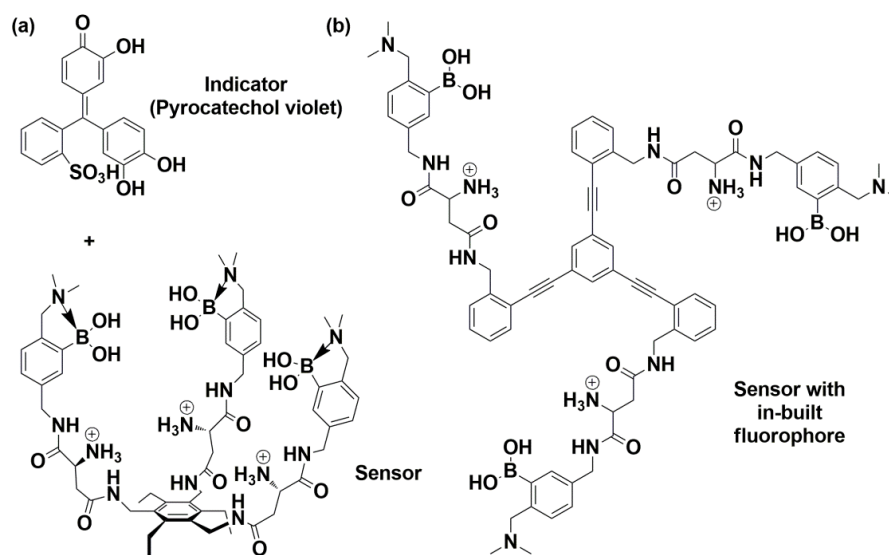


Figure 3.2 – Ansyln’s heparin sensing systems: (a) tri-boronic acid receptor and pyrocatechol violet indicator;¹⁴⁴ (b) modified fluorophore-containing receptor.¹⁴⁵ These structures are also shown in Figure 1.19.

Arguably the most impressive heparin sensing systems published recently are the benzimidazolium derivatives ‘heparin blue’ and ‘heparin orange’ from the work of Chang and co-workers.¹⁶⁰ Having exhibited fully reversible binding to both unfractionated and low-molecular-weight heparins, these molecules ostensibly appear ideal candidates for further development. A major drawback associated with investigation of these compounds, however, is their multi-step syntheses. Ease-of-preparation is a key consideration in the development of systems with the potential for widespread applicability. In order to maximize the potential uptake of any new assay, it was therefore reasoned to be important that the assay be composed of easily accessible or, at the very least, synthetically tractable components. The investigation for this purpose of an indicator dye requiring a multi-step synthesis was considered a futile exercise and so our attention turned away from these benzimidazolium-based sensors.

As shown in the previous Chapter, we recently developed a new heparin sensor, Mallard Blue (MalB), which demonstrated comparable heparin sensing abilities to the systems of Chang.²⁴² A key feature of MalB was that it could be synthesised in two straightforward synthetic steps from commercially available starting materials, and as such presents a much more attractive, less daunting synthetic challenge for researchers without specialisms in synthetic chemistry. It was therefore decided to investigate our newly developed dye, Mallard Blue, within an indicator displacement assay regime.

3.2 Mallard Blue Heparin Binding Competition Assay

3.2.1 Electrolytically Competitive Conditions

Although the heparin binding ability of MalB had been studied and rationalised using molecular dynamics modelling studies, up to this point, utilizing the reversibility of MalB-heparin interaction had not been considered. The earlier work had demonstrated that the MalB-heparin complex could be perturbed by the titration of increasing amounts of electrolytes – namely Tris HCl and NaCl – and so it was reasoned that introduction of protamine to a sample of heparin-containing MalB should result in formation of a heparin-protamine complex and release of MalB into solution. Based on the data from the previous Chapter, it was decided to introduce protamine into a sample containing 25 μM MalB, 27 μM heparin, 150 mM NaCl and 10 Tris HCl. Pleasingly, as shown in Figure 3.3, this resulted in an increase in absorbance intensity at 615 nm.

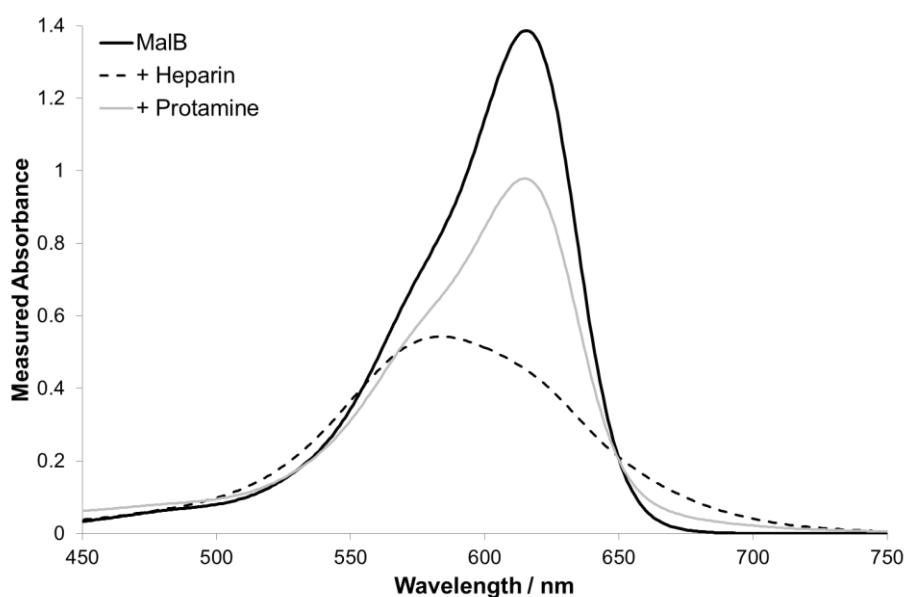


Figure 3.3 – UV-visible absorbance spectra for MalB (25 μM) in the absence and presence of heparin (27 μM), and following the subsequent addition of protamine in the presence of NaCl (150 mM) and Tris HCl (10 mM).

Following this qualitative observation, it was decided to quantitatively titrate protamine into a sample of MalB and heparin as this would permit the calculation of binding parameters and thereby enable the performance of different molecular species to be compared. Specifically, three appropriate parameters were identified: (i) CE_{50} – charge

excess, that is the number of cationic binder charges required per heparin anionic charge at 50% dye displacement. Rationalising binding ability in terms of charge excess enables the efficiency of each individual charge to be calculated, allowing the performances of binders possessing different numbers of charges to be meaningfully compared. (ii) EC_{50} – the effective concentration of binder at the same point. This provides a measure of the molarity of binder present at 50% dye displacement. (iii) Effective dose – the raw amount (mass) of binder required to displace 50% of the dye from 100IU of heparin. This is a clinically relevant parameter. The binding curve resulting from titration of protamine into MalB-heparin is shown in Figure 3.4 along with the numerical data in Table 3.1.

Table 3.1 – Heparin binding data for protamine, calculated from MalB assay.

Assay Conditions	$EC_{50} / \mu\text{M}$	CE_{50}	Dose / mg per 100IU
25 μM MalB, 27 μM heparin, 150 mM NaCl, 10 mM Tris HCl	(2.34 ± 0.23)	(0.52 ± 0.05)	(0.32 ± 0.03)

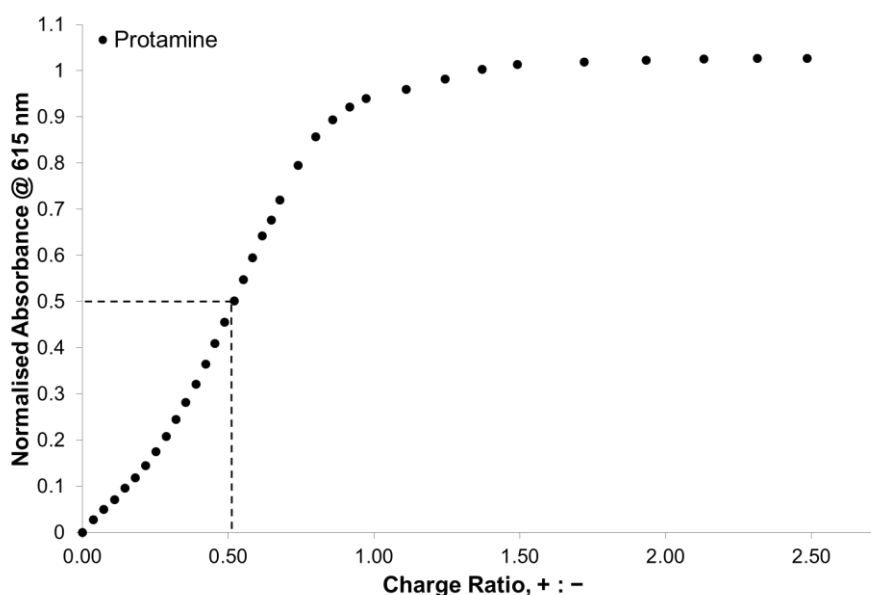


Figure 3.4 – Heparin binding curve for protamine, with the point of 50% dye displacement indicated.

The data shows that under this regime only $0.52 (\pm 0.05)$ protamine cationic charges are required to bind to each negative charge along the heparin polysaccharide, equating to a concentration of $2.34 (\pm 0.23) \mu\text{M}$ at 50% MalB displacement. Under these conditions,

the data suggests that 0.32 (\pm 0.03) mg of protamine would be able to bind to 100 IU of heparin. It should be stressed that these values should not be taken as ‘absolute’ *bona fide* binding parameters as the binding assay operates under competition and all binding of protamine to heparin is being measured relative to the binding ability of MalB. Calculation of values for other compounds under the same assay conditions would however allow for valid performance comparisons between different molecular species.

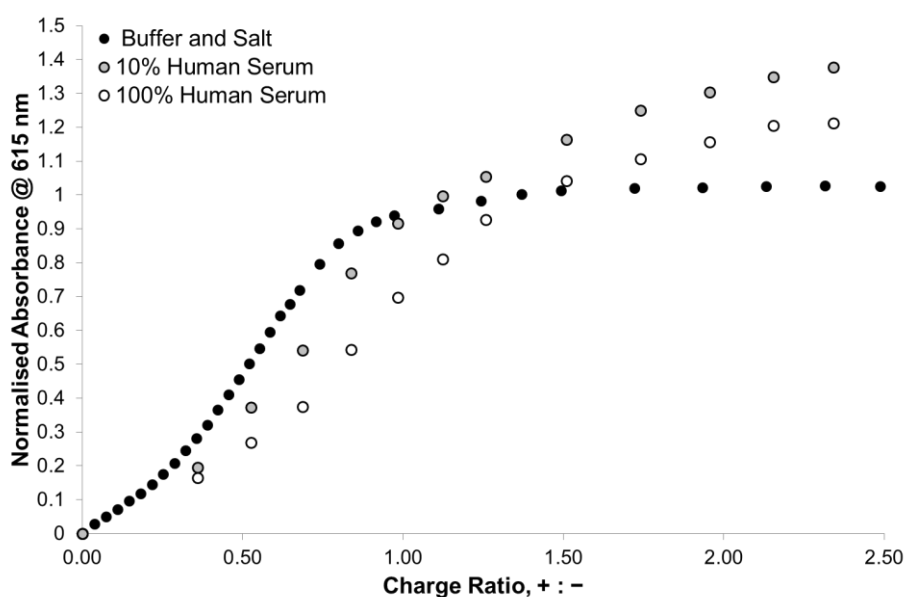
3.2.2 *Clinically Relevant Conditions*

Having established that the MalB IDA was able to operate in the presence of 150 mM NaCl, it was decided to investigate the robustness of the same system in the presence of more challenging, and biologically relevant, media. Following the MalB sensing studies in the previous Chapter, human serum was identified as a suitable biological medium. It was also reasoned that a heparin binding assay able to operate in the presence of human serum may provide a useful tool for assessing the clinical potential of candidate systems, and for beginning to understand the effects of different serum components.

Practically, the IDA protocol from the MalB assay in buffer and salt was modified by employing a multiple-cuvette approach. Rather than gradually titrating binder into a single cuvette, several individual cuvettes were prepared with each containing a different amount of binder, so as to correspond with different points on the overall ‘titration’ curve. Once prepared, an overly-concentrated solution of heparin in serum was delivered into each cuvette such that the MalB-heparin conditions were 25 μ M MalB and 27 μ M heparin in all samples to replicate the original assay. In this way, the serum percentage present in the assay could be controlled through modifying the heparin-containing solution (e.g. by dilution with buffer). In order to probe the effects of serum on the assay, the modified protocol was applied to protamine with heparin delivered in either 10% or 100% human serum. The results are shown in Figure 3.5 and Table 3.2.

Table 3.2 – Heparin binding data for protamine from MalB assay with heparin delivered in 10 and 100% human serum.

Assay Conditions	Protamine		
	EC ₅₀ / μ M	CE ₅₀	Dose / mg per 100IU
Salt and Buffer	(2.34 \pm 0.23)	(0.52 \pm 0.05)	(0.32 \pm 0.03)
Heparin in 10% Human Serum	(2.80 \pm 0.26)	(0.63 \pm 0.06)	(0.39 \pm 0.04)
Heparin in 100% Human Serum	(3.51 \pm 0.12)	(0.79 \pm 0.03)	(0.49 \pm 0.02)

**Figure 3.5** – Heparin binding curves for protamine obtained from MalB assay with heparin delivered in 10% and 100% human serum.

The data show that the presence of human serum leads to an increase in the charge excess and effective concentrations of protamine required to displace 50% of MalB from heparin. This effect can be rationalised through off-target interactions between protamine and any of the electrolytes or charged patches on serum proteins present within the media. The progressive deterioration in protamine binding efficiency as the percentage of serum present increases supports this. In the presence of serum, normalized absorbance values continue above the theoretical maximum of 1 even though the presence of serum was taken into account by its inclusion in the baseline reading. Despite this, some signal drift away from the baseline was observed during the experiment. This enhanced absorbance is thought to be caused by the increased turbidity associated with the formation of heparin-protamine complexes within this medium.²⁶⁴

Indeed it is known from the work of Măntele and co-workers that the turbidity associated with heparin-protamine aggregates has greater influence on direct absorbance measurements in serum than in plain salt water due to the presence, and involvement, of plasma proteins.²⁶⁵

3.3 Studying Generational Effects in PAMAM Dendrimers

Having established protocols for incorporation of Mallard Blue into an indicator displacement assay (IDA), and demonstrated that insights to heparin binding could potentially be gained, it was decided to attempt to validate the assay by examining a selection of known heparin binding systems for their relative binding abilities.

3.3.1 PAMAM Dendrimers

PAMAM (poly(amidoamine)) dendrimers were identified as suitable molecules with which to validate our novel assay as they are well-known commercially available materials and so could be easily sourced for testing. PAMAM dendrimers were first reported by Tomalia and co-workers in 1985 and result from the tetra-functionalisation of an ethylene diamine central core through exhaustive Michael addition with methyl acrylate, followed by amidation of the resulting esters with further ethylene diamine, Figure 3.6.^{266,267}

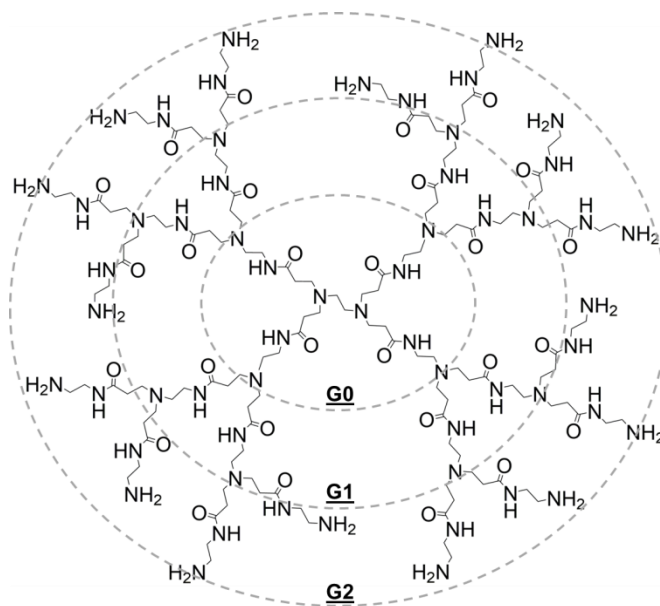


Figure 3.6 – Structure of G2-PAMAM with the generation levels G0 – G2 shown. The higher generations result from larger iterations of the dendritic structure.

In general, dendritic systems are well known to be able to mimic many aspects of protein behaviour in both structural and functional aspects.^{268,269} Indeed PAMAMs have been widely applied in biological and biomimetic applications,²⁷⁰⁻²⁷² for example as drug delivery vehicles able to encapsulate hydrophobic drugs within their core branching structure²⁷³ or as macromolecular MRI contrast agents through chelation with Gd(III) species.²⁷⁴ Most relevant to our current study, several previous groups have demonstrated PAMAM dendrimers to have heparin binding ability.^{192,193,275} As large cationic structures, however, it is perhaps not surprising that PAMAMs are known to possess inappropriate toxicity profiles for clinical deployment as heparin rescue agents, and so have not been applied for this use in a clinical setting.^{276,277} Here, with the focus on validating our new assay and gaining insights into generational effects upon heparin binding, PAMAMs offered an ideal molecular family to examine.

3.3.2 Heparin Binding in Competitive Conditions

3.3.2.1 Experimental Study

Six generations of PAMAM dendrimers (G0 – G4, and G6) were each tested for heparin binding ability in the Mallard Blue heparin binding assay. The assay was carried out under the previously optimised conditions of 25 μ M MalB, 27 μ M heparin, 150 mM NaCl and 10 mM Tris HCl. Each titration was carried out in triplicate and the results, as calculated from the point of 50% MalB displacement, are presented in Table 3.3.

Table 3.3 – Heparin binding data for PAMAM dendrimers tested in MalB assay in buffer and salt. Protamine data included for comparison.

Compound	Charge (+)	Heparin Binding		
		EC ₅₀ / μ M	CE ₅₀	Dose / mg per 100IU
Protamine	24	(2.34 \pm 0.23)	(0.52 \pm 0.05)	(0.32 \pm 0.03)
G0-PAMAM	4	<i>Not achieved - binding too weak</i>		
G1-PAMAM	8	(10.10 \pm 0.32)	(0.75 \pm 0.02)	(0.44 \pm 0.01)
G2-PAMAM	16	(2.55 \pm 0.32)	(0.38 \pm 0.04)	(0.25 \pm 0.03)
G3-PAMAM	32	(1.53 \pm 0.21)	(0.45 \pm 0.06)	(0.32 \pm 0.04)
G4-PAMAM	64	(0.64 \pm 0.04)	(0.38 \pm 0.02)	(0.27 \pm 0.02)
G6-PAMAM	256	(0.22 \pm 0.04)	(0.53 \pm 0.09)	(0.39 \pm 0.06)

The first parameter of interest is the EC₅₀, or effective concentration, for each of the dendrimers. As generation number, and molecular size increases, the concentration required to effectively displace 50% MalB into free solution decreases. This is a straightforward consequence of each subsequent dendritic generation possessing exponentially more cationic charge than the preceding one and accounts for the EC₅₀ decrease from 10.10 (\pm 0.32) μ M at G1 to 0.22 (\pm 0.04) μ M at G6. Given the effects of molecular size upon effective concentration, a more informative measure of the relative binding performances is that of CE₅₀, the charge excess or charge efficiency.

In order to calculate the CE₅₀ values, the number of protonated sites per PAMAM generation needed to be carefully considered. The 10 mM Tris HCl component of the solutions buffers the assay at pH 7.0; a regime under which only the peripheral primary amines of PAMAMs are protonated.^{278,279} This leads to the molecular charges listed in Table 3.3.

The first striking observation is that the smallest dendrimer, G0-PAMAM, is unable to displace 50% MalB from heparin, even when present in a concentration excess towards the end of the titration. Ostensibly, G0-PAMAM (517 Da, 4+) and MalB (542 Da, 5+) have comparable molecular properties, and so their markedly different heparin binding abilities further supports the structurally optimised nature of the crescent-shaped MalB compared to the more spherical PAMAM. In turn, this performance difference also

suggests charge is not the only factor controlling heparin binding; a view at odds with previous suggestions from Krämer and co-workers.²⁸⁰

The remaining PAMAM systems were all able to bind heparin well enough to at least displace 50% MalB into solution and allow CE_{50} values to be calculated. Comparison of the CE_{50} derived for each system revealed an interesting trend. The data in Table 3.3 show that the next smallest (G1) and the largest (G6) dendrimers were the least efficient heparin binders on a per-charge basis, requiring $0.75 (\pm 0.02)$ and $0.53 (\pm 0.09)$ cationic charges per negative charge respectively. It is worth noting that the performance of the largest dendrimer tested, G6, is comparable to that of protamine (which has a CE_{50} of $0.52 (\pm 0.05)$), although the larger molecular weight of the PAMAM system leads to a higher clinically relevant dose value.

The ‘medium-size’ PAMAMs (G2, G3, G4) all exhibited quite similar heparin binding performances with comparable CE_{50} and dosage values being observed. In all cases, the data suggest each PAMAM positive charge is used more efficiently than each positive charge in protamine. Overall, the data suggest that the low generation systems (G0, G1) are too small to establish effective binding interactions, while the medium sized systems (G2-G4) appear best able to marshal their individual charges to bind heparin in the most charge-efficient manner. The overwhelming charge density of the largest (G6) dendrimer surface inhibits effective use of each individual charge. Importantly, these observations are similar to those observed using isothermal calorimetry to probe heparin-PAMAM binding, which therefore served to support the results obtained from our novel MalB competition assay.¹⁹³

The assertion that the medium sized PAMAM systems are the most charge-efficient heparin binders is itself an interesting one. The well documented toxicity of PAMAM dendrimers often restricts their consideration in new biological investigations, yet G2-PAMAM is one of the less toxic PAMAMs.^{276,277} It could be suggested therefore that G2-PAMAM could be a useful ‘lead’ compound as a basis for future developmental work towards finding a suitable protamine alternative.

3.3.2.2 Computational Study

In order to further validate the PAMAM heparin binding results obtained using the new assay, a molecular dynamics (MD) modelling study was carried out in collaboration

with Professor Sabrina Pricl and her team at University of Trieste, Italy. The computational study simulated the binding interactions between different generation PAMAM systems and a representative heparin polysaccharide, enabling the energetics of binding to be calculated. In particular, the simulations were able to identify how many of the available surface charges interacted directly with heparin, Q_{eff} , as well as determining the effective free energy of binding, $\Delta G_{\text{bind}}^{\text{eff}}$, for each system. The contribution of each interacting surface charge to this energy could then be deduced to give the effective-charge-normalised free energy of binding, $\Delta G_{\text{bind}}^{\text{eff}}/Q_{\text{eff}}$. This parameter is analogous to the charge excess values derived from the experimental study and so it was hoped that comparison of these two independently obtained datasets would reveal similar trends. The data calculated from the MD study is shown in Table 3.4.

Table 3.4 – MD simulation data for PAMAM dendrimers interacting with heparin. Protamine data included for comparison. Q_{tot} : number of binder charges; Q_{eff} : number of interacting charges; $\Delta G_{\text{bind}}^{\text{eff}}$: effective free energy of binding; $\Delta G_{\text{bind}}^{\text{eff}}/Q_{\text{eff}}$: effective-charge-normalised free energy of binding.

Compound	Q_{tot} /(+)	Q_{eff} /(+)	$\Delta G_{\text{bind}}^{\text{eff}}$ / kcal mol ⁻¹	$\Delta G_{\text{bind}}^{\text{eff}}/Q_{\text{eff}}$ / kcal mol ⁻¹
Protamine	24	12 ± 1	-3.96 ± 0.41	-0.33 ± 0.04
G1-PAMAM	8	6 ± 1	-1.14 ± 0.22	-0.19 ± 0.05
G2-PAMAM	16	13 ± 1	-16.9 ± 0.5	-1.30 ± 0.11
G3-PAMAM	32	15 ± 1	-15.9 ± 0.3	-1.06 ± 0.07
G4-PAMAM	64	16 ± 3	-14.6 ± 0.8	-0.91 ± 0.18
G6-PAMAM	256	45 ± 5	-18.0 ± 1.3	-0.40 ± 0.05

In general, the computational data are in agreement with the experimental data. The Q_{eff} values are representative of the number of cationic charges per dendrimer which directly interact with a single heparin polysaccharide. Comparison of these values against the molecular charge, Q_{tot} , gives an insight into how well each PAMAM generation is able to marshal its charges. For example, *ca.* six of the eight cationic charges (75%) in G1-PAMAM make direct contact with heparin, although the overall effective free energy of binding $\Delta G_{\text{bind}}^{\text{eff}}$ is very low at -1.14 (± 0.22) kcal mol⁻¹. This leads to each binding charge contributing only -0.19 (± 0.05) kcal mol⁻¹ to the binding interaction. At the

other extreme, only 45 (± 5) of the available 256 cationic charges (18%) on G6-PAMAM directly interact with a heparin polysaccharide. In reality, of course, it is likely that G6-PAMAM may interact simultaneously with more than one polysaccharide chain but owing to the computer-time-intensive nature of such simulations, this was not modelled. The resulting $\Delta G_{bind}^{eff}/Q_{eff}$ for G6-PAMAM, despite being double that calculated for G1-PAMAM, was still relatively small at -0.40 (± 0.05).

Of the medium sized dendrimers (G2-G4), it was G2-PAMAM which utilised the highest percentage of the available charges for direct interactions with heparin, with 13 (± 1) of the 16 surface amines (82%) interacting directly with the polysaccharide. Distribution of the calculated free energy of binding, ΔG_{bind}^{eff} , between these 13 (± 1) resulted in the most energetic individual interactions observed for any of the systems tested with an $\Delta G_{bind}^{eff}/Q_{eff}$ of -1.30 (± 0.11) kcal mol⁻¹. These data compare favourably with the experimentally observed CE₅₀ value, for which G2-PAMAM had the joint lowest (i.e. most efficient) value, and confirms our initial suggestions that heparin binding using PAMAMs is not a straightforward ‘higher generation is better’ situation. Indeed, the concept of ‘less is more’ in multivalent binding has previously been examined in similar studies using MD modelling to interrogate dendritic systems interacting with DNA.²⁸¹

The computational study also allowed for further comparison against the performance of protamine, the modelling structure of which was built and refined from a consensus protein sequence. It is interesting to note that despite being regarded as the benchmark heparin binder, owing to its clinical application, protamine is only able to establish interactions directly with 12 (± 1) of the 24 cationic charges (50%) within its structure. Overall it does not interact particularly strongly either, with a ΔG_{bind}^{eff} of -3.96 (± 0.41) kcal mol⁻¹ leading to a per-binding-charge free energy $\Delta G_{bind}^{eff}/Q_{eff}$, of only -0.33 (± 0.44) kcal mol⁻¹. These relatively small interaction energies could be interpreted as surprising, although as visualised below in Figure 3.7, this may be a consequence of the relative rigidity of the protamine structure compared to the PAMAM dendrimers.

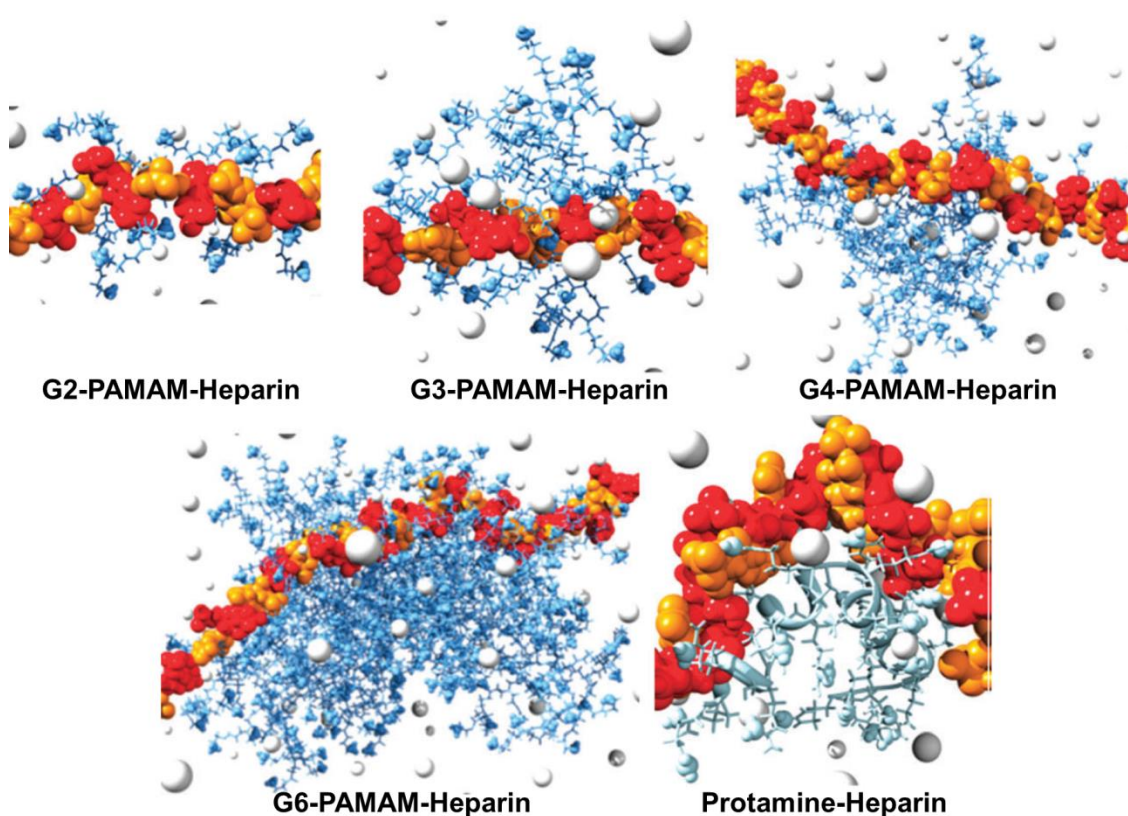


Figure 3.7 – Equilibrated MD snapshots of heparin binding to selected PAMAM dendrimers and protamine. Binders are represented as blue stick models while heparin is shown as red and orange space-filling structures.

An additional benefit of this MD modelling study is that it allowed snapshots of the binding events to be visualised, as shown in Figure 3.7. Perhaps most clear to see from these images is the struggle as PAMAM generation, and consequently molecular size, increases for all the binding groups to establish interactions with the polysaccharide chain. This is particularly clear, for example, when comparing the visibility of terminal amine group in the snapshots of G2-PAMAM-heparin against G6-PAMAM-heparin. The snapshot image of the heparin-protamine interaction is also insightful as it suggests so rigid is the protamine tertiary structure, that the normally extended heparin polysaccharide ‘wraps around’ the protein structure in an attempt to optimise the electrostatic binding interactions.

3.3.3 Heparin Binding in Clinically Relevant Conditions

Having established that G2-PAMAM was a more charge efficient heparin binder than protamine (and the other PAMAMs) in electrolytically competitive aqueous solution,

we next wanted to challenge these binding interactions in the more biological, and clinically relevant, conditions of human serum. This enabled the newly developed MalB assay with heparin delivered in serum to be employed. The data obtained for G2-PAMAM are displayed in Table 3.5.

Table 3.5 – Heparin binding data for G2-PAMAM with heparin delivered in 100% serum.

Assay Conditions	G2-PAMAM		
	EC ₅₀ / μ M	CE ₅₀	Dose / mg per 100IU
Salt and Buffer	(2.55 \pm 0.32)	(0.38 \pm 0.04)	(0.25 \pm 0.03)
Heparin in 100% Human Serum	(2.15 \pm 0.05)	(0.32 \pm 0.01)	(0.21 \pm 0.01)

G2-PAMAM fully maintained its relative heparin binding performance in human serum when compared against the data obtained in buffer and salt. This is particularly impressive given the decrease in efficiency of protamine observed earlier, see Table 3.2. Although the data appears to suggest that G2-PAMAM slightly increased its charge efficiency, the nature of this competition assay must be remembered. It is unlikely that G2-PAMAM actually improves in absolute terms but rather that its heparin binding ability improves relative to MalB in this more competitive biological media.

3.3.4 Summary

Overall, the data from the MalB assay have given insights into differing generational effects of PAMAM dendrimers when binding heparin. In particular, the ‘medium sized’ systems such as G2-PAMAM have been demonstrated as the most able to marshal their surface charges and establish meaningful efficient interactions with heparin. Molecular dynamics modelling corroborated the experimental findings. As mentioned above, G2-PAMAM is one of the least toxic PAMAM dendrimers and therefore may be suitable for consideration as a lead compound for further developmental work.

3.4 Studying Effects of Rigidity and Flexibility with Transgeden Dendrimers

3.4.1 *Transgeden (TGD) Dendrimers*

Following the insights into generational effects for PAMAM revealed by our new MalB heparin binding assay, we took an interest in the hybrid dendrimers being synthesised under the direction of our collaborator Professor Julián Rodríguez-López at Universidad de Castilla-La Mancha, Ciudad Real, Spain. For some time now, Rodríguez-López and co-workers have been interested in the study of hybrid dendrimers,²⁸²⁻²⁸⁴ with a particular focus on systems possessing poly(phenylenevinylidene) (PPV) character.²⁸⁵⁻²⁸⁷ PPV dendrimers consist, as the name suggests, of a series of phenyl rings conjugated through *trans*-alkene connections as shown in the top structure in Figure 3.8. The team of Rodríguez-López have taken an interest in controlling the surface functionality of PPV systems,²⁸⁸ for example through the introduction of specific electron-donating or electron-withdrawing groups in order to tune the photoluminescent properties of the system.²⁸⁹ Two of the most relevant approaches to our current study involved the hybridization of PPV dendrimers with PAMAM systems, firstly with PPV-groups installed at the PAMAM surface²⁹⁰ and more recently with PAMAM-groups installed at the PPV surface.²⁹¹⁻²⁹³ It was this lattermost family of compounds, known as Transgeden (TGD) dendrimers, in which we took particular interest.

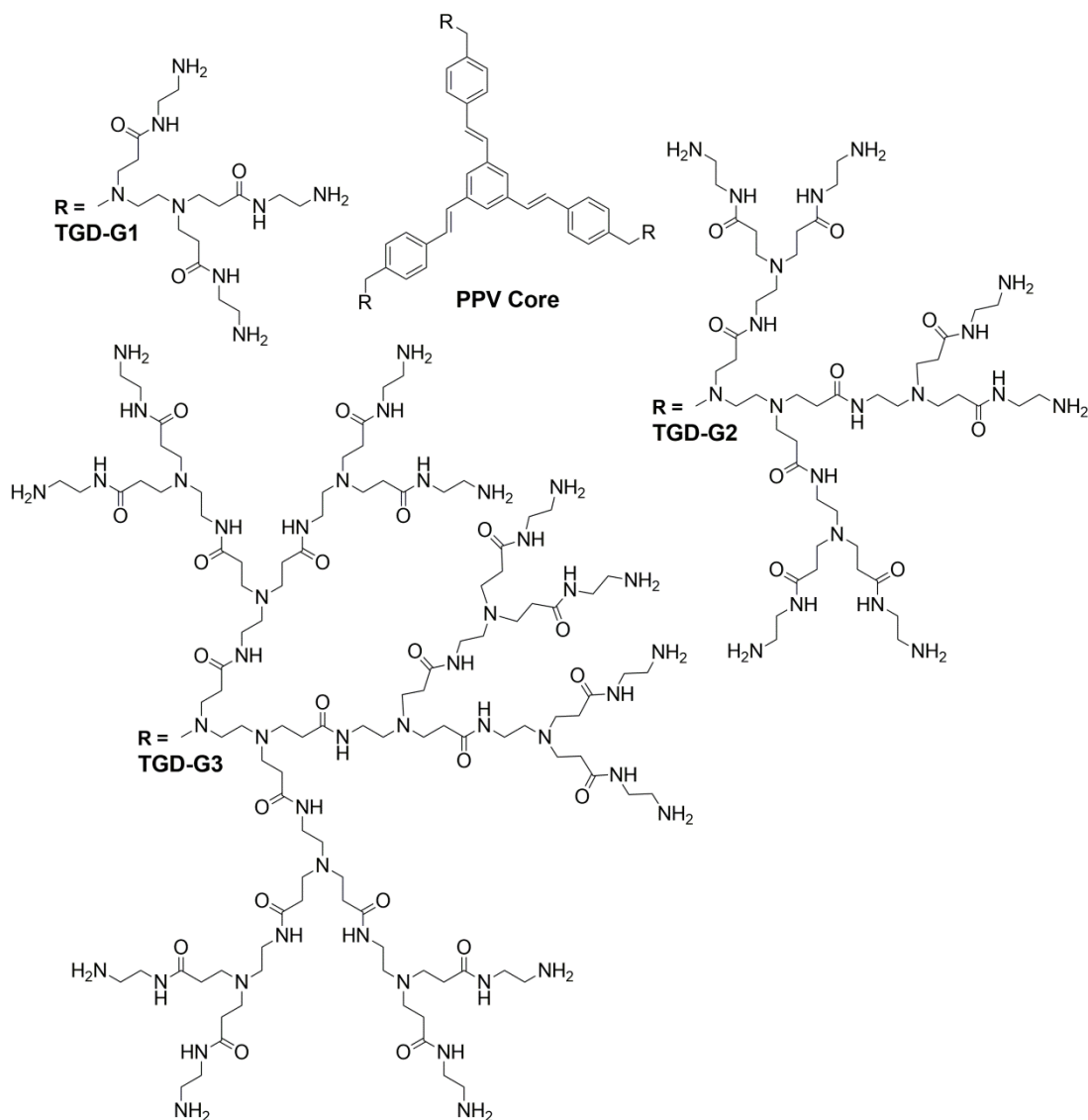


Figure 3.8 – Structure of Transgeden (TGD) dendrimers showing the PPV core unit and G1-G3 PAMAM surface groups.

It was decided to examine the heparin binding abilities of the first three generations of Transgeden dendrimers (TGD-G1, -G2, -G3) and to compare them against the corresponding native PAMAM dendrimers of equivalent generations. This allowed the increased rigidity of the TGD dendrimers conferred by the PPV cores, and more particularly its effect on the ability of the surface PAMAM ligand array to bind heparin, to be probed.

3.4.2 Heparin Binding Studies in Competitive Conditions

3.4.2.1 Experimental Study I: Mallard Blue Displacement Assay

The Transgeden dendrimers (G1-G3) were tested for their heparin binding ability using the MalB competition assay under the same conditions as had been applied earlier to the PAMAM dendrimers; namely 25 μM MalB, 27 μM heparin, 150 mM NaCl and 10 mM Tris HCl (pH 7.0). The resulting data, along with that shown earlier for the native PAMAMs, expressed in terms of dose, effective concentration and charge excess at 50% MalB displacement (EC_{50} and CE_{50} respectively) are displayed in Table 3.6.

Table 3.6 – Heparin binding data from MalB assay in buffer and salt for G1-G3 TGD dendritic systems, along with G1-G3 PAMAM data for comparison.

Compound	Charge (+)	Heparin Binding		
		EC_{50} / μM	CE_{50}	Dose / mg per 100IU
TGD-G1	9	(7.73 \pm 0.32)	(0.64 \pm 0.03)	(0.38 \pm 0.02)
TGD-G2	18	(3.78 \pm 0.25)	(0.63 \pm 0.04)	(0.42 \pm 0.03)
TGD-G3	36	(2.00 \pm 0.15)	(0.67 \pm 0.05)	(0.47 \pm 0.04)
G1-PAMAM	8	(10.10 \pm 0.32)	(0.75 \pm 0.02)	(0.44 \pm 0.01)
G2-PAMAM	16	(2.55 \pm 0.32)	(0.38 \pm 0.04)	(0.25 \pm 0.03)
G3-PAMAM	32	(1.53 \pm 0.21)	(0.45 \pm 0.06)	(0.32 \pm 0.04)

The data show that despite the rigidification of the dendritic core, all three generations of TGD dendrimers were able to bind heparin effectively, and could displace MalB during the competition assay. The EC_{50} for each TGD dendrimer decreased from 7.73 (\pm 0.32) μM at G1 to 2.00 (\pm 0.15) μM at G3, and this is again a straightforward consequence of each successive generation possessing a larger number of cationic binding sites per mole and so becoming able to out-compete MalB due to the sheer amount of charge present at lower concentrations. In terms of required dose, TGD-G1 was suggested to be marginally the best performer although the lower molecular weight of the smaller dendrimer exerts an influence over this observation.

In terms of the binding efficiency of each individual cationic charge, the CE_{50} values suggest binding performance is essentially equivalent across all three TGD generations; an observation in marked contrast to the PAMAM systems, which exhibit significant

performance improvement with increasing size to G2 and G3. Direct comparisons between equivalent generations of the two dendritic families showed that at G1, the TGD system was able to employ its 9 cationic charges in a more efficient manner than the PAMAM could its 8, while in the larger G2 and G3 systems, the native PAMAMs were the more charge efficient, despite possessing less overall charge in both cases. As informative as these CE_{50} values can be, it must be remembered that they only reflect the binding events at one specific point; namely that at which 50% MalB has been displaced from heparin. The full binding curves for each pair of dendrimers were therefore considered, Figure 3.9, in an attempt to rationalise the observed differences between the dendritic systems and probe the effects of molar dendrimer/heparin ratios.

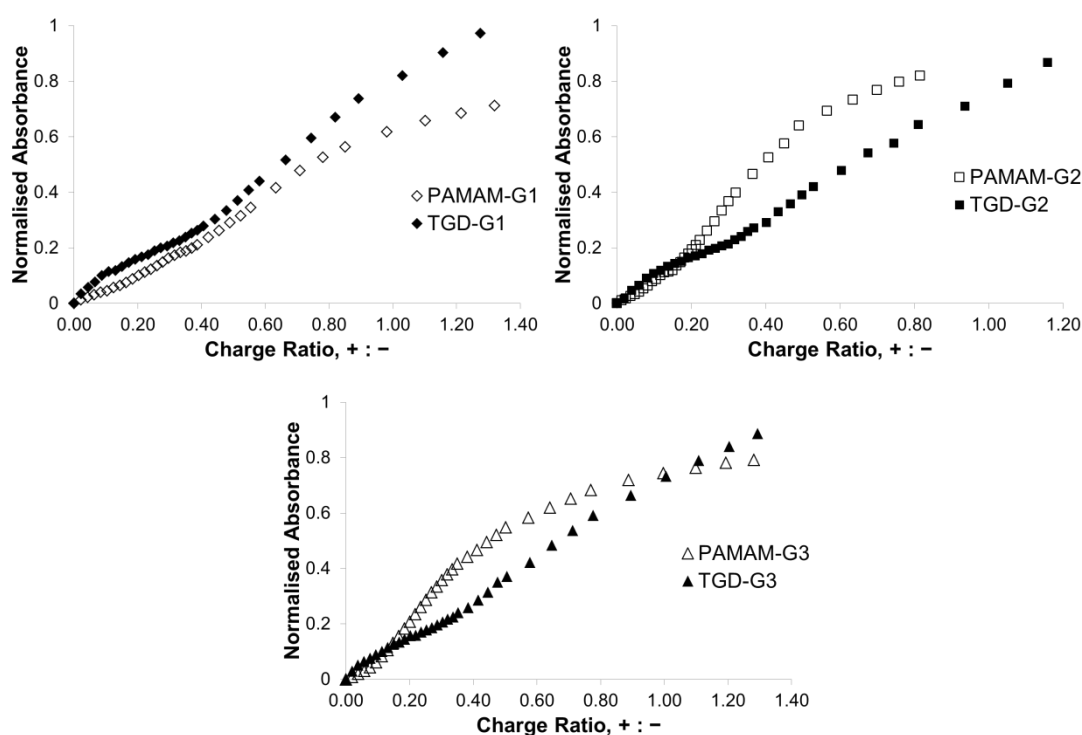


Figure 3.9 – Heparin binding curve comparisons for TGD (closed shapes) and PAMAM (open shapes) dendrimers at G1 (top left), G2 (top right) and G3 (bottom) from MalB assay in buffer and salt.

The binding curves for the smallest pair of dendrimers, TGD-G1 and G1-PAMAM shows that the hybrid TGD system is the superior heparin binder throughout the whole titration range. In this case, the single CE_{50} value is therefore representative of the overall binding. On moving to the larger G2 and G3 systems, this is not necessarily the case, as when only small amounts of dendrimer are present, the TGD systems exhibit superior binding to the native PAMAMs. As dendrimer concentrations increase beyond

a charge ratio of *ca.* 0.2 for these systems, the TGD performance drops off, leading to the observed superiority of PAMAM at the CE_{50} value. These observations suggest that the TGD dendrimers are better optimized for forming interactions with multiple heparin chains under the regime where heparin is present in significant excess, but when the stoichiometry of dendrimer to heparin is more even, the PAMAM systems are better optimized. The inherent rigidity imposed by the PPV cores upon the TGD systems may be central to these observations as, particularly at higher charge-excess values when the amount of heparin becomes limited, the hybrid dendrimers may be less well able to adapt and re-organise their ligand array to interact with a single heparin chain most optimally, while the more flexible PAMAMs may be able to more freely contort to bind the polysaccharide.

3.4.2.2 Computational Study: MD Modelling

In an attempt to validate these experimental observations, our collaborators, led by Professor Sabrina Pricl at University of Trieste, once again employed molecular dynamics (MD) modelling to study the dendrimer-heparin interactions. Binding was simulated at two different charge ratios in an attempt to understand the effect of stoichiometry on binding performance. Firstly, atomistic modelling was undertaken at a charge ratio of 0.4 as at this point on the binding curves the larger (G2 and G3) PAMAMs were significantly outperforming their TGD counterparts, while at G1 differences were minimal.

In order to compare the different dendrimers at the same charge ratio, the concentration of heparin within the simulation was kept constant and the number of individual dendrimer molecules adjusted to afford the desired charge ratio. This approach differed from the per-residue free energy decomposition technique employed in the previous section and, in practice, resulted in four (or five) G1, two G2 and one G3 dendrimer being present in each simulation. As before, the overall free energy of binding, ΔG_{bind}^{eff} , could be calculated to give an insight to the energetics of the overall binding interaction. The data show that each of the TGD dendrimers, along with G1-PAMAM, interact with a free energy of around $-10 \text{ kcal mol}^{-1}$. The larger PAMAM dendrimers bind more efficiently with G2-PAMAM affording $-44.7 (\pm 2) \text{ kcal mol}^{-1}$.

Division of these total free energy values by the total number of cationic charges present, Q_{tot} , in each simulation – which is coincidentally 36 for all three TGD

dendrimers – afforded the charge normalized free energy of binding, $\Delta G_{bind}^{eff}/Q_{tot}$, as detailed in Table 3.7. These values, which are analogous to the experimentally determined CE_{50} values, were equivalent at *ca.* 0.28 kcal mol⁻¹ for each TGD dendrimer and G1-PAMAM, with only the larger PAMAM systems offering more energy per charge.

Table 3.7 – MD simulation binding parameters at a charge excess of 0.4. Q_{tot} : number of binder charges; Q_{eff} : number of interacting charges; ΔG_{bind}^{eff} : effective free energy of binding; $\Delta G_{bind}^{eff}/Q_{tot}$: charge-normalised free energy of binding; $\Delta G_{bind}^{eff}/Q_{eff}$: effective-charge-normalised free energy of binding.

Compound	N_{mol}	Q_{tot} /(+)	Q_{eff} /(+)	ΔG_{bind}^{eff} / kcal mol ⁻¹	$\Delta G_{bind}^{eff}/Q_{tot}$ / kcal mol ⁻¹	$\Delta G_{bind}^{eff}/Q_{eff}$ / kcal mol ⁻¹
TGD-G1	4	36	26 ± 2	-9.6 ± 0.8	-0.27 ± 0.02	-0.37 ± 0.03
TGD-G2	2	36	21 ± 1	-9.9 ± 0.6	-0.28 ± 0.02	-0.47 ± 0.03
TGD-G3	1	36	14 ± 1	-10.1 ± 0.7	-0.28 ± 0.02	-0.72 ± 0.05
G1-PAMAM	5	40	35 ± 2	-10.2 ± 1.1	-0.26 ± 0.03	-0.29 ± 0.03
G2-PAMAM	2	32	29 ± 1	-44.7 ± 2.0	-1.40 ± 0.06	-1.54 ± 0.07
G3-PAMAM	1	32	15 ± 1	-15.9 ± 1.1	-0.50 ± 0.03	-1.06 ± 0.07

The simulations again allowed the number of dendrimer charges directly involved in heparin interactions, Q_{eff} , to be calculated. It is interesting to note that the smallest TGD-G1 structure is best able to utilise its charges with 72% of the available surface amines directly interacting with heparin. As size increases, this proportion drops to 58% for TGD-G2 and 39% for TGD-G3. Division of the total free energy of binding, ΔG_{bind}^{eff} , by Q_{eff} calculates the effective ‘strength’ of each individual amine-heparin interaction for the systems. These values indicate that TGD-G3 established the most energetic individual amine-heparin interactions while those of TGD-G1 were the weakest.

The smaller (G1 and G2) PAMAM dendrimers were shown to be superior to any of the TGDs at involving individual amine surface groups in direct interactions with heparin. At G1, 87.5% of the available 40 cationic charges were directly involved in binding, while at G2, this increased to an impressive 91% of the available 32 charges. These data suggest the flexibility of the PAMAM core interior structures, compared to the rigid TGD systems, significantly enhances their ability to re-organise and optimize their interactions. We termed this process ‘adaptive multivalency.’²⁹⁴ Adaptive multivalency

is a similar concept to that previously observed for DNA binding²⁹⁵ with large multivalent dendritic systems such as PAMAMs²⁹⁶ and PEI dendrimers.²⁹⁷

Further atomistic MD modelling snapshots of these interactions were captured, Figure 3.10, and these illustrate well the adaptivity of the PAMAM systems compared to the TGD-modified dendrimers. For example, inspection of the snapshots of TGD-G2-heparin and G2-PAMAM-heparin shows several large regions of TGD-system positioned away from the polysaccharide while the PAMAM-system has adapted its conformation to interact more completely with the heparin chain.

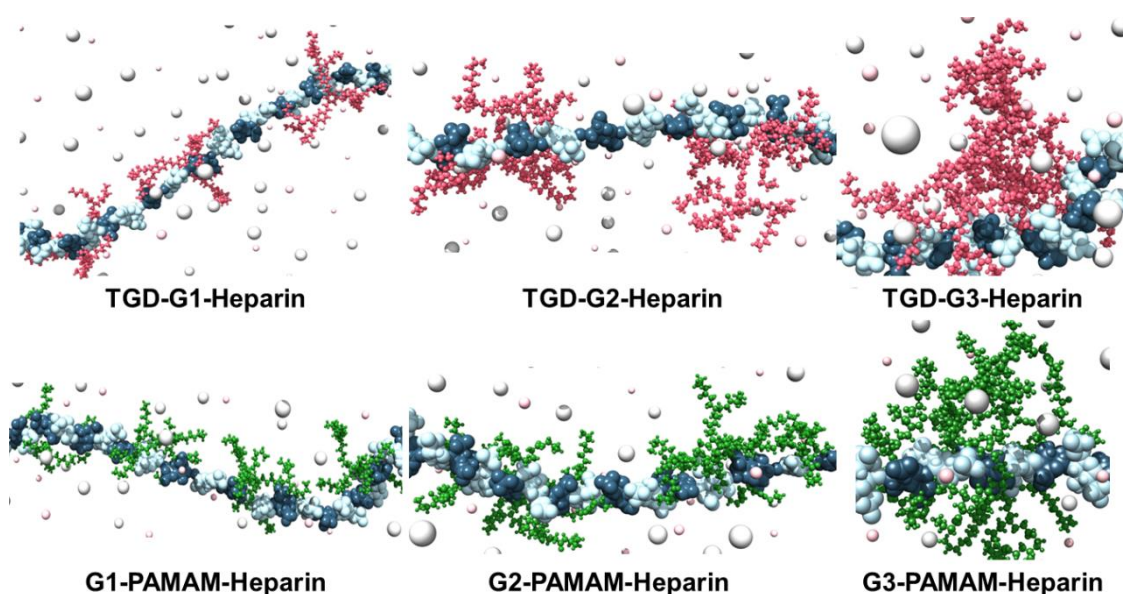


Figure 3.10 – MD simulations for TGD (red structures, top) and PAMAM (green structures, bottom) binding heparin (light and dark blue structures) at a charge excess of 0.4 across generations 1, 2 and 3 (left-to-right).

In the second part of this study, mesoscale dissipative particle dynamics (DPD) modelling was carried out at a charge excess of 0.1; a regime under which the MalB data suggested the more rigid TGD dendrimers were superior heparin binders to PAMAMs. DPD was employed for these simulations as this technique is coarse-grained and therefore allowed multiple heparin chains in constant contact with the dendrimer, and more complex binding stoichiometries, to be studied. Views of these simulations are shown in Figure 3.11.

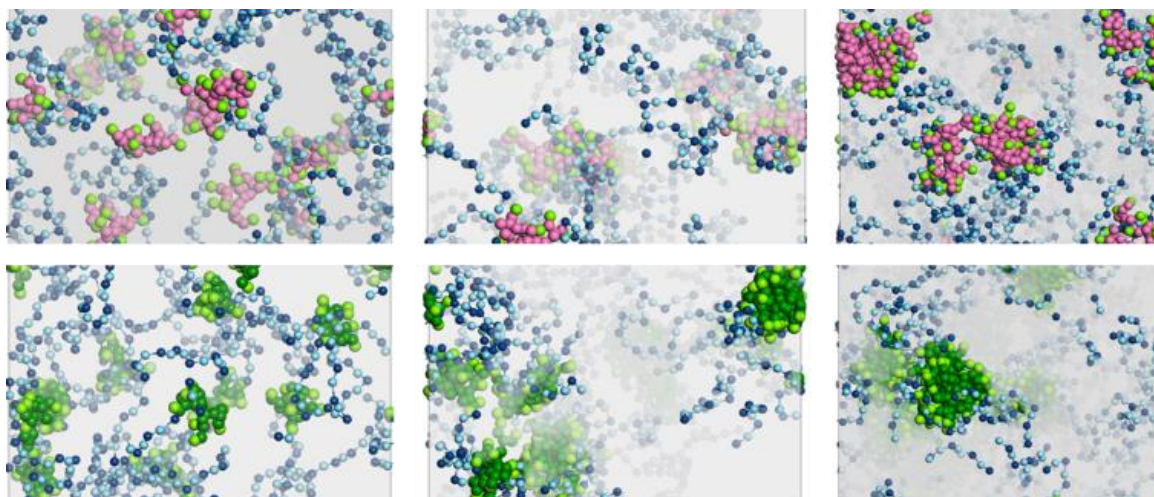


Figure 3.11 – Snapshots of the mesoscale simulations between dendrimers and heparin (light and dark blue structures) at CE = 0.1 for TGD (pink structures, top) and PAMAM (dark green structures, bottom) at G1 (left), G2 (middle) and G3 (right). In all panels, positively charged sites are shown in light green.

At G1, mesoscale models indicated that the heparin-dendrimer interactions are well defined, with each dendrimer appearing to interact with a single heparin polysaccharide. For TGD-G1, it seems likely that the rigidity of the PPV core plays a key role in locally organizing the surface groups for binding. At higher generations, meanwhile, binding is less well defined as both G2 and G3 systems appear to interact with multiple heparin chains simultaneously. The formation of these high-affinity interactions between multiple heparins and each of the TGD dendrimers appears to suggest that the same rigidity which limits effective multivalent interactions at higher CE (e.g. 0.4) is actually beneficial at lower CE (e.g. 0.1). Indeed, it seems these locally organized regions at the TGD surfaces are better optimized for interaction with heparin than the native PAMAMs, but only if there is enough heparin present for them to interact with it without having to deform their structures. We therefore categorized TGD dendrimers as exponents of a new concept: namely ‘shape-persistent multivalency.’²⁹⁴

3.4.2.3 Experimental Study II: Utilizing TGD Fluorescence

An attractive feature of the TGD dendrimers over the native PAMAM systems is that they possess a PPV core, which endows photophysical activity. As such, it was anticipated that these structures might also be able to act as heparin sensors by self-indicating interactions with heparin. To that end, solutions of each TGD dendrimer (1 μM) were titrated with heparin in the presence of 150 mM NaCl and 10 mM Tris HCl

(pH 7.0). Previous studies employing TGD-G1 in clean water observed an absorbance maximum of 319 nm giving fluorescence output at 413 nm however, under our buffered conditions, irradiation was optimised at 318 nm while the emission maximum was shifted to 427 nm.²⁹³ The term heparin ‘concentration’ again refers to the concentration of tetraanionic disaccharide rather than global heparin polysaccharide. The resulting titration curves are shown in Figure 3.12.

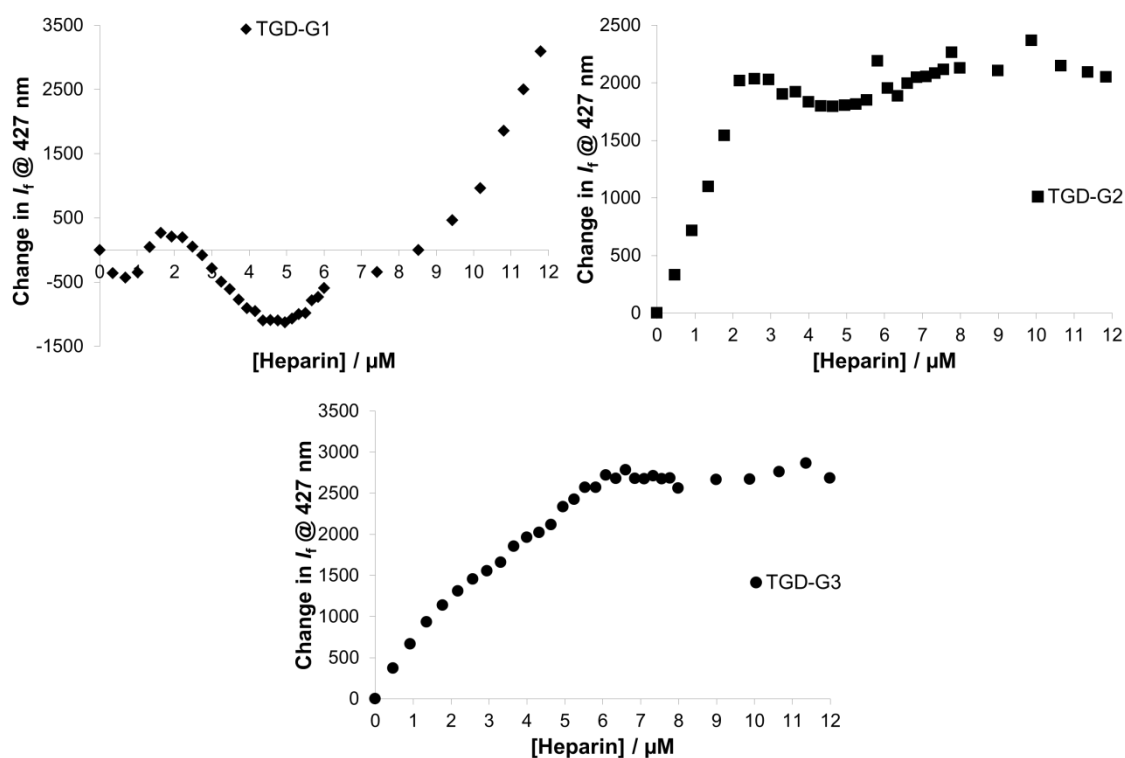


Figure 3.12 – Heparin titration curves for TGD dendrimers (G1-G3) in 150 mM NaCl and 10 mM Tris HCl, probed by fluorescence of PPV-core.

The titration curve for TGD-G1 did not result in a conventional binding lineshape, and consequently is rather uninformative. It seems likely that interaction of heparin at the surface of the relatively small dendrimer brought the polysaccharide into close enough proximity with the PPV-core to effect some form of direct quenching event. This proposal is supported by the observation of more conventional binding curves for the larger TGD-G2 and TGD-G3 systems, in which heparin is necessarily positioned further from the photoactive core upon binding. On these binding curves, the point at which the line begins to plateau can be taken to indicate the concentration of heparin disaccharide required to saturate 1 μM of Transgeden dendrimer. The data suggests each mole of TGD-G2 is saturated by two moles (2 μM in this experiment) of heparin disaccharide

while TGD-G3 requires six moles ($6\ \mu\text{M}$) to be present. Interestingly, and convincingly, these data are in agreement with the atomistic MD modelling snapshots for these interactions, Figure 3.10, which show individual dendrimer residues appearing to bind to the corresponding number of heparin saccharides suggested here.

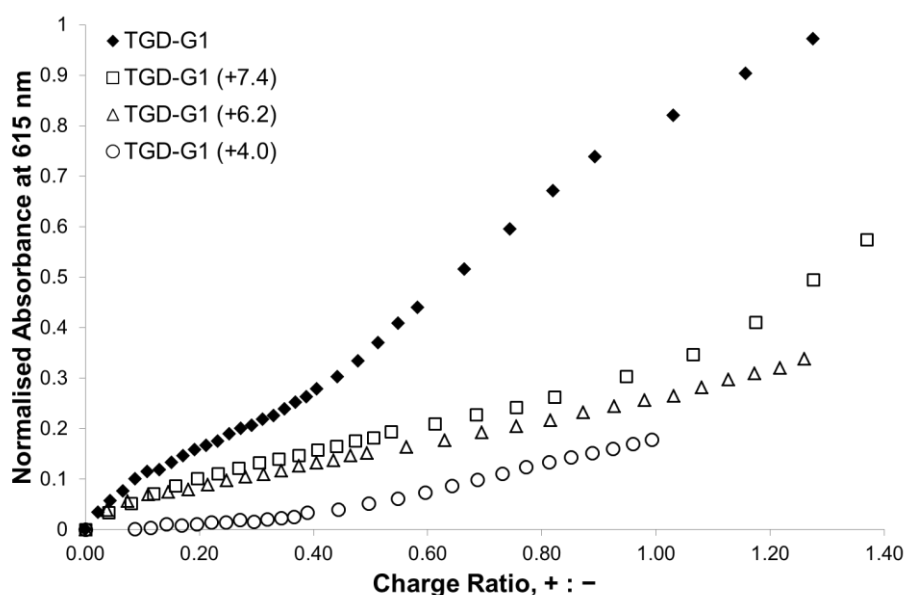
Given the obvious spectroscopic responses of the larger TGD dendrimers in electrolytically competitive conditions ($150\ \text{mM NaCl}$ and $10\ \text{mM Tris HCl}$), these systems may be of interest for further heparin sensing investigations such as those presented in the previous Chapter. Clearly, PAMAM dendrimers have no direct heparin sensing capability owing to their lack of photoactive groups and so their modification to yield TGD dendrimers offers significant advantages in this regards.

3.5 Modified Transgeden Dendrimers

In a final set of experiments, attempts were made to study the importance of each individual charge within the TGD-G1 structure by removing some of them from the system. To do this, our collaborators in the group of Professor Julián Rodríguez-López at Universidad de Castilla-La Mancha, Ciudad Real, Spain synthesised a small family of TGD-G1 derivatives, in which differing numbers of the surface primary amines were replaced non-selectively with alcohol groups. This was achieved in a statistical manner during synthesis and the degree of amine functionalization was determined using a Kaiser test. Specifically, three compounds were produced in which 82%, 69% and 45% of the surface amine groups were present when compared to the original TGD-G1. From these Kaiser test values, the average molecular charge for each new dendrimer could be estimated (+ 7.4, + 6.2 and + 4.0 respectively) and these values were used for charge excess calculations. Each molecule, along with a completely anionic control molecule TGD-G1(OH)₉, was tested for heparin binding ability in the MalB assay in buffer and salt. The data are reported in Table 3.8 and Figure 3.13.

Table 3.8 – Heparin binding data for the TGD-G1 derivatives with different numbers of surface charges.

Compound	Heparin Binding		
	EC ₅₀ / μ M	CE ₅₀	Dose / mg per 100IU
TGD-G1	(7.73 \pm 0.32)	(0.64 \pm 0.03)	(0.38 \pm 0.02)
TGD-G1 (+7.4)	(19.2 \pm 2.7)	(1.31 \pm 0.18)	(0.94 \pm 0.13)
TGD-G1 (+6.2)	<i>Not achieved - binding too weak</i>		
TGD-G1 (+4.0)	<i>Not achieved - binding too weak</i>		
TGD-G1(OH) ₉	<i>No binding observed</i>		

**Figure 3.13** – Heparin binding curves for TGD-dendrimers containing differing numbers of surface amines.

The data show that in all cases, the removal of surface amines decreases the heparin binding performance. Whilst this observation may not be surprising, it is interesting to note that removal of only *ca.* 20% of the surface amines decreases the heparin binding efficiency by around half. In the previous section, MD modelling suggested that only around 72% of the TGD-G1 surface amines actively interact with heparin upon binding, yet here, although around *ca.* 80% of the amines remain present, binding efficiency is significantly reduced. This suggests that the surface amines may be acting in pre-organised clusters of 3 amines each on the TGD surface. Loss of even one of these amines will significantly disturb the shape persistent multivalent binding. Furthermore,

when only *ca.* 70% of the amines are present, TGD-G1 (+ 6.2), binding is so perturbed that less than 50% of MalB is displaced from heparin during the assay. As would be expected, the anionic control molecule, TGD-G1(OH)₉, showed no evidence of heparin binding.

3.6 Conclusion and Future Work

Following consideration of the currently available methods for rapidly probing and comparing the heparin binding ability of different molecules, a novel straightforward competition assay was developed. The new assay employed our recently developed heparin sensor Mallard Blue (MalB) in an indicator displacement assay (IDA) regime. The performance of different candidate molecules was determined by their propensity to displace MalB from its complex with heparin and into solution, thereby causing an observable spectroscopic change. It was reasoned that the binding performance of new (and existing) molecules – measured in terms of charge excess and effective concentration at 50% MalB displacement, along with clinically relevant dose – could then be benchmarked against the clinically used heparin rescue agent, protamine to assess initial clinical potential.

The potential of this assay was initially demonstrated using protamine, and proved operable both in the presence of competitive electrolytes – specifically 150 mM NaCl and 10 mM Tris HCl – and also with the heparin component of the mixture delivered in 100% human serum. Although many existing dye systems have the potential to operate in this manner, it is believed that this work marks the first concerted attempt to develop such a straightforward assay for screening heparin binding under competitive conditions. Furthermore, the ease-of-synthesis associated with MalB makes the assay an attractive proposition for a wide range of researches, even those without specialist knowledge in synthetic chemistry such as, for example, biologists/biochemists.

The new competition assay was then validated through a study of the commercially available family of PAMAM dendrimers. The experimental data, supplemented by MD modelling, gave new insights into the multivalent binding behaviour of these systems and highlighted the importance of size dendritic size/generation for heparin binding. The results showed that the bigger, more charge dense dendrimers (e.g. G6), were not necessarily the best for heparin binding, while the smallest (e.g. G0, G1) were not

optimal either. Interestingly despite possessing a comparable number of cationic charges to MalB, G0-PAMAM was unable to displace MalB from heparin even when present in excess. The medium sized dendrimers (G2-G4) were shown to bind heparin in the most charge efficient manner indicating that these systems were best able to marshal their surface charges to maximize interactions with the polysaccharide. The MD modelling showed that G2-PAMAM was able to utilise the highest percentage (91%) of the available surface amines for interaction with heparin, and that each did so in the most energetic manner of any PAMAM system tested. Importantly, from the viewpoint of the novel assay, these results concurred with previous literature observations, indicating the suitability of the new technique for probing the relative performance of different binders.

Following this, in order to gain further understanding of multivalent effects in the binding of PAMAM-type systems to heparin, a range of hybrid dendrimers containing a rigid poly(phenylenevinylidene) (PPV) core functionalized with PAMAM surface groups were tested. Comparisons of these so-called ‘Transgeden’ (TGD) dendrimers with the native PAMAMs across low (G1) and medium (G2 and G3) generation sizes unveiled some key concepts relating to the flexibility of large dendritic systems on heparin binding. At low charge excess values – that is when heparin is present in significant excess to the binder – the rigidity of the TGD-core was beneficial to the relative binding performance of these systems by assisting in locally organizing ligand binding clusters at the dendrimer surface, while under the same regime, PAMAMs were less well organized. On moving to a larger charge excess – that is where the stoichiometric ratio is less in favour of heparin – the rigidity of the TGD core becomes detrimental to their performance as it reduces the extent to which the dendrimers can adapt their shape to maximize the number of interacting sites with heparin. Under this latter regime, the flexibility of the PAMAM dendrimers allowed them to re-organise the ligand array presented to heparin for binding. These two dendrimer families were categorized as prime exponents of “shape persistent multivalency” and “adaptive multivalency” respectively. All observations, again, were supplemented by MD modelling data.

The rigid PPV core present within the TGD systems offered the additional benefit of photophysical activity and was exploited to self-indicate the interactions of the TGD dendrimers with heparin. The titration data obtained in this manner suggested that the

larger systems (G2 and G3) required more heparin for binding to become saturated. Impressively, the saturation stoichiometries suggested by the data for TGD-G2 (2 : 1, anionic disaccharide : TGD) and TGD-G3 (6 : 1) correlated closely with the values obtained computationally during the MD modelling studies of the same systems. The self-indicating fluorescent study of TGD-G1 was unsuccessful owing to the relatively small PAMAM surface groups being unable to enforce a large enough distance between the PPV-core and the bound heparin to prevent a direct quenching event occurring. This quenching interfered with the fluorescent output of the dendrimer and resulted in the observed 'binding curve' being uninformative.

In a final experiment, the new assay was used to examine the relative heparin binding abilities of a family of modified TGD-G1 dendrimers. The compounds possessed different numbers of amines at their surface, with some groups replaced by alcohol functionalities. Most interestingly, the absence of less than 20% of the surface amines was sufficient to decrease the heparin binding ability of the system by greater than half. This is particularly profound as the complementary MD modelling work of the original TGD-G1 suggested that only 72% of the surface amines present actually interact directly with heparin. Such a decrease in performance with around 80% of the amines remaining intact supports the view that the loss of only one of the three amines in each cluster is significantly detrimental to the shape persistent multivalency. The absence of *ca.* 30% of the original charge is sufficient to prevent the dendrimer from displacing MalB during the entire titration.

The insight into fundamental multivalent binding phenomena gained from further investigations of the initial experimental data obtained from the novel MalB displacement assay is clear. This assay will now be taken forward to probe a variety of different compounds and molecular systems for their heparin binding potential, with a view to identifying molecules of interest for the development of novel heparin rescue agents. In particular, such a study could focus on self-assembling dendritic systems, which may present clinically-relevant advantages over large covalent systems for heparin binding.

4 Self-Assembling Multivalent Heparin Binders I: DAPMA-containing system

4.1 Introduction

4.1.1 Background

At the conclusion of surgery during which heparin has been used, there is an immediate need to neutralize the anti-coagulant effect of the heparin and allow the patient to begin clotting. This heparin neutralization, known widely as ‘heparin rescue’, involves the introduction of a heparin antidote into the bloodstream. Currently, there is only one licensed heparin rescue agent: protamine sulfate.¹⁰⁰ Protamine is an arginine-rich protein of ill-defined structure and was first demonstrated as a potential heparin rescue agent as early as 1937.²⁹⁸ Although mostly effective, the use of protamine is not without consequence as up to 10% of patients treated with the shell-fish or salmon derived protein at the conclusion of surgery experience some adverse effects, and close to 3% of all cardiac surgery patients experience serious problems.¹¹⁰ Consequently there is a significant interest in finding an alternative heparin rescue agent which is able to confer the desired heparin neutralization without conferring toxicity in patients.²⁹⁹

Much of the work to develop a novel heparin rescue agent can be categorized broadly into one of two sub-sets: small, well-defined ‘drug-like’ molecules or larger, less well-defined systems.²¹² Each approach has associated pros and cons. Small molecules, such as surfen for example, are often very well defined and can be easily produced to a high level of purity in large quantities.²⁰⁵ From a pharmacological perspective, smaller molecules can be more appealing than larger systems as they can offer more predictable pharmacokinetic profiles. A significant limitation of smaller systems however, can be their limited heparin binding ability when compared against their larger counterparts. Indeed although systems such as surfen are somewhat optimized for heparin binding, their low molecular weight is often associated with a low molecular charge, which in turn results in effective heparin neutralisation requiring unacceptably large amounts of binder, as measured by IC₅₀ values. Given these factors, it is perhaps not surprising that relatively few small molecule heparin binders have received serious consideration in clinical settings.

In contrast, larger systems can offer more appeal as potential protamine alternatives because their more massive and highly charged structures can lead to more effective and robust heparin binding on a per molecule basis. Larger structures, such as the covalent dendrimers discussed in Chapter 3 do not come without problems however. For example, synthesis of larger polymeric or dendritic structures is frequently far from trivial with purification often being troublesome. Unpredictable and unfavourable pharmacokinetic profiles can also detract from the employment of larger heparin binding systems. For example, the absence of a biocompatible degradation pathway can lead to toxicity problems, often as a consequence of the persistence of large cationic charge arrays in the bloodstream. As discussed in Chapter 3, this is one limitation to the use of PAMAM dendrimers in a clinical setting.^{276,277}

An effective way of generating a large ligand array whilst minimizing the synthetic challenge can be to use molecular self-assembly. This process involves multiple copies of the same ‘building-block’ molecule spontaneously organizing with one another to form a larger hierarchical structure.³⁰⁰ Such systems are routinely held together by non-covalent interactions and as seen in Chapter 1, self-assembly processes can be used to multiply-up the number of binding groups from a single monomer ligand in order to produce a self-assembled multivalent (SAMul) ligand array. Most commonly, amphiphilic monomeric building-blocks are used to promote self-assembly as they are able to arrange themselves in a predictable manner depending upon the solvent conditions used.⁴⁶

Self-assembling approaches have been widely used to achieve binding to biological target molecules such as lectins,^{301,302} integrins⁵⁶ and DNA.⁶⁴ In each of these cases, the individual monomer units contain hydrophilic binding groups attached to a hydrophobic unit. The molecular geometry is designed such that when solubilized in aqueous biological conditions, the apolar units are internalized as a consequence of the hydrophobic effect leading to the display of hydrophilic binding groups at the assembly surfaces. Of particular relevance to us is the body of work from Smith and co-workers which has focused on developing self-assembling agents able to bind either DNA or integrin for clinical purposes.^{56,303} An example of an amphiphilic binder targeted at binding integrin from Smith and co-workers is shown in Figure 4.1. The geometry of the building block, as dictated by the relative size of the hydrophobic and hydrophilic domains, promotes the formation of a spherical micellar assemblies in which the

resulting multivalent array of ligands achieve superior integrin binding compared with the equivalent concentration of non-self-assembling ligands.⁵⁶

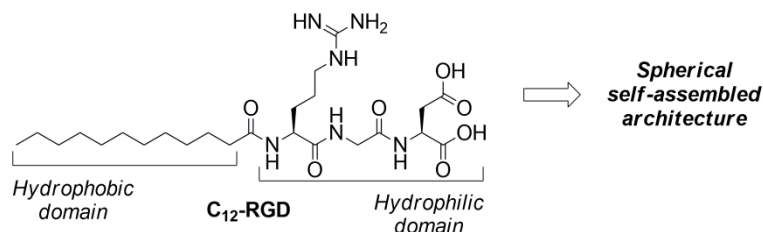


Figure 4.1 – An amphiphilic integrin binder from Smith and co-workers.⁵⁶

4.1.2 Preliminary Work²¹¹

In 2011, Smith and co-workers extended their approach of self-assembly based ligand design to target interaction with heparin. Specifically, an amphiphilic system similar to that presented above was designed and synthesised. The building block C₂₂G1DAPMA, shown in Figure 4.2, comprised several key features: (i) a twenty-two carbon aliphatic tail, which endowed the building block with amphiphilicity and promoted spontaneous formation of nanoscale assemblies in aqueous conditions; (ii) positively charged, heparin-binding DAPMA – *N,N*-di-(3-aminopropyl)-*N*-methylamine – surface groups; (iii) an ester-containing linker unit between the hydrophobic moiety and the hydrophilic head group, to encourage hydrolytic degradation in biological conditions.

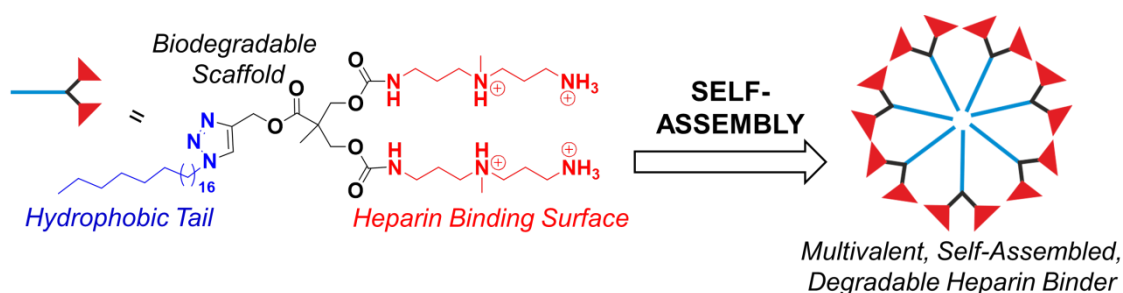


Figure 4.2 – Structure of heparin binder C₂₂G1DAPMA along with cartoon representation of self-assembly. This Figure is also shown as Figure 1.33.

It was hoped that designing the molecular building block in this way would maximize the advantages of both small and large heparin binding systems. The self-assembled system should be large enough (in assembled form) to establish meaningful interactions with heparin and act as an effective binder, while minimizing the unnecessary persistence of a cationic ligand array after administration.

The preliminary work with C₂₂G1DAPMA established that the system was able to self-assemble in aqueous conditions at concentrations above *ca.* 4 μM .²¹¹ Transmission electron microscopy (TEM) images of dried samples of C₂₂G1DAPMA showed spherical assemblies and the nanostructures were thereby categorized as micellar in nature. The micelles were sized at approximately 8.5 (\pm 1.5) nm in diameter and, importantly, appeared to remain intact upon heparin binding, Figure 4.3. The TEM images of C₂₂G1DAPMA in the presence of heparin appeared to show micelles aligned in an ordered fashion along the polysaccharide surface. In reality, this patterning is likely to arise from an integrated nanostructure composed of binder micelles distributed throughout the heparin polysaccharide chains. Such observations are similar to those previously observed by Kostianen and co-workers for self-assembling systems when binding viruses.^{304,305} Indeed, direct interactions between our SAMul binder and heparin polysaccharide chains were held responsible for the observed ‘beads on a string’ binding motif.

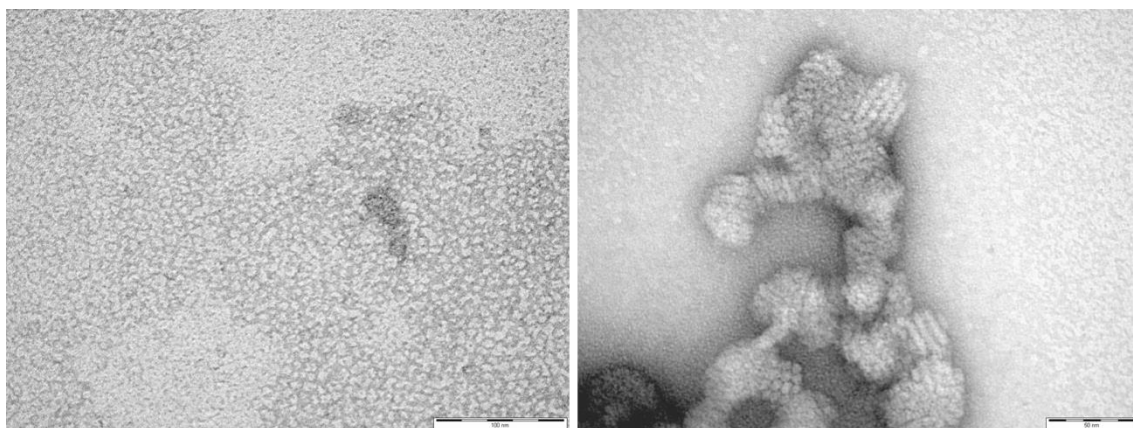


Figure 4.3 – TEM images of C₂₂G1DAPMA in absence (left, scale bar: 100 nm) and presence (right, scale bar: 50 nm) of heparin.

In this previous preliminary work, having established C₂₂G1DAPMA’s aptitude for interaction with heparin, the relative binding efficiency of the system with respect to protamine was probed using a methylene blue (MB) indicator displacement assay. Under this regime, C₂₂G1DAPMA required only 78% as much charge as protamine to bind any given amount of heparin, indicating that the self-assembling binder was employing each surface charge more efficiently than protamine. Whilst these results were impressive, the MB assay limited the scope of investigation owing to the

intolerance of MB-heparin interactions to electrolytic conditions above 1 mM Tris HCl and 5 mM NaCl; a significant way short of biologically relevant conditions.

Overall the data from the preliminary study suggested C₂₂G1DAPMA was a more charge efficient heparin binder than protamine in the presence of low concentrations of competitive electrolytes, although the SAMul system remained some way from being established as a promising heparin rescue agent. Several important factors remained unaddressed. For example, heparin binding performance was not studied under biologically relevant conditions; primarily due to the lack of a sufficiently robust straightforward assay. The role of self-assembly in conferring the apparent multivalent heparin binding performance was not unequivocally proven either. Furthermore, despite an ester linkage being incorporated into the scaffold to promote degradation, the validity of this molecular design was not examined. Following the development of the Mallard Blue heparin binding assay, presented in Chapters 2 and 3, it was decided to address some of these outstanding questions.

The C₂₂G1DAPMA compound used for testing was synthesised according to previously reported methodology in the Smith group by Ana Campo Rodrigo or Ching Wan Chan.²¹¹

4.2 Effects of Different Media on Heparin Binding

4.2.1 Heparin Binding in Competitive Conditions

4.2.1.1 Heparin Binding Assays

The Mallard Blue assay provided an ideal tool with which to investigate the effects of different media on the heparin binding ability of C₂₂G1DAPMA. The MalB assay operates in the presence of 150 mM NaCl and 10 mM Tris HCl, and so provided much sterner electrolytic competition for the SAMul system than the methylene blue assay regime. The heparin binding data for C₂₂G1DAPMA from both assays are presented in Table 4.1 along with protamine for comparison.

Table 4.1 – Heparin binding data for C₂₂G1DAPMA and protamine in the absence and presence of salt. Assay conditions: [a] 10 μ M MB, 178 μ M heparin, 1 mM Tris HCl. [b] 25 μ M MalB, 27 μ M heparin, 150 mM NaCl, 10 mM Tris HCl.

Binder		Methylene Blue ^[a] (Buffer)	Mallard Blue ^[b] (Buffer/Salt)
Protamine	EC ₅₀ / μ M	(22 \pm 1)	(2.34 \pm 0.23)
	CE ₅₀	(0.74 \pm 0.04)	(0.52 \pm 0.05)
	Dose / mg	(0.46 \pm 0.03)	(0.32 \pm 0.03)
C ₂₂ -G1-DAPMA	EC ₅₀ / μ M	(102 \pm 3)	(7.50 \pm 1.22)
	CE ₅₀	(0.58 \pm 0.02)	(0.28 \pm 0.05)
	Dose / mg	(0.47 \pm 0.01)	(0.23 \pm 0.04)

Data are reported in terms of their charge efficiency at 50% dye displacement, that is the number of cationic binder charges required per heparin anionic charge; effective concentration at the same point; and effective dose, that is the raw amount of binder required to neutralise 100IU of heparin. The MB data have been recalculated using the current working definitions of heparin and protamine, and so differ slightly from that published in the original study. Specifically, the M_r of heparin is assumed to be that of the sodiated analogue of the predominating disaccharide repeat unit, namely 665.402 g mol⁻¹, while the M_r of protamine is assumed to arise from a typical amino acid sequence of 5854.23 g mol⁻¹.

Both in the absence and presence of salt, a higher concentration of C₂₂G1DAPMA is required to displace 50% dye than is required of protamine. This discrepancy is a straightforward consequence of C₂₂G1DAPMA being relatively small and drug-like, and possessing only four cationic charges per mole compared to the larger protamine protein, which possesses twenty-four charges. Under both sets of conditions, the effective concentration values are greater than the CAC value of *ca.* 4 μ M, suggesting self-assembly of C₂₂G1DAPMA is required for effective multivalent binding of the system to occur. The importance of self-assembly is discussed further below.

A more representative, size-independent measure of relative binding performance can be obtained through consideration of the charge efficiency values. The data show that both C₂₂G1DAPMA and protamine exhibit enhanced charge efficiency in the presence of 150 mM NaCl. This observation agrees with suggestions in the original paper that

salt may be acting as a screen preventing further heparin interfering with already established heparin-binder interactions. The extra electrolytes also serve to weaken the dye-heparin interactions with which the synthetic binder molecule (or protamine) has to compete, artificially enhancing the apparent binder performances. Although the absolute improvement in binding ability upon introduction of salt could therefore not be calculated, insight could be gained from the relative improvements of C₂₂G1DAPMA and protamine.

On moving to 150 mM NaCl, the charge efficiency of protamine increased by around 30% from 0.74 (\pm 0.04) to 0.52 (\pm 0.05) while C₂₂G1DAPMA improved by around 50% from 0.58 (\pm 0.02) to 0.28 (\pm 0.05). These values suggest that C₂₂G1DAPMA is a more robust binder than protamine in the presence of 150 mM NaCl and may hint at some type of ‘ligand sacrifice’ behaviour where the flexibility of the self-assembled system allows one or more arms within the assembly to sacrifice binding interactions in order to shield the remaining binding interactions from disruption by salt. Such effects have previously been reported for structurally related systems.²⁹⁵

4.2.1.2 Modelling Heparin Binding

In an attempt to rationalise the improved performance of C₂₂G1DAPMA relative to protamine in the presence of more electrolytically rich conditions, a molecular dynamics modelling study was carried out in collaboration with Professor Sabrina Pricl at University of Trieste, Italy. The simulations allowed the assembly structure of C₂₂G1DAPMA to be visualised, Figure 4.4, and assisted in assessing sizes and properties of the binding aggregates.

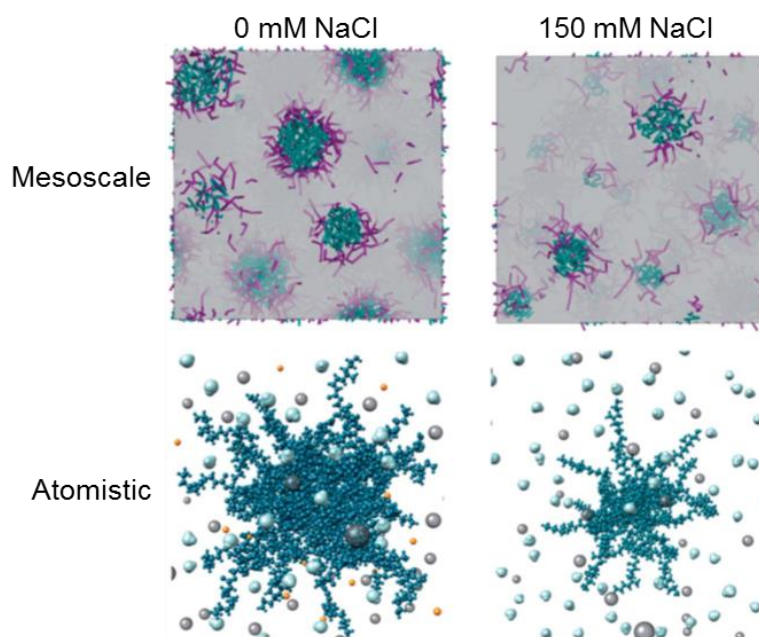


Figure 4.4 – Mesoscale (top) and atomistic (bottom) representations of C₂₂G1DAPMA in the presence (left) and absence (right) of 150 mM NaCl.

The modelling suggested the formation of C₂₂G1DAPMA aggregates with markedly different sizes in the presence and absence of 150 mM NaCl. The simulations predicted that in the absence of NaCl, C₂₂G1DAPMA might be expected to form aggregates containing $11 (\pm 3)$ individual molecules with an approximate aggregate diameter of $6.3 (\pm 0.5)$ nm. In the presence of 150 mM NaCl, a larger aggregate of $9.3 (\pm 0.1)$ nm in diameter containing around $24 (\pm 1)$ molecules might be expected. Based on these predictions, the aggregate in the presence of salt would be expected to have $96 (\pm 4)$ cationic charges compared to only $44 (\pm 12)$ in the absence. These predictions are significant, as the larger size of C₂₂G1DAPMA assemblies in the presence of salt may go some way to accounting for the relative improved performance of C₂₂G1DAPMA over protamine in the presence of greater electrolytic competition. Other authors have previously observed size increases for micellar aggregates in response to an increase in ionic strength, with the change thought to be due to a combination of charge screening and an enhancement of the hydrophobic effect.^{306,307}

In order to experimentally validate the predictions made computationally, dynamic light scattering (DLS) was carried out on aggregates of C₂₂G1DAPMA in the solution phase both in the presence and absence of 150 mM NaCl. The data, shown in Table 4.2, was

in complete agreement with the modelling predictions, as the presence of 150 mM NaCl increased the observed micelle diameter by *ca.* 3 nm.

Table 4.2 – Experimental solution-phase diameters of C₂₂G1DAPMA aggregates, as measured by DLS.

Media	Diameter / nm	Peak Width / nm
10 mM Tris HCl	(5.8 ± 0.5)	2.0
10 mM Tris HCl, 150 mM NaCl	(9.1 ± 0.1)	2.1

In addition to allowing the binding of C₂₂G1DAPMA to heparin in the absence and presence of salt to be visualised, Figure 4.5, the molecular simulations were also able to give insight into the relative efficiency of each binding interaction, Table 4.3. In the absence of salt, 18 of the 44 cationic charges (41%) per assembly appeared to be interacting with heparin (Q_{eff}), while the total effective free energy of binding ($\Delta G_{\text{bind}}^{\text{eff}}$) was predicted at $-30.2 (\pm 1.0)$ kcal mol⁻¹. The effective charge normalized free energy of binding, that is the average energy of each binding group-heparin interaction ($\Delta G_{\text{bind}}^{\text{eff}}/Q_{\text{eff}}$), was therefore calculated as $-1.68 (\pm 0.19)$ kcal mol⁻¹. In the presence of salt, 32 of the 96 cationic charges (33%) shared the effective free energy of binding $-65.0 (\pm 1.6)$ kcal mol⁻¹, with each charge therefore contributing $-2.03 (\pm 0.08)$ kcal mol⁻¹. These data suggest not only that the C₂₂G1DAPMA aggregates are larger in the presence of 150 mM NaCl, but also that each individual binding charge within the assembly interacts with heparin in a more efficient manner. As discussed in Chapter 3, the employment of each binding charge in protamine is relatively inefficient in comparison.

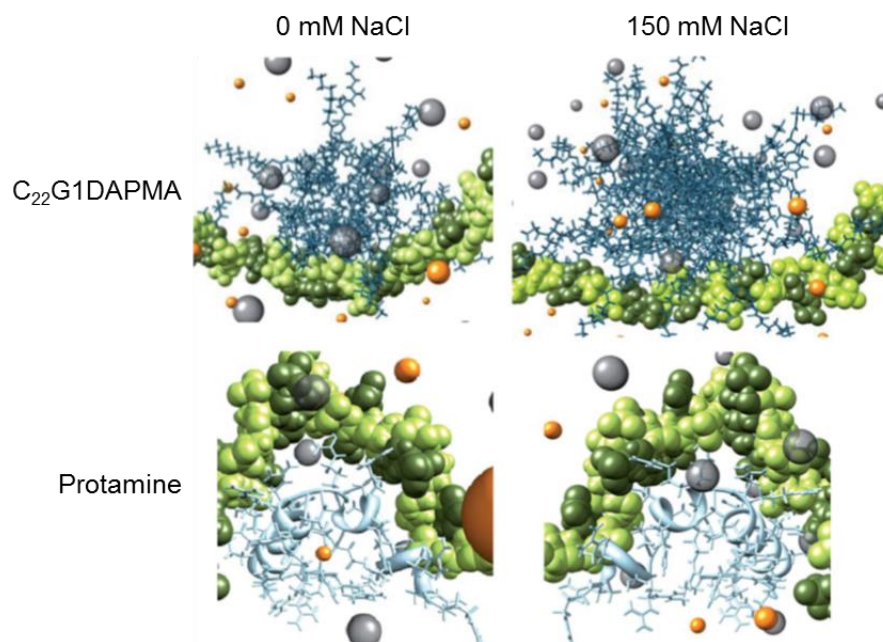


Figure 4.5 – Atomistic models of self-assembled C₂₂G1DAPMA (top) or protamine (bottom) binding heparin in absence (left) and presence (right) of 150 mM NaCl.

Table 4.3 – Modelling interpretations of effective charges per binder (Q_{eff}), effective free binding energy ($\Delta G_{\text{bind}}^{\text{eff}}$) and effective charge-normalised free energy of binding ($\Delta G_{\text{bind}}^{\text{eff}}/Q_{\text{eff}}$) for C₂₂G1DAPMA and protamine.

Simulation Conditions		Q_{eff}	$\Delta G_{\text{bind}}^{\text{eff}}$ / kcal mol ⁻¹	$\Delta G_{\text{bind}}^{\text{eff}}/Q_{\text{eff}}$ / kcal mol ⁻¹
0 mM NaCl	C ₂₂ G1DAPMA	(18 ± 2)	-(30.2 ± 1.0)	-(1.68 ± 0.19)
	Protamine	(10 ± 1)	-(2.60 ± 0.30)	-(0.26 ± 0.04)
150 mM NaCl	C ₂₂ G1DAPMA	(32 ± 1)	-(65.0 ± 1.6)	-(2.03 ± 0.08)
	Protamine	(12 ± 1)	-(3.96 ± 0.41)	-(0.33 ± 0.04)

One of the limitations of the molecular dynamics simulations is that in each case only one single binder molecule and one single heparin polysaccharide can be studied together, and this situation is of course not totally representational of reality. Simulation of the true solution phase picture would involve representing interactions between each single C₂₂G1DAPMA assembly and multiple heparin chains, which is prohibitively computer-time-intense. In lieu of this, dynamic light scattering (DLS) was employed to probe the aggregate size in solution at different binder:heparin ratios. DLS studies were carried out in collaboration with Dr Marcelo Calderon at Freie Universität Berlin, Germany. As shown in Table 4.4, as the relative amount of heparin to C₂₂G1DAPMA is

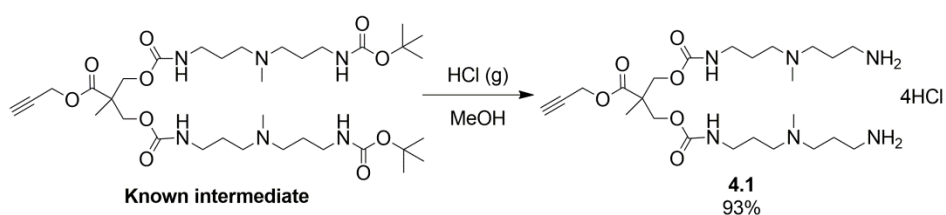
increased, the aggregate sizes in solution also increased. This observation supports the proposal that individual binder micelles interact with multiple heparin polysaccharide chains. Such aggregation processes are well known when protamine binds heparin.^{264,265}

Table 4.4 – DLS sizes observed for C₂₂G1DAPMA in the absence and presence of different amounts of heparin.

	Concentration / mg mL ⁻¹	Molar Ratio	Diameter / nm	Polydispersity Index (PDI)
Heparin	0.33	-	8.7	0.316
C ₂₂ G1DAPMA	1	-	9.0	0.641
C ₂₂ G1DAPMA + Heparin	-	0.1 : 1	13.0	0.276
C ₂₂ G1DAPMA + Heparin	-	0.5 : 1	68.9	0.155
C ₂₂ G1DAPMA + Heparin	-	1 : 1	Too big	-

4.2.1.3 Studying Self-Assembly Effects

To this point, the multivalent binding of C₂₂G1DAPMA has been assumed to be the result of a self-assembly event producing the cationic heparin binding ligand array cartooned earlier in Figure 4.2. In an attempt to prove this, a non-assembling negative control molecule was synthesised. Specifically, as shown in Scheme 4.1, a propyne-functionalised intermediate, generated during the preparation of C₂₂G1DAPMA, was subjected to a Boc-deprotection using HCl gas in methanol to afford partial binder PG1DAPMA 4.1 in a good yield, with no additional requirement for purification. The disappearance of characteristic signals at 1.40 ppm in ¹H and 79 ppm and 28 ppm in ¹³C NMR spectra respectively confirmed effective removal of the protecting group. Compound 4.1 was expected to mimic the monomeric ligand array of individual C₂₂G1DAPMA molecules and therefore provide a suitable comparison against the self-assembling system.



Scheme 4.1 – Preparation of negative control molecule PG1DAPMA.

PG1DAPMA was tested for heparin binding ability using the Mallard Blue heparin binding assay in salt and buffer and was shown to be unable to displace MalB to any significant extent. The respective performances of PG1DAPMA, C₂₂G1DAPMA and protamine can be seen in the heparin binding curves plotted in Figure 4.6.

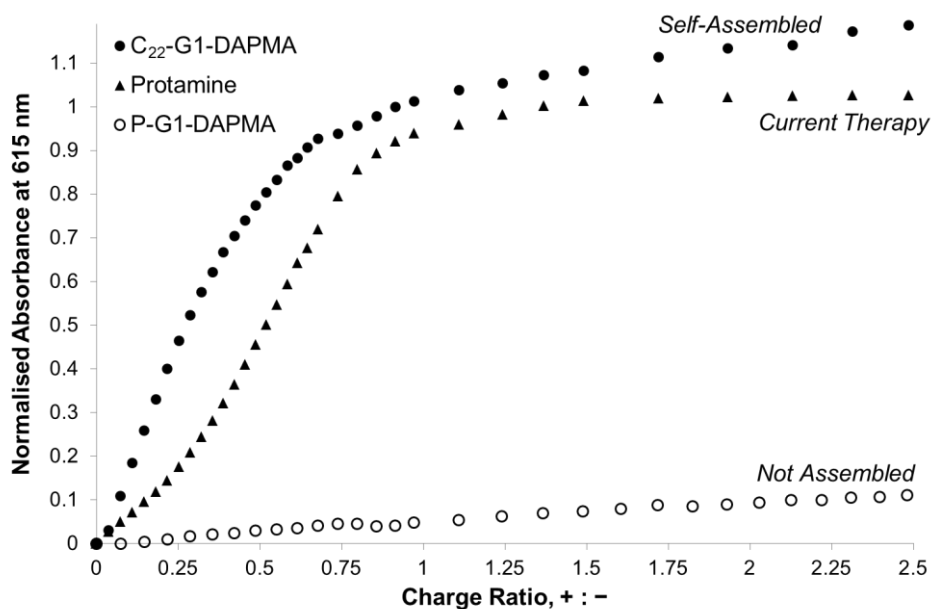


Figure 4.6 – Heparin binding curves for PG1DAPMA, C₂₂G1DAPMA and protamine from MalB heparin binding assay.

These data confirm the previous observation that self-assembly of C₂₂G1DAPMA drives the multivalent heparin binding interactions as suggested by the earlier TEM images, Figure 4.3, where the observed integrated nanostructure appeared to contain intact micelles. Similarly, a new experimental determination of the C₂₂G1DAPMA CAC in the presence of heparin demonstrated aggregate formation was not prevented by the presence of the polysaccharide, although the CAC value did increase to *ca.* 14 μ M suggesting some micelle destabilisation may have occurred. Nonetheless, aggregation of C₂₂G1DAPMA in the presence of heparin was clearly evident.

4.2.2 Heparin Binding in Clinically Relevant Conditions

4.2.2.1 Heparin Binding in Serum

Having demonstrated the ability of C₂₂G1DAPMA to bind heparin more efficiently than protamine under electrolytically competitive conditions, the next challenge was to examine performance under more biologically relevant conditions. To do this,

C₂₂G1DAPMA was tested using the previously described Mallard Blue assay with heparin delivered in 100% human serum. The data are shown in Table 4.5.

Table 4.5 – Heparin binding data from MalB assay with heparin delivered in 100% human serum.

Compound	EC ₅₀ / μ M	CE ₅₀	Dose mg/100IU
PG1DAPMA	<i>Binding too weak</i>		
C ₂₂ G1DAPMA	(25.9 \pm 1.6)	(0.96 \pm 0.06)	(0.79 \pm 0.05)
Protamine	(3.51 \pm 0.12)	(0.79 \pm 0.03)	(0.49 \pm 0.02)

The data show that in the presence of serum, the binding efficiency of both protamine and C₂₂G1DAPMA decreased, although of these two systems, protamine was least adversely affected. The CE₅₀ of protamine increased from 0.52 (\pm 0.05) in the absence of serum to 0.79 (\pm 0.03) in its presence, and this performance difference can be somewhat accounted for by consideration of off-target interactions, for example between protamine and charged patches on serum proteins. Relatively, C₂₂G1DAPMA was affected to a greater extent with CE₅₀ increasing from 0.28 (\pm 0.05) to 0.96 (\pm 0.06). Clearly, serum exerted a more disruptive effect on the ability of C₂₂G1DAPMA to bind heparin in a multivalent manner than it did for protamine. A likely explanation could be the disruption of the micellar binding arrays by hydrophobic serum components such as albumin or globulin proteins.³⁰⁸⁻³¹⁰ Interestingly, C₂₂G1DAPMA may inadvertently be well optimized for disruption by serum as long straight alkyl chains are known to interact effectively with albumins, and interaction of the hydrophobic unit in this way could be envisaged as ‘pulling monomers out’ of the micellar ligand array.³¹¹ In order to probe this disruption mechanism, attempts were made to saturate serum albumin binding sites by introduction of 1-docosanol prior to carrying out the heparin binding assay although the insolubility of the fatty alcohol made these attempts unsuccessful.

The heparin binding performance of C₂₂G1DAPMA was found to be acutely sensitive to the presence of serum. For example, as shown in Figure 4.7, the disruptive effects of heparin delivery in 0 – 10% human serum were roughly linear when delivered into a cuvette containing a fixed amount of binder. Interestingly, the disruption caused by

delivery in 10% human serum found to be broadly equivalent to that when heparin was delivered in 100% human serum.

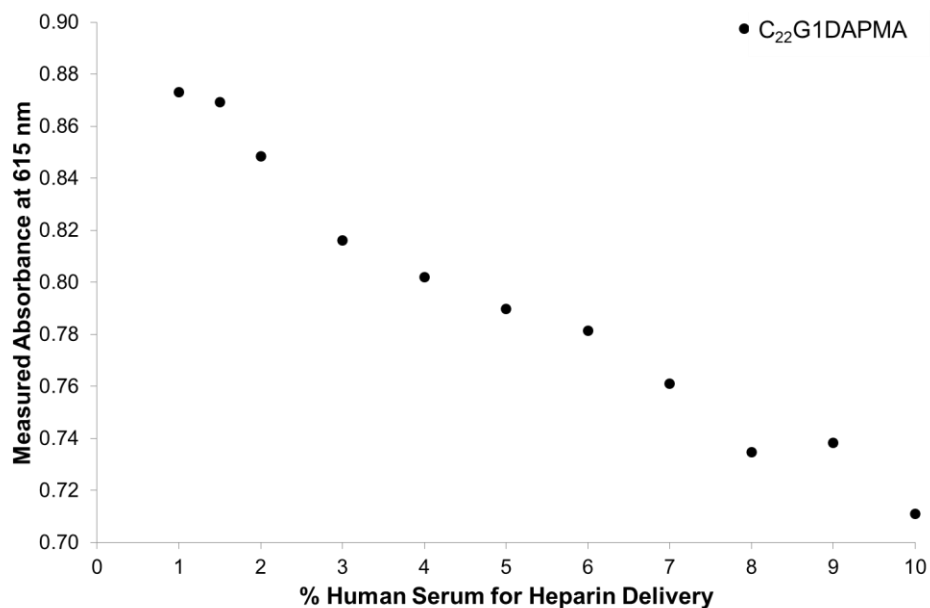


Figure 4.7 – Measured absorbance for heparin delivered into solution of C₂₂G1DAPMA at a (+ : -) = 0.67 in 0 – 10 % human serum.

Whilst the micellar assemblies of C₂₂G1DAPMA appeared to be somewhat disrupted in the presence of serum, the inability of PG1DAPMA to displace MalB from heparin under these conditions, Table 4.5, nonetheless suggested that a significant amount of C₂₂G1DAPMA assemblies remained intact, or in other words, self-assembly was not being completely switched-off by the presence of serum. In order to examine this further, our collaborators led by Dr Marcelo Calderon at Freie Universität Berlin, Germany, used dynamic light scattering (DLS) to monitor the size of a binder-heparin complex over time in the presence of albumin. As shown in Table 4.6, the aggregates decreased in size over time, suggesting some destabilization of the assemblies occurred, but the aggregates clearly did not completely disassemble and heparin binding was not completely switched-off. This retention of heparin binding ability, as indicated by successful displacement of 50% MalB during the assay motivated us to test C₂₂G1DAPMA under even more challenging clinically relevant conditions.

Table 4.6 – DLS sizes observed for C₂₂G1DAPMA-heparin aggregates in the absence and presence of albumin (1 mg mL⁻¹) over time.

C ₂₂ G1DAPMA	Molar Ratio	Diameter / nm	Polydispersity Index (PDI)
+ Heparin	0.5 : 1	68.9	0.155
+ Heparin + albumin	0.5 : 1	62.6	0.272
+ Heparin + albumin (after 30 min)	0.5 : 1	55.9	0.220

4.2.2.2 Plasma Clotting Assays

Despite being more adversely affected through disruption by hydrophobic serum components than covalent protamine, the non-covalent assemblies of C₂₂G1DAPMA still exhibited impressive heparin binding ability ($CE_{50} < 1$). Combined with the other advantages of a SAMul approach, this suggested clinical potential. To that end, C₂₂G1DAPMA was tested for its ability to neutralise heparinized plasma samples.

As insightful as the plethora of available heparin binding assays can be, the ultimate test of a potential heparin rescue agent is its ability to reverse the anti-coagulant effect of heparin in a clinically relevant sample. Plasma clotting assays such as the PT assay, which monitors the prothrombin clotting time of the ‘extrinsic’ clotting pathway originating from tissue damage, and the aPTT assay, which monitors the activated partial thromboplastin time of the ‘intrinsic’ clotting pathway originating from surface contact trauma are two widely employed clinical assays.³¹² Practically, each of these assays involves measuring the time taken for a heparinized sample of plasma, which is extracted from blood by centrifugation in the clinic, to clot. A longer clotting time is indicative more anti-coagulation and higher heparin levels. For the present study, C₂₂G1DAPMA was tested in each of these assays for its ability to reverse anti-coagulation. These experiments were carried out in the laboratory of Professor Jeremy Turnbull at University of Liverpool, UK.

Firstly, a sample of human plasma was taken and allowed to clot in the absence of heparin or binder. The sample clotted in 35.7 (\pm 0.7) seconds in the aPTT assay and 12.8 (\pm 0.8) seconds in the PT assay. When this procedure was repeated in the presence of heparin, clotting was not observed in either assay as heparin exerted its anticoagulant

effect. C₂₂G1DAPMA was then introduced into these samples at an appropriate dose and clotting was re-established, indicating functional heparin reversal. Practically, samples in the aPTT assay contained 2.5 units of heparin and those in the PT assay contained 5 units, while both assays had C₂₂G1DAPMA dosed at 0.79 mg/100IU. The results are shown in Table 4.7.

Table 4.7 – Plasma clotting data for C₂₂G1DAPMA in aPTT and PT assays.

Compound	Clotting Time / s	
	aPTT Assay	PT Assay
Plasma only	(35.7 ± 0.7)	(12.8 ± 0.8)
+ Heparin	No clot	No clot
+ C ₂₂ G1DAPMA	(81.8 ± 4.6)	(13.1 ± 0.4)

The heparin rescue performance of C₂₂G1DAPMA in these clinically relevant heparin neutralization assays is highly significant. In particular, the re-establishment of a clotting time of *ca.* 13 seconds in the PT assay indicates full heparin neutralization, while the slight extension of the clotting time in the aPPT assay may be an artefact of the previously observed disruption of the SAMul system by plasma components such as albumins. Importantly, despite this perturbation of the binding nanostructures, they remained operational in reversing the anti-coagulant effect of heparin. Clearly, if the stability of the nanostructures in the presence of serum can be enhanced, SAMul systems such as C₂₂G1DAPMA could have high clinical potential as functional heparin rescue agents.

4.2.3 Degradation Studies

Heparin binding ability is not the only important consideration when designing a heparin rescue agent of clinical relevance. Degradability and the potential for toxicity are important factors. As mentioned in the introduction to this Chapter, degradation of SAMul nanostructures can occur either through straightforward disassembly of the nanoparticles or through triggered bond cleavage. An ester group was specifically designed into the central linker unit of C₂₂G1DAPMA as previous work from the groups of Smith^{68,69} and Fréchet³¹³⁻³¹⁵ had established ester hydrolysis as an effective way of achieving temporary multivalency and minimizing the biopersistence of multivalent ligand arrays. Hydrolysis of the ester linkage in C₂₂G1DAPMA was expected to

disconnect the hydrophobic and hydrophilic regions thereby negating self-assembly and ‘switching off’ the multivalent ligand array.

The degradation of C₂₂G1DAPMA was probed using two complementary approaches.

4.2.3.1 Nile Red Release Assays

To probe the disassembly of C₂₂G1DAPMA, a Nile Red (NR) release assay was carried out. NR is a fluorescent hydrophobic dye, which exhibits high fluorescence output when dissolved or encapsulated in a hydrophobic environment such as the interior of a micelle, while fluorescence is readily quenched in aqueous conditions.

Practically, a solution of C₂₂G1DAPMA was made up at a concentration above the CAC – namely 50 μ M – and an aliquot of NR was added. Following irradiation at 550 nm, the fluorescence intensity at 635 nm was measured at short time intervals over a 35 hour period to afford the degradation curve represented by solid circles in Figure 4.8.

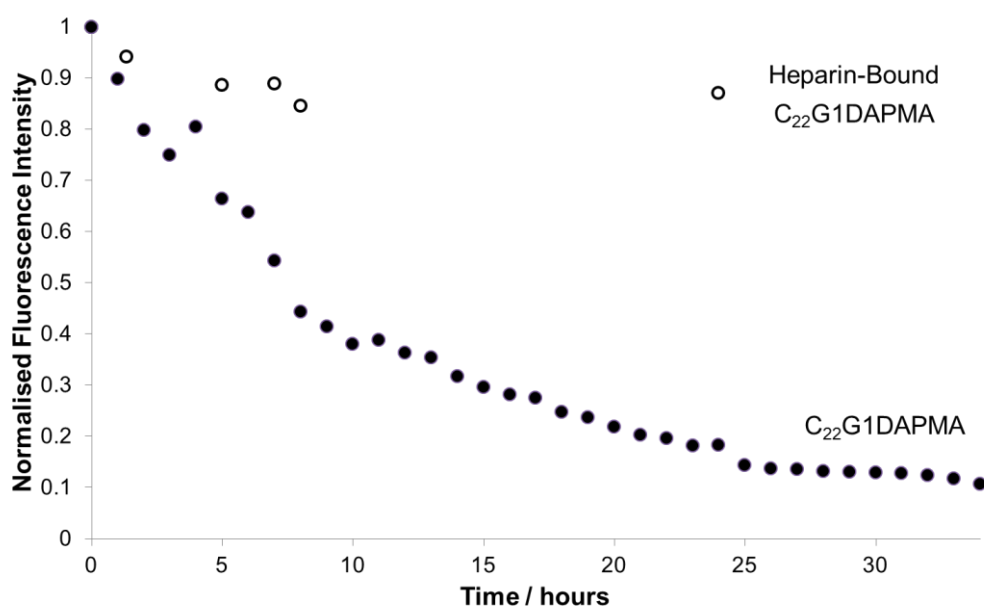


Figure 4.8 – Fluorescence intensity of NR in PBS buffer over time in the presence of C₂₂G1DAPMA in the absence (solid circles) and presence (open circles) of heparin.

The degradation curve indicated that NR was released from the C₂₂G1DAPMA assemblies with a half-life of approximately 7 hours in PBS buffer, although it is not possible to state unequivocally whether NR release is due to micelle disassembly, molecular degradation, or a combination of both. Interestingly, and importantly, when the experiment was repeated in the presence of heparin, NR release was significantly

retarded with the micelles appearing to remain almost completely intact after 24 hours. This outcome suggested NR release in the absence of heparin may be caused primarily by molecular degradation, as this would correlate with the previously mentioned works of Smith and Fréchet. Specifically, interaction of the surface binding groups with heparin can be thought of as ‘tying up’ the arms of C₂₂G1DAPMA, preventing them folding back on themselves to intramolecularly catalyse the hydrolysis of the ester group, thereby leading to the enhanced stability and retention of NR in the presence of heparin.

This degradation profile is pharmacologically interesting as once C₂₂G1DAPMA has established interactions with heparin, thereby neutralizing anticoagulancy, the complex formed appeared to remain stable. This would permit the binder-heparin aggregates to be metabolized as one species, potentially in a similar process to that of heparin-protamine aggregates.³¹⁶ Meanwhile, excess C₂₂G1DAPMA would degrade, thereby limiting biopersistence and toxicity.

Heparin re-bound is a widely acknowledged problem associated with heparin therapy, and particularly heparin rescue, whereby the release of plasma-protein-bound heparin back into the systemic bloodstream confers a second anticoagulation event, some time after initial neutralization.¹⁰⁹ Although used clinically, protamine is not well suited for dealing with heparin re-bound owing to its rapid *in vivo* half-life of *ca.* 8 minutes.¹⁰⁴ Consequently, in the event of re-bound, a second protamine dose is often required as the toxicity problems associated with a larger initial dose preclude this ‘front-loading’ approach being an option.^{103,104} A *ca.* 7 hour half-life of unbound C₂₂G1DAPMA may offer a suitable compromise between minimising overall biopersistence of cationicity and remaining present long enough to deal with any potential heparin rebound events, however it should be noted that the half-life of C₂₂G1DAPMA *in vivo* may be significantly shorter than 7 hours due to the increased competition and effects of shear/flow processes. Despite conjecture in the literature, considerations of heparin re-bound remain important.^{106,108}

4.2.3.2 Mass Spectrometric Studies

To confirm that NR release over time was due to molecular degradation, a mass spectrometric degradation assay was carried out with the aim of identifying the evolution of molecular species over time. Practically, mass spectra of C₂₂G1DAPMA

were obtained in the presence of a Gly-Ala dipeptide internal standard before and after incubation at 37°C for 24 hours.⁶⁹ Degradation events were revealed through comparison of the relative amounts of different species against the non-degradable internal standard. The molecular species of interest, along with some example spectra are shown in Figure 4.9.

As shown in Figure 4.9, at time zero, the molecular ions associated with C₂₂G1DAPMA ($m/z = 433 [M]^{2+}$ and $289 [M]^{3+}$) could be seen, along with some evidence of ester hydrolysis (alcohol, $m/z = 408 [M]^{1+}$; carboxylic acid, $m/z = 239 [M]^{2+}$). After 24 hours, the molecular ions for intact C₂₂G1DAPMA had completely disappeared and the peaks for the ester hydrolysis products were dominant, along with a new signal corresponding to decarboxylation of the carboxylic acid hydrolysis product ($m/z = 217 [M]^{2+}$). These data show degradation of C₂₂G1DAPMA occurs under biologically relevant aqueous conditions at pH 7, and support the NR released in the previous assay being due to a triggered disassembly event induced by molecular degradation rather than an independent disassembly event.

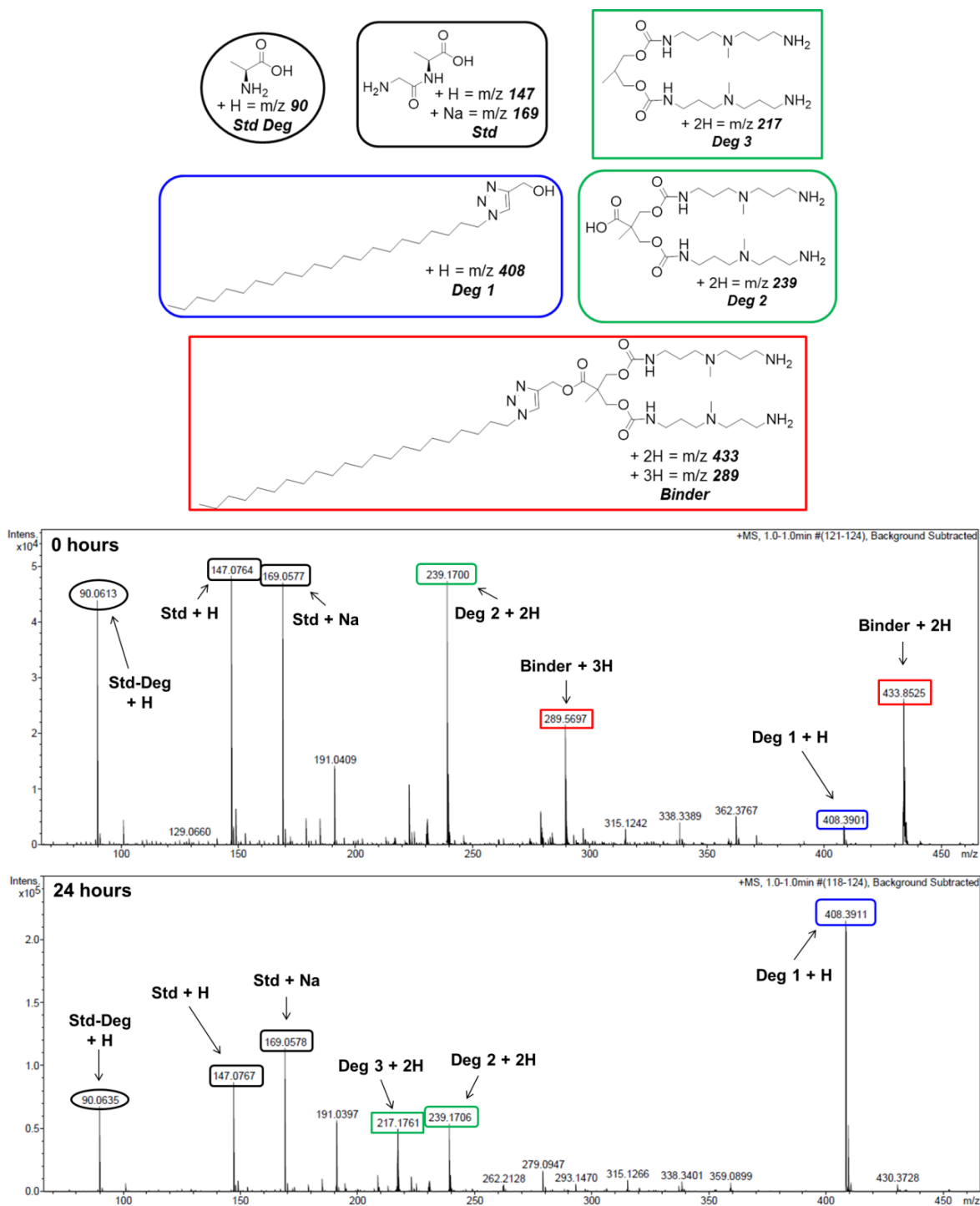


Figure 4.9 – Mass spectrometric degradation assay: observed species (top) after 0 hours (middle) and 24 hours (bottom) incubation at 37 °C.

4.3 Conclusions and Future Work

Following the preliminary studies from Smith and co-workers,²¹¹ the heparin binding ability of self-assembling system C₂₂G1DAPMA was studied in the presence of more competitive and biologically relevant conditions using the Mallard Blue heparin binding assay. The results showed that introducing competitive electrolytes such as 150 mM NaCl to the system increased the apparent heparin binding efficiencies of both C₂₂G1DAPMA and protamine. The performance improvement of the SAMul system over-and-above that of protamine was especially noteworthy. Molecular dynamics modelling revealed that introduction of salt into the assay triggered an enlargement of the self-assembled nanosystems formed by C₂₂G1DAPMA, leading to an increased number of monomer units coming together to form each aggregate and, consequently, an increase in the number of cationic binding groups expressed at each assembly surface. Experimental DLS studies corroborated these suggestions by characterising larger aggregates in the presence of salt.

The C₂₂G1DAPMA system was also tested for heparin binding in the presence of human serum, where the relative performance was shown to decrease somewhat, becoming inferior to that of protamine. Hydrophobic serum components such as albumin proteins were shown to interfere with the aggregation and performance of C₂₂G1DAPMA to some extent although, significantly, control experiments demonstrated the self-assembled nanosystem remained intact to some extent, as a non-self-assembling control molecule was unable to interact with heparin in the presence (or indeed absence) of serum.

Despite this disruption by serum proteins, C₂₂G1DAPMA was shown to be effective at reversing the anticoagulant effect of heparin in clinically relevant PT and aPTT plasma clotting assays. This heparin neutralization performance is highly significant given the non-covalent nature of C₂₂G1DAPMA assemblies, and the attractive advantages over similarly-sized covalent structures that this approach brings; for example, the relative simplicity of synthesis.

In a final set of experiments, a Nile Red release assay was used to show that C₂₂G1DAPMA degraded over a clinically interesting time scale, with a half-life of *ca.* 7 hours. The same assay also demonstrated that the presence of heparin stabilized the

assemblies, making the overall degradation process potentially more appealing from a heparin re-bound perspective than protamine. A further mass spectrometric assay indicated degradation occurred through hydrolysis of the linker unit ester groups, validating the molecular design, and leading to disconnection of the hydrophobic and hydrophilic regions of binder molecule. Ultimately, this led to the desired ‘switching-off’ of self-assembled multivalency.

Future work in this area will focus on enhancing the stability of the self-assemblies formed in the presence of serum. This could be achieved by increasing the hydrophobicity of the aliphatic unit by, for example, introducing branching or dendritic character into the alkyl chain. Alternative approaches could target bio-derived hydrophobic units such as cholesterol-like steroid units or bile acids. Choosing a hydrophobic unit of biological origin may additionally reduce the potential for toxicity from the degradation products. Variation of the hydrophobic unit will additionally impact upon the geometry of the binder molecule, which may in turn affect the morphology of the assembly formed. Other modifications could include variation of the surface binding groups to examine the effects of different cationic ligands on heparin binding performance. Careful selection of the appropriate building blocks may permit both stability and morphology effects on SAMul heparin binders not only to be probed but also optimised.

5 Self-Assembling Multivalent Heparin Binders II: Lysine-containing systems

5.1 Introduction

The use of a self-assembled multivalent approach to binding biological targets has many advantages. As exemplified in Chapter 4, a SAMul approach allows: (i) the heparin binding ligand array to be generated spontaneously as a consequence of molecular self-assembly; (ii) the individual building blocks to be relatively small and ‘drug-like’, well-defined and easy-to-make; (iii) the SAMul activity to be switched off through disassembly which in turn can be triggered by predictable degradation of the individual building blocks. A further key advantage of this approach is that the system is highly tunable, making it relatively straightforward to change the heparin binding properties of the system, for example through simple synthetic modification of the surface groups.

Following on from the C₂₂G1DAPMA SAMul system presented in Chapter 4, it was decided to further investigate the success of this approach by modifying the molecular building blocks used. In particular, increasing the biomimetic character of the system became an aim with the hydrophilic heparin binding DAPMA groups identified as a potential region for modification. Much like in the design of Mallard Blue in Chapter 2, the manner in which proteins establish strong interactions with heparin was considered.⁸² From this consideration, the amino acid lysine was selected as a suitable alternative surface group to use in place of DAPMA.

Much like DAPMA, lysine is able to interact effectively with heparin due to the two cationic charges within its structure. Alongside arginine – another cationic amino acid – lysine is present in a wide array of heparin binding proteins, including protamine.^{82,100} This known heparin binding ability has led to lysine being incorporated into several noteworthy attempts to develop novel heparin rescue agents. For example, work on calix[8]arene systems by Cunsolo and co-workers, and foldamer systems in the group of DeGrado both demonstrated lysine to be amongst the most effective heparin binding groups studied.^{200,202} Within our system, the incorporation of an amino acid such as lysine in place of DAPMA may also reduce the potential for toxicity within our system, as well as tuning heparin binding performance.

In order for both lysine amine groups to be available for interaction with heparin in the final SAMul construct, the entire building block required a modest structural redesign. Specifically, the functional group connecting the surface group to the rest of the binder molecule was modified from a carbamate to an ester. This change was expected to increase the (bio)degradability of the system, potentially enhancing the pharmacological appeal of the system.

As an amino acid, lysine also introduced a new variable to our SAMul approach which was not present within C₂₂G1DAPMA: chirality. It was reasoned that chirality could prove to be an interesting property for this study as the binding target heparin is itself chiral. As mentioned in Chapter 1, the heparin polysaccharide is composed primarily of an α -1,4-linked D-glucosamine–L-iduronic acid disaccharide repeat unit and, indeed, the investigation of chirality effects with heparin is not new.³¹⁷ Previous studies have shown heparin to be able to discriminate between a variety of chiral substrates. For example, several groups have used heparin as a chiral additive in capillary electrophoresis to enantiomerically separate underivatized drugs such as anti-malarials and anti-histamines.³¹⁸⁻³²⁰ It was proposed that heparin was able to chirally discriminate in this way due to a combination of ionic, hydrogen bonding and hydrophobic interactions with a specific arrangement of nitrogen containing aromatic heterocyclic or ionisable substituents.³¹⁸ Other, more recent studies from the group of Rabenstein, showed a sequence of exclusively D amino acids interacted with heparin in exactly the same manner as the corresponding sequence of L amino acids.^{321,322} It was suggested that the specific spatial arrangement of lysine and arginine residues in this peptide sequence promoted heparin interaction, rather than the presence of an enantiomerically complementary structure to heparin.³²¹

Despite these studies, to the best of our knowledge, there has been no study in which the chirality of the heparin binding system was expressed at the surface of a self-assembled nanostructure. Indeed, there are no examples in which chirality effects in the binding of self-assembled nanostructures have been explored. To investigate this new area through the use of a more biomimetic SAMul design, an initial pair of lysine-containing target molecules was identified for synthesis. These target molecules, C₂₂G1LLys and C₂₂G1DLys, are shown in Figure 5.1.

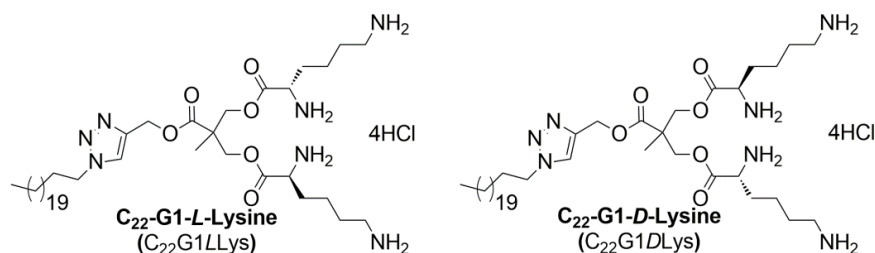


Figure 5.1 – Target molecules $C_{22}\text{G1LLys}$, $C_{22}\text{G1DLys}$.

5.2 Generation 1 Systems

5.2.1 Synthesis of $C_{22}\text{G1LLys}$ and $C_{22}\text{G1DLys}$

The synthesis of the first generation (G1) structures $C_{22}\text{G1LLys}$ and $C_{22}\text{G1DLys}$ was achieved in a convergent manner. For the purposes of synthesis, the binder molecules were broken up into three segments – the aliphatic tail, ester-rich linker unit and lysine surface group, Figure 5.2 – which were each prepared separately. The linker unit was then functionalized with two suitably-protected lysine surface groups before the aliphatic tail was installed to afford, after removal of the remaining protecting groups, the binder target molecules. A negative control molecule lacking hydrophobic functionalisation was also synthesised to allow the effects of self-assembly to be quantified for our new system.

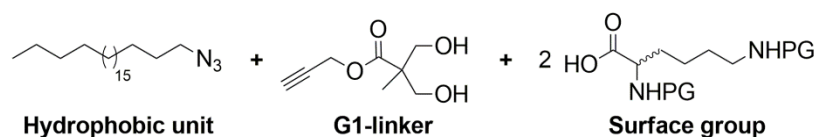
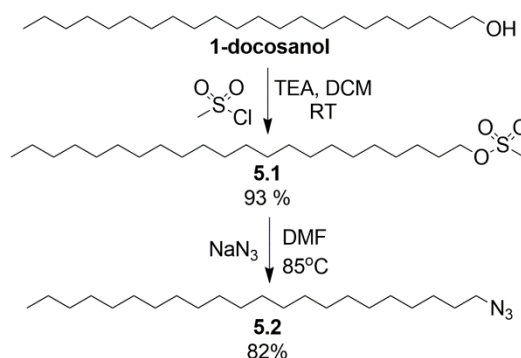


Figure 5.2 – The three distinct components of G1 target molecules $C_{22}\text{G1LLys}$ and $C_{22}\text{G1DLys}$, where ‘PG’ represents a protecting group.

5.2.1.1 Preparation of the aliphatic tail²¹¹

In line with the previous work described in Chapter 4, the hydrophobic unit of the new target molecules took the form of a twenty-two carbon *n*-alkyl chain. The same methodology applied in the preparation of $C_{22}\text{G1DAPMA}$ was used here to prepare the hydrophobic unit for connection to the binder scaffold. Specifically, as shown in Scheme 5.1, commercial fatty alcohol 1-docosanol (aka. behenoyl alcohol) was reacted with methanesulfonyl chloride in the presence of triethylamine to produce mesylate 5.1 in a good yield, characterized by the appearance of a methyl signal at 3.00 ppm in the

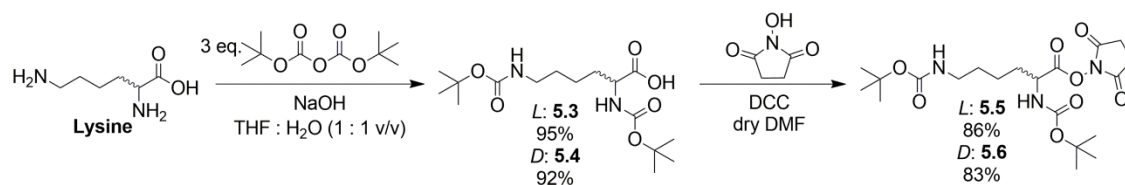
^1H NMR spectrum. Refluxing 5.1 with sodium azide in DMF successfully transformed the alkyl-mesylate into the desired 1-azidodocosane (aka. behenoyl azide) 5.2 in a good yield with no need for further purification. Once in hand, species 5.2 was ready for connection to the rest of the binder scaffold at a later stage using copper(II) mediated click chemistry.



Scheme 5.1 – Synthesis of alkyl hydrophobic tail unit.

5.2.1.2 Preparation of the lysine surface group

Lysine possesses two primary amine groups and a carboxylic acid within its structure. In order to facilitate connection of the lysine carboxylic acids to the alcohol termini of the linker unit, the amine groups required suitable protection to avoid unwanted side reactions such as lysine polymerization. The *tert*-butyloxycarbonyl (Boc) protecting group was identified as suitable owing to its acid-lability, as its removal in the final step would not expose the ester linkages present in the final binder molecule to nucleophilic or basic conditions. This protection strategy for lysine is well-known and has been widely utilised previously by, amongst others, Smith and co-workers.^{323,324} As shown in Scheme 5.2, Llys(Boc)₂ 5.3 or Dlys(Boc)₂ 5.4 can be prepared in a good yield by treatment of lysine with di-*tert*-butyl-dicarbonate and sodium hydroxide in THF/water.



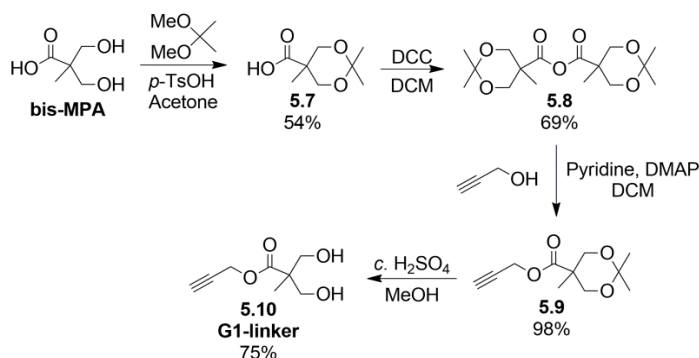
Scheme 5.2 – Preparation of Llys(Boc)₂ or Dlys(Boc)₂.

The lysine carboxylic acid group was then activated to increase its reactivity to nucleophilic attack. This activation was found to be necessary as when not activated,

reaction with the alcohol termini of the linker unit was found to be extremely slow or in some cases non-existent. For example, DCC-mediated, TBTU-mediated and general base-catalysed esterification conditions were all unable to successfully furnish the linker unit with lysine surface groups 5.3 or 5.4. *N*-hydroxysuccinimide was chosen as a suitable activating group and installed in a good yield through reaction with DCC in DMF to produce activated lysine species 5.5 and 5.6, which were then carried forward in the synthesis.

5.2.1.3 Preparation of G1 linker group

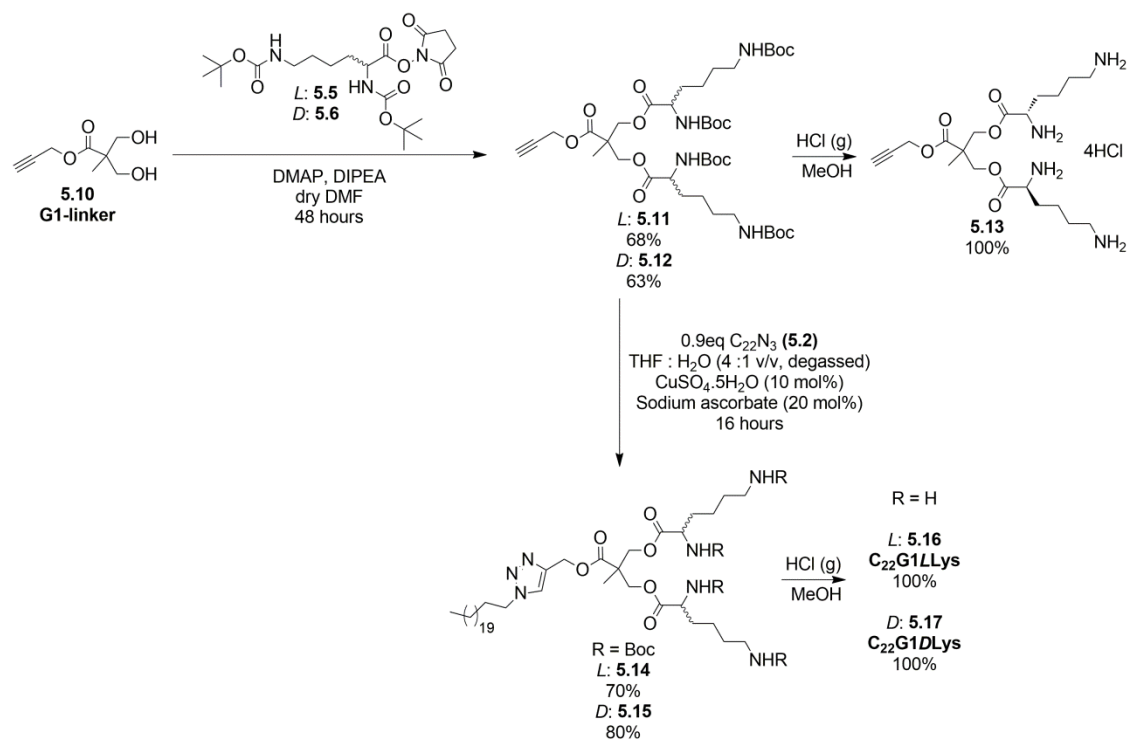
The linker unit is derived from the commercial starting material 2,2-bis(hydroxymethyl)propionic acid (aka. bis-MPA). Ultimately, the lysine surface groups were connected to the alcohol functionalities of bis-MPA but, initially, the carboxylic acid of bis-MPA had to be converted to an alkyne to prepare the molecule up for installation of the aliphatic tail via ‘click’ methodology. To do this, the methodology of Sharpless and Hawker was applied.³²⁵ Firstly, the two alcohol groups of bis-MPA were protected as acetal 5.7 in a moderate yield using 2,2-dimethoxypropane in the presence of a *p*-toluenesulfonic acid catalyst and acetone. The appearance of two methyl signals at 1.45 and 1.41 ppm in the ¹H NMR spectrum indicated successful protection. The remaining carboxylic acid functionality of 5.7 was then coupled to another molecule of itself using DCC to mediate the process and generate the more reactive symmetric anhydride 5.8 in a reasonable yield. Anhydride 5.8 was promptly reacted with propargyl alcohol to afford propyne-functionalised species 5.9 in a near-quantitative yield. Appearance of a ¹H NMR triplet signal at 2.47 ppm indicated successful installation of the alkyne functionality. Subsequent deprotection of 5.9 under acidic condition unveiled the alcohol groups in a good yield to afford desired linker 5.10. The synthetic scheme is shown in Scheme 5.3.



Scheme 5.3 – Synthetic scheme for preparation of G1 linker unit.³²⁵

5.2.1.4 Connecting the pieces

With the three components of the binder in hand, connection could now proceed. Firstly, lysine-succinimide-ester 5.5 or 5.6 was coupled to G1-linker 5.10 in a base catalysed esterification reaction to generate protected partial-binder 5.11 or 5.12 respectively in a reasonable yield, after purification by gel permeation chromatography in 95:5 DCM:methanol. At this stage, a small amount of L-partial binder 5.11 was deprotected using HCl gas in methanol to afford negative control molecule 5.13 for use as a self-assembly comparison tool in subsequent studies. Next, the hydrophobic azide-containing building block was introduced into the system. The pre-prepared 1-azidodocosane 5.2 was reacted with alkyne functionalized components 5.11 or 5.12 in a copper(II) catalysed ‘click’ reaction to generate the still-protected final binders molecules 5.14 and 5.15 in good yields, after purification by gel permeation chromatography in 100% DCM. The appearance of a ¹H NMR signal at 8.06 ppm was diagnostic of presence of the 1,2,3-triazole moiety. In a final step, the acid-labile Boc-protecting groups were removed in an excellent yield using HCl gas in methanol to afford the target molecules C₂₂G1LLys 5.16 and C₂₂G1DLys 5.17. The synthetic scheme showing the connection of the component units is shown in Scheme 5.4.



Scheme 5.4 – Synthetic scheme showing connection of the component parts to generate PG1LLys, C₂₂G1LLys and C₂₂G1DLys.

With the two target molecules in hand, circular dichroism spectroscopy was used to probe the chiral character of the final products to ensure amino acid chirality had been successfully preserved throughout the synthesis. As can be seen in Figure 5.3, at concentrations of 10 mM, the molar ellipticity for the two systems is effectively equal and opposite. This indicates that the two target molecules are of approximately equal enantiopurity, and crucially that chirality has not been scrambled during synthesis.

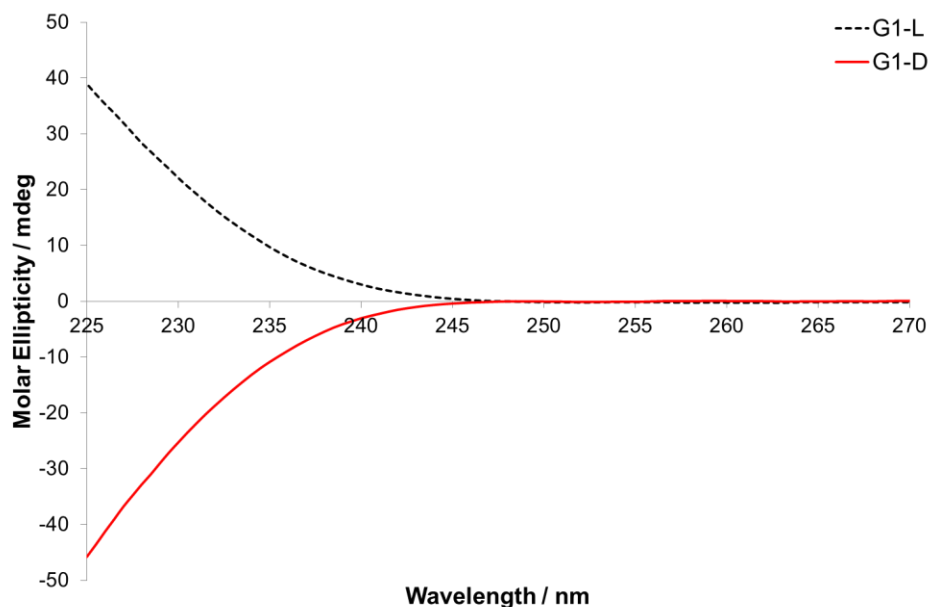


Figure 5.3 – Circular dichroism spectra of target molecules $C_{22}G1LLys$ and $C_{22}G1DLys$ (10 mM in methanol) indicating opposing chirality.

Now in hand, the G1 target molecules were interrogated for their ability to self-assemble into nanosized aggregates and subsequently bind heparin.

5.2.2 Self-Assembly Studies

5.2.2.1 Nile Red Data

The amphiphilic design of the G1 lysine-containing systems should promote molecular self-assembly in aqueous conditions. The hydrophobic aliphatic units are expected to assemble together on the interior of the formed aggregate, leading to the heparin binding groups being displayed at the surface. In order to experimentally probe this, and to determine an approximate critical aggregation concentration (CAC), a Nile Red (NR) encapsulation assay was used. NR is a hydrophobic dye, Figure 5.4, which exhibits a fluorescence signal at 635 nm following irradiation at 550 nm.³²⁶ When ‘free’ in aqueous solution, this NR fluorescence signal is readily quenched, for example by nearby solvent molecules, while when solubilized in a hydrophobic environment, such as the interior of a micelle, the signal remains intense. As the concentration of self-assembling material $C_{22}G1LLys$ or $C_{22}G1DLys$ increases across a titration range, the point at which aggregates form is indicated by a sharp rise in fluorescence intensity (I_f)

at 635 nm. The Nile Red encapsulation assay has been widely used in this manner by, amongst others, the groups of Smith²¹¹ and Lee.³²⁷

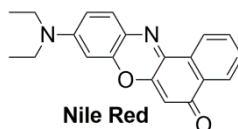


Figure 5.4 – Chemical structure of hydrophobic dye probe, Nile Red (NR)

The data from the NR encapsulation assay for PG1LLys, C₂₂G1LLys and C₂₂G1DLys are shown numerically in Table 5.1 and graphically in Figure 5.5.

Table 5.1 – Nile Red encapsulation assay data for PG1LLys, C₂₂G1LLys and C₂₂G1DLys.

G1 Systems	CAC / μM
P-G1-L-Lysine	N/A
C ₂₂ -G1-L-Lysine	(29 \pm 9)
C ₂₂ -G1-D-Lysine	(27 \pm 13)

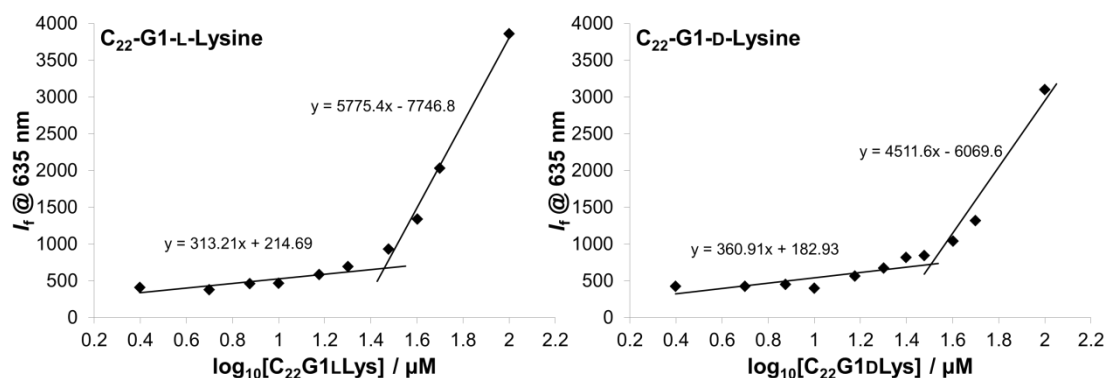


Figure 5.5 – Nile Red encapsulation curves for C₂₂G1LLys and C₂₂G1DLys.

Both C₂₂G1LLys and C₂₂G1DLys were able to assemble into nanostructures at *ca.* 28 μM . When compared directly against C₂₂G1DAPMA in Chapter 4 (CAC of *ca.* 4 μM), it can be seen that these lysine-containing systems have higher CAC values. This may suggest that the increased size-in-space of the lysine residues at the surface somewhat hinders the formation of the assembly. Additionally, the lysine-containing systems may form assemblies composed of a greater number of individual monomer building blocks than the DAPMA system. Nonetheless it is clear from the data that chirality does not have any meaningful impact on CAC values observed for these systems, and nor would it be expected to, given that chirality should only influence the ‘handedness’ of the

resulting assemblies, rather than the specifics of formation/morphology. Importantly, the negative control molecule PG1LLys was unable to assemble up to concentrations of 1 mM, demonstrating the self-assembly process is indeed driven by the amphiphilic nature of the structure conferred by the presence of the aliphatic tail.

The data in Table 5.1 are calculated from three runs of this self-assembly assay, with error values reported as one standard deviation of the triplicated data. These relatively large error values are thought to arise from a degradation event occurring on the timescale of the assay. This is discussed further in Section 5.2.5.

Whilst the NR encapsulation data convincingly suggests C₂₂G1LLys and C₂₂G1DLys self-assemble in aqueous solution, the data are unable to provide information about the size or morphology of the assemblies formed. To that end, TEM imaging was carried out.

5.2.2.2 TEM Images

Transmission Electron Microscopy (TEM) imaging was used in order to observe the self-assembled morphologies of C₂₂G1LLys and C₂₂G1DLys. For the purpose of imaging, solutions were prepared at concentrations of 200 μ M (i.e. above [CAC]) to ensure binders were present in their assembled form. Each binder was also imaged in the presence of heparin. Heparin was introduced to the samples at a charge ratio (+ : -) of 2 as, under this concentration regime, both binders exhibited significant interaction with heparin, see section 5.2.3. Once prepared, aliquots of each solution were loaded on a formvar grid, negatively stained with uranyl acetate and allowed to dry before imaging. Solutions were prepared in clean water as the presence of buffer or other electrolytes are known to interfere with the imaging process. The images for C₂₂G1LLys in the absence and presence of heparin are shown in Figure 5.6 and Figure 5.7 respectively, while the equivalent images for C₂₂G1DLys are shown in Figure 5.8 and Figure 5.9 respectively. The observations are discussed below.

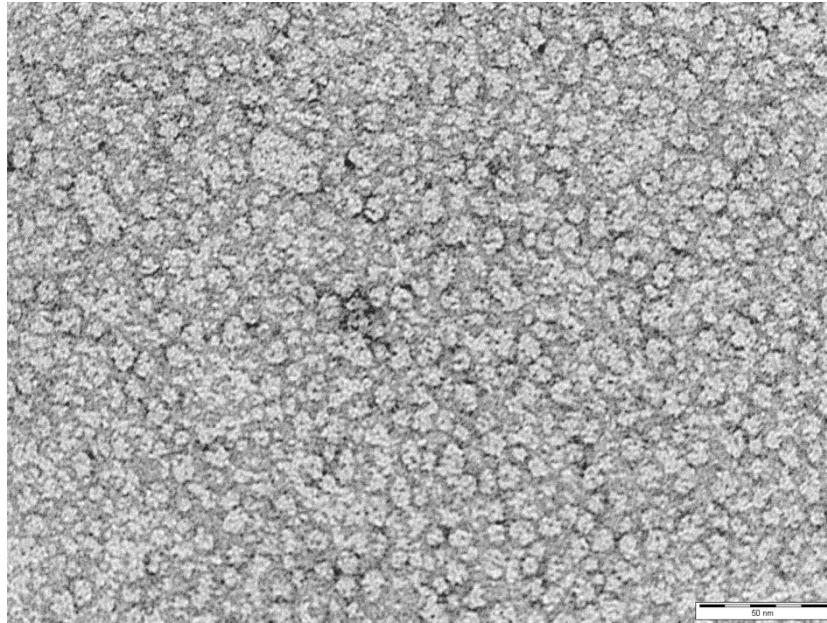


Figure 5.6 – TEM image of 200 μM C₂₂G1LLys (scale bar: 50 nm).

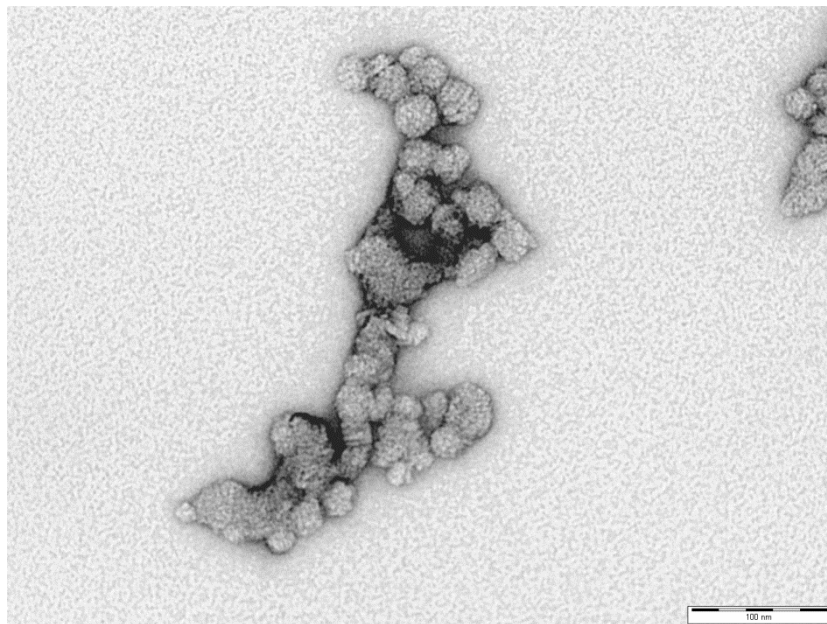


Figure 5.7 – TEM image of 200 μM C₂₂G1LLys in the presence of heparin (scale bar: 100 nm).

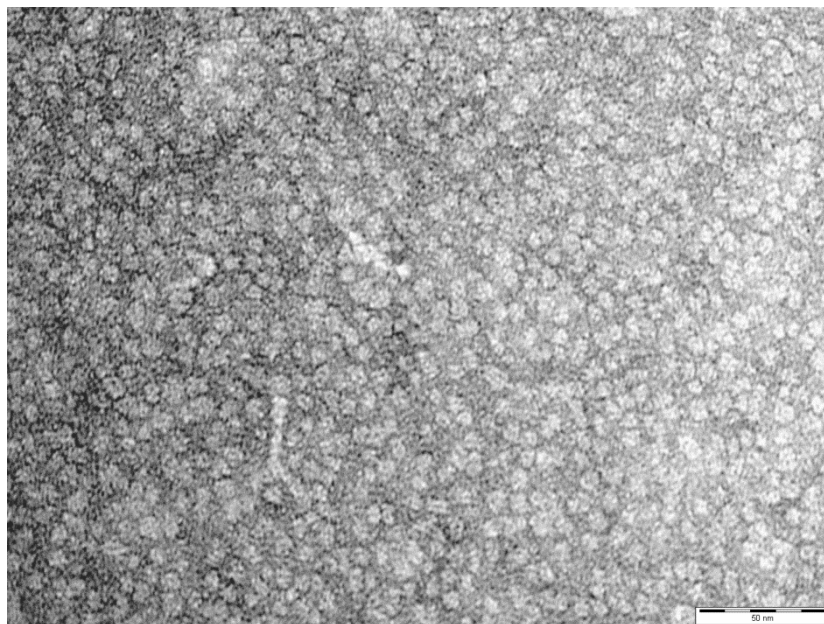


Figure 5.8 – TEM image of 200 μM C₂₂G1DLys (scale bar: 50 nm).

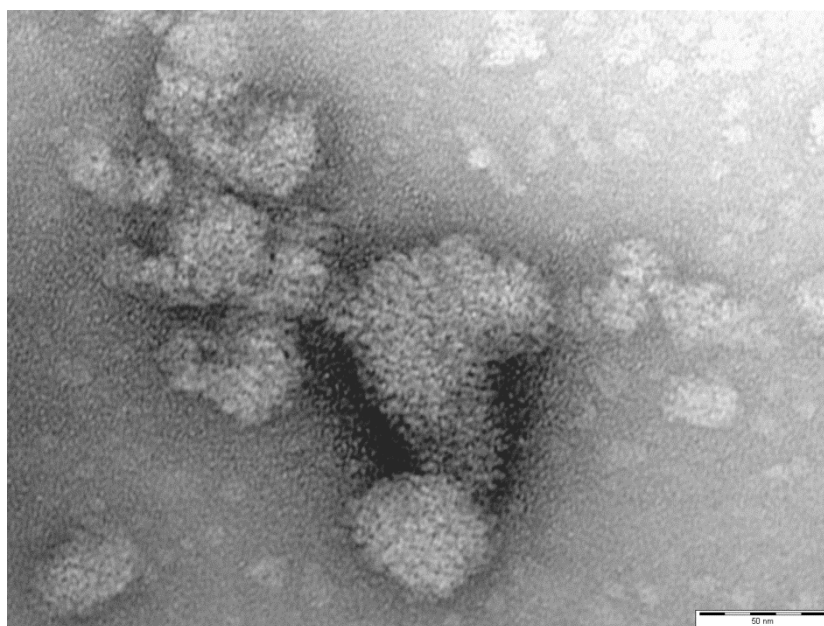


Figure 5.9 – TEM image of 200 μM C₂₂G1DLys in the presence of heparin (scale bar: 100 nm).

As can be seen in both Figure 5.6 and Figure 5.8, each of the binders C₂₂G1LLys and C₂₂G1DLys assemble into small spherical objects which decorate the grid in a uniform manner. This is suggestive of micellar aggregation similar to that seen for the DAPMA system in Chapter 4. Each aggregate has an approximate diameter of *ca.* 7 nm, which is comparable to the size of the earlier system. In the heparin-containing samples shown in Figure 5.7 and Figure 5.9, the larger shaped objects are assigned to be integrated binder-

heparin aggregates, with the smaller, spherical patterning recognized as the SAMul binders distributed throughout the heparin chains. There are clearly some meaningful interactions between the heparin and nanoscale binder assemblies as the micelles appear organized into a pattern not dissimilar to the beads-on-a-string motif previously observed by Smith and co-workers.²¹¹

One of the limitations of using TEM to characterize the morphology of the SAMul aggregates in this way is that only dried samples can be imaged. Micelles (or other aggregates) exist primarily in the solution phase and so dynamic light scattering measurements (DLS) were carried out in collaboration with Dr Marcelo Calderon at Freie Universität Berlin to measure the solution-phase size of C₂₂G1LLys and C₂₂G1DLys. Each binder was measured under two different sets of electrolytic conditions: 10 mM Tris HCl, and the same conditions additionally endowed with 150 mM NaCl. The results are shown in Table 5.2.

Table 5.2 – DLS data for C₂₂G1LLys and C₂₂G1DLys under different electrolytic conditions.

Compound	Average Diameter / nm	
	10 mM Tris HCl only	10 mM Tris HCl, 150 mM NaCl
C ₂₂ -G1-L-Lysine	(7.6 ± 0.3)	(9.0 ± 0.2)
C ₂₂ -G1-D-Lysine	(7.8 ± 0.2)	(9.0 ± 0.2)

In the presence of 10 mM Tris HCl, the DLS results show each of C₂₂G1LLys and C₂₂G1DLys to form aggregates which are *ca.* 7.7 nm in diameter. This sizing correlates well with the TEM imaging. When the conditions are more electrolytically rich, the aggregates form larger aggregates with diameters of *ca.* 9 nm. This increase in size with increasing electrolyte concentration is analogous to the results observed for C₂₂G1DAPMA in Chapter 4 and is thought to be due to a combination of charge screening and an enhancement of the hydrophobic effect.^{306,307}

5.2.3 Heparin Binding in Competitive Conditions

The compounds PG1LLys, C₂₂G1LLys and C₂₂G1DLys were then tested for their ability to bind heparin in competitive conditions using the Mallard Blue heparin binding assay described in Chapter 3. As before, the data are reported in terms of charge excess at

50% MalB displacement (CE_{50}), binder concentration at 50% MalB displacement (EC_{50}) and effective dose (raw amount of binder required to neutralise 100 IU heparin). The data are presented in Table 5.3 with the binding curves shown in Figure 5.10.

Table 5.3 – Heparin binding data from MalB assay for PG1LLys, C₂₂G1LLys and C₂₂G1DLys.

Compound	Heparin Binding		
	$EC_{50} / \mu\text{M}$	CE_{50}	Dose / mg
Propyne-G1-L-Lysine	<i>Not achieved - binding too weak</i>		
C ₂₂ -G1-L-Lysine	(52 ± 10)	(1.94 ± 0.38)	(1.45 ± 0.29)
C ₂₂ -G1-D-Lysine	(30 ± 5)	(1.13 ± 0.19)	(0.85 ± 0.14)

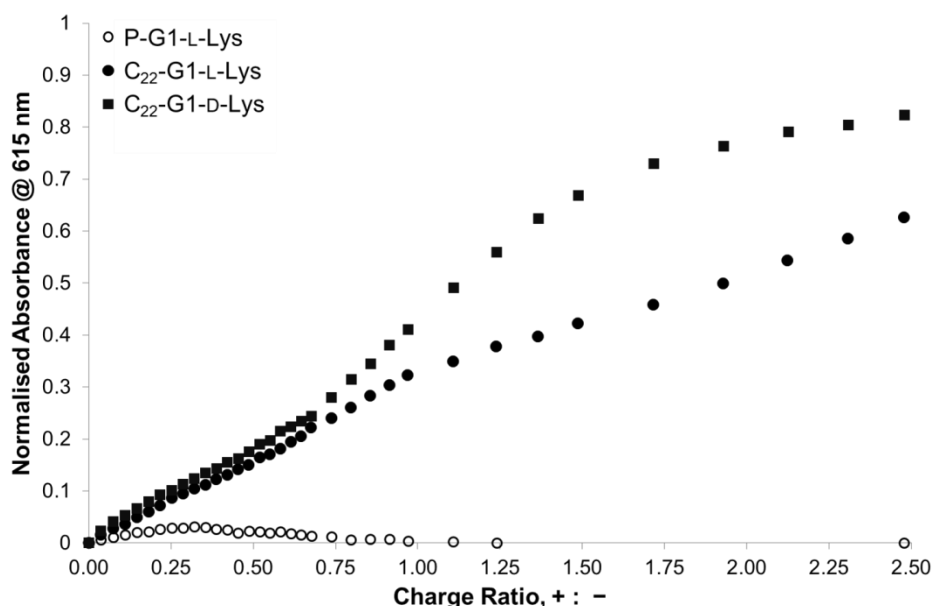


Figure 5.10 – Heparin binding curves for PG1LLys, C₂₂G1LLys and C₂₂G1DLys.

The data shows PG1LLys is unable to displace MalB from heparin, as indicated by the binding curve remaining proximal to the baseline throughout titration. This is an interesting observation as each PG1LLys molecule (433 Da, 4+) is not dissimilar in size and charge to MalB (545 Da, 5+) yet negligible MalB displacement is observed, even when PG1LLys is present in excess. In addition to behaving as a negative control for self-assembly, the PG1LLys data additionally reinforces just how optimised the charge organisation and crescent shape of MalB must be.

With the aliphatic tail in place the heparin binding ability of the system increased significantly. Clearly, the multivalent binding of C₂₂G1LLys is a direct result of

molecular self-assembly as each individual molecule possesses the same number of cationic charges as PG1LLys yet is now able to displace MalB from heparin; a clear SAMul effect. Despite this improvement over the negative control molecule, the heparin binding of C₂₂G1LLys is not especially charge efficient. The data shows 1.94 (\pm 0.38) times as much cationic charge as anionic charge must be present to displace 50% of MalB from heparin. At this point the effective concentration of C₂₂G1LLys is 52 (\pm 10) μ M – well above the CAC value – and so it can confidently be asserted that the binder is operating in micellar form. The effective dose of C₂₂G1LLys is 1.45 (\pm 0.29) mg per 100IU heparin, which is relatively high compared to previously tested systems.^{102,328} Nonetheless, C₂₂G1LLys is another exponent of self-assembled multivalency.

C₂₂G1DLys, meanwhile, is able to achieve 50% MalB displacement with a charge efficiency of 1.13 (\pm 0.19) at an effective concentration of 30 (\pm 5) μ M, leading to an effective dose of 0.85 (\pm 0.14) mg per 100IU. Again, these data suggest C₂₂G1DLys is operating in micellar form. These data are very interesting because C₂₂G1DLys utilizes its charges almost twice as efficiently as C₂₂G1LLys, with only 59% as much cationic binder charge being required to displace half of the MalB from heparin. Despite the sizeable uncertainty values associated with each parameter (the origins of this are discussed below), the difference between enantiomers is statistically significant; that is to say ‘real’.

It must be noted that the data presented in Table 5.3 are calculated from a single, albeit averaged, point during the titration: that at which exactly 50% MalB has been displaced from heparin. As such, they only provide a limited window of insight into the overall binding process. Consideration of the full binding curves in Figure 5.10 is more informative and provides insights into the binding mode of the systems. The respective lineshapes of C₂₂G1LLys and C₂₂G1DLys are essentially identical over the first period of titration up to charge ratio *ca.* 0.65, after which the two lines diverge, almost mirroring each other in shape as amount of binder and cationic charge increases. This may indicate that heparin binding interactions are first established between heparin and the outermost terminal amines of the binder and that only in the presence of sufficient heparin do the α -amines, located 5 bonds from the binder surface, need to become involved in the interaction with heparin. These α -amines are attached directly to the lysine chiral centres and so it follows that the observed line shape divergence appears to relate to these sites becoming involved in binding interactions. Importantly, this

observation suggests that the spatial arrangement of cationic charge, and not just charge-density, is an important consideration for binding heparin with these SAMul systems as the chirality is the only difference between C₂₂G1LLys and C₂₂G1DLys. This is particularly noteworthy as it contradicts the previously mentioned observations of Rabenstein, which suggested that only charge density played a significant role.³²¹ Indeed we reason that these observations are of significance for all chemists involved in micellar or nanostructure binding events.

5.2.4 Heparin Binding in Clinically Relevant Conditions

The data from the heparin binding assay carried out in the presence of buffer and salt suggested that C₂₂G1DLys was a more efficient heparin binder than C₂₂G1LLys and therefore required a lower dose per unit of heparin. For that reason, C₂₂G1DLys was carried forward for testing under more clinically relevant conditions. As discussed in earlier chapters, the Mallard Blue heparin binding assay can also be carried out with heparin delivered in 100% human serum to simulate more realistically the clinical situation experienced by a heparin rescue agent. C₂₂G1DLys was tested using the MalB assay in serum and the resulting data are shown in Table 5.4 and Figure 5.11, and discussed below.

Table 5.4 – Heparin binding data for C₂₂G1DLys obtained from MalB assay carried out in salt and buffer, and with heparin delivered in 100% human serum.

Assay Conditions	Heparin Binding: C ₂₂ -G1-D-Lysine		
	EC ₅₀ / μ M	CE ₅₀	Dose / mg
Salt and Buffer	(30 \pm 5)	(1.13 \pm 0.19)	(0.85 \pm 0.14)
Heparin in 100% Human Serum	(68 \pm 2)	(2.52 \pm 0.08)	(1.83 \pm 0.06)

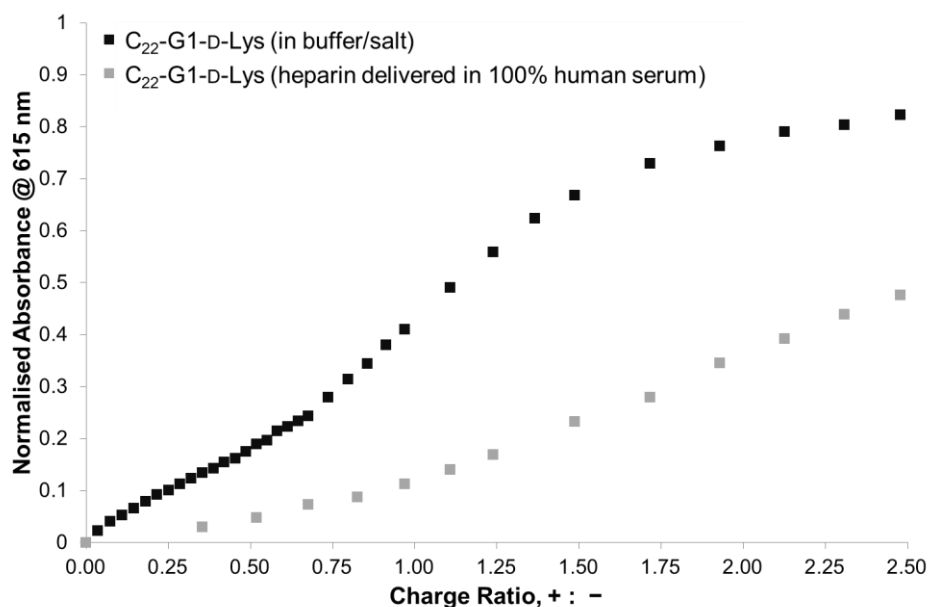


Figure 5.11 – Heparin binding curves for C₂₂G1DLys obtained from MalB assay carried out (i) in salt and buffer (black) and (ii) with heparin delivered in 100% human serum (grey).

The heparin binding efficiency of C₂₂G1DLys decreases in the presence of human serum, with more than twice as much cationic charge being required to neutralize a given amount of heparin than in the absence of serum. It is worth noting that 50% MalB displacement fell marginally outside the titration range and so the parameters reported in Table 5.4 were calculated by extrapolation. It seems likely that the presence of hydrophobic species such as albumins in serum may be disrupting the micellar ligand array of C₂₂G1DLys in a similar manner to that previously observed for C₂₂G1DAPMA. Given their similar structures, C₂₂G1DLys and C₂₂G1DAPMA could reasonably be expected to have comparable propensities for disruption by serum. Impressively, despite the disruption, C₂₂G1DLys still showed significant heparin binding under these more challenging conditions. Building on this promise, C₂₂G1DLys was tested in a plasma clotting based prothrombin assay (PT assay) to examine its ability to not only interact with heparin, but also to neutralize its anticoagulant activity in a clinically relevant assay. Once again, clotting studies were carried out in the laboratory of Professor Jeremy Turnbull at University of Liverpool, UK.

Table 5.5 – Plasma clotting data for C₂₂G1DLys in PT assay.

Compound	Binder Dose, mg / 100IU	Clotting time / seconds
None	-	(12.8 ± 0.8)
Heparin	-	no clot
C ₂₂ -G1-D-Lysine	0.85	(19.7 ± 2.7)
C ₂₂ -G1-D-Lysine	1.83	(19.4 ± 2.6)

The PT assay results shown in Table 5.5 show that introduction of heparin to the sample of plasma led to a suspension of clotting as heparin exerted its anticoagulant effect. Subsequent introduction of C₂₂G1DLys at the dose calculated from the MalB assay in buffer and salt (0.85 mg per 100IU) resulted in clotting been reestablished, although the clotting time was somewhat extended compared to the control sample. The extended clotting time may be due to disruption of a portion of the binder by some of the hydrophobic plasma components. Introduction of C₂₂G1DLys at the higher dose suggested by the MalB assay in serum (1.85 mg per 100IU) also resulted in clotting being reestablished, but did not result in a shortening of the clotting time. From these limited clotting studies, it would appear that regardless of applied dose, the clotting time for C₂₂G1DLys remained roughly consistent in the PT assay at around 19 seconds.

Despite this extended clotting time, it is particularly impressive that C₂₂G1DLys, a self-assembling binder which is less efficient in its use of individual charges than other systems tested, is able to clot heparinized human plasma samples. It is another excellent demonstration of the genuine potential of this simple and biocompatible SAMul approach in the development of functional heparin rescue agents.

5.2.5 Degradation

5.2.5.1 Nile Red Release Assay

Part of the rationale behind the SAMul approach to heparin binding is the enhanced degradability of the binder molecules compared to larger covalent systems, which gives SAMul binders greater pharmacological appeal. To that end, the ability of C₂₂G1DLys to degrade and/or disassemble under biologically relevant conditions was tested. It was hoped that comparison against data for C₂₂G1DAPMA may give insights into the effects of connecting the surface groups through ester linkages rather than carbamates.

Although only the D-system was tested here, *in vivo* each of C₂₂G1LLys and C₂₂G1DLys may have subtly different degradation profiles owing to their opposing chiralities. In particular, the D-system might be metabolized more slowly owing to the natural absence of D-amino acids in humans. Indeed it is known that humans have no natural mechanism for utilizing or dealing with D-lysine derivatives yet they can derive around 1% of their nutritional intake from L-lysine derivatives.^{329,330}

The propensity of C₂₂G1DLys to degrade was tested using the same time-resolved Nile Red release assay employed for C₂₂G1DAPMA in Chapter 4. Specifically, a solution of C₂₂G1DLys was made up at a concentration above the CAC (50 μM) in PBS buffer at pH 7. An aliquot of Nile Red was added to the cuvette before inversion ensured thorough mixing. Thereafter, the fluorescence intensity (I_f) at 635 nm following irradiation at 550 nm, was recorded at 10 minute intervals over 6.5 hours to monitor the release of dye from the micellar interior. The resulting values were normalised between I_f at the start of the experiment and I_f of a PBS-Nile Red control. The resulting degradation curve is shown in Figure 5.12.

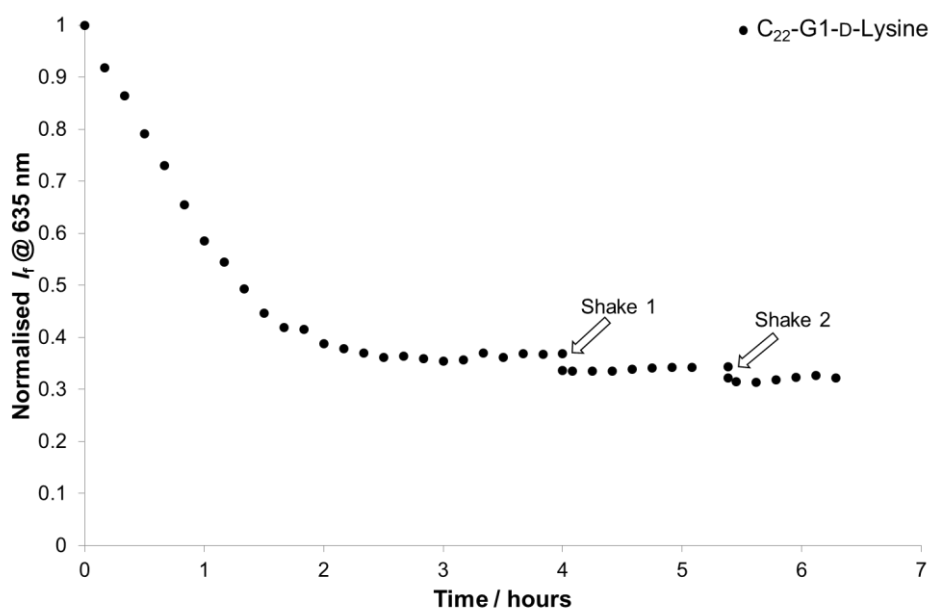


Figure 5.12 – Time resolved degradation curve of C₂₂G1DLys. Discontinuities are indicated where the sample was vigorously shaken to simulate blood-flow shear forces.

As shown in Figure 5.12, C₂₂G1DLys degrades with a half-life ($t_{1/2}$) of *ca.* 1.25 hours. This half-life is significantly shorter than for C₂₂G1DAPMA, which exhibited a half-life of *ca.* 7 hours under the same conditions. Clearly, the connection of the surface groups

to the linker unit through ester bonds rather than carbamates significantly increases degradability. It seems likely that the degradation process of C₂₂G1DLys is driven by an intramolecular base-catalyzed hydrolysis process, much like that previously reported by Smith and co-workers.⁶⁹ Indeed the closer proximity of the ester groups to the surface amine in C₂₂G1DLys may assist in this increased degradation rate over C₂₂G1DAPMA.

The short $t_{1/2}$ of C₂₂G1DLys is significant with respect to much of the data reported earlier in this chapter. For example, all the parameters calculated from MalB heparin binding assays have relatively large uncertainty values associated with them; in some cases as much as *ca.* 19% of the mean value. The instability of the binder molecules would appear to account for this uncertainty because MalB heparin binding assays can take around 3 hours to perform in triplicate, during which time the binder may have degraded somewhat. Degradation during MalB assays will likely be slower than suggested by the Nile Red release study however, as any solutions containing binder also contain heparin and, as shown in Chapter 4, interaction with heparin significantly retards degradation as the binder amines are bound to heparin and less able to intramolecularly catalyse the hydrolytic degradation process.

An important further consideration for any potential heparin rescue agent is the effect of dosing into the fast-flowing bloodstream. In particular, the role of shear forces is especially important for our non-covalent assemblies. In order to simulate the effect of shear forces on our SAMul system, the cuvette was shaken vigorously between the acquisitions of two data points. These points are indicated in Figure 5.12. The shear forces manifest themselves as clear discontinuities in the line shape, indicative of an accelerated degradation event. Interestingly, the points following the shaking appear to revert back to the initial degradation regime. Importantly, in the bloodstream such shear forces would be constant rather than intermittent, albeit somewhat lower in intensity. That is to say, the half-life of C₂₂G1DLys in a flowing bloodstream would be expected to be significantly shorter than the 1.25 hours observed in this degradation experiment.

5.2.5.2 Mass Spectrometric Studies

Whilst the Nile Red release assay is indicative of degradation, it is unable to identify which bonds specifically are being broken, or whether indeed the assembly is simply disrupted rather than degraded over time. A mass spectrometric degradation assay was carried out in order to identify the species resulting from degradation. As for

C₂₂G1DAPMA in Chapter 4, mass spectra were obtained in the presence of a Gly-Ala non-degradable internal standard before and after incubation at 37°C for 24 hours. Some example spectra, along with the molecular species of interest are shown in Figure 5.13.

At time zero, the molecular ions associated with C₂₂G1DLys ($m/z = 391 [M]^{2+}$ and $261 [M]^{3+}$) were clearly visible. After 24 hours, these molecular ions had disappeared and peaks corresponding to the hydrolysis products of the linker ester (alcohol, $m/z = 408 [M]^{1+}$; carboxylic acid, $m/z = 391 [M]^{1+}$) were now visible, albeit at low relative intensity to the standard. This suggests that the connection of the surface groups to the scaffold by ester groups rather than carbamates, as was the case for C₂₂G1DAPMA, promoted further degradation of the carboxylic acid fragment, although direct evidence of such secondary degradants was not seen.

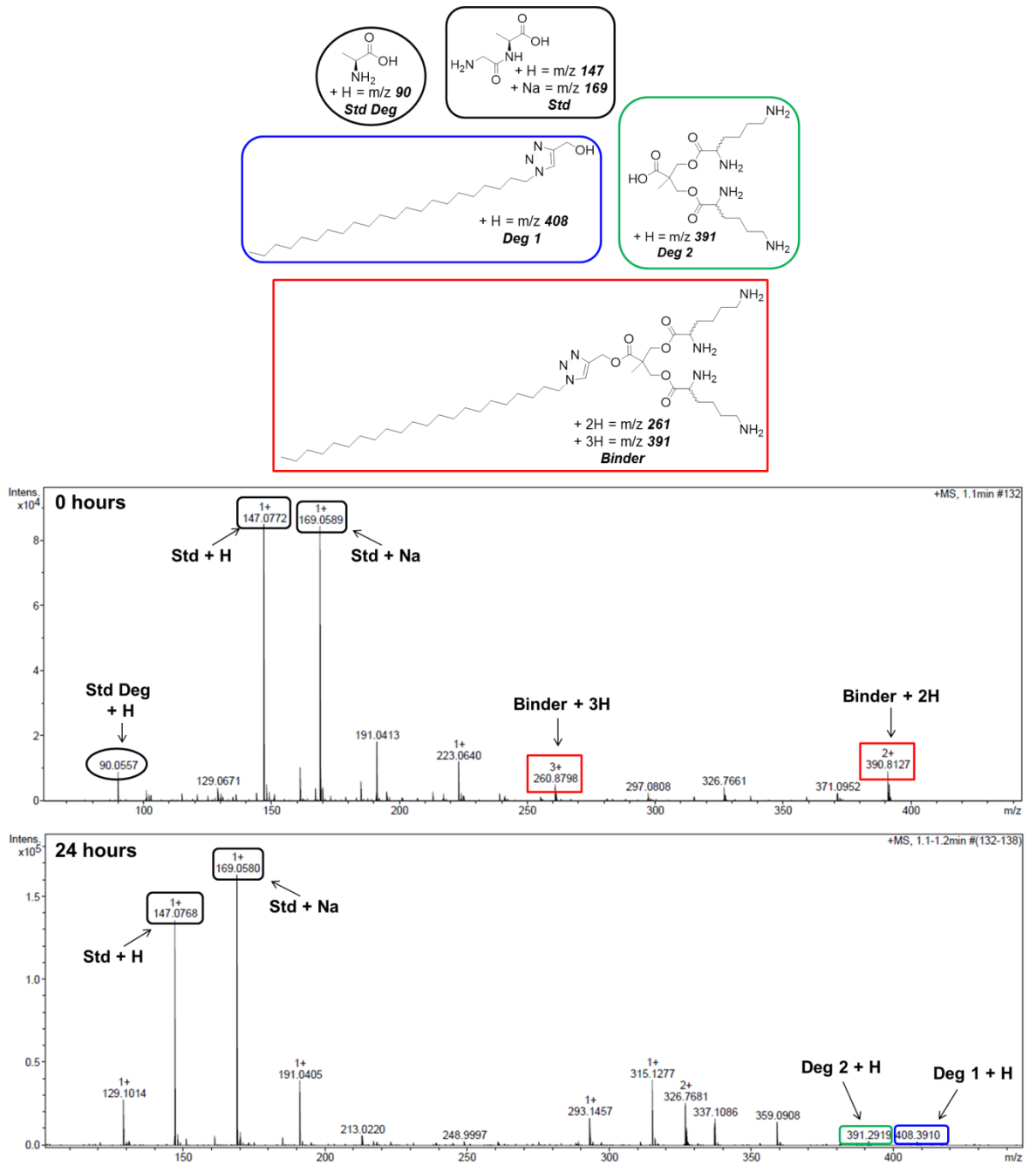


Figure 5.13 – Mass spectrometric degradation assay: observed species (top) after 0 hours (middle) and 24 hours (bottom) incubation at 37°C.

5.2.5.3 Plasma Clotting Study

The Nile Red release data presented above demonstrated that molecular degradation switched off the self-assembly processes of C₂₂G1DLys, however it did not unequivocally indicate a switch off in heparin binding activity. Therefore, to confirm that a degraded sample of C₂₂G1DLys would be unable to operate as a heparin rescue agent (i.e. the activity had been lost), a solution of binder was made up in aqueous solution and left to stand for 24 hours before being tested in the prothrombin plasma clotting assay (PT assay) as before. The results, shown in Table 5.6, indicate that after degradation, the heparin-neutralizing activity was lost and no plasma clotting was observed.

Table 5.6 – Plasma clotting data for C₂₂G1DLys in PT assay before and after degradation.

Compound	Binder Dose, mg / 100IU	Clotting time / seconds
C ₂₂ -G1-D-Lysine	0.85 (0 hours)	(19.7 ± 2.7)
C ₂₂ -G1-D-Lysine	0.85 (24 hours)	no clot

In a further experiment to probe binder degradability, a sample of C₂₂G1DLys was taken approximately 18 months after synthesis and analysed by NMR spectroscopy. Despite refrigeration under an inert atmosphere, comparison of the spectra obtained after this extended time period with those from immediately following synthesis indicated the molecule had degraded somewhat. The most informative signals in the spectra corresponded to the -CH₂ positioned between the linker unit ester group and the 1,2,3-triazole ring. As shown in Figure 5.14, the individual signals observed after synthesis in ¹H spectrum (a) and ¹³C spectrum (c) became accompanied by new signals in spectra (b) and (d). These new signals were assigned to the degradant product resulting from hydrolysis of the adjacent ester group. The ratio of intact binder to hydrolysed binder was estimated from these spectra to be approximately 3 : 1, suggesting slow degradation had occurred during prolonged storage.

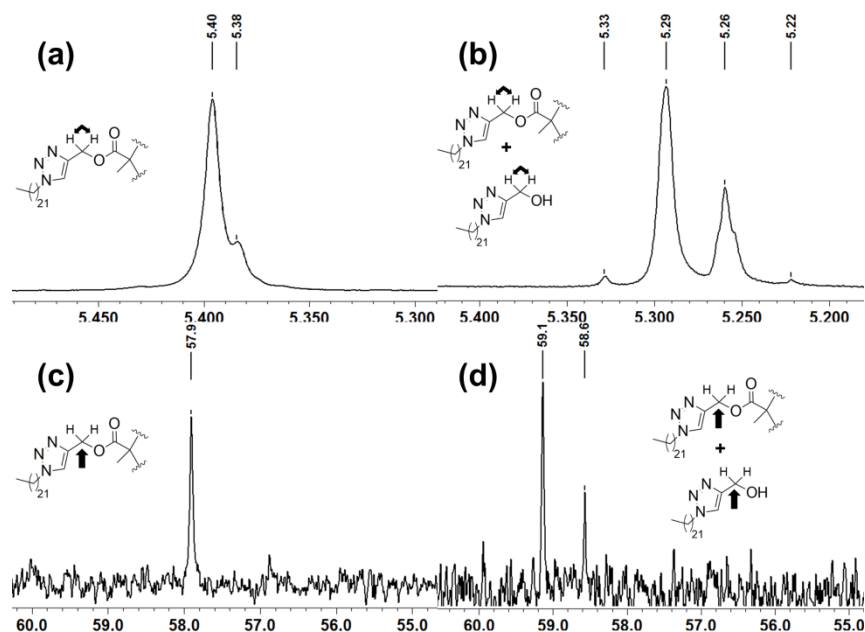


Figure 5.14 – ^1H and ^{13}C NMR spectra for $\text{C}_{22}\text{G1DLys}$ before (left) and after (right) refrigeration under an inert atmosphere for 18 months.

The effect of this apparent partial-degradation on heparin binding performance was also studied by re-testing the ‘old’ samples of $\text{C}_{22}\text{G1LLys}$ and $\text{C}_{22}\text{G1DLys}$ using the Mallard Blue heparin binding assay in buffer and salt. As shown in Figure 5.15, the degradation affected the performance of both binder systems. It is noteworthy, however, that the binding curves obtained (shown in grey) mimic those obtained initially by following the same lineshape up to a charge ratio of *ca.* 0.65 before diverging, with $\text{C}_{22}\text{G1DLys}$ again emerging as the superior heparin binder of the pair.

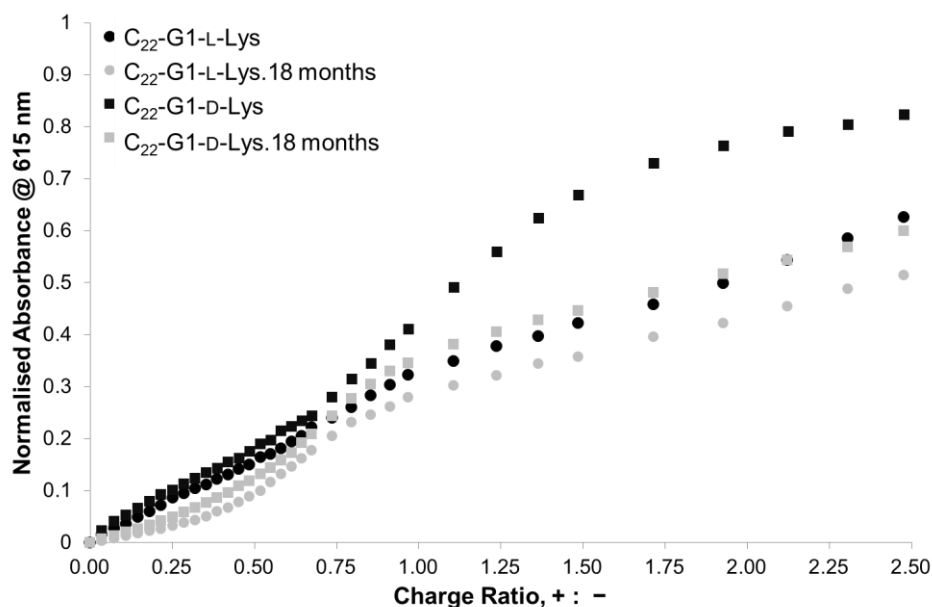


Figure 5.15 – Heparin binding curves for C₂₂G1LLys and C₂₂G1DLys obtained using the MalB assay in buffer and salt initially following synthesis (black) and after 18 months of storage (grey).

5.2.6 DNA Binding

5.2.6.1 A Different Chiral Biological Polyanion

Following the chiral preferences exhibited by C₂₂G1LLys and C₂₂G1DLys when binding heparin, we became interested in whether such differences would be observed when binding an alternative chiral biological polyanion. To that end, DNA was identified as a suitable binding target.

The double-helical structure of DNA was famously first solved by Watson and Crick in 1952.³³¹ DNA consists of a backbone of alternating phosphate groups and 2-deoxyribose sugar residues, each of which is functionalised with a nucleobase. There are four nucleobases, which can be categorised into two classes: the purine-bases, adenine and guanine; and the pyrimidine bases, thymine and cytosine. Direct hydrogen bonding interactions between pairs of these nucleobases bring together two DNA strands. Specifically, adenine interacts with thymine, and guanine interacts with cytosine, as shown in Figure 5.16.

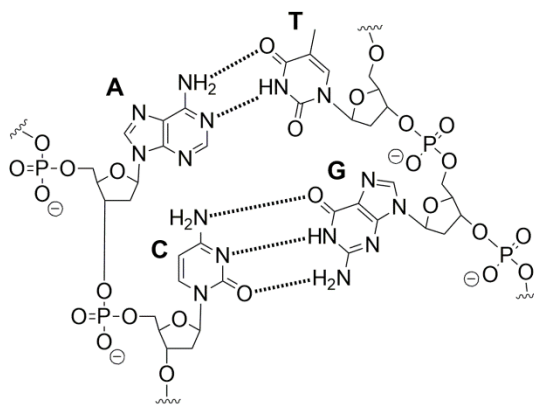


Figure 5.16 – Segment of DNA showing the 2-deoxyribose sugar-phosphate backbone and the hydrogen bonding interactions between the labelled nucleobases.

Genetic code allowing the synthesis of every protein within an organism is contained within DNA. When errors are present within this code, an incorrect or mutated gene is synthesised within cells, which can lead to genetic diseases such as sickle-cell anaemia or cystic fibrosis. Gene Therapy (also known as gene delivery) is a medicinal approach which has been developed in attempt to remedy these conditions through correcting these genetic code errors.^{332,333} The process involves delivering a section of healthy DNA into a cell, which can code for a working version of a faulty/mutated gene or a therapeutic protein drug. Generally, delivery of such genetic material (DNA) is achieved by vectors, which act to protect the DNA as it enters cells. Vectors tend to ‘package up’ DNA, often inside themselves, to mediate transport across cell membranes such that once inside the cell, and access is gained to the cell-machinery, coding can begin to produce the therapeutic protein or gene.

Over recent years, many synthetic (or non-viral) vectors have been designed to bind DNA and facilitate gene delivery.³³⁴ Cationic polymers³³⁵ and cationic lipids^{336,337} are the two largest molecular classes showing promise as effective gene delivery vectors although dendritic systems are also becoming increasingly studied.³³⁸ Indeed, of interest to us is work from the group of Smith, which has focussed on this dendritic approach and produced a range of DNA binding system, some of which utilise the same self-assembling approach to multivalent binding being targeted as part of the current project.^{65,69,339,340}

Chirality in DNA arises from the deoxyribose sugar moieties along its backbone and leads to the famous right-handed double helix.³³¹ There has been much interest in

5.2.6.2 Testing C₂₂G1LLys and C₂₂G1DLys

In order to test the ability of C₂₂G1LLys and C₂₂G1DLys to bind DNA, an indicator displacement assay involving ethidium bromide was employed. The ethidium bromide assay is well-known, having been used for many decades, and has been utilized previously in the Smith group.^{68,356}

Ethidium bromide (EthBr), shown in Figure 5.18, is a planar aromatic indicator dye which is able to intercalate between base pairs of free DNA. Once intercalated in this manner, EthBr exhibits a strong fluorescence signal at 595 nm following excitation at 550 nm. When a DNA-binder is added to a solution of EthBr and DNA, EthBr becomes indirectly displaced into free solution as binder-DNA interactions are established. Once in free solution, EthBr fluorescence is readily quenched, and the change in fluorescence intensity (ΔI_f) can be used to calculate the degree of DNA-binding. Normalised binding curves can be plotted in the same manner applied to the heparin binding studies, with data similarly reported in terms of charge efficiency (CE₅₀) and effective concentration (EC₅₀) at 50% EthBr displacement. This assay is useful for comparing families of related molecules and quantifying their DNA binding ability.



Figure 5.18 – Chemical structure of fluorescent dye ethidium bromide.

The EthBr DNA binding assay was used to test PG1LLys, C₂₂G1LLys and C₂₂G1DLys under conditions of 5.07 μ M EthBr and 4 μ M DNA (with respect to each base) in the presence of SHE buffer (2 mM HEPES, 0.05 mM EDTA and 150 mM NaCl) at pH 7.5. The resulting DNA binding data are shown numerically in Table 5.7 and graphically in Figure 5.19.

Table 5.7 – DNA binding data from EthBr assay for PG1LLys, C₂₂G1LLys and C₂₂G1DLys. *EC₅₀ and CE₅₀ are numerically equivalent due to experimental conditions.

Compound	DNA Binding	
	EC ₅₀ / μM	CE ₅₀
Propyne-G1-L-Lysine	<i>Not achieved - binding too weak</i>	
C ₂₂ -G1-L-Lysine*	(1.99 ± 0.54)	(1.99 ± 0.54)
C ₂₂ -G1-D-Lysine*	(3.51 ± 0.37)	(3.51 ± 0.37)

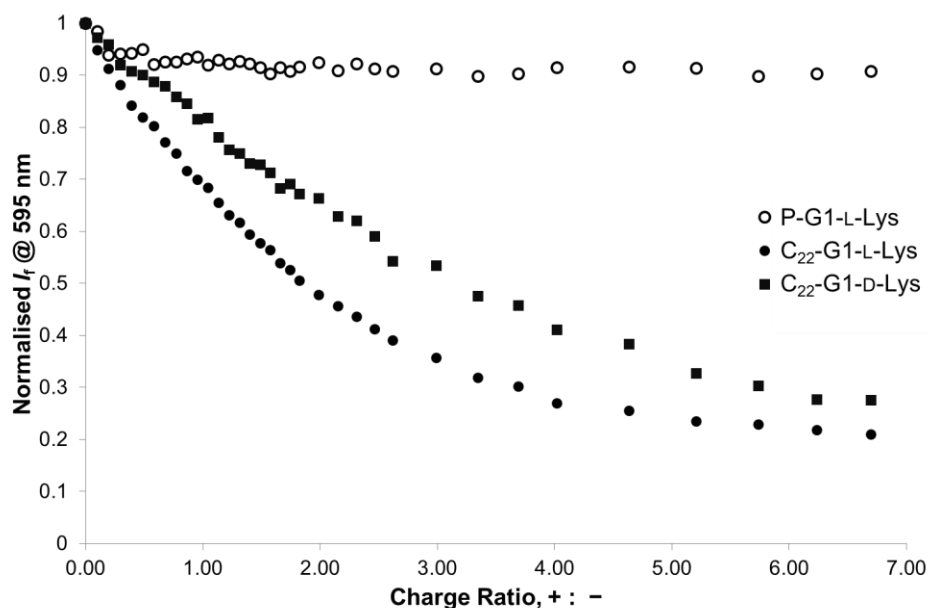


Figure 5.19 – DNA binding curves from EthBr assay for PG1LLys, C₂₂G1LLys and C₂₂G1DLys.

The DNA binding data shows that in the absence of a hydrophobic unit, PG1LLys is unable to displace EthBr from DNA even when there are seven times as many binder cationic charges present as DNA anionic charges. When the alkyl chain is in place however, DNA binding ability increases significantly with C₂₂G1LLys displacing 50% EthBr at a charge excess of (1.99 ± 0.54) and binder concentration of (1.99 ± 0.54) μM. These values are numerically equivalent as, under the conditions of the assay, one mole of DNA possesses one anionic charge and is present at 4 μM, while the SAMul binders each possess four cationic charges per mole. The presence of the aliphatic tail is having an effect on the DNA binding ability of C₂₂G1LLys despite, according to the data in Table 5.1, being present at a concentration significantly below the CAC. This may suggest that the CAC is lowered in the presence of DNA as interactions between individual non-assembled molecules and DNA may serve to enhance the assembly of

subsequent binder molecules, which in turn enhance DNA binding by promoting multivalent interactions. This phenomenon may indicate that multivalency enhanced self-assembly is a corollary of self-assembled multivalency.

In order to examine the CAC of the system in the presence of DNA, the Nile red encapsulation assay was repeated for C₂₂G1DLys under the conditions of the DNA binding assay (i.e. in the presence of 4 μM per DNA base, 0.05 mM EDTA, 150 mM NaCl and 2 mM HEPES). The resulting encapsulation curve, Figure 5.20, gave a CAC value for C₂₂G1DLys of 11 (± 2) μM.

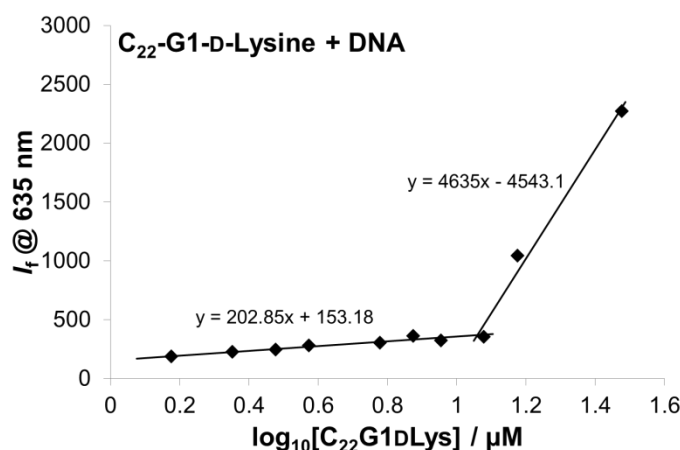


Figure 5.20 – Nile red encapsulation curve for C₂₂G1DLys in the presence of DNA.

Although the presence of DNA served to lower the CAC somewhat, this observed value is still over three times larger than the concentration required to displace half of the ethidium bromide in the DNA binding assay. This suggests that DNA is assisting the formation of the self-assemblies somewhat although it appears to suggest that effective DNA binding is being achieved in the absence of full micellar assemblies. This leads to the possibility that in the presence of DNA, several monomers may cluster together at the DNA surface in order to establish multivalent interactions with the polyanion. This may account for the superior binding over the alkyne-tailed negative control molecules while explaining the NR encapsulation data.

The charge efficiency of both C₂₂G1LLys and C₂₂G1DLys is significantly reduced when binding DNA compared to binding heparin. This is most likely a straightforward consequence of heparin being a more charge-dense polyanion and so presenting each cationic charge with more opportunities to establish meaningful interactions than DNA.

Comparison of the DNA binding data for C₂₂G1LLys and C₂₂G1DLys suggests that each enantiomer binds DNA with a significantly different charge efficiency. Specifically, C₂₂G1LLys is the more charge efficient of the pair requiring (1.99 ± 0.54) positive charges per negative charge of DNA, while C₂₂G1DLys requires (3.51 ± 1.37) positive charges. The difference in binding efficiency between the opposing enantiomers is likely to arise as a result of the differing interaction of each chiral centre with the anionic target. Importantly, the observation that the L-system is the more charge efficient DNA binder of the pair is in direct contrast to observations from the heparin binding data, where the D-system was the more charge efficient. Excitingly, the data therefore suggests the C₂₂G1Lys SAMul systems have opposing chiral preferences when binding to different biological polyanions. To the best of our knowledge, these contrasting preferences for heparin and DNA binding have not previously been reported; particularly not with chirality expressed at the surface of a self-assembled nanosystem.

It is often proposed that charge density is the only factor of importance when establishing multivalent ion-ion interactions,²⁸⁰ however the data presented here clearly demonstrate the arrangement of the individual charges in space can have a significant impact. It is perhaps not surprising that an enantiomeric pair of substrate molecules would have different binding efficiencies when interacting with a chiral target, or, arguably, that this preference may change for chiral binding targets. Rather more noteworthy is that for our SAMul binders these chiral differences are brought about only by very small changes at the molecular level. Physically, the only difference between the systems lies at the α -carbon positions on each lysine residue, five bonds from the surface of the assembly. Consequently for C₂₂G1LLys and C₂₂G1DLys, it is only the orientation of this part of the molecules that differ, suggesting that heparin and DNA can be acutely sensitive to the spatial arrangement of binding ligand arrays. Interestingly this also suggests that oligosaccharides and oligonucleotides have different chiral preferences when binding to arrays of cationic, lysine-based amino acids. This observation may have biological or evolutionary significance.

In order gain more meaningful insights to these chiral differences, a molecular dynamics modelling study has been carried out in collaboration with Professor Sabrina Pricl at University of Trieste, Italy. Unfortunately the results from this study are not available for inclusion here.

5.3 Generation 2 Systems

Following on from the exciting chiral recognition observations for the G1 lysine-containing SAMul binders in the previous section, it was decided to design and synthesise some larger second generation (G2) analogues. Specifically, $C_{22}G2LLys$ and $C_{22}G2DLys$ were identified as suitable target molecules, shown in Figure 5.21. The G2 analogues differ from their G1 counterparts in the degree of dendritic branching present within the linker unit. At G2, the additional branching points result in the surface being decorated by four, rather than two, lysine groups. It was postulated that the larger system, in possession of more binding groups at the assembly surface, might be capable of more charge efficient heparin binding. Similarly sized systems have previously been shown by the groups of Smith⁶⁹ and Haag⁷² to be effective DNA/RNA delivery agents. It was also hoped that increasing the number of chiral centers at the binding surface may serve to amplify the chiral differences observed when binding to different chiral target molecules such as heparin and DNA.

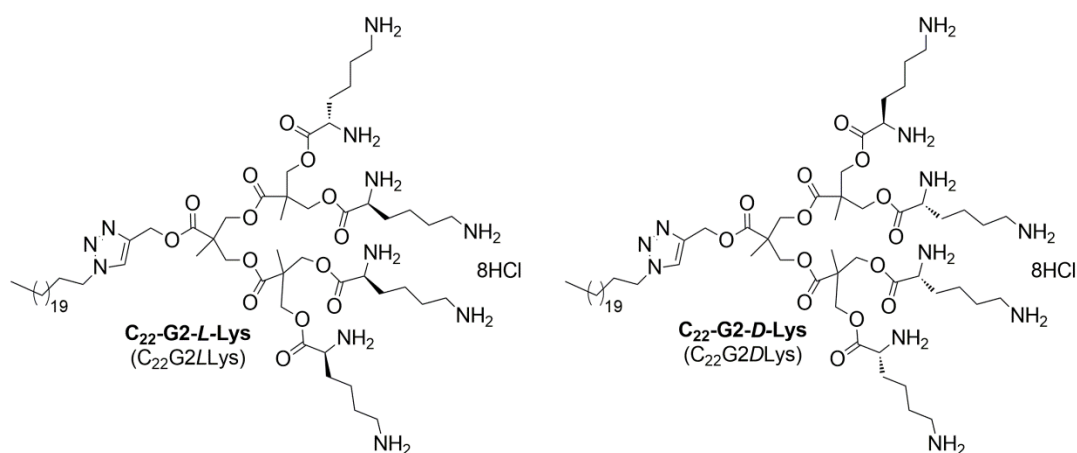


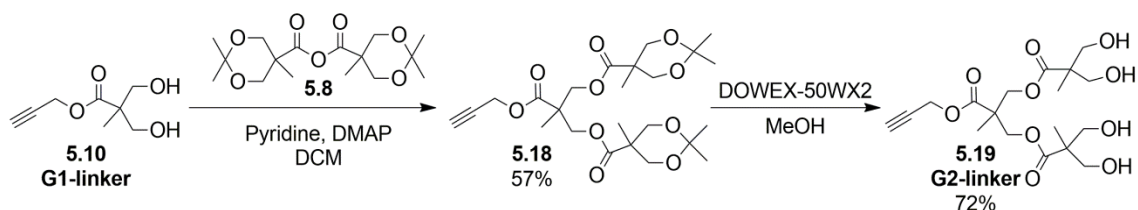
Figure 5.21 – G2 target molecules $C_{22}G2LLys$ and $C_{22}G2DLys$.

5.3.1 Synthesis of $C_{22}G2LLys$ and $C_{22}G2DLys$

5.3.1.1 Preparation of G2 linker group

The G2 target molecules were synthesized in the same convergent manner as the G1 systems. In order to create the extra layer of branching within the G2 linker unit, alkyne-functionalised-diol 5.10 was reacted with symmetrical anhydride 5.8 in a moderate yielding base-catalysed coupling reaction.³²⁵ This generated G2-isopropylidene 5.18 which was deprotected using DOWEX-50WX2 to afford G2-linker

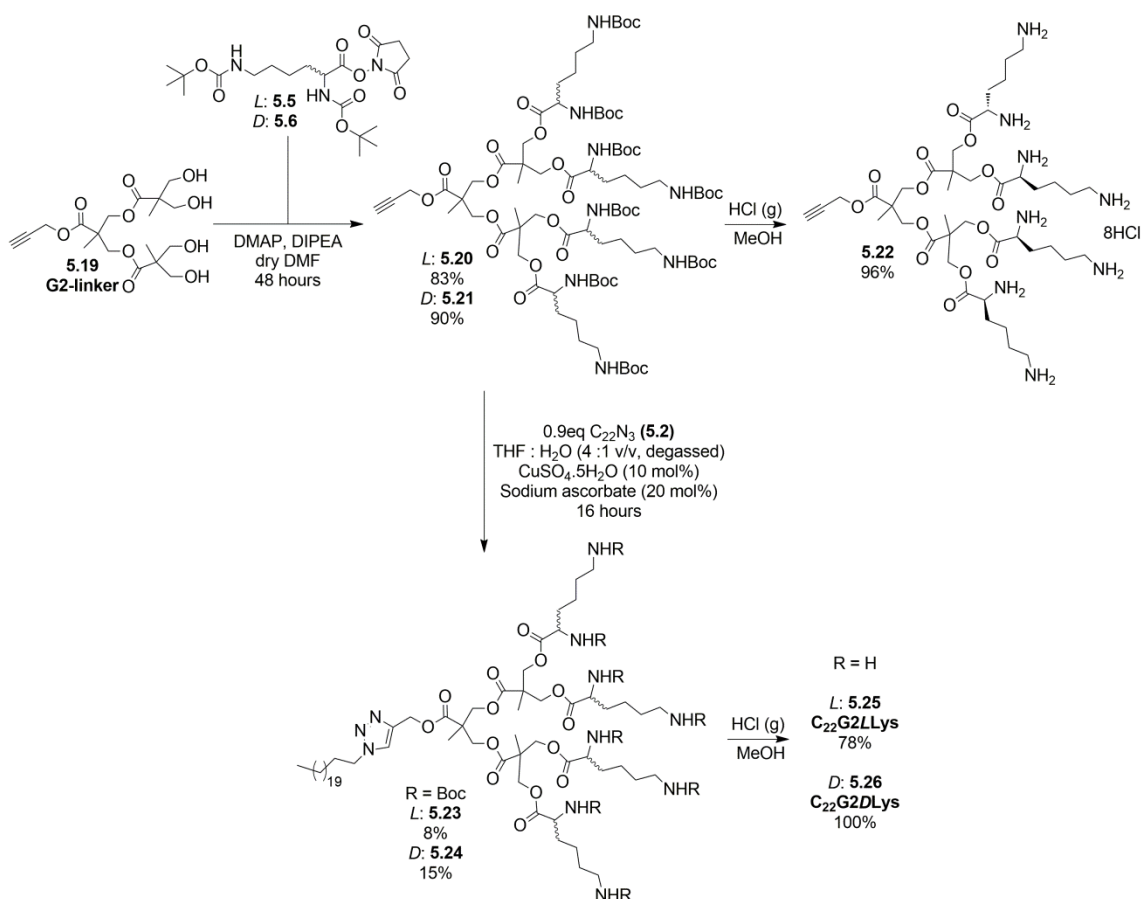
5.19. Although concentrated sulfuric acid was able to unveil the alcohol groups, DOWEX resin was found to be a more reliable approach for the larger system. This observation agrees with work from the group of Hult.³⁵⁷ The synthetic scheme showing the preparation of G2-linker is shown in Scheme 5.5.



Scheme 5.5 – Synthetic scheme showing preparation of G2-linker.^{325,357}

5.3.1.2 Connecting the pieces

In the same manner utilised in the preparation of the G1 system, the alcohol groups of G2-linker 5.19 were coupled with either LLys(Boc)₂ or DLys(Boc)₂ to afford protected partial binders 5.20 and 5.21 respectively, in good yields after purification by gel permeation chromatography in 95:5 DCM:methanol. Once again, a small portion of L-enantiomer 5.20 was deprotected using HCl gas in methanol to generate negative control for self-assembly 5.22 in excellent yield. Partial binders 5.20 and 5.21 were then connected to alkyl azide 5.2 using copper(II) mediated ‘click’ chemistry to afford, after purification by gel permeation chromatography in 100% DCM, protected final binder molecules 5.23 and 5.24. The yields of the G2 click reactions were very low (*ca.* 8 %) when compared with the G1 systems (*ca.* 70%). This is thought to be due to the steric crowding around the G2 alkyne functionality perturbing the interaction with the copper catalyst. Hindering the alkyne-Cu interaction prevents the alkyl LUMO becoming reduced in energy sufficiently to permit easy electron transfer from the azide HOMO. There are also a significant number of coordinating ligands present which could provide competitive binding sites for copper. Consequently, a low product yield of 5.23 and 5.24 is observed. Copper-free ‘click’ approaches may circumvent some of these issues, however this was not attempted here. The material obtained was deprotected in an excellent yield using HCl gas in methanol to afford target molecules C₂₂G2LLys 5.25 and C₂₂G2DLys 5.26. The reaction scheme for the preparation of these target molecules is shown in Scheme 5.6.



Scheme 5.6 – Synthetic scheme for production of target molecules PG2LLys, $C_{22}G2LLys$ and $C_{22}G2DLys$.

With $C_{22}G2LLys$ and $C_{22}G2DLys$ in hand, circular dichroism spectroscopy was used to establish whether amino acid chirality had been successfully preserved throughout the synthesis. As can be seen in Figure 5.22, at concentrations of 10 mM, the molar ellipticity for the two systems is essentially equal and opposite. This indicates that the two target molecules are of approximately equal enantiopurity, and crucially that chirality has not been scrambled during synthesis.

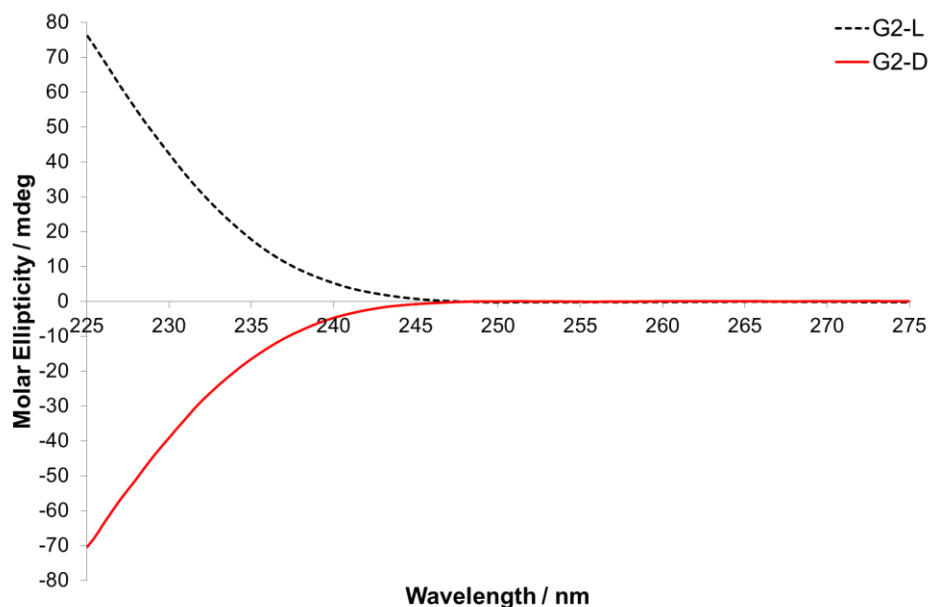


Figure 5.22 – Circular dichroism spectra of target molecules C₂₂G₂LLys and C₂₂G₂DLys indicating opposing chirality.

5.3.2 Self-Assembly Studies

5.3.2.1 Nile Red Data

The self-assembling ability of C₂₂G₂LLys and C₂₂G₂DLys was tested using the Nile Red encapsulation assay discussed earlier. The data are shown numerically in Table 5.8 and graphically in Figure 5.23.

Table 5.8 – Nile Red encapsulation assay data for PG₂LLys, C₂₂G₂LLys and C₂₂G₂DLys.

G2 Systems	CAC / μM
P-G ₂ -L-Lysine	N/A
C ₂₂ -G ₂ -L-Lysine	(25 \pm 8)
C ₂₂ -G ₂ -D-Lysine	(20 \pm 6)

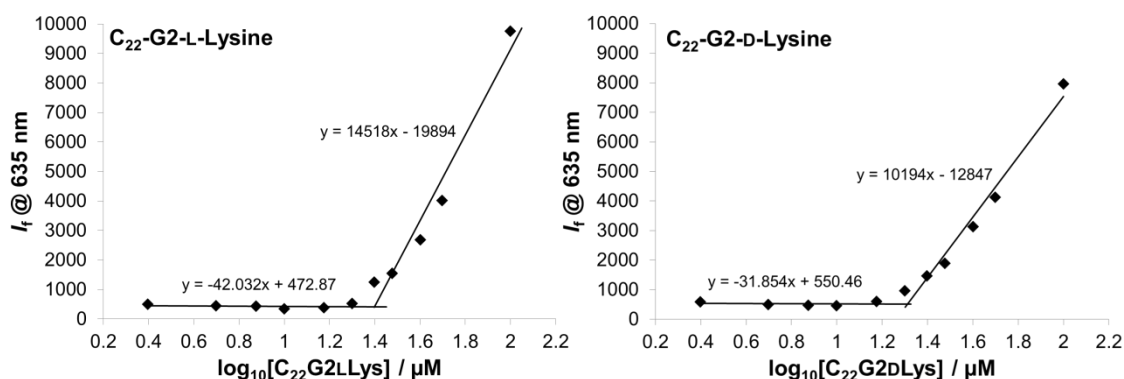


Figure 5.23 – Nile Red encapsulation curves for C₂₂G2LLys and C₂₂G2DLys.

These data clearly demonstrate once more that the aliphatic tail provides the driving force for aggregation of the SAMul systems. In the absence of the hydrophobic unit, PG2LLys is unable to encapsulate Nile Red up to concentrations of 1 mM. The data do suggest that C₂₂G2DLys self-assembled at marginally lower concentrations than C₂₂G2LLys although, given the large error values associated with each measurement, this is not a significant difference. As discussed for the G1 systems, the opposing chiralities would not be expected to influence any parameter, such as CAC, where handedness is unimportant.

The data suggests that these larger G2 molecules assemble, on average, at lower concentrations to their G1 counterparts. The greater number of lysine residues at the surface makes the G2 system significantly larger and bulkier than the G1. Fewer molecules may therefore be required to form each individual micelle, thereby accounting for the reduced CAC. These observations also align with work from the group of Haag which noted that an increase in hydrophilicity can sometimes lead to a decrease in observed CMC values.³⁵⁸

With the self-assembly of C₂₂G2LLys and C₂₂G2DLys evidenced, TEM imaging was carried out in an attempt to characterize the approximate size and morphology of the self-assembled architecture.

5.3.2.2 TEM Images

Transmission electron microscopy (TEM) was used to image samples of C₂₂G2LLys and C₂₂G2DLys both in the absence and presence of heparin. Solutions of C₂₂G2LLys and C₂₂G2DLys were prepared in clean water at concentrations of 125 μM to ensure the binder molecules were present in assembled form. Heparin was introduced at a charge

ratio of 2.25 as, under this concentration regime, both binders exhibited significant interaction with heparin. Once prepared, aliquots of each solution were loaded onto a formvar grid, negatively stained with uranyl acetate and allowed to dry before imaging. The images for C₂₂G2LLys in the absence and presence of heparin are shown in Figure 5.24 and Figure 5.25 respectively, while the equivalent images for C₂₂G2DLys are shown in Figure 5.26 and Figure 5.27 respectively. The observations are discussed below.

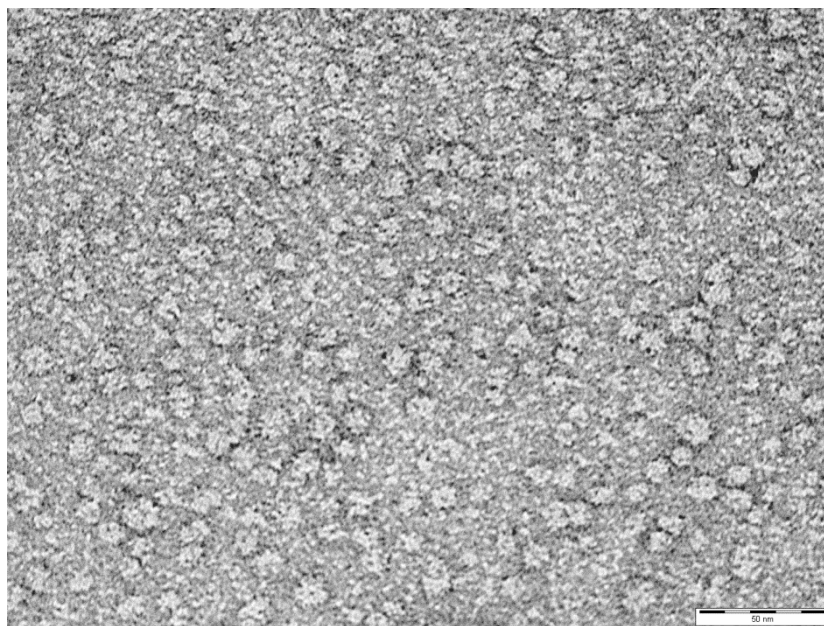


Figure 5.24 – TEM image of 125 μM C₂₂G2LLys (scale bar: 50 nm).

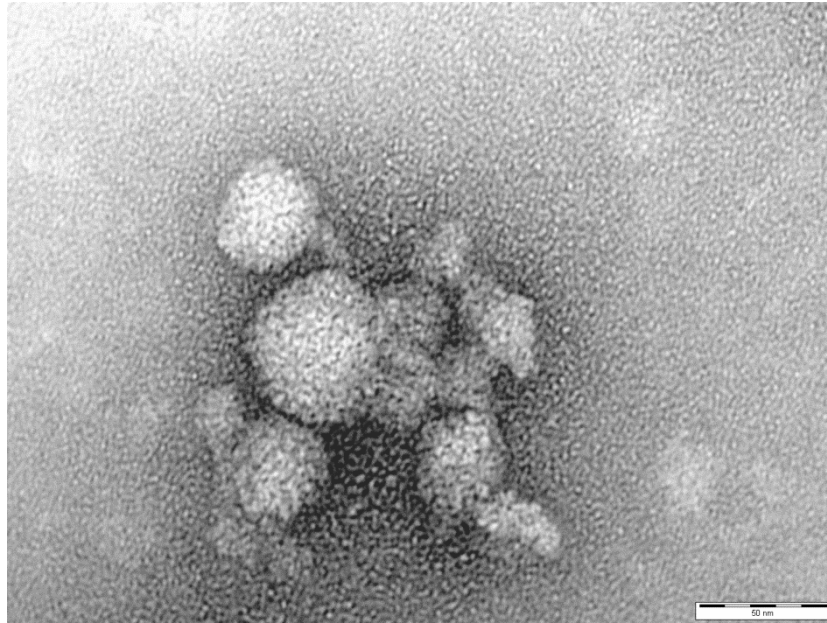


Figure 5.25 – TEM image of 125 μM C₂₂G₂LLys in the presence of heparin (scale bar: 50 nm).

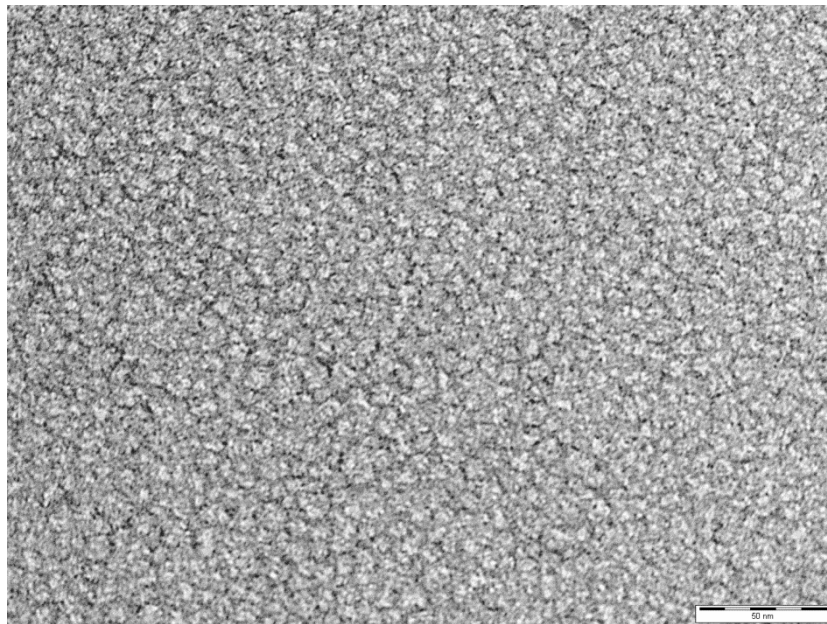


Figure 5.26 – TEM image of 125 μM C₂₂G₂DLys (scale bar: 50 nm).

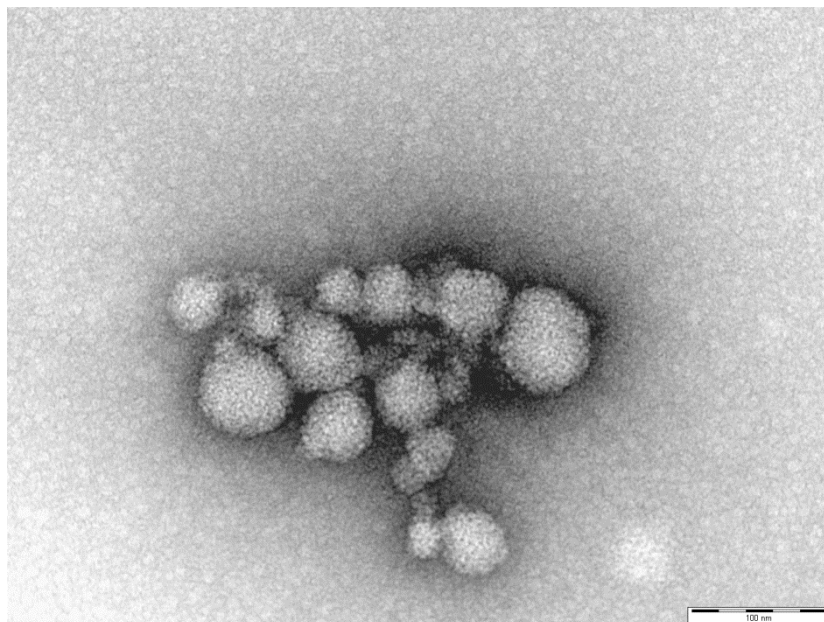


Figure 5.27 – TEM image of 125 μM $\text{C}_{22}\text{G2DLys}$ in the presence of heparin (scale bar: 100 nm).

The TEM images in Figure 5.24 and Figure 5.26 each show roughly spherical objects which decorate the grid in an even manner, suggesting $\text{C}_{22}\text{G2LLys}$ and $\text{C}_{22}\text{G2DLys}$ form micelles. Each micelle appears to be *ca.* 9 – 11 nm in diameter which, logically, is slightly larger than those formed by the smaller G1 systems and equates roughly to double the molecular length of monomer units. In the presence of heparin, the micelles appear to be arranged throughout heparin structure suggesting an integrated nanoscale aggregate, although the micelles appear somewhat reduced in size with apparent diameters of *ca.* ≤ 7 nm. It is worth noting that approximate sizing of the micelles from the TEM images was complicated by the tendency of the samples to deteriorate under the electron beam, which had the effect of ‘blurring’ the images.

With the self-assembly of the system demonstrated and characterized, the compounds were examined for heparin binding ability.

5.3.3 Heparin Binding in Competitive Conditions

The compounds $\text{C}_{22}\text{G2LLys}$ and $\text{C}_{22}\text{G2DLys}$ were tested for their ability to bind heparin using the Mallard Blue heparin binding assay carried out in buffer and salt. As before, the data were reported in term of charge efficiency and effective concentration at 50% MalB displacement along with the effective dose of binder required to neutralize 100 IU

of heparin. The data are reported numerically in Table 5.9 with the binding curves shown in Figure 5.28.

Table 5.9 – Heparin binding data for PG2LLys, C₂₂G2LLys and C₂₂G2DLys obtained from MalB assay.

Compound	Heparin Binding		
	EC ₅₀ / μ M	CE ₅₀	Dose / mg
Propyne-G2-L-Lysine	<i>Not achieved - binding too weak</i>		
C ₂₂ -G2-L-Lysine	(15 \pm 3)	(1.07 \pm 0.20)	(0.68 \pm 0.13)
C ₂₂ -G2-D-Lysine	(17 \pm 4)	(1.28 \pm 0.26)	(0.81 \pm 0.17)

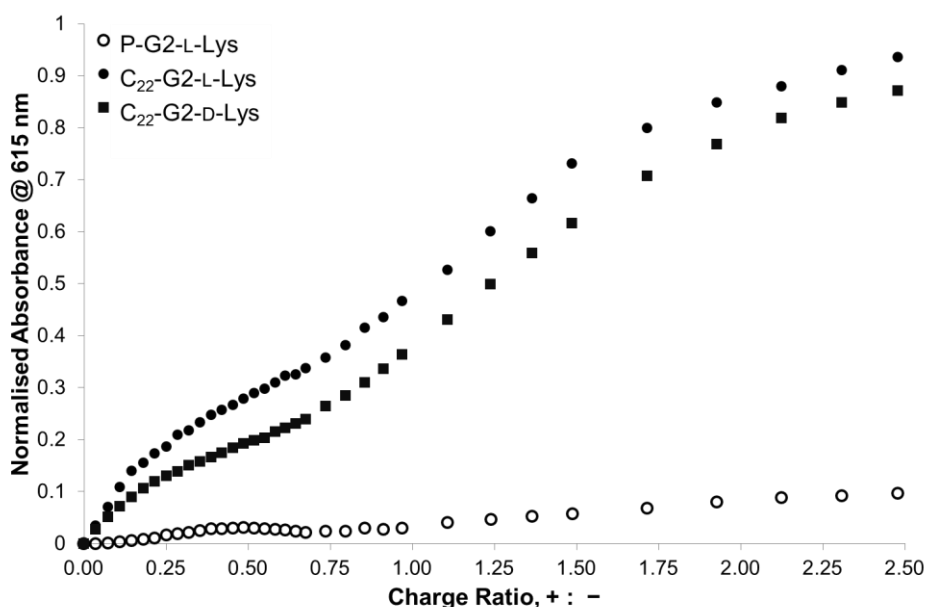


Figure 5.28 – Heparin binding curves for PG2LLys, C₂₂G2LLys and C₂₂G2DLys obtained from MalB assay.

The data again show that in the absence of hydrophobic unit, PG2LLys is unable to displace MalB from heparin to any significant extent even when present in excess. Close comparison of the binding curve for PG2LLys against that for PG1LLys however, shows the additional positive charges on the larger system do increase MalB displacement slightly, but not sufficiently to make PG2LLys a noteworthy heparin binder in its own right.

Following introduction of the hydrophobic unit, the heparin binding ability ‘switches-on’ with 50% MalB readily being displaced by C₂₂G2LLys at a concentration of (15 ± 3) μM and at a charge efficiency of (1.07 ± 0.20). The binding ability is clearly driven by the ability of the system to self-assemble although, according to the data in Table 5.8, C₂₂G2LLys appears to be operating in a self-assembled multivalent manner at a concentration below the apparent CAC. It is possible, as discussed in the previous section, that the presence of heparin in the solution may assist the self-assembly leading both to a reduction in CAC and improvement in binding ability. Comparison against C₂₂G1LLys – CE₅₀ of (1.94 ± 0.38), Table 5.4 – shows the larger G2 system to be almost twice as efficient at marshalling its charges and interacting with the anionic biopolymer. It is possible that this increased binding efficiency indicates a better size-matching of the larger system with heparin. Additionally, it is plausible that the greater flexibility in the larger system aids C₂₂G2LLys in arranging its charges into a more favourable configuration for interaction with heparin.

The D-enantiomer, C₂₂G2DLys, exhibits comparable heparin binding performance to C₂₂G2LLys with a charge efficiency of (1.28 ± 0.26) achieving 50% MalB displacement at a concentration of (17 ± 4) μM. Within error, each of the binding parameters for C₂₂G2LLys and C₂₂G2DLys can be considered the same. This equivalence is supported by the heparin binding curves for each enantiomer in Figure 5.28 which show the same lineshape throughout the titration; in contrast to the G1 heparin binding curves which exhibited a discernable lineshape divergence beyond a charge ratio of *ca.* 0.65.

The lower charge efficiency values for the G2 systems indicate that each individual charge is used more effectively in the larger system. This would seem to suggest that the four amines positioned directly at the chiral centres in C₂₂G2LLys and C₂₂G2DLys are more heavily involved in interacting with heparin than the two equivalent positions in C₂₂G1LLys and C₂₂G1DLys yet, paradoxically, there is minimal difference in heparin binding ability between the G2 enantiomers. It appears that despite ‘more’ chirality being present in the G2 binders, it is less apparent to heparin upon binding. This may suggest that the increased steric crowding at the surface of the dendritic structure masks the subtle difference in chiral expression between C₂₂G2LLys and C₂₂G2DLys. The closer proximity of the binder charges to each other may simply lead heparin to respond to the greater electrostatic attraction, hence accounting for the more efficient binding, without registering any difference in how the ligand array is expressed.

5.3.4 Degradation

5.3.4.1 Nile Red Release Assay

Having characterized the heparin binding ability of C₂₂G2LLys and C₂₂G2DLys, the degradation profile of these larger systems was assessed. In possessing an extra layer of branching, and double the number of surface groups, C₂₂G2LLys and C₂₂G2DLys each have a total of eight ester linkages present within their structures; five more than their G1 counterparts. For consistency, C₂₂G2DLys was selected for testing using the Nile Red release assay. The resulting degradation curve is shown in Figure 5.29.

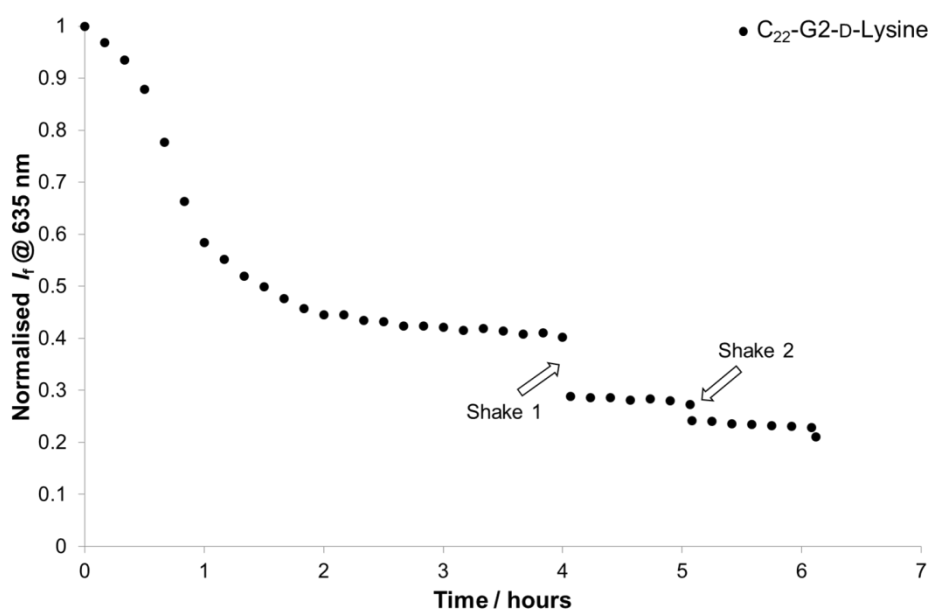


Figure 5.29 – Time resolved degradation curve for C₂₂G2DLys. Discontinuities are indicated where the sample was vigorously shaken to simulate blood-flow shear forces.

The data show that C₂₂G2DLys degrades with a half-life ($t_{1/2}$) of *ca.* 1.4 hours. The lineshape is somewhat sigmoidal in nature suggesting the initial degradation rate upon introduction to solution is relatively slow before accelerating considerably. This initial regime may correspond to the binder molecules being tightly packed into self-assembled nanostructures and it being hard for nucleophilic attack of the ester groups to occur due to their concealment away from the assembly surface. The steepest section of the curve may correspond to a situation where some binder molecules have degraded to an extent, for example through loss of one arm from the dendritic surface. Once partially degraded, it may become easier for a hydrolysis event to occur in which the hydrophobic unit is detached, removing the amphiphilicity and liberating Nile Red into

free solution. The absence of sigmoidal character in the G1 lineshape in Figure 5.12 may also hint at a more complex mechanism for the larger G2 system. This more convoluted pathway may also account for the slightly longer observed $t_{1/2}$ for C₂₂G2DLys compared to C₂₂G1DLys, although this difference may also fall within experimental error as each degradation plot was obtained from a single experimental run.

After the half-life had been observed, the cuvette containing the sample was vigorously shaken to simulate shear forces which would be experienced in a fast-flowing system such as the bloodstream. The two marked discontinuities in Figure 5.29 suggest that agitation may cause a reorganization of the remaining assemblies, during which some of the remaining ester bonds become temporarily more accessible and so are also broken. This assertion would seem to fit the line-shape, which reverts to the slower degradation rate once the remaining assemblies have re-stabilised.

5.3.4.2 Mass Spectrometric Studies

In order to identify the species resulting from the degradation events, mass spectrometry was used to probe a sample before and after 24 hours incubation at 37°C under the same conditions applied previously. Examples spectra along with the species of interest are shown in Figure 5.30.

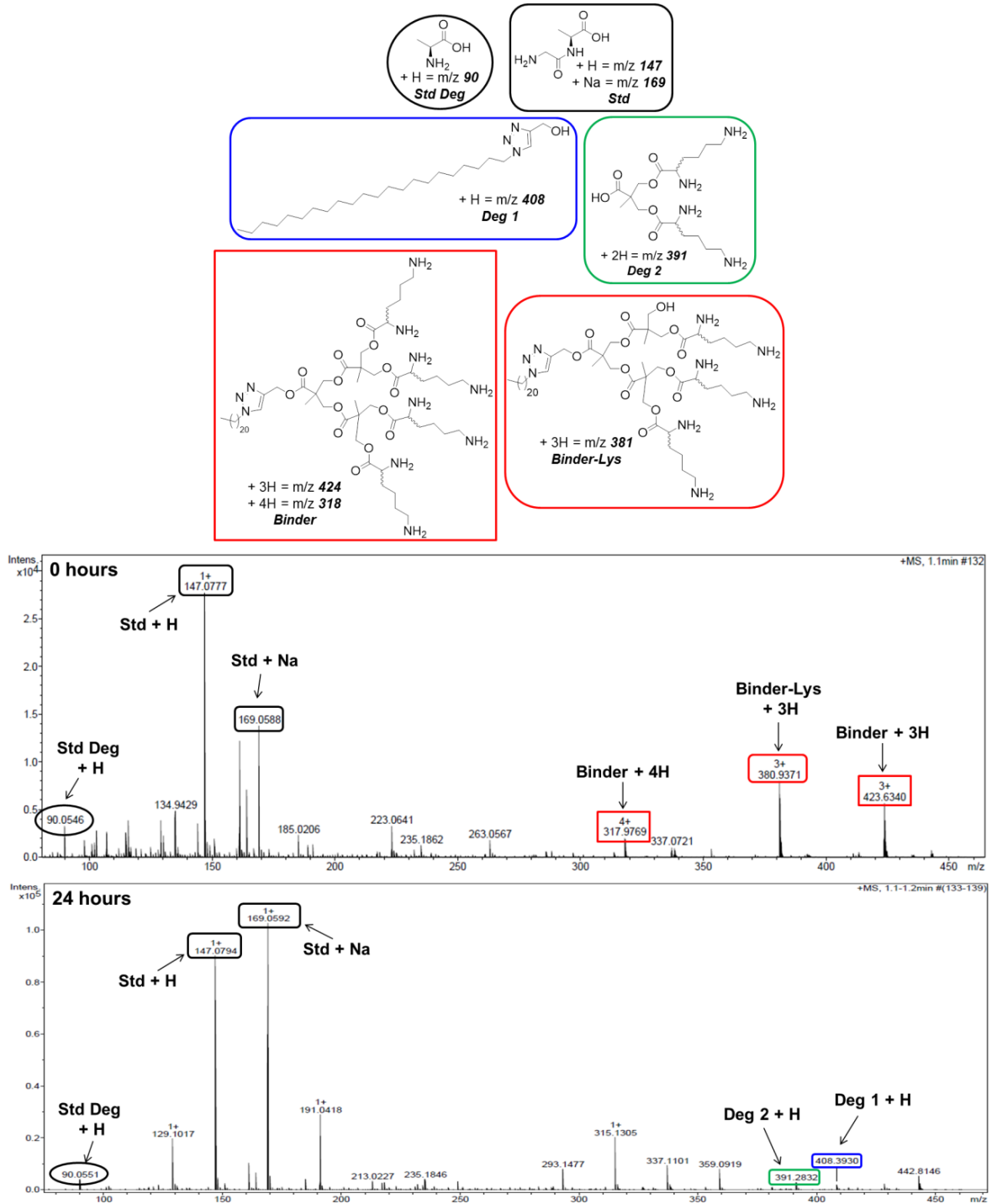


Figure 5.30 – Mass spectrometric degradation assay: observed species (top) after 0 hours (middle) and 24 hours (bottom) incubation at 37°C.

At time zero, the molecular ions associated with C₂₂G2DLys ($m/z = 424 [M]^{3+}$ and $318 [M]^{4+}$) were clearly visible along with that of the same species having lost a lysine residue ($m/z = 381 [M]^{3+}$). This observation of this lattermost species was assigned as a mass spectrometric artefact as no evidence of incomplete lysine functionalization was observed from orthogonal characterization techniques such as NMR. After 24 hours, these molecular ions had disappeared and peaks corresponding to the hydrolysis products of both G1 and G2 linker ester groups (alcohol, $m/z = 408 [M]^{1+}$; carboxylic acid, $m/z = 391 [M]^{1+}$) were now visible, albeit at low relative intensity to the standard. No evidence was seen for the presence of an intact G2-lysine carboxylic acid species despite inspecting higher charge-to-mass ranges, which may suggest that once formed, further degradation of such a species occurs to afford the observed G1-lysine carboxylic acid fragment. Similarly, the relatively low intensity of the observed degradant at m/z 391 appears to suggest that further degradation, for example, through cleavage of the ester groups connecting the lysine moieties to the scaffold occurred. Unfortunately, no direct evidence of these lower mass species was seen. Importantly, however, the mass spectrometric assay did demonstrate that the premise of installing ester groups within the linker unit was valid, because direct evidence relating to cleavage of these bonds was seen.

5.3.5 DNA Binding

The larger SAMul systems C₂₂G2LLys and C₂₂G2DLys were also tested for their ability to bind to DNA in order to probe whether the chiral trends observed previously were evident. The compounds were tested using the ethidium bromide displacement assay and the data are reported numerically in Table 5.10 and graphically in Figure 5.31.

Table 5.10 – DNA binding data from EthBr assay for PG2LLys, C₂₂G2LLys and C₂₂G2DLys.

Compound	DNA Binding	
	EC ₅₀ / μ M	CE ₅₀
Propyne-G2-L-Lysine	<i>Not achieved - binding too weak</i>	
C ₂₂ -G2-L-Lysine	(1.07 \pm 0.15)	(2.15 \pm 0.31)
C ₂₂ -G2-D-Lysine	(1.02 \pm 0.12)	(2.03 \pm 0.25)

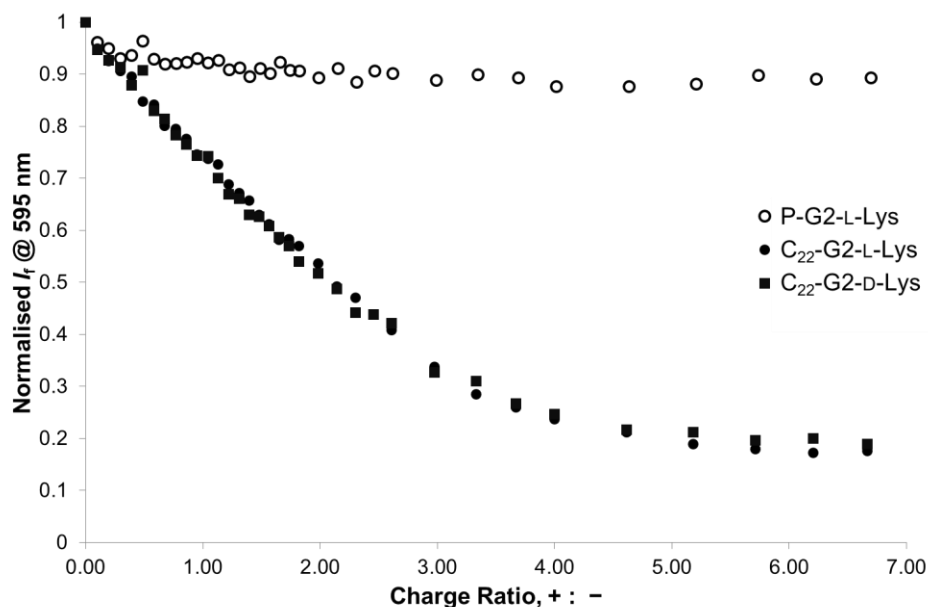


Figure 5.31 – DNA binding curves from EthBr assay for PG1LLys, C₂₂G1LLys and C₂₂G1DLys.

The data show, once again, that in the absence of an aliphatic tail, minimal indicator dye is displaced from DNA. After the introduction of the hydrophobic unit, binding ability significantly increases. In line with their G1 counterparts, the G2 systems bind DNA less efficiently than heparin, presumably as a consequence of the less charge-dense character of the polyanion.

The most noteworthy observation here is that C₂₂G2LLys and C₂₂G2DLys bind DNA with almost identical efficiencies. Indeed, the two binding curves are ostensibly overlaid, suggesting the opposing chirality of each enantiomer has no bearing on DNA binding ability. A possible explanation for this could be that the amine groups attached to the lysine chiral centres may not be directly involved in the interactions with DNA or, alternatively, the steric crowding at the surface of the G2 dendritic structures prevents the differing chiralities being expressed fully. Whilst it is difficult to pinpoint the reasoning, the evidence is consistent: C₂₂G2LLys and C₂₂G2DLys exhibit minimal chiral differences when binding to DNA, or heparin.

Attempts are underway to understand this absence of binding differences between C₂₂G2LLys and C₂₂G2DLys using molecular dynamic modelling approaches in collaboration with Professor Sabrina Pricl at University of Trieste, Italy. Unfortunately the results from this study are not available for inclusion here.

5.4 Conclusions and Future Work

5.4.1 Conclusions

A small family of lysine-containing self-assembling multivalent (SAMul) systems were synthesized and studied for their abilities to interact with heparin under a variety of conditions including in human plasma, and also with DNA. The effects of size, charge and chirality were considered from a binding perspective and the degradation profile of each system was also characterized.

The smaller enantiomeric pair of SAMul binder molecules, C₂₂G1LLys and C₂₂G1DLys, were shown to form micellar aggregates in aqueous solution of *ca.* 7 nm diameter and to be able to bind heparin effectively in the presence of biologically relevant salt concentrations. Interestingly, the system containing D-lysine surface groups was able to marshal its charges more efficiently than the system containing L-lysine surface groups when interacting with heparin. Furthermore, when the polyanionic binding partner was changed to DNA, rather than heparin, this chiral binding preference was shown to be reversed, with the L-binder being the more charge efficient.

Following on from the promising heparin binding results, C₂₂G1DLys was shown to be able to bind heparin in the presence of human serum, although binding was less efficient. This decrease in performance was assigned to disruption of the self-assembled nanosystem by hydrophobic components of serum such as albumins. Despite this performance decrease, C₂₂G1DLys was shown to be largely able to reverse the anti-coagulant effect of heparin in clinically relevant plasma clotting assays.

The degradation of C₂₂G1DLys was demonstrated to occur with a first half-life of *ca.* 1.25 hours, and to be accelerated by shear forces. This degradation time scale would likely be too short to be of clinical relevance due to the constant high velocity flow- and shear-forces experienced in the systemic bloodstream. Nonetheless, the greater number of ester groups compared to the C₂₂G1DAPMA system reported in Chapter 4 clearly accelerated the degradation process.

A larger pair of SAMul binders, C₂₂G2LLys and C₂₂G2DLys, were synthesized and tested for heparin and DNA binding. These systems possessed four lysine surface groups and were able to bind the anionic target molecules in a more charge efficient

manner than their G1 counterpart, presumably owing to the greater charge per self-assembling unit and better size-matching. The micelles formed by these G2 systems were *ca.* 11 nm in diameter. Interestingly, the opposing surface group chiralities were shown to have no influence over binding ability, with C₂₂G2LLys and C₂₂G2DLys exhibiting equivalent heparin and DNA binding performances. It was reasoned that the increased crowding at the surface of the G2-system prevented the subtle difference in ligand spatial arrangement being fully expressed. It was reasoned that in this sense the greater charge density at the binder surfaces, rather than their specific spatial arrangements, dictated the increased binding efficiencies of C₂₂G2LLys and C₂₂G2DLys with heparin and DNA.

The C₂₂G2DLys species was also shown to degrade with a first half-life of *ca.* 1.40 hours, and to be affected by shear forces caused through agitation in the same manner as C₂₂G1DLys.

5.4.2 Future Work

Future work in this area will include investigating the observed chiral preferences between systems containing L-lysine and D-lysine surface groups using molecular dynamic modelling techniques, in collaboration with Professor Sabrina Pricl at University of Trieste. It is hoped that these modelling studies will give an insight into why chiral preferences appear to be reversed when binding DNA as opposed to heparin; and, additionally, why this chiral preference appears to be lost as the size of the binder increases.

In order to understand these differing chiral preferences, it may be interesting to carry out a control study using a straightforward monoamine such as 6-aminohexanoic acid in place of lysine as this would afford binder molecules lacking the primary amine groups attached to the chiral α -carbons. Performance comparison against the lysine-surfaced binders would allow the binding contribution of the α -amines to be quantified. An alternative approach to study this could involve use of a shorter amino acid such as ornithine at the binder surface. The carbon backbone of ornithine is one -CH₂ unit shorter than lysine and so would position the chiral centres slightly closer to the binder group surface without greatly affecting the overall structure. This subtle change may serve to amplify the effects of the chiral centres.

From the perspective of developing a novel heparin SAMul heparin rescue agent, the hydrophobic character of the next generation of binders should be enhanced in order to increase the robustness of assemblies in the presence of hydrophobic serum components. This could be achieved by introducing branching into the alkyl-tail moiety, for example through use of biologically relevant hydrophobes such as dual- or tri-tailed bile acids or cholesterol units. In making these modifications, it may be prudent to reduce the number of ester groups present in the system as connection of the surface groups to the linker unit through ester bonds here promoted degradation to unacceptably fast levels.

6 Hydrophobically-Enhanced Self-Assembling Heparin Binders

6.1 Introduction

Chapter 4 established self-assembled multivalency (SAMul) as an effective approach for developing novel heparin rescue agents, while Chapter 5 demonstrated that employing chiral binding groups at the surface could influence the heparin binding ability of the SAMul systems. One common feature shared by the families of SAMul binder molecules studied in the previous chapters was possession of a single twenty-two carbon atom aliphatic tail to promote self-assembly of the nanoscale heparin binding architectures. Although capable of heparin binding; these aggregates were susceptible to disruption and/or destabilisation by hydrophobic serum components such as albumin proteins. It was postulated that the long alkyl chain making up the hydrophobic unit may have inadvertently been rather optimised for interaction with albumin-type species, and that this therefore promoted disruption.³¹¹ Although this disruption did not normally prevent the SAMul systems from binding heparin in serum, it did impact on the relative effectiveness of binding when compared against measurements made in aqueous buffer. This disruption also manifested itself in other ways, for example by extending the observed clotting time in clinically relevant plasma clotting assays. It was reasoned that an alternative hydrophobic unit might be able to overcome some of this serum disruption and help stabilise the self-assembled nanostructures.

Through its role promoting molecular self-assembly, the hydrophobic unit is also able to influence the morphology of the nanosized aggregates formed.⁴⁵ To this point, all of the SAMul systems studied in this project have formed spherical, or roughly spherical, assemblies as dictated by the geometry of the individual ‘building block’ monomers. This was partly due to their mutual construction from the same ester-containing dendritic linker unit. It was therefore decided to redesign the heparin binding building block such that the monomer unit had a different molecular geometry, which would then in turn be able to generate a different (i.e. non-spherical) self-assembled architecture.

The work reported in previous chapters reported the effects of changing chirality on heparin binding performance and so, in order to probe this further, the amino acid lysine was retained as the heparin binding group to be displayed at the surface of the self-assembled structure. A second amino acid, aspartic acid, was chosen to form the linker unit of the new binding system. The choice of an amino acid within the linker unit made chirality inherent within the entire building block structure, rather than only being present at the terminus. It was hoped that this linear arrangement of amino acids and therefore chirality throughout the monomer structure might amplify the chiral effects previously seen in our earlier SAMul constructs.

Aspartic acid was identified as a suitable linker unit as the two terminal carboxylic acid groups were suitable for functionalisation with hydrophobic groups while the pendant amine group could be furnished with a cationic lysine moiety, through an amide linkage. The linear twelve-carbon alkyl chain of 1-dodecanol was selected as an appropriate hydrophobe owing to its similar, albeit shorter, character to the twenty-two carbon hydrophobic units used previously. Following this design, the two first generation (G1) species $(C_{12})_2\text{LAspLLys}$ and $(C_{12})_2\text{DAspDLys}$, Figure 6.1, were identified as target molecules.

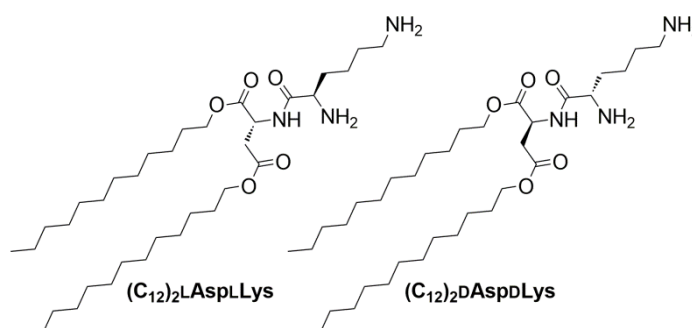


Figure 6.1 – Twin-tailed G1 target molecules $(C_{12})_2\text{LAspLLys}$ and $(C_{12})_2\text{DAspDLys}$.

It was anticipated that these twin-tailed target molecules may self-assemble into non-spherical architectures owing to their differing geometries compared to the previously synthesised systems. According to the packing parameters outlined by Israelachvili and co-workers in 1976, an increase in relative hydrophobicity might be expected to lead to the formation of cylindrical, rather than spherical, assembly structures.⁴⁵ In turn it was reasoned that these structures may have the potential to better ‘shape-match’ the approximately linear polysaccharide heparin chains, which may result in improved

heparin binding over spherical constructs and potentially lead to more promising candidates for development as novel protamine alternatives.

The initial syntheses of the G1 systems in this part of the project, along with the associated heparin and DNA binding studies were undertaken, under my supervision, by final year MChem student Ellis Wilde. Optimisation of the synthetic route to the G1-lysine-containing systems was carried out, also under my supervision, by summer project student Mark Dowsett.

6.2 Generation 1 (G1) Systems

6.2.1 Lysine-containing system (G1)

6.2.1.1 Synthesis of $(C_{12})_2LAspLLys$ and $(C_{12})_2DAspDLys$

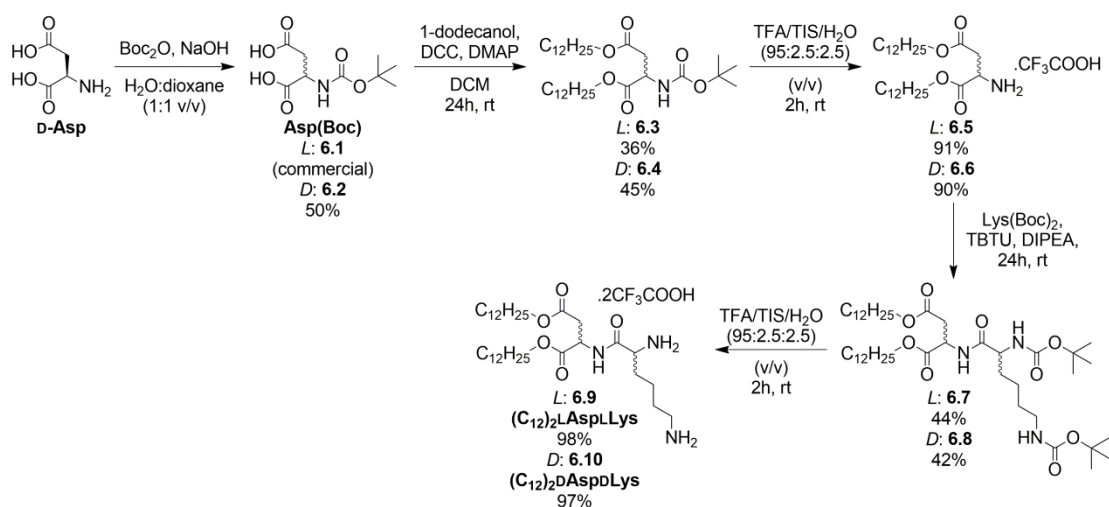
The Asp-Lys binders were synthesised in a step-wise manner from the three molecular components shown in Figure 6.2: the hydrophobic chains of 1-dodecanol, the aspartic acid linker unit, and heparin binding lysine group. For the purposes of synthesis, aspartic acid was first derivatised with the alkyl tails before the lysine group was attached.



Figure 6.2 – The three component pieces of G1 target molecules $(C_{12})_2LAspLLys$ and $(C_{12})_2DAspDLys$.

Initially, L-Asp(Boc) 6.1, a commercially available reagent, was identified as a suitable starting point for synthesis owing to the potential for functionalization of both carboxylic acid groups along with the acid lability of the amine Boc protecting group, Scheme 6.1. This species was firstly functionalised with two molecules of 1-dodecanol in a modestly yielding ester-forming reaction facilitated by DCC and DMAP to afford protected intermediate 6.3. Removal of the Boc protecting group was achieved using trifluoroacetic acid (TFA) conditions to afford intermediate salt 6.5 in an excellent yield. With the aspartic acid amine group now available, this was next coupled with the carboxylic acid of L-Lys(Boc)₂ in a TBTU-mediated peptide coupling reaction to afford,

after purification by silica gel flash column chromatography, the protected final binder 6.7 in reasonable yield. Final subsection of this compound to TFA deprotection conditions once again removed the Boc protecting groups and afforded the final ‘LL’ target molecule $(C_{12})_2\text{LAspLLys}$ 6.9 in a good yield. Synthesis of the ‘DD’ system proceeded in an analogous fashion except at the first stage where the commercial unavailability of D-Asp(Boc) required the reaction of native D-Asp with di-*tert*-butyl-dicarbonate and sodium hydroxide in a water/dioxane mixture to generate D-Asp(Boc) 6.2 for use in the production of $(C_{12})_2\text{DAspDLys}$ 6.10.



Scheme 6.1 – Preparation of G1 target molecules $(C_{12})_2\text{LAspLLys}$ and $(C_{12})_2\text{DAspDLys}$.

A key consideration in the preparation of these target molecules was the retention of chirality. To that end, circular dichroism (CD) spectroscopy was carried out at each stage to interrogate the relative enantiomeric character of the growing systems. As shown in Figure 6.3, throughout the synthesis, CD spectroscopy suggested each system remained of equal and opposite enantiomeric character. Importantly, these data demonstrated that the synthetic steps undertaken do not appear to have scrambled, or in any identifiable way damaged, the chiral information within the systems.

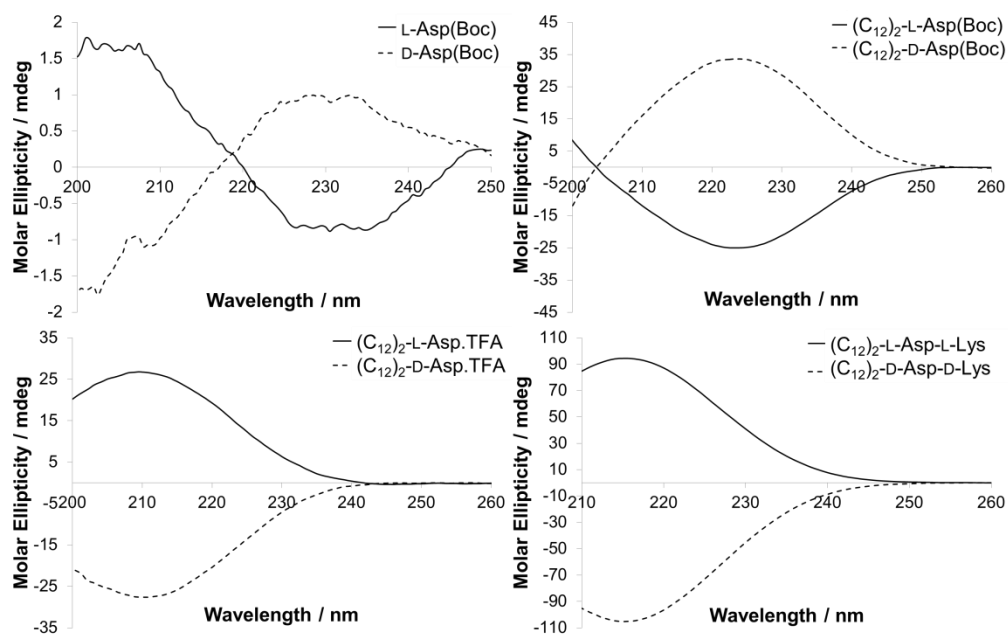


Figure 6.3 – Circular dichroism data at different stages during the preparation of $(C_{12})_2$ LAspLLys (solid lines) and $(C_{12})_2$ DAspDLys (dashed lines) measured at 10 mM in methanol.

6.2.1.2 Self-Assembly Studies

The twin tailed SAMul molecules $(C_{12})_2$ LAspLLys and $(C_{12})_2$ DAspDLys were tested for their ability to self-assemble using the Nile Red encapsulation assay. The data suggested the CAC values for each of these systems were $67 (\pm 10) \mu\text{M}$ for the ‘LL’ analogue and $74 (\pm 5) \mu\text{M}$ for ‘DD’. The encapsulation curves are shown in Figure 6.4.

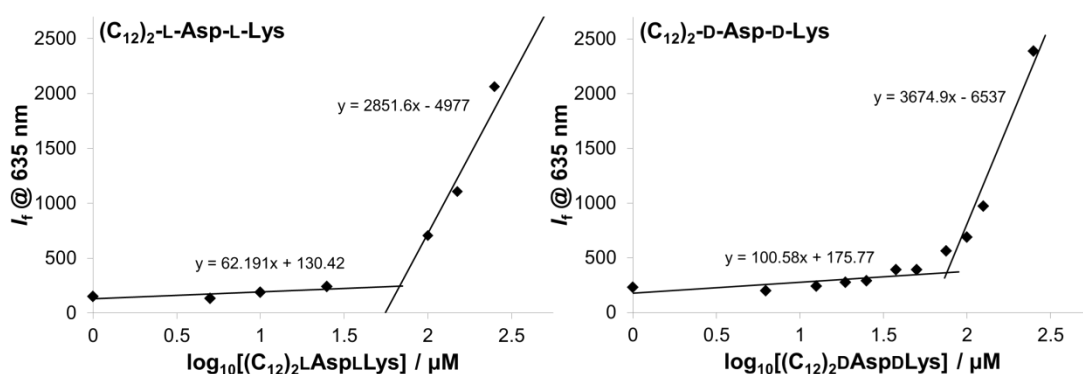


Figure 6.4 – Nile Red encapsulation curve for $(C_{12})_2$ DAspDLys.

The CAC value is significantly larger than for the single-tailed systems reported in previous Chapters. This is an interesting observation as thermodynamically the CAC value might be expected to decrease as the degree of hydrophobic character within the

assembling monomers increases. Such a decrease in CAC would be likely to arise from the larger entropic benefit associated with the liberation of ‘frozen’ water molecules at the interface with the hydrophobic groups, although an increase in CAC may be seen if the difficulty associated with packing the charged surface groups together increases. The CAC values for these twin-tailed systems are around 20 μM higher than for single-tailed analogues such as $\text{C}_{22}\text{G1Lys}$, which appears to suggest that there may be increased difficulty associated with positioning the charge surface groups close together at the assembly surface. This seems particularly likely as qualitative macroscopic observations, such as aqueous solubility, do not corroborate the possibility that each monomer is ‘less’ hydrophobic in relative terms than the single-tailed systems in earlier Chapters. In order to examine whether these structural changes have had an effect on the morphologies of the self-assembled architectures, they were examined by transmission electron microscopy.

6.2.1.3 TEM Images

TEM imaging was carried out on the $(\text{C}_{12})_2\text{DAspDLys}$ system in the absence and presence of heparin in clean water, at a concentration of 100 μM to ensure the compound was present in self-assembled form. Heparin was introduced at a charge ratio (+ : -) of 2, as under this concentration regime, the binder was known to interact well with heparin. Samples were negatively stained with uranyl acetate and allowed to dry on the formvar grid before imaging. The images are shown in Figure 6.5 and Figure 6.6.

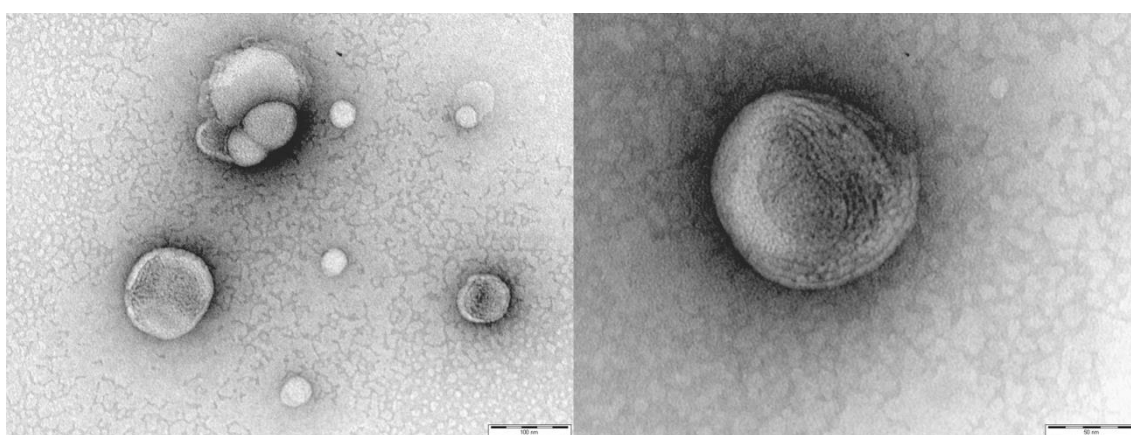


Figure 6.5 – TEM images of 100 μM $(\text{C}_{12})_2\text{DAspDLys}$ (scale bars: 100 nm (left), 50 nm (right)).

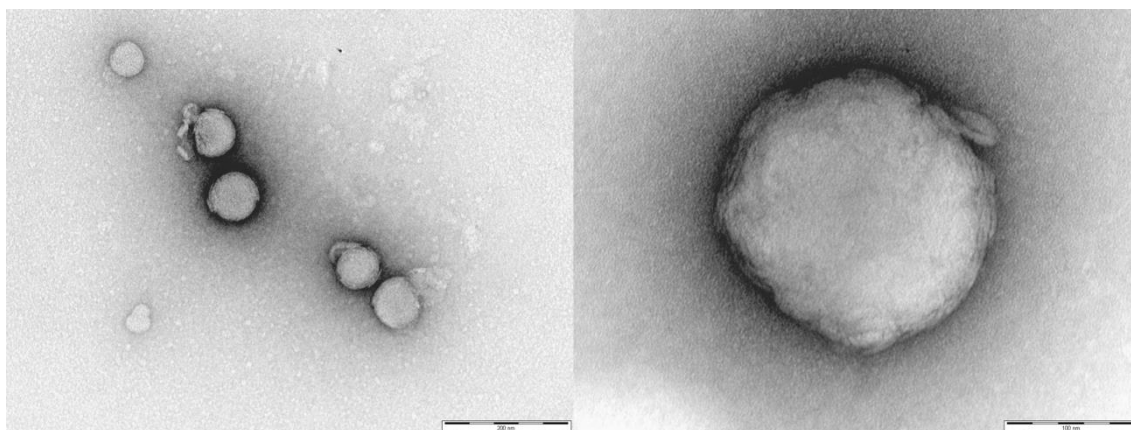


Figure 6.6 – TEM image of 100 μM $(\text{C}_{12})_2\text{DAspDLys}$ in the presence of heparin (scale bars: 200 nm (left), 100 nm (right)).

The TEM images of $(\text{C}_{12})_2\text{DAspDLys}$ alone showed aggregates of different sizes, ranging approximately between 80 – 140 nm in diameter. The surfaces of the aggregates appeared textured, which may suggest the formation of closely packed lamellar aggregates by $(\text{C}_{12})_2\text{DAspDLys}$. Lamellar structures are theoretically predicted when the critical packing parameter takes a value larger than 1; the situation when the overall molecular volume-in-space is composed of slightly more hydrophobic than hydrophilic domains.⁴⁵ This observation suggests that the re-design of the self-assembling system has increased the overall hydrophobicity of the monomer building blocks so significantly that the cylindrical and vesicular-assembly morphologies – corresponding to critical packing parameters between 0.3 and 1 – have been completely bypassed. With the increase in relative hydrophobicity evidenced, the decrease in aqueous solubility of the twin-tailed systems compared to their single-tailed counterparts can be understood. The different (i.e. non-spherical) morphology may also account for the relative increase in CAC values discussed in the previous section as surface groups must be packed closely together in lamellae.

In the presence of heparin, the images showed a variety of textured assemblies of sizes somewhat larger than observed in the absence of polysaccharide. This may suggest that in the presence of heparin we are observing a mixed heparin-binder aggregate in order to maximise binder-heparin interactions, as within a lamellar assembly some of the surface binding groups may be less accessible to heparin. Such rearrangement processes further emphasise the adaptability of a SAMul approach to heparin binding.

6.2.1.4 DLS Measurements

In order to further assess the sizes of the aggregates formed in the absence of heparin, (C₁₂)₂LAspLLys and (C₁₂)₂DAspDLys were probed by dynamic light scattering (DLS) in collaboration with Dr Marcelo Calderon at Freie Universität Berlin. In line with work reported in earlier chapters, each compound was examined in 10 mM Tris HCl both in the absence and presence of 150 mM NaCl. The data are shown in Table 6.1.

Table 6.1 – Dynamic Light Scattering (DLS) data for (C₁₂)₂LAspLLys and (C₁₂)₂DAspDLys in 10 mM Tris HCl in the absence and presence of 150 mM NaCl.

Compound	Average Diameter / nm	
	10 mM Tris HCl only	10 mM Tris HCl, 150 mM NaCl
(C ₁₂) ₂ -L-Asp-L-Lys	(138.4 ± 3.6)	(172.4 ± 6.4)
(C ₁₂) ₂ -D-Asp-D-Lys	(183.4 ± 9.8)	(204.1 ± 11.6)

The DLS data shows that (C₁₂)₂LAspLLys and (C₁₂)₂DAspDLys form relatively large solution-phase aggregates of 138.4 (± 3.6) nm and 183.4 (± 9.82) nm diameters respectively. The solution-phase diameters are somewhat larger than those observed for dried samples by TEM imaging, which further supports the formation of vesicles or lamellar assemblies. It is likely that in the solution phase, some aqueous solvent media becomes encapsulated inside the vesicular assembly causing the apparent aggregate size to ‘swell’. The observed size difference between the LL and DD systems is surprising as the difference in chiral expression between the two systems should not impact on assembly size. The difference may indicate a discrepancy in relative compound purity although other spectroscopic data does not support this. Alternatively, the difference may merely serve to highlight the variability of the aggregates of the aspartic acid-lysine system dependent on preparation. It is also noteworthy that DLS showed the presence of a small proportion of superaggregates measuring larger than 4 μM diameter, which may result from the fusion and/or hierarchical aggregation of individual assembled species. In future it may be desirable to exert more control over aggregate size during preparation, for example, by subjecting samples to ultrafiltration or casting the compound as a thin film prior to solubilisation. Such techniques are often employed by colloid chemists during vesicle formation.

When DLS measurements were repeated in the presence of 150 mM NaCl, both compounds formed larger aggregates. This expansion is analogous to observations made previously for the other SAMul systems; specifically that the electrolytes both ‘shield’ the formed aggregates from one another and enhance the hydrophobic effect.

6.2.1.5 Heparin Binding in Competitive Conditions

With the self-assembling ability of $(C_{12})_2LAspLLys$ and $(C_{12})_2DAspDLys$ established and characterised, the compounds were examined for their heparin binding ability using the Mallard Blue assay. Each compound was tested under the standard experimental conditions of 25 μ M MalB, 27 μ M heparin, 150 mM NaCl and 10 mM Tris HCl. The heparin binding results are shown numerically in Table 6.2 and the binding curves are shown in Figure 6.7.

Table 6.2 – Heparin binding data for $(C_{12})_2LAspLLys$ and $(C_{12})_2DAspDLys$ obtained from MalB assay in 150 mM NaCl and 10 mM Tris HCl.

Compound	Heparin Binding		
	EC ₅₀ / μ M	CE ₅₀	Dose / mg per 100IU
L-LysOMe	<i>No binding observed</i>		
$(C_{12})_2$ -L-Asp-L-Lys	(59.9 \pm 11.3)	(1.11 \pm 0.21)	(1.43 \pm 0.27)
$(C_{12})_2$ -D-Asp-D-Lys	(52.2 \pm 0.3)	(0.97 \pm 0.01)	(1.25 \pm 0.01)

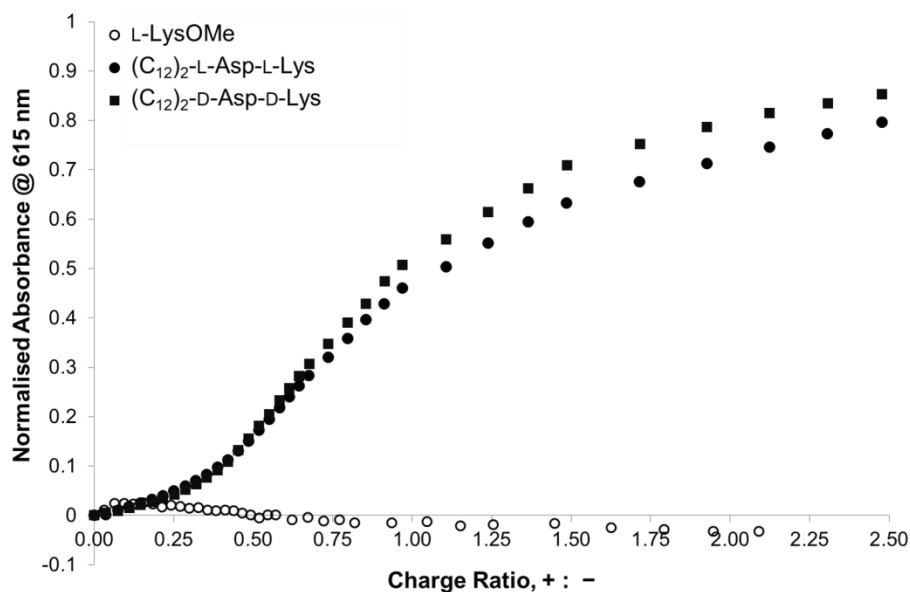


Figure 6.7 – Heparin binding curves for (C₁₂)₂LAspLLys and (C₁₂)₂DAspDLys obtained from MalB assay in 150 mM NaCl and 10 mM Tris HCl.

The heparin binding data suggest that there is little difference in heparin binding charge efficiency (CE₅₀) between (C₁₂)₂LAspLLys and (C₁₂)₂DAspDLys, with both compounds requiring around one cationic charge per anionic heparin charge to displace 50% MalB into solution. This efficiency is comparable with the performance of C₂₂G1DLys in Chapter 5 although the (C₁₂)₂AspLys system achieves the same effect with less charge per monomer (2+ vs 4+). The effective concentrations of (C₁₂)₂LAspLLys and (C₁₂)₂DAspDLys at 50% MalB displacement are 59.9 (± 11.3) μM and 52.2 (± 0.3) μM respectively; values which are slightly below the calculated CACs. This trend matches observations in earlier Chapters and may support the postulation that heparin serves to artificially lower the CAC through multivalently ‘templating’ the assembly process.

In order to study the effect of self-assembly on this system, a commercial L-lysine methyl ester (L-LysOMe) was tested using the MalB heparin binding assay. This amino acid, which represents just the surface group of the self-assembling monomers, was completely unable to displace MalB from heparin. The appearance of some of the normalised absorbance values slightly below zero suggests not only that individual lysine residues are ineffective binders but also that at higher concentrations they may also interfere with the buffering of the system, impacting upon the spectrophotometric properties of MalB. Despite this, the evidence clearly indicates the heparin binding ability of (C₁₂)₂LAspLLys is primarily conferred by a SAMul process.

The relatively similarity in heparin binding abilities of $(C_{12})_2\text{LAspLLys}$ and $(C_{12})_2\text{DAspDLys}$ contrasts with the differences observed for the $C_{22}\text{G1Lys}$ structures in Chapter 5. Structurally, there are several important differences between the two enantiomeric pairs which may account for the absence of chiral binding preferences in the aspartic acid-lysine systems. In particular, although the families both contain the same number of chiral centres per molecule (two), within the new aspartic acid-lysine systems they are arranged in a linear manner along the molecule rather than being present only at the surface. This arrangement results in the chiral centres of $(C_{12})_2\text{AspLys}$ being located more closely to the hydrophobic unit, which may serve to suppress the chiral expression of the system thereby restricting differentiability of the enantiomeric molecules. As shown in Figure 6.8, this contrasts against $C_{22}\text{G1Lys}$, in which the achiral linker unit enforces a distance between the ‘frozen’ hydrophobic micellar interior and the chiral binding groups at the surface.

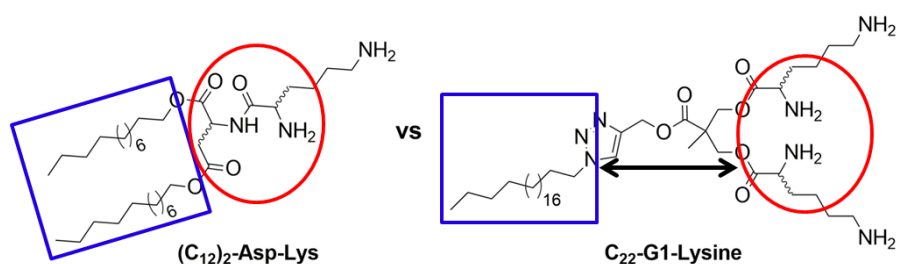


Figure 6.8 – Comparison of the relative proximity of the hydrophobic units (blue squares) and chiral region (red circles) of $(C_{12})_2\text{AspLys}$ and $C_{22}\text{G1Lys}$ systems.

Additionally, the lamellar nature of the $(C_{12})_2\text{AspLys}$ assemblies may also contribute to the suppression of chiral binding differences as this architecture dictates that the surface groups are packed very closely together.

6.2.1.6 Heparin Binding in Clinically Relevant Conditions

In order to probe the robustness of the assemblies in the presence of human serum, $(C_{12})_2\text{DAspDLys}$ was tested for heparin binding ability using the MalB assay with heparin delivered in 100% serum. The results are shown in Table 6.3.

Table 6.3 – Heparin binding data for (C₁₂)₂DAspDLys with heparin delivered in 100% human serum.

Assay Conditions	Heparin Binding: (C ₁₂) ₂ -D-Asp-D-Lys		
	EC ₅₀ / μM	CE ₅₀	Dose / mg per 100IU
Salt and Buffer	(52.2 ± 0.3)	(0.97 ± 0.01)	(1.25 ± 0.01)
Heparin in 10% Human Serum	(57.0 ± 6.7)	(1.06 ± 0.12)	(1.42 ± 0.17)
Heparin in 100% Human Serum	(50.5 ± 8.8)	(0.93 ± 0.16)	(1.25 ± 0.22)

The data suggests that in the presence of human serum, the heparin binding performance of (C₁₂)₂DAspDLys remains, within error, approximately the same as in the absence of serum. Interestingly, the percentage of serum present did not impact of the degree of binding observed. This may suggest that the lamellar assemblies formed are substantially more robust in the presence of hydrophobic serum and albumin proteins than the spherical aggregates formed by our previous SAMul systems. Alternatively, if the aggregates rearrange to incorporate heparin into their assemblies as hinted at by the TEM images, the apparent lack of serum disruption may suggest interactions between the binder and heparin are preferable to interactions between the binder and serum components. It may also be possible that the bilayer-character of the vesicle/lamellar walls remains intact during any rearrangement/heparin encapsulation event. If this were the case, the tightly packed nature of the monomer units which make up the bilayer may prevent serum components from gaining access to the ‘frozen’ hydrophobic interior of such a bilayer to cause disruption.

It is worth emphasising that the maintenance of heparin binding performance by (C₁₂)₂DAspDLys is noteworthy as this ligand array is held together entirely by non-covalent interactions. When compared against our earlier SAMul systems, this performance is most impressive, and is even superior to the covalent protamine structure which was somewhat affected by serum/albumin proteins. The retention of performance by (C₁₂)₂DAspDLys has so far only been matched by the larger covalent PAMAM-G2.

6.2.1.7 Plasma Clotting Assays

Having retained heparin binding performance in human serum, (C₁₂)₂DAspDLys was tested in both the prothrombin (PT) and activated partial thromboplastin (aPTT) plasma

clotting assays in order to assess the potential for heparin neutralisation in clinically relevant samples. These experiments were carried out in the laboratory of Professor Jeremy Turnbull at University of Liverpool, UK. No reversal of anticoagulation was observed, Table 6.4, although this may be due to solubility problems experienced during the preparation of the stock solutions. These issues may have resulted in the concentration of test compound being below the intended 1.25 mg/100IU dosed into the assay. It is thought that if the protocol was modified to avoid the preparation of a concentrated stock solution, the observed performance may improve.

Table 6.4 – Plasma clotting data for $(C_{12})_2DAspDLys$ from PT and aPTT assays.

Compound	Clotting Time / s	
	aPTT Assay	PT Assay
None	(35.7 ± 0.7)	(12.8 ± 0.8)
Heparin only	no clot	no clot
$(C_{12})_2\text{-D-Asp-D-Lys}$	no clot	no clot

6.2.1.8 DNA Binding

Given the absence of chiral preference between $(C_{12})_2LAspLLys$ and $(C_{12})_2DAspDLys$ when binding to heparin, the compounds were tested for their abilities to bind DNA. The compounds were tested using the Ethidium Bromide (EthBr) displacement assay employed in Chapter 5, using the same conditions of 5.07 μM EthBr, 4 μM DNA (with respect to each base) in SHE buffer (2 mM HEPES, 0.05 mM EDTA and 150 mM NaCl) at pH 7.4. The results are shown numerically in Table 6.5 while the binding curves are shown in Figure 6.9.

Table 6.5 – DNA binding data for $(C_{12})_2LAspLLys$ and $(C_{12})_2DAspDLys$ obtained in EthBr displacement assay.

Compound	DNA Binding	
	$EC_{50} / \mu\text{M}$	CE_{50}
$(C_{12})_2\text{-L-Asp-L-Lys}$	(3.11 ± 0.07)	(1.55 ± 0.04)
$(C_{12})_2\text{-D-Asp-D-Lys}$	(8.97 ± 0.32)	(4.39 ± 0.16)

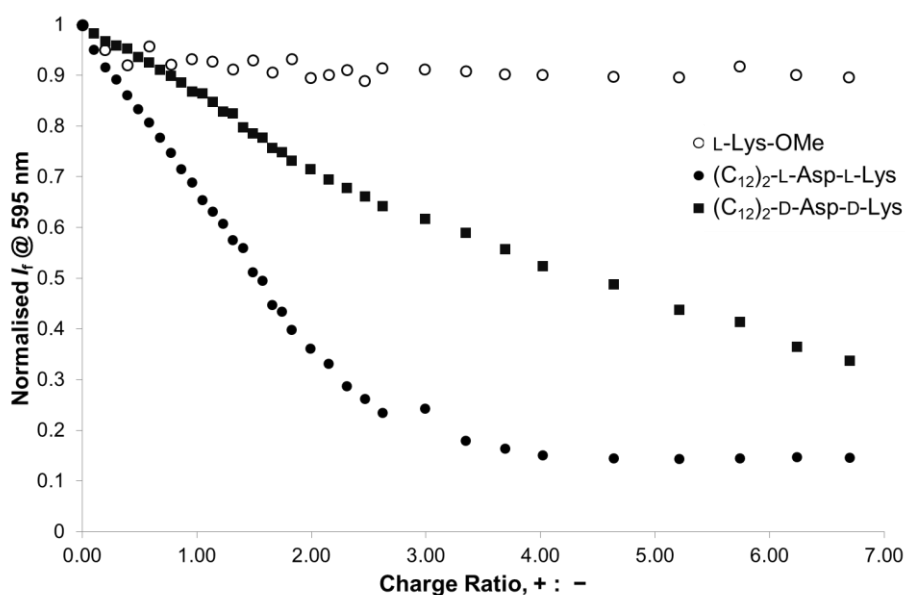


Figure 6.9 – DNA binding curves for $(C_{12})_2$ LAspLLys and $(C_{12})_2$ DAspDLys obtained from EthBr displacement assay.

Significantly, the data shows the enantiomeric systems bound DNA with very different charge efficiencies. The L-system employed its positive charges much more effectively than the D-system, as emphasised by relative CE_{50} values of 1.55 (± 0.04) and 4.39 (± 0.16) respectively. This performance difference is also reflected in the effective concentration at the same point, with $(C_{12})_2$ DAspDLys requiring over double the amount of binder as $(C_{12})_2$ LAspLLys. The EC_{50} values of 3.11 (± 0.07) and 8.97 (± 0.32) suggest the twin-tailed SAMul systems are operating below their CAC values although, as discussed in previous Chapters, the presence of DNA may be serving to artificially lower the assembly concentration of the binders, allowing multivalent binding to occur during this assay concentration range. The non-assembling control molecule L-Lys-OMe was unable to displace EthBr to any significant extent during the assay suggesting DNA binding is a SAMul-driven process.

These chiral binding preferences are interesting on several levels. Firstly, the observation of a performance difference between the systems for DNA binding where none was observed for heparin binding suggests DNA is more acutely sensitive to the spatial arrangement of binding ligands. Heparin is a more charge-dense polyanion than DNA and these data may suggest heparin is more promiscuous; being less sensitive to spatial arrangement and/or in-space complementarity of its binding partner. The second interesting feature of the DNA data is the relative inefficiency with which the binder

molecules, particularly the D-system, are using their individual charges. Such large values – 1.55 (\pm 0.04) for LL and 4.39 (\pm 0.16) for DD – may suggest that only one of the two cationic charges per binder molecule interacts directly with DNA. If this is the case, it is arguably more surprising that such profound chiral difference was observed.

6.2.2 Ornithine-containing systems

Given the interesting chiral preferences observed for the aspartic acid-lysine SAMul systems, a family of related molecules were designed and synthesised. The new systems contained an ornithine residue at the binder surface in place of the lysine group, Figure 6.10. Ornithine is structurally related to lysine, with the two species differing only in one $-\text{CH}_2$ group within the side-chain. The shortening of the alkyl chain should serve to marginally increase the charge-density of the resulting binders, and was hoped to increase heparin (or DNA) binding ability. Additionally, shortening the chain positioned the outermost chiral centre closer to the extremity of the binder, and it was anticipated that this may amplify any chiral differences exhibited upon binding with anionic partners.

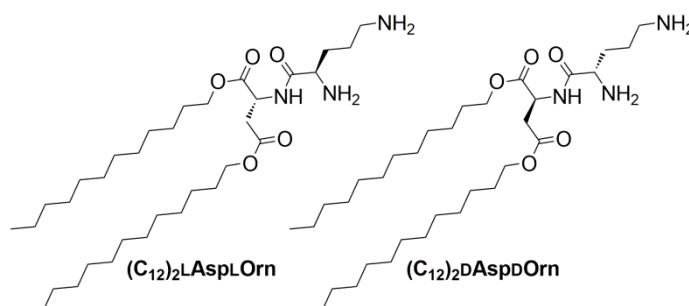
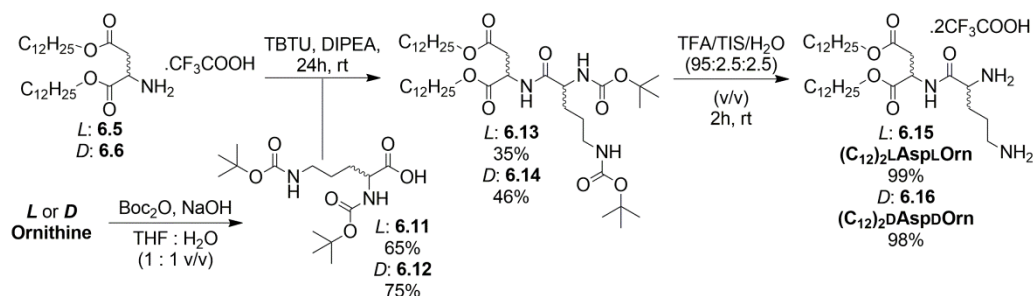


Figure 6.10 – Ornithine-containing twin-tailed target molecules $(\text{C}_{12})_2\text{LAspLOrn}$ and $(\text{C}_{12})_2\text{DAspDOrn}$.

6.2.2.1 Synthesis of $(\text{C}_{12})_2\text{LAspLOrn}$ and $(\text{C}_{12})_2\text{DAspDOrn}$

$(\text{C}_{12})_2\text{LAspLOrn}$ and $(\text{C}_{12})_2\text{DAspDOrn}$ were synthesised in an analogous strategy to their lysine-containing counterparts, as shown in Scheme 6.2. Specifically, ornithine was Boc-protected using di-*tert*-butyl-dicarbonate and sodium hydroxide in dioxane to produce 6.11 and 6.12 in a moderate yield, before the carboxylic acid was coupled to the corresponding alkylated aspartic acid moiety 6.5 or 6.6. The resulting protected target molecules 6.13 or 6.14 were obtained in a modest yield, after purification by silica gel flash column chromatography. Removal of the remaining protecting groups

using trifluoroacetic acid deprotection conditions proceeded in a near-quantitative yield to afford the target molecules $(C_{12})_2\text{LAspLOrn}$ 6.15 and $(C_{12})_2\text{DAspDOrn}$ 6.16.



Scheme 6.2 – Preparation of modified twin-tailed SAMul systems $(C_{12})_2\text{LAspLOrn}$ and $(C_{12})_2\text{DAspDOrn}$.

Once synthesised, the compounds were examined by circular dichroism spectroscopy to ensure that the chirality had been retained during synthesis. As shown in Figure 6.11, the molar ellipticity traces demonstrated the equal and opposite enantiomeric character of the two target molecules.

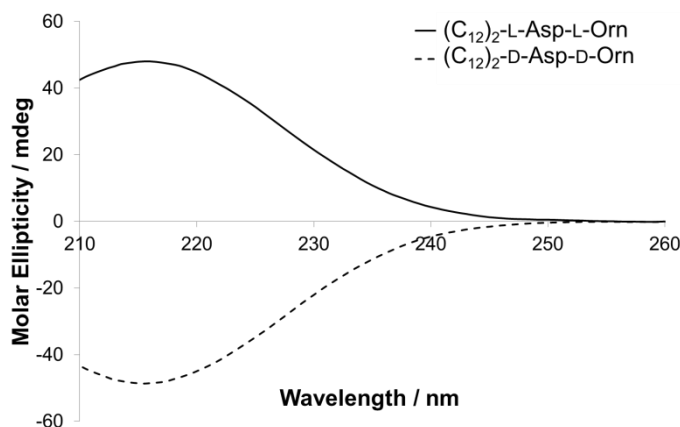


Figure 6.11 – Circular dichroism spectra for $(C_{12})_2\text{LAspLOrn}$ and $(C_{12})_2\text{DAspDOrn}$.

6.2.2.2 Self-Assembly Studies

The self-assembling ability of the ornithine-containing twin-tailed systems was tested using the Nile Red encapsulation assay. The critical aggregation concentration was found to be $30 (\pm 5) \mu\text{M}$ for $(C_{12})_2\text{LAspLOrn}$ and $44 (\pm 8) \mu\text{M}$ for $(C_{12})_2\text{DAspDOrn}$. The Nile red encapsulation curves are shown in Figure 6.12.

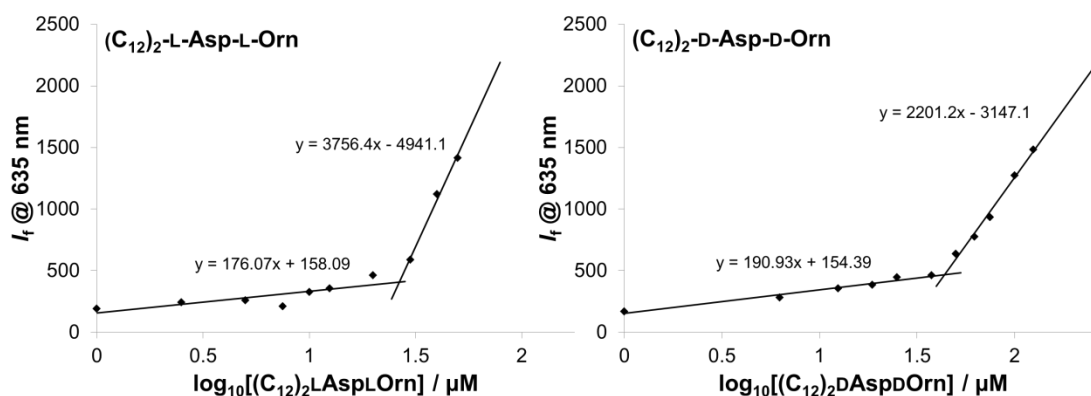


Figure 6.12 – Nile Red encapsulation data for $(C_{12})_2\text{LAspLOrn}$ and $(C_{12})_2\text{DAspDOrn}$.

The ornithine-containing derivative self-assembled at a lower concentration than its lysine-containing counterpart. This may be a reflection of the small difference in hydrophobicity between the two systems. Nonetheless, with the self-assembling ability of the twin-tailed aspartic acid-ornithine system demonstrated, TEM imaging was employed to observe the morphology of the assemblies formed.

6.2.2.3 TEM Imaging

The compounds $(C_{12})_2\text{LAspLOrn}$ and $(C_{12})_2\text{DAspDOrn}$ were imaged both in the absence and presence of heparin on a formvar grid following negative staining with uranyl acetate and drying. Heparin was introduced into the samples at a charge ratio (+ : -) of 2.5 as, under this regime, the binders were known to interact favourably with heparin. The images are shown below.

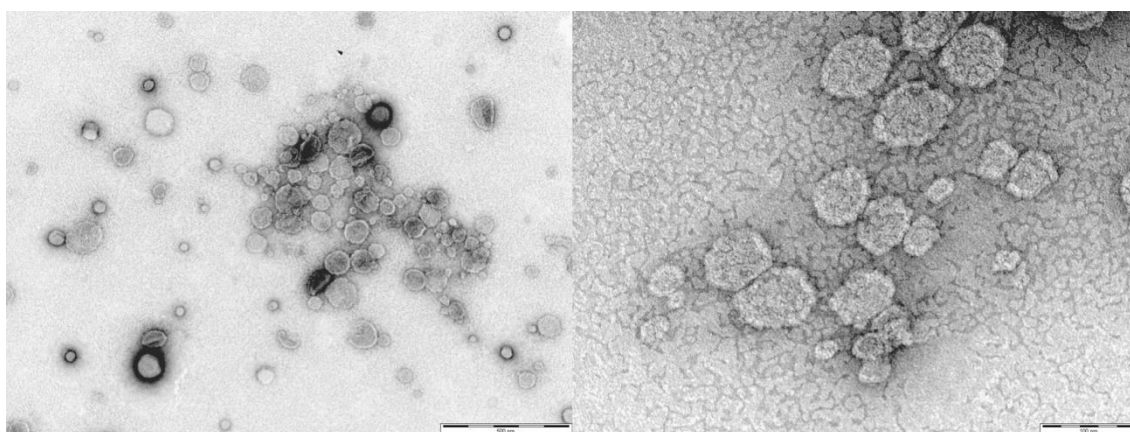


Figure 6.13 – TEM images of 100 μM $(C_{12})_2\text{LAspLOrn}$ (scale bars: 500 nm (left), 100 nm (right)).

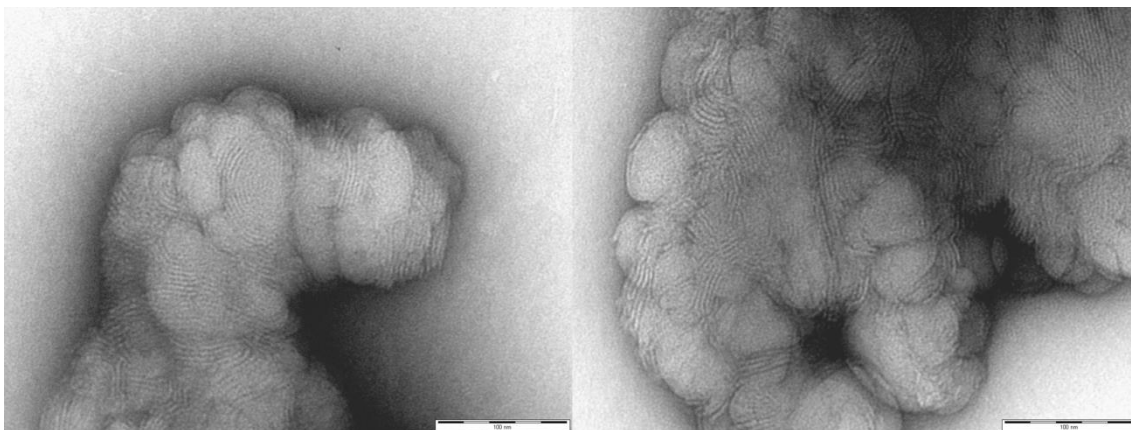


Figure 6.14 – TEM images of 100 μM $(C_{12})_2LAspLOrn$ in the presence of heparin (scale bars: 100 nm (both images)).

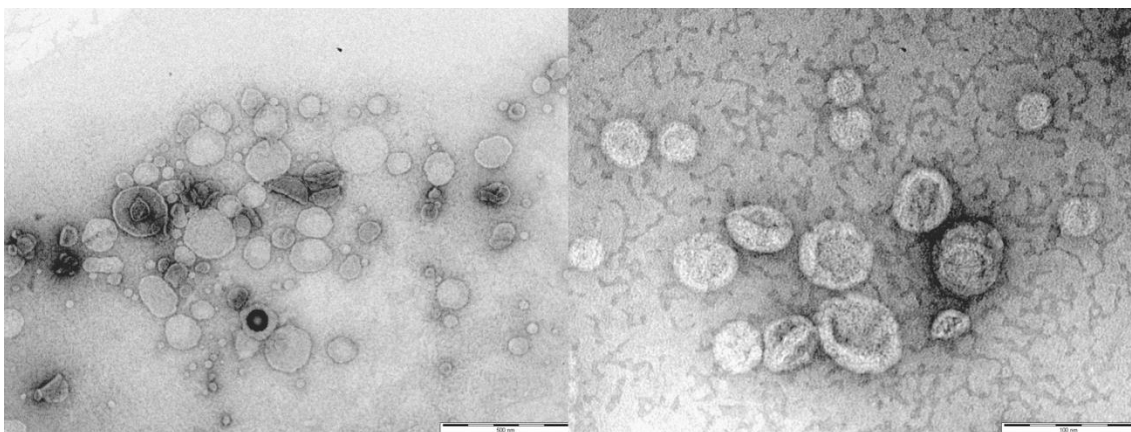


Figure 6.15 – TEM images of 100 μM $(C_{12})_2LAspLOrn$ (scale bars: 500 nm (left), 100 nm (right)).

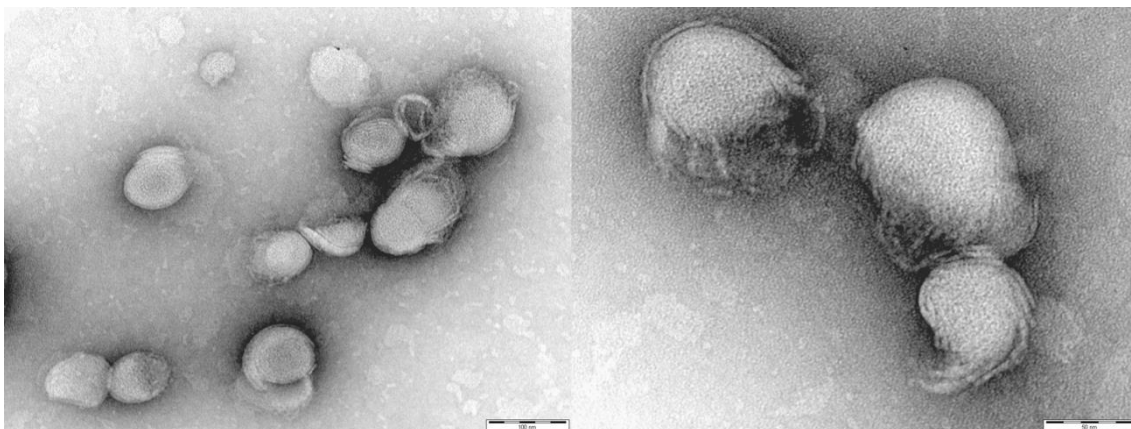


Figure 6.16 – TEM image of 100 μM $(C_{12})_2DAspDOrn$ in the presence of heparin (scale bar: 100 nm (left), 50 nm (right)).

The TEM images show the aspartic acid-ornithine structures form aggregates of differing sizes between *ca.* 20 – 100 nm diameters in a similar manner to the lysine-containing analogues. In the absence of heparin, the images are suggestive of vesicular or lamellar assemblies. The images also appear to show some evidence of collapsed vesicles and smaller assemblies appearing ‘inside’ larger structures, which is typical for lamellar structures, although this could simply be a drying effect. In the presence of heparin, the textured appearance and variety of aggregate sizes again appears indicative of mixed binder-heparin aggregates. The difference in appearance of the species observed in the absence and presence of heparin for the $(C_{12})_2\text{AspOrn}$ systems seems much greater than for the $(C_{12})_2\text{AspLys}$ systems.

6.2.2.4 Heparin Binding in Competitive Conditions

The ornithine-containing systems were tested for their heparin binding ability using the Mallard Blue assay in the presence of buffer and salt. The data are shown numerically in Table 6.6 with the binding curves in Figure 6.17.

Table 6.6 – Heparin binding data for $(C_{12})_2\text{LAspLOrn}$ and $(C_{12})_2\text{DAspDOrn}$ obtained from MalB assay.

Compound	Heparin Binding		
	$EC_{50} / \mu\text{M}$	CE_{50}	Dose / mg per 100IU
$(C_{12})_2\text{-L-Asp-L-Orn}$	(135 ± 5)	(2.50 ± 0.09)	(3.29 ± 0.12)
$(C_{12})_2\text{-D-Asp-D-Orn}$	(125 ± 9)	(2.35 ± 0.17)	(3.09 ± 0.22)

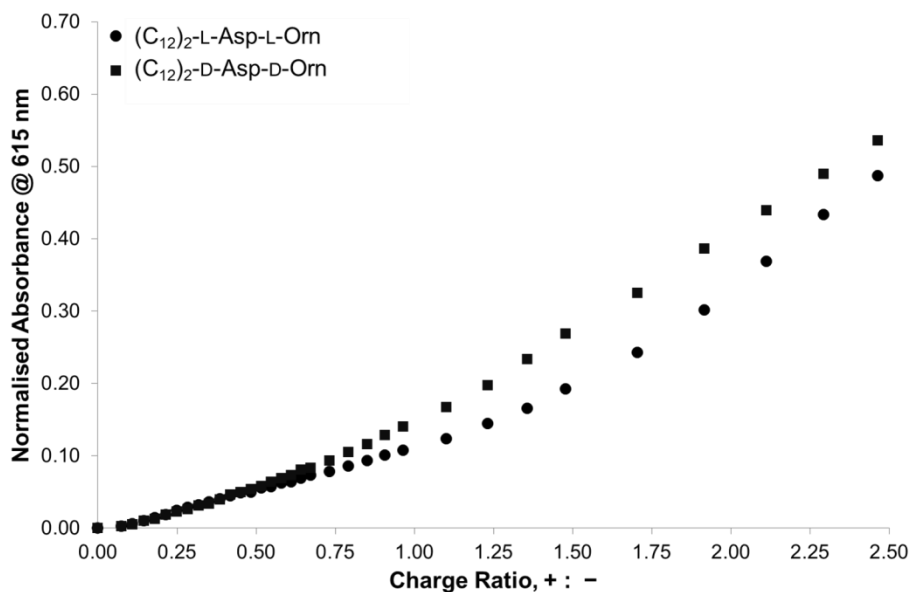


Figure 6.17 – Heparin binding curves for $(C_{12})_2LAspLOrn$ and $(C_{12})_2DAspDOrn$ obtained from MalB assay.

The data show that a concentration of ornithine-containing monomer in excess of 125 μM was required to displace 50% MalB from heparin. The CE_{50} values of 2.50 (± 0.09) for LL and 2.35 (± 0.17) for DD confirm this rather inefficient heparin binding. Indeed, counter-intuitively, despite being marginally more charge dense than their lysine-containing counterparts, the $(C_{12})_2AspOrn$ systems exhibit inferior heparin binding efficiencies. Clearly, this is another example of charge density not being the only factor controlling binding ability.

Additionally, positioning the chiral centres closer to the binder extremity did not enhance the ability of heparin to discriminate between the enantiomeric systems. To some extent however, this absence of discrimination may be influenced by the inefficiency of binding and failure of the amines closest to the chiral centres to interact with heparin.

6.2.2.5 Heparin Binding in Clinically Relevant Conditions

Although less efficiently than the lysine-containing systems, $(C_{12})_2LAspLOrn$ and $(C_{12})_2DAspDOrn$ both successfully displaced MalB from heparin in the presence of competitive electrolytes. Next, the robustness of the heparin binding interactions was challenged by subjecting $(C_{12})_2DAspDOrn$ to the MalB assay with heparin delivered in

100% human serum. For consistency with our earlier studies, the DD-system was examined. The data are shown in Table 6.7.

Table 6.7 – Heparin binding data for $(C_{12})_2DAspDOrn$ with heparin delivered in 100% human serum.

Assay Conditions	Heparin Binding: $(C_{12})_2D-Asp-D-Orn$		
	$EC_{50} / \mu M$	CE_{50}	Dose / mg per 100IU
Salt and Buffer	(127 ± 9)	(2.35 ± 0.17)	(3.09 ± 0.22)
Heparin in 100% Human Serum	(121 ± 7)	(2.23 ± 0.12)	(2.94 ± 0.16)

The data show that $(C_{12})_2DAspDOrn$ fully maintained heparin binding performance in the presence of human serum. This result further supports the earlier observations that the assemblies formed by the twin-tailed systems are robust enough to maintain effective heparin binding interactions even in the presence of serum and its many hydrophobic components.

6.2.2.6 DNA Binding

The ornithine-containing systems were also tested for their ability to bind DNA using the ethidium bromide assay under the same conditions previously employed. The data are presented numerically in Table 6.8 along with the binding curves in Figure 6.18.

Table 6.8 – DNA binding data for $(C_{12})_2LAspLOrn$ and $(C_{12})_2DAspDOrn$ obtained from EthBr assay.

Compound	DNA Binding	
	$EC_{50} / \mu M$	CE_{50}
$(C_{12})_2L-Asp-L-Orn$	(3.24 ± 0.19)	(1.61 ± 0.10)
$(C_{12})_2D-Asp-D-Orn$	(5.89 ± 0.39)	(2.93 ± 0.19)

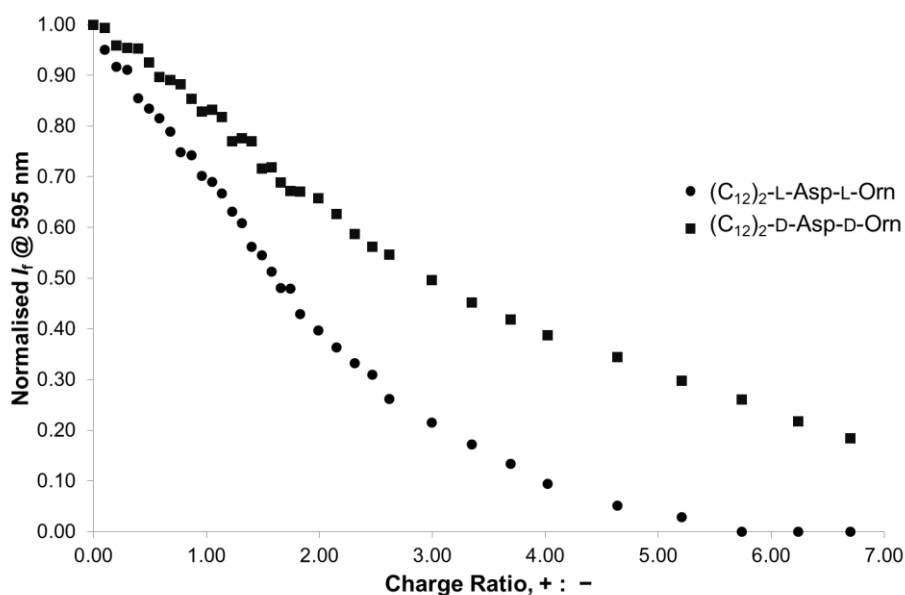


Figure 6.18 – DNA binding curves for $(C_{12})_2LAspLOrn$ and $(C_{12})_2DAspDOrn$ obtained from EthBr assay.

The DNA data are interesting as the ornithine-containing binders were able to displace 50% EthBr at comparable concentrations to their lysine-containing counterparts. In terms of charge efficiency (CE_{50}), the DD-ornithine-system outperformed the DD-lysine-system while the LL-ornithine system was inferior to its LL-lysine counterpart. This observation contrasts somewhat with the heparin binding data, where both lysine-containing systems were significantly more charge efficient than the ornithine-derivatives. This hints, once again, at fundamental binding differences for heparin and DNA. Further differences between the polyanion preferences were observed when considering the relative performance of $(C_{12})_2LAspLOrn$ and $(C_{12})_2DAspDOrn$. With DNA as the binding target, the LL-system was clearly a superior binder, requiring only 60% as much charge as the DD-system ($1.61 (\pm 0.10)$ vs $2.93 (\pm 0.19)$) to effectively displace 50% of EthBr and, although striking, this discrimination is less than observed for the lysine-containing systems ($1.55 (\pm 0.04)$ vs $4.39 (\pm 0.16)$). This LL superiority here correlates with the aspartic acid-lysine data and again points to DNA being more sensitive than heparin to the spatial arrangement of the interaction sites within binding partners.

6.3 Generation 2 (G2) Lysine-containing System

A limitation of the twin-tailed heparin binders presented in the previous section was their poor raw heparin binding ability. It was reasoned that the heparin binding ability of the system might be increased through introduction of a larger, more highly charged, binding group at the assembly surface. This size increase was achieved through the introduction of further lysine residues to afford a ‘G2’ version of the aspartic acid-lysine structure presented in the previous section. An advantage of this approach was that it increased the number of chiral centres per monomer from two to four and it was hoped that this may enhance the ability of heparin to discriminate between the enantiomeric systems. It was also noted that the additional lysine residues may enhance the solubility of the binder monomers. Specifically, the target molecules shown in Figure 6.19 were designed.

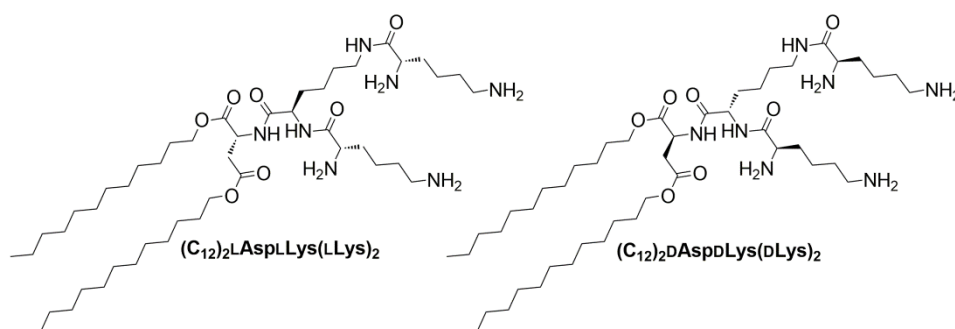


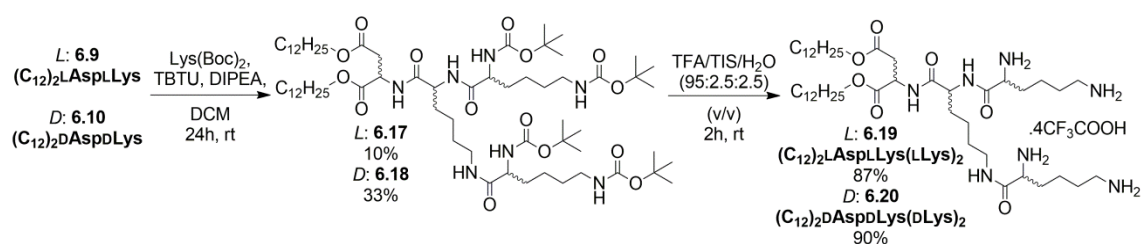
Figure 6.19 – Two G2 aspartic acid-lysine target molecules $(C_{12})_2LAspLLys(LLys)_2$ and $(C_{12})_2DAspDLys(DLys)_2$.

Each of the new target molecules contained a dendritic lysine tri-peptide as the heparin binding surface group. Dendritic lysine structures are well-known³⁵⁹ and have been widely studied for medicinal applications.³⁶⁰ For example, recent work led by Kostarelos and Al-Jamal demonstrated the ability of high generation lysine dendrimers to delay tumour growth both through systemic antiangiogenic activity³⁶¹ and the ability of such dendrimers to complex with, and enhance the cytotoxicity of, known chemotherapeutic drugs such as doxorubicin.³⁶² Lysine dendrimers have also shown potential as gene transfection agents *in vitro*³⁶³ and been investigated in a variety of soft materials³⁶⁴ and gel-based studies.^{365,366} Most commonly, however, lysine moieties are appended onto a molecular scaffold such as another dendrimer,³⁶⁷ a growing polymer³⁶⁸ or are themselves functionalised in some other way³⁶⁹ to generate functional species. In

particular, the haemolytic compatibility of Hashida and co-workers' PEG-functionalised lysine dendrimers³⁶⁹ fuelled our optimism about the potential biocompatibility of our enlarged aspartic acid-lysine species.

6.3.1 Synthesis of $(C_{12})_2LAspLLys(LLys)_2$ and $(C_{12})_2DAspDLys(DLys)_2$

These new target molecules were synthesised from the same 1-dodecanol, aspartic acid and lysine building blocks as the smaller G1 systems, however the chronology of each synthetic step required careful consideration here. It was considered that the generation and installation of the dendritic lysine moiety at the binder surface could proceed in either a convergent or divergent manner, whereby the tri-peptide would be either synthesised and then attached to the binder or generated layer-by-layer once on the 'growing' binder molecule. As demonstrated by Smith and co-workers in 2003, only the divergent methodology – that is the layer-by-layer approach – was appropriate here in order to retain the chiral integrity of the lysine residues within the final structure.³⁷⁰ Practically, this approach involved the peptide coupling of 'additional' protected lysine residues to the already-synthesised $(C_{12})_2LAspLLys$ 6.9 or $(C_{12})_2DAspDLys$ 6.10, Scheme 6.3. The yield of this coupling was low, although it is thought that either an increased stoichiometric excess of $Lys(Boc)_2$, a longer reaction time and/or an increased reaction temperature may assist in fortifying this yield. The final target molecules $(C_{12})_2LAspLLys(LLys)_2$ 6.19 and $(C_{12})_2DAspDLys(DLys)_2$ 6.20 were afforded in good yields following Boc-deprotection under trifluoroacetic acid conditions. Only a very small amount of $(C_{12})_2LAspLLys(LLys)_2$ 6.19 (<7 mg) was produced and this restricted some of the studies presented below.



Scheme 6.3 – Preparation of $(C_{12})_2LAspLLys(LLys)_2$ and $(C_{12})_2DAspDLys(DLys)_2$.

Once synthesised, the relative chiral character of the systems was probed using optical rotation and the approximately equal and opposite values (LLLL: + 8.0, DDDD: – 6.5) confirmed the opposing chirality had been retained following the introduction of the

new amino acids. Owing to the limited amount of $(C_{12})_2LAspLLys(LLys)_2$ available, circular dichroism studies were not conducted.

6.3.2 Self-Assembly Studies

6.3.2.1 Nile Red Assay

The ability of the G2 twin-tailed system to self-assemble was studied using a Nile red encapsulation assay. Again, owing to the limited amount of $(C_{12})_2LAspLLys(LLys)_2$ available, only the D-system was examined. In previous examples, both members of each enantiomeric pair of molecules exhibited comparable CAC values so this was not a concern. The data, Figure 6.20, showed the CAC to be $14 (\pm 3) \mu\text{M}$.

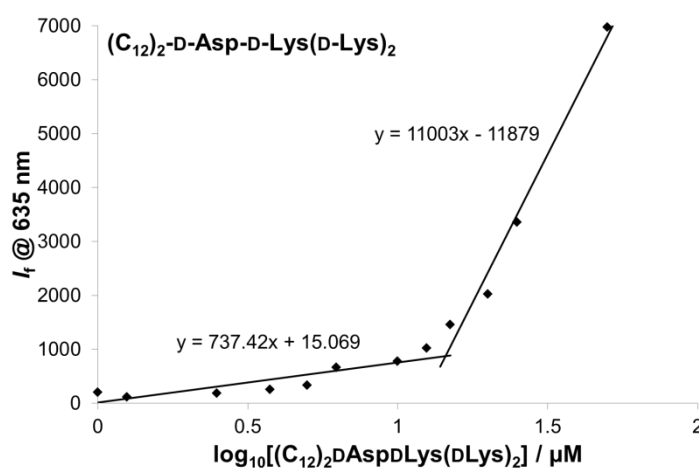


Figure 6.20 – Nile Red encapsulation curve for $(C_{12})_2DAspDLys(DLys)_2$.

The introduction of the lysine tri-peptide at the surface of the monomer unit resulted in a significant decrease in the observed CAC value. This observation appears counter-intuitive as the additional lysine groups increase the overall monomer hydrophilicity, which may be expected to hinder aggregation/self-assembly. The observations do agree with other previous studies however, for example the recent work of Haag and co-workers, which noted a decrease in CACs as hydrophilic character of their systems increased.⁷² In order to assess whether aggregate architecture may be influencing the observed CAC values, TEM imaging was carried out.

6.3.2.2 TEM Images

Having established that self-assembly was occurring, $(C_{12})_2DAspDLys(DLys)_2$ was examined by transmission electron microscopy to probe the morphology of the

aggregates formed. As before, samples were prepared in the absence and presence of heparin at a charge ratio of 1 on a formvar grid, stained with uranyl acetate and allowed to dry prior to imaging. Representative TEM images are shown in Figure 6.21 and Figure 6.22.

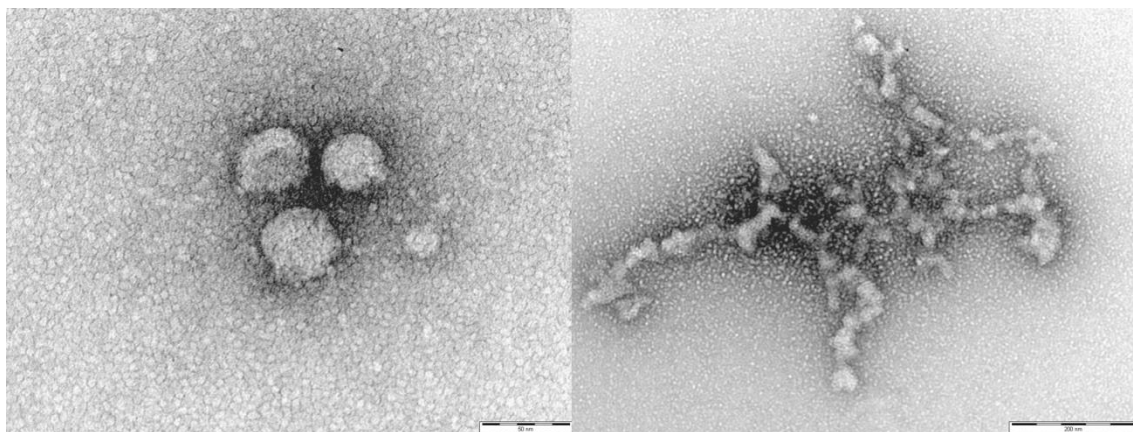


Figure 6.21 – TEM images of $(C_{12})_2DAspDLys(DLys)_2$ alone (scale bars: 50 nm (left), 200 nm (right)).

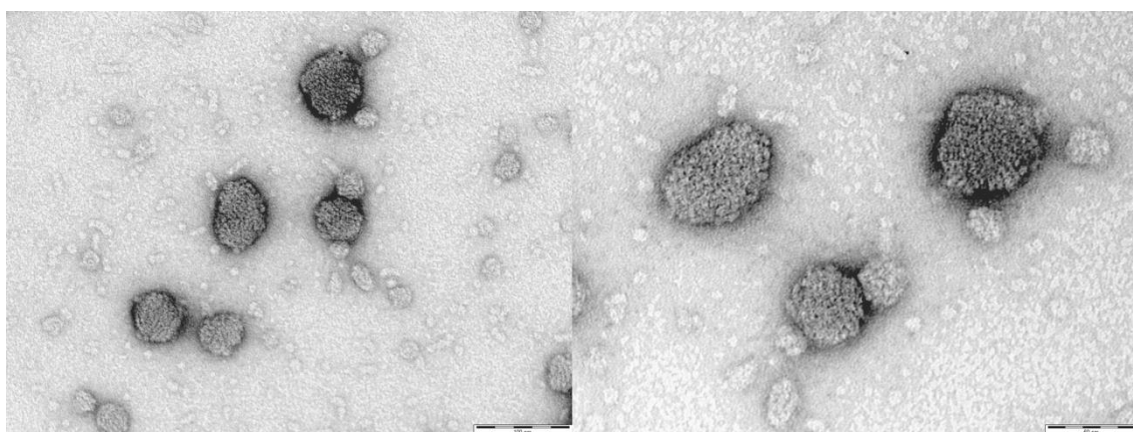


Figure 6.22 – TEM images of $(C_{12})_2DAspDLys(DLys)_2$ in the presence of heparin (scale bars: 100 nm (left), 50 nm (right)).

The TEM images of $(C_{12})_2DAspDLys(DLys)_2$ alone show some interesting features; there is evidence of several different assembled morphologies. For example, across the background of the left grid in Figure 6.21, individual micelle-like aggregates can be seen, each *ca.* 5 nm in diameter. There are also larger roughly-spherical species seen in other regions of the grid with *ca.* 45 nm diameter. These larger species may arise either due to the formation of superaggregates, which result from the further co-assembly of many individual smaller micelles. It is also possible that these larger species are vesicles

formed by $(C_{12})_2DAspDLys(DLys)_2$, although the evidence of smaller apparently-micelles species on the surfaces of these larger objects appears to support the former interpretation. Nonetheless, the introduction of extra lysine groups at the surface has clearly altered the geometry of the monomer and dis-favoured the formation of exclusively lamellar aggregates. Several regions of elongated, tubular assemblies were also seen – right grid in Figure 6.21 – which may indicate formation of some cylindrical assemblies. This collection of different morphologies may suggest that the geometry of the modified twin-tailed systems is particularly versatile, permitting the formation of different shaped assemblies in different situations. Indeed, controlling the self-assembly step in order to direct the morphology more precisely may be an interesting focus for further study. Nonetheless, the non-vesicular morphologies here may also account for the significantly lower CAC values of $(C_{12})_2AspLys(Lys)_2$ compared to $(C_{12})_2AspLys$.

In the presence of heparin – Figure 6.22 – the images show objects of various sizes, which appear to be mixed binder-heparin assemblies. The majority of these assemblies are spherical, or roughly oval, in shape with diameters of ca. 45 nm and all appear to have internal fine structures which can be identified as binder assemblies interacting with the heparin polysaccharide. Given the variety of morphologies observed in the absence of heparin, these images may suggest that the smaller binder assemblies observed in the presence of the polysaccharide are best able to optimise their multivalent ligand arrays for successful binding interactions.

6.3.3 Heparin Binding in Competitive Conditions

The G2 twin-tailed systems were examined for their ability to bind heparin in the presence of buffer and salt using the Mallard Blue assay. The data are presented numerically in Table 6.9, with the binding curves shown in Figure 6.23.

Table 6.9 – Heparin binding data for $(C_{12})_2LAspLLys(LLys)_2$ and $(C_{12})_2DAspDLys(DLys)_2$ from MalB assay in buffer and salt.

Compound	Heparin Binding		
	EC ₅₀ / μ M	CE ₅₀	Dose / mg per 100IU
$(C_{12})_2-L-Asp-L-Lys(L-Lys)_2$	(19.6 ± 0.3)	(0.73 ± 0.01)	(0.75 ± 0.01)
$(C_{12})_2-D-Asp-D-Lys(D-Lys)_2$	(16.9 ± 0.5)	(0.63 ± 0.02)	(0.64 ± 0.02)

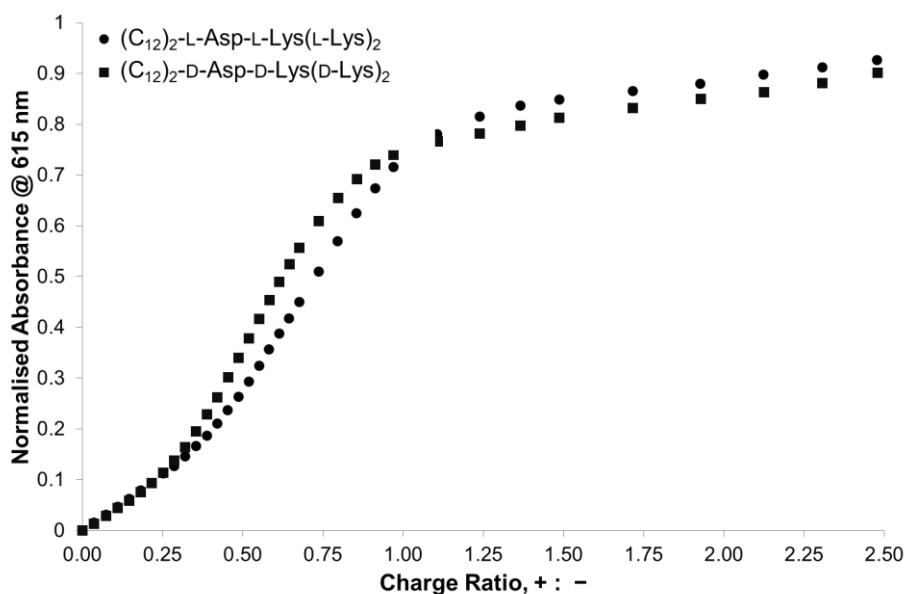


Figure 6.23 – Heparin binding curves for $(C_{12})_2LAspLLys(LLys)_2$ and $(C_{12})_2DAspDLys(DLys)_2$ from MalB assay in buffer and salt.

The data show that increasing the number of cationic groups at the surface of the binder molecule through introduction of additional lysine residues served to increase the binding efficiency, and ability, of the twin-tailed SAMul systems. Indeed, the ‘LLLL’ and ‘DDDD’ systems are able to displace 50% of MalB from heparin at $19.6 (\pm 0.3) \mu\text{M}$ and $16.8 (\pm 0.5) \mu\text{M}$ respectively; that is approximately a third of the concentration of their smaller G1 counterparts. The data indicates that each of the individual charges within the G2-systems is employed in a more charge efficient manner than in the G1-systems. This may be due to a combination of the increased binder charge and the different, more micellar, self-assembled morphologies.

More interestingly, heparin exhibited a chiral preference between $(C_{12})_2LAspLLys(LLys)_2$ and $(C_{12})_2DAspDLys(DLys)_2$ upon binding, with the DDDD system requiring less cationic charges to be present – $0.63 (\pm 0.02)$ compared to $0.73 (\pm 0.01)$ for LLLL – to bind to a given amount of heparin. Although the CE_{50} values for each system are relatively close, the difference is statistically significant, falling outside of error. The D-system being the preferred of the two is in concordance with observations in earlier Chapters and suggests that when heparin is able to distinguish

differences between the spatial arrangement of a pair of enantiomeric binders, it finds the charges of the D-system to be more optimally arranged.

Comparison of the performance of these G2 SAMul binders against the C₂₂G1Lys and C₂₂G2Lys systems from Chapter 5 is insightful here. Both C₂₂G1Lys and (C₁₂)₂AspLys(Lys)₂ present heparin with two lysine groups and four cationic charges for binding yet clearly the twin-tailed systems are much superior binders. This may suggest that the binding charges in the twin-tailed system are displayed in a more complementary manner to the anionic charges along the heparin polysaccharide. In terms of molecular weight, the twin-tailed systems are more massive than the C₂₂G1Lys monomers (858 Da vs 784 Da) and so can be argued to be less charge dense, thereby providing another example of charge density not being the sole factor controlling heparin binding ability. Additional comparison against the C₂₂G2Lys monomer family gives insights into the relative chiral expression of the two systems. Each monomer presents heparin with four chiral centres yet the C₂₂G2Lys systems, in which all the chiral groups are present at the monomer/assembly surface, exhibited no discrimination upon binding. The G2-twin-tailed system meanwhile, in which the chiral centres are arranged linearly along the monomer structure, exhibited a small chiral difference upon binding suggesting this arrangement promoted expression of the opposing molecular ‘handedness.’

6.3.4 Heparin Binding in Clinically Relevant Conditions

With the heparin binding ability of the twin-tailed G2 SAMul binders demonstrated in buffer and salt, (C₁₂)₂DAspDLys(DLys)₂ was examined in the presence of human serum using the MalB assay. The data are shown in Table 6.10.

Table 6.10 – Heparin binding data for (C₁₂)₂DAspDLys(DLys)₂ from MalB assay with heparin delivered in 100% human serum.

Assay Conditions	Heparin Binding: (C ₁₂) ₂ -D-Asp-D-Lys(D-Lys) ₂		
	EC ₅₀ / μM	CE ₅₀	Dose / mg per 100IU
Salt and Buffer	(16.9 ± 0.5)	(0.63 ± 0.02)	(0.64 ± 0.02)
Heparin in 100% Human Serum	(33.5 ± 0.7)	(1.24 ± 0.03)	(1.27 ± 0.03)

The data show that in the presence of human serum, the performance of $(C_{12})_2DAspDLys(DLys)_2$ decreased significantly, with twice as much cationic charge required to displace 50% MalB during in the assay. This performance decrease suggests the hydrophobic serum components may be disturbing the self-assembled aggregates, thereby perturbing the display of a multivalent ligand array for binding. Such a significant disruptive effect by serum is perhaps surprising given the robustness of the smaller G1 twin-tailed aspartic acid-lysine systems in the previous section. So far, of the systems presented in earlier Chapters, all of those perturbed by serum have adopted spherical micellar self-assembled structures, while the G1 aspartic acid-lysine and aspartic acid-ornithine molecules, which experienced minimal serum disruption, adopted lamellar structures. The disruption of $(C_{12})_2DAspDLys(DLys)_2$, a twin-tailed system which forms predominantly micellar assemblies, appears to suggest that the choice of hydrophobic unit is not the only factor to influence disruption, but rather that the architecture/morphology of the self-assembled systems exerts a more controlling role over serum stability. This suggests that serum components such as, for example, albumin proteins are better able to gain access to the hydrophobic interior of a micelle than penetrate the ‘double-layered’ nature of a vesicle wall in order to interfere with the hydrophobically driven assembly. This assertion suggests that the individual monomers are more tightly packed along the surface of a vesicle or lamellar structure than when in a micellar formation and that this makes them less susceptible to serum/albumin attack.^{308,371}

6.4 Conclusions and Future Work

Three enantiomeric pairs of SAMul binder molecules were synthesised and examined for their abilities to self-assemble and to interact with anionic targets heparin and DNA. The first pair of molecules, $(C_{12})_2AspLys$ contained two twelve-carbon aliphatic tails in their hydrophobic unit and were connected through a central aspartic acid linker unit to a single lysine surface group. The use of a twin-tailed hydrophobe yielded hydrophobically enhanced monomer units, which exhibited different packing geometries to the systems examined previously. Indeed, self-assembly of these systems was shown by TEM imaging to produce lamellar, rather than micellar, architectures, which were shown to form spontaneously above *ca.* 70 μ M by a Nile Red encapsulation assay.

These $(C_{12})_2\text{AspLys}$ systems were able to bind heparin in the presence of salt and buffer, although performance was inferior to the previously tested $C_{22}\text{G1Lys}$ systems. Importantly however, the hydrophobically enhanced $(C_{12})_2\text{AspLys}$ systems retained their heparin binding performance in the presence of human serum; a feat none of the previously tested SAMul binders achieved. Alongside these positive effects, the increased hydrophobicity impacted negatively on the water solubility of the final monomers, and this is thought to have affected the results of the plasma clotting assays, where the compounds were unable to neutralise the anticoagulant action of heparin.

The pair of enantiomeric molecules exhibited identical heparin binding performances suggesting that the spatial arrangement of charge in these systems had negligible impact on interaction with heparin. When the same molecules were investigated for DNA binding, however, a chiral difference was observed, with $(C_{12})_2\text{LAspLLys}$ binding 50% of DNA at significantly lower concentrations, and more charge efficiently than $(C_{12})_2\text{DAspDLys}$.

In order to probe this chiral difference, a related family of twin-tailed binders containing ornithine as the surface binding group instead of lysine were synthesised and tested. The $(C_{12})_2\text{AspOrn}$ systems self-assembled to form lamellar aggregates above *ca.* 30 μM . When tested for their heparin and DNA binding ability, these $(C_{12})_2\text{AspOrn}$ systems were shown to bind the polyanions less efficiently than when lysine was the surface group. Heparin exhibited minimal chiral preference between $(C_{12})_2\text{LAspLOrn}$ and $(C_{12})_2\text{DAspDOrn}$ yet DNA bound the LL-enantiomer more efficiently than the DD, again hinting strongly at fundamental binding differences between heparin and DNA. Despite the poor heparin binding performance, the presence of serum caused minimal perturbation.

In an attempt to increase the heparin binding performance of these twin-tailed systems, a final iteration of the structure afforded a larger ‘second generation’ pair of enantiomers $(C_{12})_2\text{LAspLLys(LLys)}_2$ and $(C_{12})_2\text{DAspDLys(DLys)}_2$, containing a lysine tripeptide binding group at the surface. These larger monomers exhibited more charge efficient heparin binding than their smaller ‘G1’ counterparts; however performance was significantly perturbed in the presence of human serum. The presence of two additional lysine groups was shown to alter the monomer geometry leading to the formation primarily of spherical micellar assemblies. It was noted that these species

shared the same morphology as the previously discussed C₂₂G1Lys structures, which themselves suffered significant perturbation by serum. This led to the suggestion that the relative stability of the smaller (C₁₂)₂AspLys and (C₁₂)₂AspOrn systems was primarily due to their non-micellar vesicular/lamellar self-assembled architectures.

In order to investigate this suggestion more thoroughly, mesoscale modelling could be employed to simulate the effect of, for example, an albumin protein upon the non-covalent interactions holding the self-assembled structures together. Future experimental work could target the synthesis of alternative monomer units with geometries specifically designed to afford cylindrical and/or vesicular assemblies. To achieve this, other hydrophobic units could be employed such as cholesterol-like steroid species or multi-tailed/branched natural fatty acids and bile acids. Maintaining lysine as the binding surface group may provide consistency within test conditions but would also permit further studies of enantiomeric pairs of binder molecules, which may further elucidate the fundamental binding differences between biological polyanions such as heparin and DNA uncovered here.

7 Experimental

7.1 Synthetic Materials and Methods

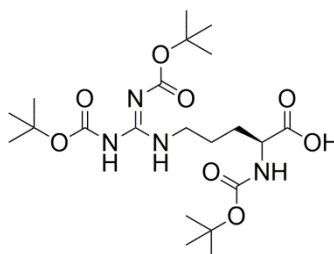
General Reagents and Methods

All reagents were obtained from commercial sources and were used without further purification unless stated. In particular, thin layer chromatography (TLC) was performed on Merck aluminium backed plates, coated with 0.25 nm silica gel 60; flash column chromatography was performed on silica gel 60 (35 – 70 μm) supplied by Fluka Ltd and preparative gel permeation chromatography (GPC) was performed on Biobeads SX-1 supplied by Bio-Rad and Sephadex LH-20.

NMR spectra were recorded on a JEOL ECX400 (^1H 400 MHz, ^{13}C 100 MHz) spectrometer and assignments were made through corroboration of 2D ^1H - ^1H COSY and ^1H - ^{13}C HSQC spectra with their 1D counterparts. For some compounds, high molecular weight or molecular aggregation led to quaternary carbon signals not being observed. HRMS and ESI mass spectra were recorded on a Bruker Daltonics Microtof mass spectrometer. Infrared spectra were recorded on a Shimadzu IR Prestige-21 FT-IR spectrometer while optical rotation values were obtained using a Jasco DIP-370 digital polarimeter with filter fitted at 589 nm. Circular Dichroism was carried out on a Jasco J810 CD Spectrophotometer (150w Xe lamp).

Where both enantiomeric forms of a compound have been made, unless stated, D-compounds were synthesised using identical conditions to those reported herein for L-compounds.

L-Arg(Boc)₃ (2.1)



Molecular Formula: $\text{C}_{21}\text{H}_{38}\text{N}_4\text{O}_8$

Molecular Weight: 474.55

L-Arginine (4.00 g, 22.96 mmol, 1 eq.) and sodium hydroxide pellets (2.75 g, 68.75 mmol, 3 eq.) were dissolved together in deionised water (70 mL). Di-*tert*-butyl dicarbonate (20.00 g, 91.64 mmol, 4 eq., pre-dissolved in THF (70 mL)) was added to the basic arginine solution dropwise in one portion over 55 minutes before the resulting reaction mixture was stirred at 45°C under an N₂ atmosphere for 4 hours. The volatiles were removed *in vacuo* and the resulting residue was taken up in deionised water (300 mL) and washed with cyclohexane (100 mL). The aqueous layer was acidified to pH 3 (1.33 M NaHSO₄, pH paper) before the product was extracted into ethyl acetate and washed successively with brine (75 mL, sat.) and deionised water (75 mL). The organic layer was collected, dried over MgSO₄ and the resulting filtrate was concentrated *in vacuo* to afford the product as a golden oil, which was taken up in DCM and concentrated *in vacuo* once more to afford the product as a white crystalline solid (1.30 g, 2.74 mmol, 12%).

R_f = 0.56 (9 : 1, DCM : methanol, UV/ninhydrin)

¹H NMR (400 MHz, CD₃OD) δ: 4.10 (exp dd, app q, CHNH, ³J = 7.2 Hz, 1H); 3.88 (t, CH₂NH, ³J = 6.8 Hz, 2H); 1.90 – 1.76 (m, CH_aH_bCHNH, 1H); 1.67 (br s, CH_aH_bCHNH, CH₂CH₂NH, 3H); 1.55, 1.48, 1.44 (s, C(CH₃)₃, 9H).

¹³C NMR (100 MHz, CD₃OD) δ: 176.26 (C=O, acid); 158.56 (C=N); 158.15 (3 × C=O, carbamate); 80.44, 79.85 (total 3 × C(CH₃)₃); 54.83 (CHNH); 41.01 (CH₂NH); 30.56 (CH₂CHNH); 28.86, 28.79, 28.62 (3 × C(CH₃)₃); 24.17 (CH₂CH₂NH).

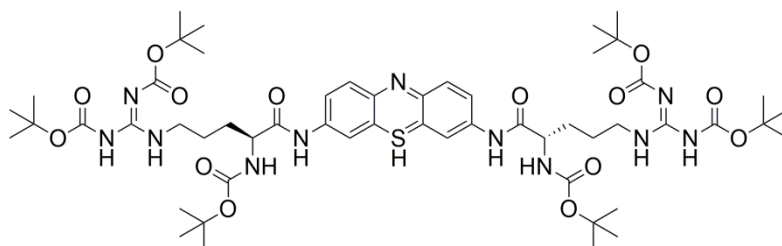
ESI-MS: 475.28 [M+H]⁺ (100%).

HRMS: Calcd. [M+H]⁺ (C₂₁H₃₉N₄O₈) *m/z* = 475.2762, found [M+H]⁺ *m/z* = 475.2769 (error – 1.0).

IR ν [cm⁻¹]: 3354br w (N–H), 2979m (O–H, C–H), 1710s (C=O, acid), 1640m (C=O, carbamates), 1609m (C=N), 1503m (N–H), 1454w, 1391m, 1366s, 1273m, 1249s (C–O), 1144s (C–O), 1052m, 852m, 812w.

Lα_D: + 17.7 (c. 1.0, CHCl₃).

Thionine-(L-Arg(Boc)₃)₂ (aka. Mallard Blue(Boc)₆)



Molecular Formula: C₅₄H₈₂N₁₁O₁₄S

Molecular Weight: 1141.36

Thionine acetate (124 mg, 0.43 mmol), L-Arg(Boc)₃ (450 mg, 0.95 mmol), TBTU (304 mg, 0.95 mmol) and DIPEA (330 μL, 1.90 mmol) were dissolved together in DCM (50 mL). The resulting reaction mixture was stirred at room temperature overnight before volatiles were removed *in vacuo* to afford the crude product. This solid was purified by flash column chromatography (SiO₂, 3 : 2 ethyl acetate : cyclohexane) to afford the pure product as a purple solid (145 mg, 0.13 mmol, 30%).

R_f = 0.39 (3 : 2, ethyl acetate : cyclohexane)

¹H NMR (400 MHz, DMSO-d₆) δ: 9.76 (br s, NH, 2H); 9.07 (br s, NH, 4H); 8.43 (br s, NH, 2H); 7.26 (s, CHCS, 2H); 7.10 (d, ArCH, ³J = 8.3 Hz, 1H); 7.00 (d, ArCH, ³J = 8.3 Hz, 1H); 6.60 (d, ArCH, ³J = 8.3, 2H); 4.04 – 3.91 (m, 2 × CHNH, 2H); 3.80 – 3.73 (m, 2 × CH₂NH, 4H); 1.66 – 1.51 (m, 2 × CH₂CHCONH, 2 × CH₂CH₂NH, 8H); 1.43 (s, C(CH₃)₃, 18H); 1.37 (s, C(CH₃)₃, 36H).

¹³C NMR (100 MHz, DMSO-d₆) δ: 170.37 (2 × C=O, amides); 162.84, 159.51, 154.07 (2 × C=O, carbamates); 137.73 (C=N); 117.04 (ArCH); 115.71 (CHCS); 114.08 (ArCH); 77.92, 77.57 (3 × C(CH₃)₃); 51.31 (CHNH); 43.95 (CH₂NH); 27.91, 27.36 (3 × C(CH₃)₃); 26.26 (CH₂CHNH); 25.01 (CH₂CH₂NH).

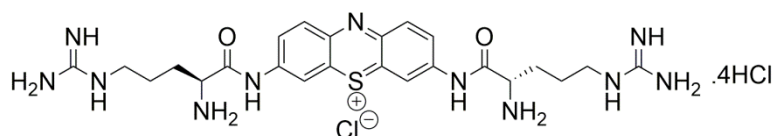
ESI-MS: 1142.59 [M+H]⁺ (100%).

HRMS: Calcd. [M+H]⁺ (C₅₄H₈₄N₁₁O₁₄S) *m/z* = 1142.5914, found [M+H]⁺ *m/z* = 1142.5866 (error 4.2 ppm).

IR ν [cm⁻¹]: 3372*br m* (N–H), 2978*w* (C–H); 1713*s* (C=O, amides); 1674*s* (C=O, carbamates), 1605*s* (C=N), 1481*s*, 1366*m*, 1242*s*, 1142*s*, 1049*m*, 980*w*, 849*w*, 779*w*, 502*s*.

λ_D: – 2.2 (c. 0.5, MeOH).

Thionine-(L-Arginine)₂ (aka. Mallard Blue) (2.2)



Molecular Formula = C₂₄H₃₈Cl₅N₁₁O₂S

Molecular Weight = 721.96

Thionine-(L-Arg(Boc)₃)₂ (108 mg, 95 μmol) was dissolved in methanol (20 mL) and gaseous HCl was bubbled through the solution for 20 seconds. The resulting reaction mixture was stirred at room temperature for 3 hours before the volatiles were removed *in vacuo*. The dissolution in methanol and HCl gas treatment was repeated until TLC showed no presence of starting material, and the product was afforded, after drying, as a dark green solid. (71 mg, 93 μmol, 98%).

R_f = 0.00 (ammonium hydroxide).

¹H NMR (400 MHz, DMSO-d₆) δ: 8.44 (s, ArCH, 4H); 7.88 (s, ArCH, 2H); 7.43 (br s, NH, 14H); 3.19 (br s, 2 × CHNH, 2 × CH₂NH, 6H); 1.83 (br s, CH₂CHNH, 4H); 1.56 (br s, CH₂CH₂NH, 4H).

¹³C NMR (100 MHz, DMSO-d₆) δ: Poor solubility and compound aggregation limited the ability to obtain meaningful spectrum.

ESI-MS: 271.64 [M+2H]²⁺ (100%), 181.42 [M+3H]³⁺ (60%).

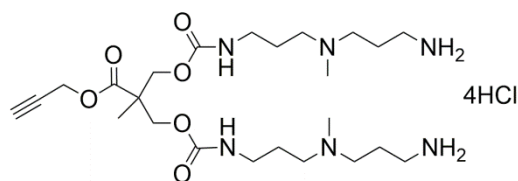
HRMS: Calcd. [M+2H]²⁺ (C₂₄H₃₇N₁₁O₂S) *m/z* = 271.6421, found [M+2H]²⁺ *m/z* = 271.6404 (error 6.3 ppm).

IR ν [cm⁻¹]: 3248br s (N–H); 2924br s (C–H); 1651s (C=O, amides); 1466s, 1296w, 1227w, 1096w, 1011m, 818w.

Lα_D: – 186.4 (c. 0.5, MeOH).

Dα_D: – 167.5 (c. 1.0, MeOH).

Propyne-G1-DAPMA (4.1)



Chemical Formula: C₂₄H₅₀Cl₄N₆O₆

Molecular Weight: 660.50

Propyne-G1-DAPMA(Boc)₄ (50 mg, 70 μmol) was dissolved in methanol (10 mL) and gaseous HCl was bubbled through the solution for 15 seconds. The resulting reaction mixture was stirred at room temperature for 2 hours before being concentrated *in vacuo* to afford the product as a golden solid (43 mg, 65 μmol, 93%).

R_f = 0.15 streak (95 : 5, methanol : ammonium hydroxide, ninhydrin).

^1H NMR (400 MHz, CD_3OD) δ : 4.74 (d, $\text{CH}\equiv\text{CCH}_2$, $^4\text{J} = 2.0$ Hz, 2H); 4.21 (s, $2 \times \text{CH}_2\text{O}$, 4H); 3.43 – 3.32 (m, $2 \times \text{CHNH}_3^+$, 4H); 3.31 – 3.17 (m, $4 \times \text{CH}_2\text{NCH}_3$, 8H); 3.14 – 3.07 (m, $2 \times \text{CH}_2\text{NHCO}$, 4H); 3.04 (t, $\text{CH}\equiv\text{CCH}_2$, $^4\text{J} = 2.0$ Hz, 1H); 2.21 – 2.10 (m, $2 \times \text{CH}_2\text{CH}_2\text{NH}$, 4H); 2.05 – 1.90 (m, $\text{CH}_2\text{CH}_2\text{NH}_2$, 4H); 1.27 (s, CH_3 , 3H).

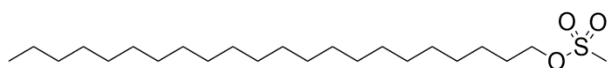
^{13}C NMR (100 MHz, CD_3OD) δ : 173.82 (C=O, Fréchet-ester); 158.58 ($2 \times \text{C}=\text{O}$, carbamates); 77.93 ($\text{HC}\equiv\text{CCH}_2$); 76.93 ($\text{HC}\equiv\text{CCH}_2$); 67.83, 66.94 (CH_2O); 55.41, 55.33 ($2 \times \text{CH}_2\text{NCH}_3$); 54.29 ($2 \times \text{CH}_2\text{NH}_2$); 53.66 ($\text{HC}\equiv\text{CCH}_2$); 40.63, 40.55 (NCH_3); 38.75, 37.98 (CH_2NHCO); 25.87, 25.40 ($2 \times \text{CH}_2\text{CH}_2\text{N}$); 17.86 (CH_3).

ESI-MS: 515.36 $[\text{M}+\text{H}]^+$ (100%).

HRMS: Calcd. $[\text{M}+\text{H}]^+$ ($\text{C}_{24}\text{H}_{47}\text{N}_6\text{O}_6$) $m/z = 515.3557$, found $[\text{M}+\text{H}]^+ = 515.3571$ (error 2.7 ppm).

IR ν [cm^{-1}]: 3375 $br w$ (N–H), 2975 m (C–H), 1735 m (C=O, ester), 1687 s (C=O, carbamates), 1526 m , 1454 w , 1365 w , 1250 m , 1166 m , 1040 m , 970 w , 861 w , 776 w .

***Behenoyl methanesulfonate*³⁷² (5.1)**



Molecular Formula: $\text{C}_{23}\text{H}_{48}\text{O}_3\text{S}$

Molecular Weight: 404.33

1-Docosanol (5.29 g, 16.20 mmol) was suspended in DCM (130 mL) and triethylamine (5.23 mL, 37.52 mmol) was added. Methanesulfonyl chloride (2.00 mL, 25.84 mmol) was added causing dissolution of the other reagents and turning the reaction mixture yellow. The reaction mixture was stirred at room temperature for 4 hours before being washed successively with deionised water (40 mL), HCl (40 mL, 2 M), deionised water (40 mL), NaHCO_3 (40 mL, sat.) and deionised water (40 mL). The organic phase was collected, dried over MgSO_4 and the resulting filtrate concentrated *in vacuo* to afford the product as a yellow-white solid (6.10 g, 15.1 mmol, 93 %). The spectroscopic data presented below is in agreement with that previously published.

$R_f = 0.55$ (9 : 1, DCM : methanol, UV).

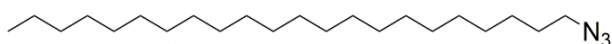
^1H NMR (400 MHz, CDCl_3) δ : 4.21 (t, CH_2O , $^3\text{J} = 6.4$ Hz, 2H); 3.00 (s, CH_3SO_3 , 3H); 1.74 (quint, $\text{CH}_2\text{CH}_2\text{O}$, $^3\text{J} = 6.4$ Hz, 2H); 1.25 (s, $19 \times \text{CH}_2$, 38H); 0.88 (t, alkyl CH_3 , $^3\text{J} = 7.8$ Hz, 3H).

^{13}C NMR (100 MHz, CDCl_3) δ : 70.19 (CH_2O); 37.36 (CH_3SO_3); 29.69, 29.67, 29.65, 29.61, 29.52, 29.42, 29.36, 29.12 (alkyl CH_2); 29.03 ($\text{CH}_2\text{CH}_2\text{O}$); 25.41, 22.69 (alkyl CH_2); 14.12 (alkyl CH_3).

ESI-MS: Calcd. $[\text{M}+\text{Na}]^+$ ($\text{C}_{23}\text{H}_{48}\text{NaO}_3\text{S}$) $m/z = 427.3216$, found $[\text{M}+\text{Na}]^+$ $m/z = 427.3203$ (error – 3.0 ppm).

IR ν [cm^{-1}]: 2914 s (C–H), 2848 m (C–H), 2161 w , 2025 w , 1975 w , 1469 m , 1335 s , 1164 m , 979 m , 940 s , 847 s , 748 w , 715 m .

Behenoyl Azide³⁷² (5.2)



Molecular Formula: $\text{C}_{22}\text{H}_{45}\text{N}_3$

Molecular Weight: 351.36

Docosyl methanesulfonate (5.80 g, 14.34 mmol) was dissolved in DMF (100 mL) and sodium azide (2.32 g, 35.69 mmol) was added. The reaction was stirred at room temperature for 30 minutes before warming to 85°C for 5.5 hours. After cooling to room temperature, hexane (100 mL) and deionised water (10 mL) were added. The organic layer was collected and washed successively with NaHCO_3 (20 mL, sat.) and brine (20 mL, sat.). The organic layer was dried over Na_2SO_4 and the resulting filtrate was concentrated *in vacuo* to afford the product as a sticky white solid (4.10 g, 11.66 mmol, 82%). The spectroscopic data presented below is in agreement with that previously published.

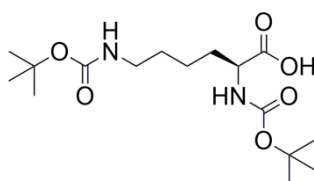
$R_f = 0.70$ (9 : 1, DCM : methanol, KMnO_4).

^1H NMR (400 MHz, CDCl_3) δ : 3.25 (t, CH_2N_3 , $^3\text{J} = 7.2$ Hz, 2H); 1.59 (quint, $\text{CH}_2\text{CH}_2\text{N}_3$, $^3\text{J} = 7.2$ Hz, 2H); 1.25 (s, $19 \times$ alkyl CH_2 , 38H); 0.88 (t, alkyl CH_3 , $^3\text{J} = 6.4$ Hz, 3H).

^{13}C NMR (100 MHz, CDCl_3) δ : 51.35 (CH_2N_3); 31.69, 29.45, 29.43, 29.41, 29.37, 29.29, 29.23, 29.11, 28.90, 28.58, 26.45 (alkyl CH_2); 22.40 (CH_2CH_3); 13.78 (CH_3).

ESI-MS: Calcd. $[\text{M}+\text{H}]^+$ ($\text{C}_{22}\text{H}_{45}\text{N}_3$) $m/z = 351.36$. No peak found, ionisation technique too soft.

IR ν [cm^{-1}]: 2916 s (C–H), 2849 s (C–H), 2095 s (N_3), 1644 m , 1351 w , 1255 m , 1063 w , 892 w , 720 m .

L-Lys(Boc)₂ (L: 5.3, D: 5.4)Molecular Formula: C₁₆H₃₀N₂O₆

Molecular Weight: 346.42

L-Lysine (4.00 g, 27.36 mmol, 1 eq.) and sodium hydroxide pellets (2.19 g, 54.75 mmol, 2 eq.) were dissolved together in deionised water (50 mL) while di-*tert*-butyl dicarbonate (12.50 g, 57.27 mmol, 2.1 eq.) was dissolved separately in THF (50 mL). The dicarbonate solution was added to the basic lysine solution dropwise in one portion over 30 minutes and the resulting reaction mixture was stirred at 45°C under an N₂ atmosphere for 3 hours. The volatiles were removed *in vacuo* and the resulting residue was taken up in deionised water (200 mL) and washed with cyclohexane (100 mL). The aqueous layer was acidified to pH 3 (1.33 M NaHSO₄, pH paper) before the product was extracted into ethyl acetate and washed successively with saturated brine (75 mL) and deionised water (50 mL). The organic phase was collected, dried over MgSO₄ and the resulting filtrate was concentrated *in vacuo* to afford the product as an off-white crystalline solid (9.00 g, 25.99 mmol, 95%). D-yield: 92%.

R_f = 0.34 (9 : 1, DCM : methanol, ninhydrin).

¹H NMR (400 MHz, CD₃OD) δ: 4.05 (exp dd, app q, CHNH, ³J = 4.4 Hz, 1H); 3.04 (t, CH₂NH, ³J = 6.6 Hz, 2H); 1.91 – 1.78 (m, CH_aH_bCHNH, 1H); 1.73 – 1.61 (m, CH_aH_bCHNH, 1H); 1.44 (br s, CH₂CH₂CH₂NH, 2 × C(CH₃)₃, 22H).

¹³C NMR (100 MHz, CD₃OD) δ: 176.47 (C=O, acid); 158.02, 157.97 (C=O, carbamate); 80.97, 80.40 (C(CH₃)₃); 55.04 (CHNH); 41.40 (CH₂NH); 30.30 (CH₂CHNH); 30.10 (CH₂CH₂NH); 28.83, 28.64 (2 × C(CH₃)₃); 26.34 (CH₂CH₂CH₂NH).

ESI-MS: 369.20 [M+Na]⁺ (100%), 347.22 [M+H]⁺ (41%).

HRMS: Calcd. [M+Na]⁺ (C₁₆H₃₀N₂O₆Na) *m/z* = 369.1996, found [M+Na]⁺ *m/z* = 369.1981 (error 3.6 ppm).

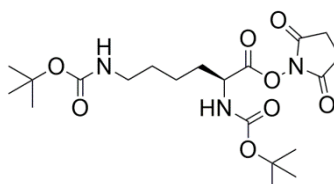
IR ν [cm⁻¹]: 3339*br w* (N–H), 2978*m* (C–H), 2933*m* (C–H), 2870*w* (C–H), 1710*m* (C=O, acid), 1688*s* (CONH, carbamates I), 1517*m* (CONH, carbamates II), 1452*m* (C–

H), 1392 m , 1365 s (C–H), 1249 s (C–O), 1159 s (C–O), 1047 m (C–N), 1018 m (C–N), 860 m .

θ_L : + 61.5 mdeg (211 nm, 10 mM, MeOH).

θ_D : – 56.9 mdeg (211 nm, 10 mM, MeOH).

L-Lys(Boc)₂-succinimide (L: 5.5, D: 5.6)



Molecular Formula: C₂₀H₃₃N₃O₈

Molecular Weight: 443.49

L-Lys(Boc)₂ (3.50 g, 10.10 mmol), *N*-hydroxysuccinimide (1.16 g, 10.10 mmol) and DCC (2.08 g, 10.10 mmol) were dissolved together in dry DMF (60 mL) and stirred at room temperature under an N₂ atmosphere for 24 hours. The DCU by-product was removed by filtration through a celite-containing sinter funnel. The resulting filtrate was concentration *in vacuo* to afford the crude product as a soft golden wax (5.10 g, 11.5 mmol, 114% crude). This crude product carried forward in synthesis, however a portion of crude product (1.00 g) was taken for purification by flash column chromatography (SiO₂, DCM : ethyl acetate, 8 : 2) to afford product as an off-white solid (750 mg, 1.7 mmol, 86% effective yield). D-yield: 83%.

R_f = 0.44 (9 : 1 DCM : methanol, ninhydrin).

¹H NMR (400 MHz, CD₃OD) δ : 4.45 (dd, CHNH, ³J = 8.8, 5.2 Hz, 1H); 3.05 (br s, CH₂NH, 2H); 2.83 (s, 2 × succinimideCH₂, 4H); 1.98 – 1.90 (m, CH_aH_bCHNH, 1H); 1.86 – 1.78 (m, CH_aH_bCHNH, 1H); 1.52 (s, CH₂CH₂NH and CH₂CH₂CH₂NH, 4H); 1.45 (s, 2 × C(CH₃)₃, 18H).

¹³C NMR (100 MHz, CD₃OD) δ : 170.03 (C=O, lysine ester); 163.53 (2 × C=O, succinimide); 157.22, 156.38 (C=O, carbamate); 79.55, 78.53 (C(CH₃)₃); 52.04 (CHNH); 39.60 (CH₂NH); 31.08 (CH₂CHNH); 29.09 (CH₂CH₂NH); 27.52 (2 × C(CH₃)₃); 25.21 (2 × succinimideCH₂); 22.51 (CH₂CH₂CH₂NH).

ESI-MS: 466.22 [M+Na]⁺ (100%), 444.24 [M+H]⁺ (46%).

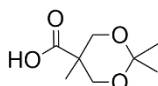
HRMS: Calcd. [M+Na]⁺ (C₂₀H₃₃N₃O₈Na) m/z = 466.2160, found [M+Na]⁺ m/z = 466.2174 (error – 3.0 ppm).

IR ν [cm^{-1}]: 3380 w (N–H), 3364 w (N–H), 2980 w (C–H), 2936 w (C–H), 1814 w , 1788 w , 1736 s (C=O, ester), 1678 s (CONH, carbamates I), 1511 s (CONH, carbamates II), 1462 w (C–H), 1390 w , 1368 m (C–H), 1341 w , 1247 m , 1211 m , 1159 s (C–O), 1086 s (C–N), 1071 m (C–N), 1046 w , 998 m , 961 m , 868 m .

$L\alpha_D$: – 9.2 (c. 1.0, CHCl_3).

$D\alpha_D$: + 7.0 (c. 1.0, CHCl_3).

***Isopropylidene-2,2,bis(hydroxymethyl)propionic acid*³⁵⁷ (5.7)**



Molecular Formula: $\text{C}_8\text{H}_{14}\text{O}_4$

Molecular Weight: 174.19

2,2-Bis(hydroxymethyl)propionic acid (15.00 g, 111.83 mmol), 2,2-dimethyloxopropane (20 mL, 162.65 mmol) and *p*-toluenesulfonic acid monohydrate (1.00 g, 5.25 mmol) were dissolved together in acetone (60 mL) and stirred at room temperature until TLC showed no presence of starting material (4 h). The acid catalyst was neutralised by addition of ammonium hydroxide : ethanol (3 mL, 1 : 1) leading to formation of a white precipitate after ten minutes. The volatiles were removed *in vacuo* to afford a white sludge which was taken up in DCM (60 mL) and washed with distilled water (2×30 mL). The organic layer was collected, dried over MgSO_4 and the resulting filtrate concentrated *in vacuo* to afford the product as a white crystalline solid (10.30 g, 59.13 mmol, 53%). The spectroscopic data presented below is in agreement with that previously published.

R_f = 0.56 (9 : 1, DCM : methanol, UV).

^1H NMR (400 MHz, CDCl_3) δ : 4.18 (d, $\text{CH}_{ax}\text{H}_{eq}\text{O}$, $^2J = 12.0$ Hz, 2H); 3.67 (d, $\text{CH}_{ax}\text{H}_{eq}\text{O}$, $^2J = 12.0$ Hz, 2H), 1.45 (s, CH_3CO_2 , 3H); 1.41 (s, CH_3CO_2 , 3H); 1.21 (s, CH_3CCO , 3H).

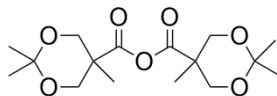
^{13}C NMR (100 MHz, CDCl_3) δ : 180.32 (C=O, acid); 98.27 ($\text{C}(\text{CH}_3)_2$); 65.77 ($2 \times \text{CH}_2\text{O}$); 41.70 (CCOOH); 25.10, 21.96, 18.40 (CH_3).

ESI-MS: 197.08 $[\text{M}+\text{Na}]^+$ (100%), 175.10 $[\text{M}+\text{H}]^+$ (51%).

HRMS: Calcd. $[\text{M}+\text{Na}]^+$ ($\text{C}_8\text{H}_{14}\text{O}_4\text{Na}$) $m/z = 197.0784$, found $[\text{M}+\text{Na}]^+$ $m/z = 197.0781$ (error 1.6 ppm).

IR ν [cm^{-1}]: 2994 $br w$ (O–H), 2159 s (C–H), 2028 s (C–H), 1975 $br s$, 1719 m (C=O, acid), 1380 w (C–H), 1255 s (C–O), 1073 s , 862 w , 826 s , 718 m .

***Isopropylidene-2,2,bis(hydroxymethyl)propionic anhydride*³¹³(5.8)**



Molecular Formula: $\text{C}_{16}\text{H}_{26}\text{O}_7$

Molecular Weight: 330.37

Isopropylidene-2,2,bis(hydroxymethyl)propionic acid (9.00 g, 51.67 mmol) was dissolved in DCM (50 mL) before DCC (5.33 g, 25.83 mmol, pre-dissolved in DCM (40 mL)), was added. The resulting white reaction mixture was stirred at room temperature for 3 hours before the precipitate (DCU by-product) was filtered off through a celite-containing sinter funnel. The filter cake washings (DCM) were combined with the filtrate and concentrated *in vacuo* to afford a residue which was taken up in ethyl acetate, causing further by-product precipitation. The precipitate was filtered off as before to afford, after drying, the product as a golden viscous oil (5.90 g, 17.86 mmol, 69%). The spectroscopic data presented below is in agreement with that previously published.

$R_f = 0.62$ (9 : 1, DCM : methanol, UV).

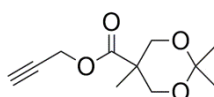
^1H NMR (400 MHz, CDCl_3) δ : 4.20 (d, $\text{CH}_{ax}\text{H}_{eq}\text{O}$, $^2J = 12.0$ Hz, 4H); 3.68 (d, $\text{CH}_{ax}\text{H}_{eq}\text{O}$, $^2J = 12.0$ Hz, 4H); 1.43 (s, $2 \times \text{CH}_3\text{CO}_2$, 6H); 1.38 (s, $2 \times \text{CH}_3\text{CO}_2$, 6H); 1.23 (s, $2 \times \text{CH}_3\text{CCO}$, 6H).

^{13}C NMR (100 MHz, CDCl_3) δ : 169.42 ($2 \times \text{C}=\text{O}$); 98.27 ($2 \times \text{C}(\text{CH}_3)_2$); 65.59 ($4 \times \text{CH}_2\text{O}$); 43.57 ($2 \times \text{CCOO}$); 25.48, 21.48, 17.56 ($3 \times \text{CH}_3$).

ESI-MS: 353.16 $[\text{M}+\text{Na}]^+$ (100%), 331.16 $[\text{M}+\text{H}]^+$ (59%).

HRMS: Calcd. $[\text{M}+\text{Na}]^+$ ($\text{C}_{16}\text{H}_{26}\text{O}_7\text{Na}$) $m/z = 353.1571$, found $[\text{M}+\text{Na}]^+$ $m/z = 353.1750$ (error 0.0 ppm).

IR [cm^{-1}]: 2991 w (C–H), 2159 m (C–H), 2032 m (C–H), 1976 m , 1812 m (C=O, anhydride), 1736 m (C=O, anhydride), 1455 w , 1373 m , 1205 m , 1152 m , 1133 m , 1081 m , 1013 s , 984 m , 935 w , 917 w , 826 s , 731 w .

Propyne isopropylidene-2,2-bis(hydroxymethyl) propionate³²⁵ (5.9)Molecular Formula: C₁₁H₁₆O₄

Molecular Weight: 212.24

Propargyl alcohol (0.73 mL, 12.54 mmol), DMAP (0.23 g, 1.88 mmol) and pyridine (3.06 mL, 37.79 mmol) were dissolved in DCM (11 mL) and isopropylidene-2,2-bis(hydroxymethyl)propionic anhydride (5.00 g, 15.13 mmol, pre-dissolved in DCM (23 mL)), was added slowly in one portion. The reaction mixture was stirred overnight at room temperature before being quenched with deionised water (5 mL), diluted with DCM (50 mL) and washed successively with NaHSO₄ (3 × 30 mL, 1.33 M), Na₂CO₃ (3 × 30 mL, 10%) and saturated brine (1 × 30 mL). The organic layer was collected, dried over MgSO₄ and the resulting filtrate was concentrated *in vacuo* to afford the product as a pale yellow oil (2.65 g, 12.49 mmol, 98%). The spectroscopic data presented below is in agreement with that previously published.

R_f = 0.91 (9 : 1, DCM : methanol, UV).

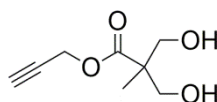
¹H NMR (400 MHz, CDCl₃) δ: 4.74 (d, CH≡CCH₂, ⁴J = 2.4 Hz, 2H); 4.20 (d, CH_{ax}H_{eq}O, ²J = 12.0 Hz, 2H); 3.70 (d, CH_{ax}H_{eq}O, ²J = 12.0 Hz, 2H); 2.47 (t, CH≡CCH₂, ⁴J = 2.4 Hz, 1H); 1.43 (s, CH₃CO₂, 3H); 1.39 (s, CH₃CO₂, 3H); 1.21 (s, CH₃CCO, 3H).

¹³C NMR (100 MHz, CDCl₃) δ: 173.33 (C=O, ester); 98.01 (C(CH₃)₂); 77.37 (CH₂C≡CH); 74.94 (C≡CH); 65.80 (CH₂O); 52.25 (C≡CH); 41.77 (CCOO); 24.52, 22.48, 18.31 (CH₃).

ESI-MS: 235.09 [M+Na]⁺ (100%), 213.11 [M+H]⁺ (30%).

HRMS: Calcd. [M+Na]⁺ (C₁₁H₁₆NaO₄) *m/z* = 235.0941, found [M+Na]⁺ *m/z* = 235.0942 (error – 0.8 ppm).

IR ν [cm⁻¹]: 2160br w (C≡C, C–H), 1737m (C=O, ester), 1453w, 1372w, 1251m (C–O), 1218m (C–O), 1198m, 1120m, 1078s, 1040w, 997w, 934w, 830s.

Propyne-[G1]-OH³²⁵ (5.10)Molecular Formula: C₈H₁₂O₄

Molecular Weight: 172.18

Propyne isopropylidene-2,2-bis(hydroxymethyl) propionate (2.55 g, 12.01 mmol) was dissolved in methanol (102 mL, 25 mg mL⁻¹) and c.H₂SO₄ (2.04 mL, 2% v/v) was added. After stirring at room temperature overnight, the reaction was neutralised with ammonium hydroxide : methanol (8 mL, 1 : 1) causing ammonium sulfate to precipitate. After 30 minutes further stirring, the precipitate was filtered off through a celite-containing sinter funnel and the filtrate concentrated *in vacuo*. This crude product was taken up in chloroform, re-filtered as before and the resulting filtrate concentrated *in vacuo* to afford the product as a yellow oil (1.56 g, 9.06 mmol, 75%). The spectroscopic data presented below is in agreement with that previously published.

R_f = 0.60 (9 : 1, DCM : methanol, UV).

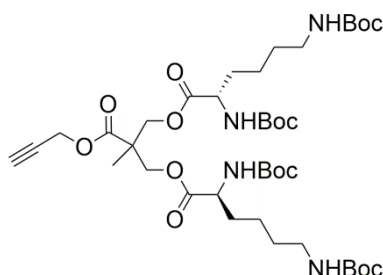
¹H NMR (400 MHz, CDCl₃) δ: 4.75 (d, CH≡CCH₂, ⁴J = 2.5 Hz, 2H); 3.92 (d, CH_aH_bO, ²J = 8.0 Hz, 2H); 3.72 (d, CH_aH_bO, ²J = 8.0 Hz, 2H); 2.48 (t, CH≡CCH₂, ⁴J = 2.5 Hz, 1H); 1.08 (s, CH₃CCO, 3H).

¹³C NMR (100 MHz, CDCl₃) δ: 174.92 (C=O, ester); 77.31 (CH₂C≡CH); 75.19 (C≡CH); 66.88 (2 × CH₂OH); 52.35 (C≡CH); 49.31 (CCOO); 16.95 (CH₃).

ESI-MS: 195.06 [M+Na]⁺ (100%), 171.06 [M+H]⁺ (37%).

HRMS: Calcd. [M+Na]⁺ (C₈H₁₂NaO₄) *m/z* = 195.0628, found [M+Na]⁺ = 195.0629 (error – 0.4 ppm).

IR ν [cm⁻¹]: 3279br w (C–H, alkyne), 2160m (C≡C), 2032m (C–H), 1971m, 1728m (C=O, ester), 1451w (C–H), 1030s, 1000m, 966m, 763m.

Propyne-[G1]-L-Lys(Boc)₂ (L: 5.11, D: 5.12)Molecular Formula: C₄₀H₆₈N₄O₁₄

Molecular Weight: 828.47

L-Lys(Boc)₂-succinimide (1.00 g, 2.25 mmol, 4 eq.), DMAP (138 mg, 1.13 mmol, 2 eq.) and DIPEA (491 μL, 2.82 mmol, 5 eq.) were dissolved together in dry DMF (15 mL). Propyne-[G1]-OH (97 mg, 0.56 mmol, 1 eq., pre-dissolved in dry DMF (10 mL)) was added to the reaction mixture, which was stirred at room temperature under an N₂ atmosphere for 48 hours. The volatiles were removed *in vacuo* to afford the crude product as a golden viscous oil. The crude product was purified in a portion-wise manner by gel permeation chromatography (DCM : methanol, 95 : 5) to afford the pure product as a golden foam (316 mg, 0.4 mmol, 68% effective yield). D-yield: 63%.

R_f = 0.78 (9 : 1, DCM : methanol, UV/ninhydrin).

¹H NMR (400 MHz, CD₃OD) δ: 4.76 (d, CH≡CCH₂, ⁴J = 2.6 Hz, 2H); 4.35 – 4.22 (m, 2 × CH₂O, 4H); 4.08 (br s, 2 × CHNH, 2H); 3.04 (t, 2 × CH₂NH, ³J = 6.4 Hz, 4H); 2.99 (t, CH≡CCH₂, ⁴J = 2.6 Hz, 1H); 1.82 – 1.73 (m, 2 × CH_aH_bCHNH, 2H); 1.69 – 1.57 (m, 2 × CH_aH_bCHNH, 2H); 1.44 (br s, 4 × C(CH₃)₃, 2 × CH₂CH₂NH, 2 × CH₂CH₂CH₂NH, 44H); 1.30 (s, CH₃, 3H).

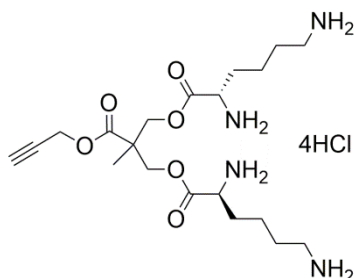
¹³C NMR (100 MHz, CD₃OD) δ: 173.80 (2 × C=O, lysine esters); 173.25 (C=O, Fréchet ester); 158.56, 158.06 (2 × C=O, carbamate); 80.61, 79.88 (2 × C(CH₃)₃); 78.47 (CH≡CCH₂); 76.97 (CH≡CCH₂); 66.86, 66.81 (CH₂O); 55.05 (2 × CHNH); 53.72 (CH≡CCH₂); 47.73 (CCOO); 40.98 (CH₂NH); 32.21 (CH₂CHNH); 30.56 (CH₂CH₂NH); 28.89, 28.84 (2 × C(CH₃)₃); 24.16 (CH₂CH₂CH₂NH); 18.09 (CH₃).

ESI-MS: 851.46 [M+Na]⁺ (100%), 829.48 [M+H]⁺ (81%).

HRMS: Calcd. [M+Na]⁺ (C₄₀H₆₈N₄O₁₄Na) *m/z* = 851.4624, found [M+Na]⁺ *m/z* = 851.4609 (error 2.0 ppm).

IR ν [cm^{-1}]: 3363 w (N–H), 2975 w (C–H), 1745 m (C=O, ester), 1689 s (CONH, carbamates I), 1512 m (CONH, carbamates II), 1454 w , 1365 m , 1247 m , 1158 s (C–O), 1101 m , 865 w , 781 w .

Propyne-[G1]-L-Lysine (5.13)



Chemical Formula: $\text{C}_{20}\text{H}_{40}\text{Cl}_4\text{N}_4\text{O}_6$

Molecular Weight: 574.37

Propyne-[G1]-L-Lys(Boc)₂ (52 mg, 63 μmol) was dissolved in methanol (10 mL) and gaseous HCl was bubbled through the solution for 15 seconds. The resulting reaction mixture was stirred at room temperature for 3 hours before being concentrated *in vacuo* to afford the product as an off-white crystalline solid (36 mg, 63 μmol , quantitative yield).

R_f = 0.15 streak (95 : 5, methanol : ammonium hydroxide, ninhydrin).

^1H NMR (400 MHz, CD_3OD) δ : 4.81 (exp d, app s, $\text{CH}\equiv\text{CCH}_2$, 2H); 4.85 – 4.40 (m, 2 \times CH_2O , 4H); 4.16 (exp dd, app br s, 2 \times CHNH_3^+ , 2H); 3.12 (exp t, app s, $\text{CH}\equiv\text{CCH}_2$, 1H); 2.99 (exp t, app s, 2 \times CH_2NH_3^+ , 4H); 1.98 (br s, 2 \times $\text{CH}_2\text{CHNH}_3^+$, 4H); 1.76 (br s, 2 \times $\text{CH}_2\text{CH}_2\text{NH}$, 4H); 1.59 – 1.48 (br m, 2 \times $\text{CH}_2\text{CH}_2\text{CH}_2\text{NH}_3^+$, 4H); 1.38 (s, CH_3 , 3H).

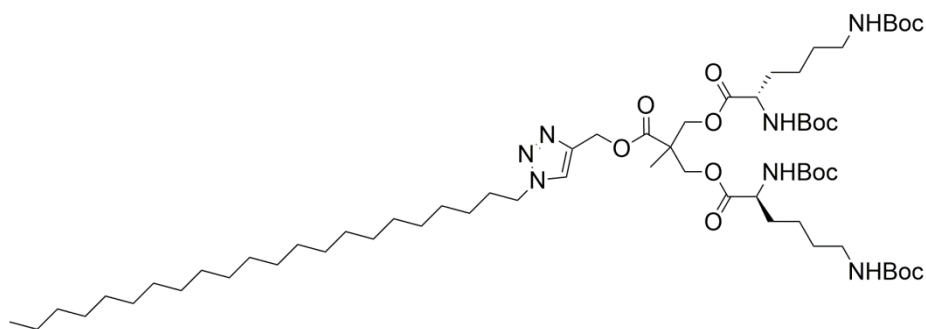
^{13}C NMR (100 MHz, CD_3OD) δ : 172.93 (C=O, Fréchet-ester); 170.17, 170.12 (C=O, lysine-ester); 78.48 ($\text{CH}\equiv\text{CCH}_2$); 77.35 ($\text{CH}\equiv\text{CCH}_2$); 68.18, 68.09 (CH_2O); 54.09 ($\text{CH}\equiv\text{CCH}_2$); 53.77 (2 \times CHNH_3^+); 47.62 (CCH_3); 40.36 (CH_2NH_3^+); 30.97 (CH_2CHNH_2); 28.04 ($\text{CH}_2\text{CH}_2\text{NH}_2$); 23.27 ($\text{CH}_2\text{CH}_2\text{CH}_2\text{NH}_3^+$); 17.99 (CH_3).

ESI-MS: 215.13 $[\text{M}+2\text{H}]^{2+}$ (100%), 429.27 $[\text{M}+\text{H}]^+$ (24%).

HRMS: Calcd. $[\text{M}+\text{H}]^+$ ($\text{C}_{20}\text{H}_{37}\text{N}_4\text{O}_6$) m/z = 429.2708, found $[\text{M}+\text{H}]^+$ m/z = 429.2715 (error – 2.0 ppm).

IR ν [cm^{-1}]: 3380 $br w$ (N–H), 3200 w (C–H, alkyne), 2917 s (C–H), 2850 s (C–H), 1740 m (C=O, esters), 1467 m , 1398 w , 1216 m , 1137 m (C–O), 1056 w , 997 m , 841 w .

α_D : + 7.4 (c. 1.0, MeOH).

***C*₂₂-[G1]-L-Lys(Boc)₂ (L: 5.14, D: 5.15)**Molecular Formula: C₆₂H₁₁₃N₇O₁₄

Molecular Weight: 1180.60

Propyne-[G1]-L-Lys(Boc)₂ (150 mg, 181 μmol, 1.1 eq.), behenoyl azide (58 mg, 164 μmol, 1 eq.), CuSO₄·5H₂O (4 mg, 16 μmol, 0.1 eq.) and sodium ascorbate (7 mg, 33 μmol, 0.2 eq.) were dissolved together in a mixture of degassed THF : water (4 : 1 v/v, 10 mL). The reaction mixture was stirred at room temperature under an N₂ atmosphere for 16 hours before being concentrated *in vacuo*. The resulting sludge was taken up in DCM (35 mL) and washed with deionised water (2 × 15 mL). The organic phase was collected, dried over MgSO₄ and the resulting filtrate concentrated *in vacuo* to afford the crude product as an off-white sticky solid. The crude product was purified by gel permeation chromatography (DCM) to afford the product as an off-white sticky foam (135 mg, 114 μmol, 70%). D-yield: 80%.

R_f = 0.70 (9 : 1, DCM : methanol, ninhydrin).

¹H NMR (400 MHz, CD₃OD) δ: 8.06 (s, triazoleCH, 1H); 5.26 (s, (triazole)CH₂O, 2H); 4.42 (t, CH₂Ntriazole, ³J = 7.0 Hz, 2H); 4.34 – 4.20 (m, 2 × CH₂O, 4H); 4.04 (exp dd, app br t, 2 × CHNH, ³J = 4.0 Hz, 2H); 3.04 (t, 2 × CH₂NH, ³J = 6.4 Hz, 4H); 1.91 (exp tt, app t, CH₂CH₂(triazole), ³J = 7.0 Hz, 2H); 1.77 – 1.69 (m, 2 × CH_aH_bCHNH, 2H); 1.65 – 1.56 (m, 2 × CH_aH_bCHNH, 4H); 1.44 (br s, 4 × C(CH₃)₃, 2 × CH₂CH₂NH, 40H); 1.29 (br s, 19 × alkylCH₂, CH₃CCO, 41H); 1.26 (br s, 2 × CH₂CH₂CH₂NH, 4H); 0.90 (t, alkylCH₃, ³J = 7.2 Hz, 3H).

¹³C NMR (100 MHz, CD₃OD) δ: 172.39 (3 × C=O, esters); 157.19, 157.15, 156.67 (total 4 × C=O, carbamate); 142.21 (triazoleCCH₂O); 124.62 (triazoleCH); 79.15, 78.45 (2 × C(CH₃)₃); 65.50 (2 × CH₂O); 57.90 ((triazole)CH₂O); 53.72, 53.68 (CHNH); 50.16 ((triazole)CH₂CH₂); 46.04 (Fréchet-C(CH₃)); 39.80, 39.67 (CH₂NH); 31.84 (2 × CH₂CHNH); 30.82 (2 × CH₂CH₂NH); 30.09 ((triazole)CH₂CH₂); 29.58 (19 ×

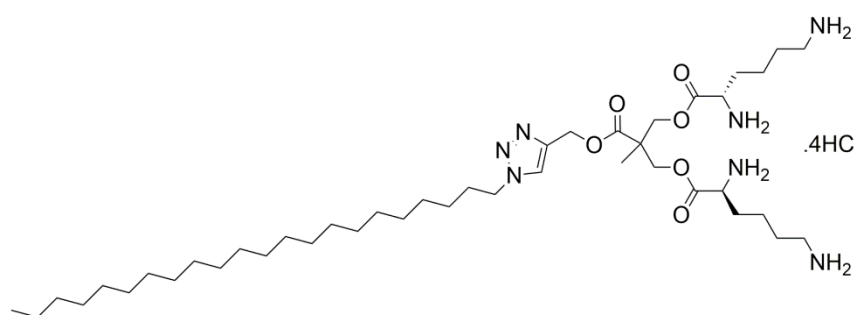
alkylCH₂); 28.89 (CH₃CH₂CH₂); 27.66, 27.61 (2 × C(CH₃)₃); 26.27 (CH₃CH₂); 22.82, 22.51 (CH₂CH₂CH₂NH); 16.87 (Fréchet-C(CH₃)); 13.35 (alkylCH₃).

ESI-MS: 1202.82 [M+Na]⁺ (100%), 1180.84 [M+H]⁺ (83%).

HRMS: Calcd. [M+Na]⁺ (C₆₂H₁₁₃N₇O₁₄Na) *m/z* = 1202.8238, found [M+Na]⁺ *m/z* = 1202.8224 (error 1.5 ppm).

IR ν [cm⁻¹]: 3356*br w* (N–H), 2976*m* (C–H), 2924*s* (C–H), 2854*m* (C–H), 1745*m* (C=O, esters), 1694*s* (CONH, carbamates I), 1516*m* (CONH, carbamates II), 1456*m*, 1392*w*, 1366*m*, 1248*m*, 1163*s* (C–O), 1048*m*, 1019*m*, 866*w*, 781*w*.

C₂₂-[G1]-L-Lysine (L: 5.16, D: 5.17)



Molecular Formula: C₄₂H₈₅N₇O₆Cl₄

Molecular Weight: 925.98

C₂₂-[G1]-L-Lys(Boc)₂ (127 mg, 108 μmol) was dissolved in methanol (10 mL) and gaseous HCl was bubbled through the solution for 15 seconds. The reaction mixture was stirred at room temperature for 3 hours before being concentrated *in vacuo* to afford the product as a cream crystalline solid (100 mg, 108 μmol, quantitative yield). D-yield: quantitative.

R_f = 0.00 (ammonium hydroxide, ninhydrin).

¹H NMR (400 MHz, CD₃OD) δ: 8.56 (s, triazoleCH, 1H); 5.40 (s, (triazole)CH₂O, 2H); 4.61 – 4.42 (comp m, 2 × Fréchet-CH₂O, (triazole)CH₂CH₂, 6H); 4.17 (exp dd, app t, 2 × CHNH₃⁺, ³J = 6.0 Hz, 2H); 3.01 (t, 2 × CH₂NH₃⁺, ³J = 7.0 Hz, 4H); 2.05 – 1.91 (br s, 2 × CH₂CHNH₂, CH₂CH₂(triazole), 6H); 1.82 – 1.74 (m, 2 × CH₂CH₂NH₃⁺, 4H); 1.66 – 1.48 (br m, 2 × CH₂CH₂CH₂NH₃⁺, 4H); 1.37 (s, CH₃CCOO, CH₂CH₂CH₂CH₂(triazole), 7H); 1.28 (br s, 17 × alkylCH₂, 34H); 0.89 (t, CH₃(CH₂)₂₁, ³J = 6.8 Hz, 3H).

¹³C NMR (100 MHz, CD₃OD) δ: 173.17, 170.04 (total 3 × C=O, esters); 141.46 (triazoleCCH₂O); 128.07 (triazoleCH); 67.88 (2 × Fréchet-CH₂O); 57.91 ((triazole)CH₂O); 53.80, 53.74 (CHNH₃⁺); 53.05 ((triazole)CH₂CH₂); 47.62 (Fréchet-

C(CH₃); 40.37, 40.28 (CH₂NH₃⁺); 33.07 (CH₂CH₂CH₃); 30.79 (17 × alkylCH₂); 30.48 (2 × CH₂CHNH₃⁺); 30.13 (CH₂CH₂NH₃⁺); 27.88, 27.42 (CH₂CH₂CH₂(triazole)); 23.74, 23.16 (CH₂CH₂CH₂NH₂⁺); 18.00 (Fréchet-C(CH₃)); 14.55 (alkylCH₃).

ESI-MS: 390.82 [M+2H]²⁺ (100%), 274.56 [M+2Na+H]³⁺ (80%), 260.88 [M+3H]³⁺ (75%), 780.63 [M+H]⁺ (11%).

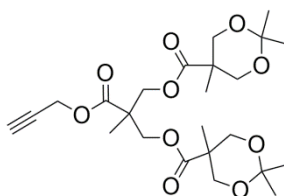
HRMS: Calcd. [M+2H]²⁺ (C₄₂H₈₃N₇O₆) *m/z* = 390.8197, found [M+2H]²⁺ *m/z* = 390.8179 (error 4.6 ppm).

IR ν [cm⁻¹]: 3393*br w* (N–H), 2917*s* (C–H), 2850*s* (C–H), 1743*s* (C=O, ester), 1600*w*, 1506*m*, 1468*m*, 1380*w*, 1280*m*, 1214*s*, 1134*s*, 1054*w*, 998*m*.

θ_L: + 38.9 mdeg (225 nm, 10 mM, MeOH).

θ_D: – 45.8 mdeg (225 nm, 10 mM, MeOH).

***Propyne-[G2]-isopropylidene*³²⁵ (5.18)**



Molecular Formula: C₂₄H₃₆O₁₀

Molecular Weight: 484.23

Propyne-[G1]-OH (1.53 g, 8.89 mmol) and DMAP (0.83 g, 6.79 mmol) were dissolved together in DCM (50 mL) before pyridine (2.7 mL, 34.52 mmol) was added. To this, isopropylidene-2,2-bis(hydroxymethyl)propionic anhydride (8.80 g, 26.64 mmol, pre-dissolved in DCM (15 mL)) was added and the reaction was stirred overnight at room temperature. The excess anhydride was quenched with a mixture of pyridine : deionised water (1 : 1, 10 mL) and the reaction was stirred overnight once more. After diluting with DCM (60 mL), the reaction mixture was washed successively with NaHSO₄ (3 × 30 mL, 1.33 M), Na₂CO₃ (3 × 30 mL, 10%) and saturated brine (30 mL). The organic phase was dried over MgSO₄ and the resulting filtrate was concentrated *in vacuo* to afford the crude product as an opaque cream oil. This crude product was purified by flash column chromatography (SiO₂, cyclohexane : ethyl acetate, 3 : 1 → 1 : 1) to afford the product as a golden oil (2.65 g, 5.47 mmol, 57 %). The spectroscopic data presented below is in agreement with that previously published.

R_f = 0.51 (1 : 1, cyclohexane : ethyl acetate, UV).

^1H NMR (400 MHz, CDCl_3) δ : 4.71 (d, $\text{CH}\equiv\text{CCH}_2$, $^4\text{J} = 2.4$ Hz, 2H); 4.32 (d, $2 \times \text{CH}_{ax}\text{H}_{eq}\text{O}$, $^2\text{J} = 12.0$ Hz, 2H); 4.15 (d, $2 \times \text{CH}_{ax}\text{H}_{eq}\text{O}$, $^2\text{J} = 12.0$ Hz, 4H); 3.61 (d, $\text{CH}_a\text{H}_b\text{O}$, $^2\text{J} = 12.0$ Hz, 4H); 2.46 (t, $\text{CH}\equiv\text{CCH}_2$, $^4\text{J} = 2.4$ Hz, 1H); 1.40 (d, $4 \times \text{CH}_3$, $^4\text{J} = 2.4$ Hz, 12H); 1.35 (s, $2 \times \text{CH}_3$, 6H); 1.30 (s, CH_3 , 3H).

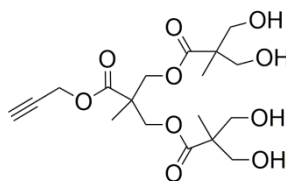
^{13}C NMR (100 MHz, CDCl_3) δ : 173.58, 171.92 (total $3 \times \text{C}=\text{O}$, ester); 98.16 ($2 \times \text{C}(\text{CH}_3)_2$); 77.27 ($\text{CH}_2\text{C}\equiv\text{CH}$); 75.40 ($\text{C}\equiv\text{CH}$); 66.02 ($6 \times \text{CH}_2\text{O}$); 52.74 ($\text{C}\equiv\text{CH}$); 46.87, 42.12 (total $3 \times \text{CCOO}$); 25.14, 22.22, 18.56, 17.65 (total $5 \times \text{CH}_3$).

ESI-MS: 507.22 $[\text{M}+\text{Na}]^+$ (100%).

HRMS: Calcd. $[\text{M}+\text{Na}]^+$ ($\text{C}_{24}\text{H}_{36}\text{NaO}_{10}$) $m/z = 507.2201$, found $[\text{M}+\text{Na}]^+$ $m/z = 507.2196$ (error 0.9 ppm).

IR ν [cm^{-1}]: 3264 w (C–H, alkyne), 2986 m (C–H), 2100 w (C=C), 1736 s (C=O, esters), 1458 m , 1373 m , 1219 s , 1118 s , 1080 s , 1003 m , 934 m , 826 s .

Propyne-[G2]-OH³²⁵ (5.19)



Molecular Formula: $\text{C}_{18}\text{H}_{28}\text{O}_{10}$

Molecular Weight: 404.17

Propyne-[G2]-isopropylidene (2.16 g, 4.46 mmol) and DOWEX-50WX2 (3.24 g, 1.5 eq. wt.) were dissolved in methanol (55 mL) and stirred at 40°C for 2 hours. The reaction mixture was filtered through a celite-containing sinter funnel and the resulting filtrate was concentrated *in vacuo* affording a sludge which was taken up in chloroform. A precipitate was allowed to form overnight, before being collected by filtration as a white crystalline solid (1.30 g, 3.22 mmol, 72%). The spectroscopic data presented below is in agreement with that previously published.

$R_f = 0.50$ (9 : 1, DCM : methanol, UV).

^1H NMR (400 MHz, CDCl_3) δ : 4.74 (d, $\text{CH}\equiv\text{CCH}_2$, $^4\text{J} = 2.4$ Hz, 2H); 4.47 – 4.25 (m, $4 \times \text{CH}_2\text{O}$, 8H); 3.81 – 3.62 (m, $2 \times \text{CH}_2\text{O}$, 4H); 3.24 (br s, $4 \times \text{OH}$, 4H); 2.49 (t, $\text{CH}\equiv\text{CCH}_2$, $^4\text{J} = 2.4$ Hz, 1H); 1.33 (s, CH_3 , 3H); 1.05 (s, $2 \times \text{CH}_3$, 6H).

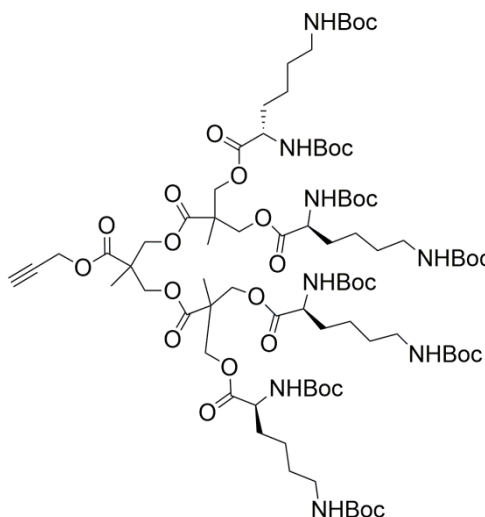
^{13}C NMR (100 MHz, CD_3OD) δ : 175.87, 173.62 (total $3 \times \text{C}=\text{O}$); 78.52 ($\text{CH}_2\text{C}\equiv\text{CH}$); 76.72 ($\text{C}\equiv\text{CH}$); 66.28, 66.78, ($3 \times \text{CH}_2\text{O}$); 53.56 ($\text{C}\equiv\text{CH}$); 51.76 ($2 \times \text{G2-CCOO}$); 47.83 (G1-CCOO); 18.09, 17.29 (total $3 \times \text{CH}_3$).

ESI-MS: 427.16 $[\text{M}+\text{Na}]^+$ (100%), 405.18 $[\text{M}+\text{H}]^+$ (56%).

HRMS: Calcd. $[\text{M}+\text{Na}]^+$ ($\text{C}_{18}\text{H}_{28}\text{NaO}_{10}$) $m/z = 427.1575$, found $[\text{M}+\text{Na}]^+$ $m/z = 427.1579$ (error – 1.1 ppm).

IR ν [cm^{-1}]: 3397 $br w$ (O–H), 3256 m (C–H, alkyne), 2944 w (C–H), 2160 m ($\text{C}\equiv\text{C}$), 1731 s (C=O, esters), 1716 s (C=O, ester), 1236 m (C–O), 1210 s (C–O), 1129 s , 1065 m , 1019 s , 1006 s , 717 m , 681 m , 654 m .

Propyne-[G2]-L-Lys(Boc) $_2$ (L: 5.20, D: 5.21)



Molecular Formula: $\text{C}_{82}\text{H}_{140}\text{N}_8\text{O}_{30}$

Molecular Weight: 1718.02

L-Lys(Boc) $_2$ -succinimide (1.00 g, 2.25 mmol, 8 eq.), DMAP (138 mg, 1.13 mmol, 4 eq.) and DIPEA (442 μL , 2.54 mmol, 9 eq.) were dissolved together in dry DMF (15 mL). Propyne-[G2]-OH (114 mg, 0.28 mmol, 1 eq., pre-dissolved in dry DMF (10 mL)), was added to the reaction mixture, which was stirred at room temperature under an N_2 atmosphere for 48 hours. The volatiles were removed *in vacuo* to afford the crude product as a golden viscous oil. The crude product was purified by gel permeation chromatography (DCM : methanol, 95 : 5) to afford the pure product as a golden foam (400 mg, 0.20 mmol, 83%). D-yield: 90%.

$R_f = 0.68$ (9 : 1, DCM : methanol, UV/ninhydrin).

^1H NMR (400 MHz, CD_3OD) δ : 4.79 (d, $\text{CH}\equiv\text{CCH}_2$, $^4\text{J} = 2.4$ Hz, 2H); 4.37 – 4.22 (m, $6 \times \text{CH}_2\text{O}$, 12H); 4.09 (exp dd, app br s, $4 \times \text{CHNH}$, 4H); 3.04 (t, $4 \times \text{CH}_2\text{NH}$, $^3\text{J} = 6.8$ Hz, 8H); 2.99 (t, $\text{CH}\equiv\text{CCH}_2$, $^4\text{J} = 2.4$ Hz, 1H); 1.83 – 1.74 (m, $4 \times \text{CH}_a\text{H}_b\text{CHNH}$, 4H); 1.69 – 1.60 (m, $4 \times \text{CH}_a\text{H}_b\text{CHNH}$, 4H); 1.51 – 1.36 (br s, $8 \times \text{C}(\text{CH}_3)_3$, $4 \times \text{CH}_2\text{CH}_2\text{NH}$, $4 \times \text{CH}_2\text{CH}_2\text{CH}_2\text{NH}$, 88H); 1.33 (s, $[\text{G1}]\text{-CH}_3\text{CCO}$, 3H); 1.29 (s, $2 \times [\text{G2}]\text{-CH}_3\text{CCO}$, 6H).

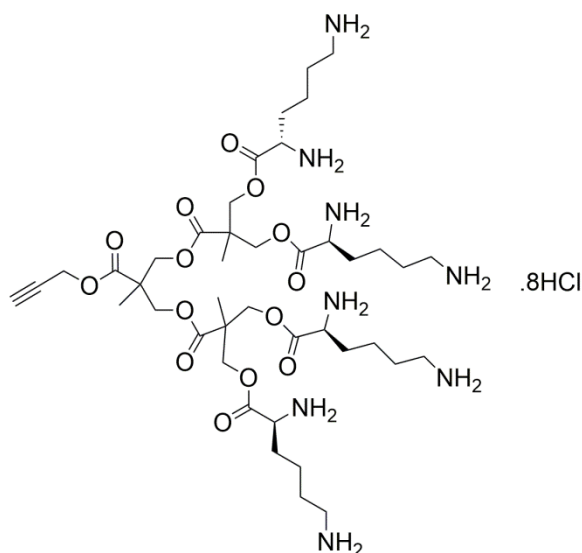
^{13}C NMR (100 MHz, CD_3OD) δ : 173.84 ($4 \times \text{C}=\text{O}$, lysine-esters); 173.39, 173.20 (total $3 \times \text{C}=\text{O}$, Fréchet-esters); 158.52, 157.98 ($4 \times \text{C}=\text{O}$, carbamates); 80.59, 79.86 ($4 \times \text{C}(\text{CH}_3)_3$); 78.61 ($\text{CH}\equiv\text{CCH}_2$); 77.17 ($\text{CH}\equiv\text{CCH}_2$); 67.09, 66.75 (total $6 \times \text{CH}_2\text{O}$); 55.07 ($4 \times \text{CHNH}$); 53.88 ($\text{CH}\equiv\text{CCH}_2$); 48.01, 47.87 (total $3 \times \text{Fréchet-C}(\text{CH}_3)$); 41.02 (CH_2NH); 32.23 (CH_2CHNH); 30.59 ($\text{CH}_2\text{CH}_2\text{NH}$); 28.93 ($8 \times \text{C}(\text{CH}_3)_3$); 24.20 ($\text{CH}_2\text{CH}_2\text{CH}_2\text{NH}$); 18.30, 18.15 (total $3 \times \text{Fréchet-C}(\text{CH}_3)$).

ESI-MS: 1717.98 $[\text{M}+\text{H}]^+$ (100%).

HRMS: Calcd. $[\text{M}+\text{H}]^+$ ($\text{C}_{82}\text{H}_{141}\text{N}_8\text{O}_{30}$) $m/z = 1717.9748$, found $[\text{M}+\text{H}]^+$ $m/z = 1717.9798$ (error – 1.9 ppm).

IR ν [cm^{-1}]: 3368 w (N–H), 2972 w (C–H), 1745 m (C=O, esters), 1688 s (CONH, carbamates I), 1515 m (CONH, carbamates II), 1365 m , 1247 m , 1160 s (C–O), 1011 m , 866 w , 763 w , 763 w .

Propyne-[G2]-L-Lysine (5.22)



Molecular Formula: $\text{C}_{42}\text{H}_{84}\text{Cl}_8\text{N}_8\text{O}_{14}$

Molecular Weight: 1208.79

Propyne-[G2]-L-Lys(Boc)₂ (74 mg, 43 μmol) was dissolved in methanol (12 mL) and gaseous HCl was bubbled through the solution for 20 seconds. The resulting reaction mixture was stirred at room temperature for 2.5 hours before being concentrated *in vacuo* to afford the product as transparent needle-like crystals (50 mg, 41 μmol, 96%).

R_f = 0.00 (9 : 1, DCM : methanol, ninhydrin); 0.88 (100% ammonium hydroxide, ninhydrin).

¹H NMR (400 MHz, CD₃OD) δ: 4.82 (exp d, app s, CH≡CCH₂, 2H); 4.51 – 4.28 (br m, 6 × CH₂O, 12H); 4.20 (exp dd, app br s, 4 × CHNH₃⁺, 4H); 3.13 (exp t, app s, CH≡CCH₂, 1H); 3.00 (br t, 4 × CH₂NH₃⁺, ³J = 6.4 Hz, 8H); 2.01 (br s, 4 × CH₂CHNH₃⁺, 8H); 1.78 (br s, 4 × CH₂CH₂NH₃⁺, 8H); 1.60 – 1.54 (br m, 4 × CH₂CH₂CHNH₃⁺, 8H); 1.38 (s, 3 × CH₃, 9H).

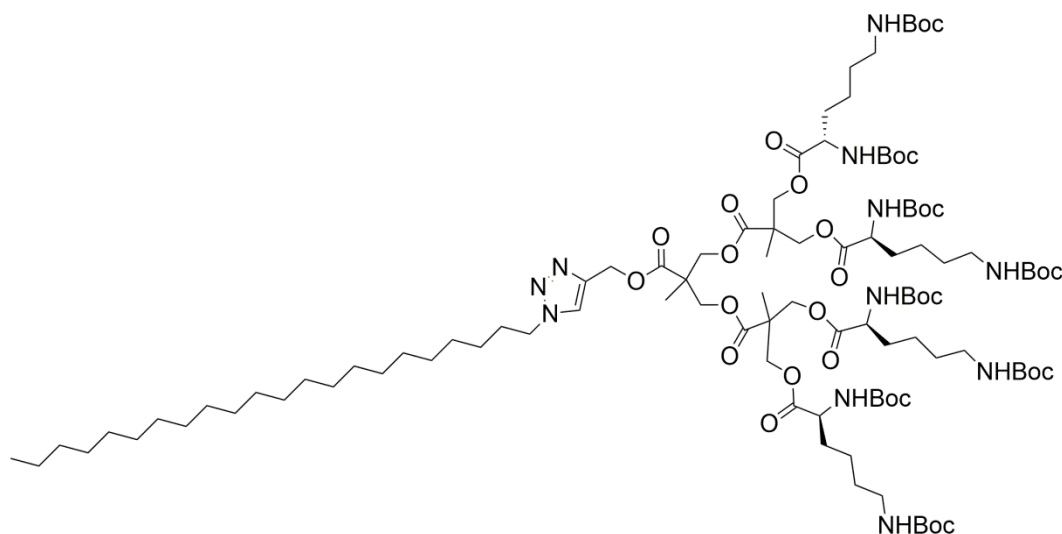
¹³C NMR (100 MHz, CD₃OD) δ: 173.37, 173.12 (total 3 × C=O, Fréchet-esters); 170.21 (4 × C=O, lysine-esters); 78.68 (CH≡CCH₂); 77.46 (CH≡CCH₂); 67.87, 67.50 (total 6 × CH₂O); 54.05 (CH≡CCH₂); 53.83 (4 × CHNH₃⁺); 47.73 (3 × C(CH₃)); 40.44, 40.35 (2 × CH₂NH₃⁺); 30.93 (CH₂CHNH₃⁺); 28.01 (CH₂CH₂NH₃⁺); 23.27 (CH₂CH₂CH₂NH₃⁺); 18.29, 18.08 (total 3 × CH₃).

ESI-MS: 230.14 [M+4H]⁴⁺ (100%), 306.52 [M+3H]³⁺ (49%).

HRMS: Calcd. [M+3H]³⁺ (C₄₂H₇₉N₈O₁₄) *m/z* = 306.5233, found [M+3H]³⁺ *m/z* = 306.5220 (error 3.8).

IR ν [cm⁻¹]: 3384*br w* (N–H), 3201*w* (C–H, alkyne), 2918*s* (C–H), 2851*m* (C–H), 2250*w* (C≡C), 1739*s* (C=O, esters), 1601*w*, 1508*m*, 1470*m*, 1397*w*, 1294*m*, 1211*s*, 1132*s*, 996*m*.

α_D: + 7.1 (c. 1.0, MeOH).

***C*₂₂-[G2]-L-Lys(Boc)₂ (L: 5.23, D: 5.24)**Molecular Formula: C₁₀₄H₁₈₅N₁₁O₃₀

Molecular Weight: 2069.64

Propyne-[G2]-L-Lys(Boc)₂ (200 mg, 116 μmol, 1.1 eq.), behenoyl azide (37 mg, 106 μmol, 1 eq.), CuSO₄·5H₂O (3 mg, 12 μmol, 0.1 eq.) and sodium ascorbate (4 mg, 21 μmol, 0.2 eq.) were dissolved together in a mixture of degassed THF : water (4 : 1 v/v, 10 mL). The reaction mixture was stirred at room temperature under an N₂ atmosphere for 15.5 hours before being concentrated *in vacuo*. The resulting sludge was taken up in DCM (35 mL) and washed with deionised water (2 × 15 mL). The organic phase was collected, dried over MgSO₄ and the resulting filtrate was concentrated *in vacuo* to afford the crude product as a grey-white viscous oil. The crude product was purified by gel permeation chromatography (DCM) to afford the product as a transparent golden oil (18 mg, 9 μmol, 8%). D-yield: 15%.

R_f = 0.67 (9 : 1, DCM : methanol, ninhydrin).

¹H NMR (400 MHz, CD₃OD) δ: 8.08 (s, triazoleCH, 1H); 5.29 (s, (triazole)CH₂O, 2H); 4.23 (t, CH₂Ntriazole, ³J = 7.2 Hz, 2H); 4.36 – 4.15 (m, 6 × Fréchet-CH₂O, 12H); 4.09 (exp dd, app br t, 4 × CHNH, ³J = 4.0 Hz, 4H); 3.04 (t, 4 × CH₂NH, ³J = 6.6 Hz, 8H); 1.96 – 1.88 (m, CH₂CH₂(triazole), 2H); 1.82 – 1.73 (m, 4 × CH_aH_bCHNH, 4H); 1.68 – 1.59 (m, 4 × CH_aH_bCHNH, 4H); 1.44 (br s, 8 × C(CH₃)₃, 4 × CH₂CH₂NH and [G1]-CH₃, 83H); 1.33 (br s, 4 × CH₂CH₂CH₂NH, 8H); 1.29 (s, 19 × alkylCH₂, 38H); 1.23 (s, 2 × [G2]-CH₃, 6H); 0.90 (t, CH₃(CH₂)₂₁, ³J = 7.2 Hz, 3H).

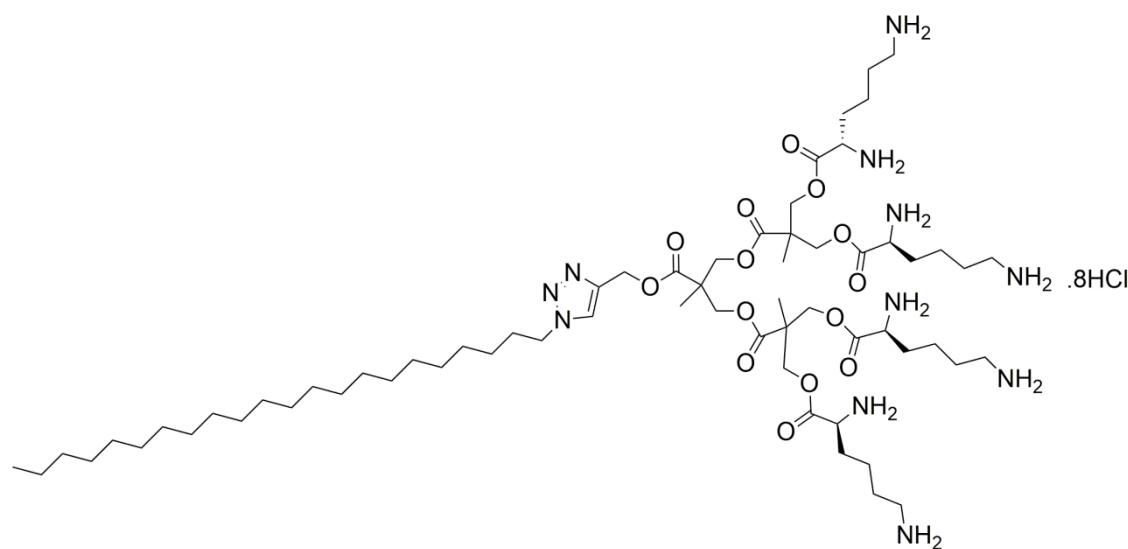
¹³C NMR (100 MHz, CD₃OD) δ: Absence of some signals due to large molecular weight / small amount of material in sample. 177.83, 173.87 (total 7 × C=O, esters);

158.57, 158.03, ($4 \times \text{C}=\text{O}$, carbamate); expt ~ 142 , not seen (triazole CCH_2O); 121.17 (triazole CH); 80.57, 79.87 ($4 \times \text{C}(\text{CH}_3)_3$); 67.11, 67.08, 66.71 ($2 \times \text{Fréchet-CH}_2\text{O}$); 60.17 ((triazole) CH_2O); 55.11 ($4 \times \text{CHNH}$); 51.42 ((triazole) CH_2CH_2); 48.01 (Fréchet- $\text{C}(\text{CH}_3)$); 41.05 ($4 \times \text{CH}_2\text{NH}$); 33.14 ($4 \times \text{CH}_2\text{CHNH}$); 32.26 ($4 \times \text{CH}_2\text{CH}_2\text{NH}$); 31.41 ((triazole) CH_2CH_2); 30.83 ($18 \times \text{alkylCH}_2$); 30.54 (CH_2CH_3); 28.94 ($8 \times \text{C}(\text{CH}_3)_3$); 24.56 ($4 \times \text{CH}_2\text{CH}_2\text{CH}_2\text{NH}$); 18.26, 18.21, 17.76 (Fréchet- $\text{C}(\text{CH}_3)$); 14.53 (alkyl CH_3).
ESI: 1057.64 $[\text{M}+2\text{Na}]^{2+}$ (100%), 2092.31 $[\text{M}+\text{Na}]^+$ (23%).

HRMS: Calcd. $[\text{M}+\text{Na}]^+$ ($\text{C}_{104}\text{H}_{186}\text{N}_{11}\text{O}_{30}\text{Na}$) $m/z = 2092.3259$, found $[\text{M}+\text{Na}]^+$ $m/z = 2092.3098$ (error 9.0 ppm).

IR ν [cm^{-1}]: 3366 $br w$ (N–H), 2983 m (C–H), 2924 m (C–H), 2855 m (C–H), 1741 m (C=O, esters), 1694 s (CONH, carbamates I), 1514 m (CONH, carbamates II), 1456 m , 1392 w , 1365 m , 1247 m , 1160 s (C–O), 1047 m , 1012 m , 864 w , 779 w .

*C*₂₂-[G2]-L-Lysine (L: 5.25, D: 5.26)



Molecular Formula: $\text{C}_{64}\text{H}_{129}\text{N}_{11}\text{O}_{14}\text{Cl}_8$

Molecular Weight: 1560.40

*C*₂₂-[G2]-L-Lys(Boc)₂ (18 mg, 9 μmol) was dissolved in methanol (10 mL) and gaseous HCl was bubbled through the solution for 15 seconds. The reaction mixture was stirred at room temperature for 3 hours before being concentrated *in vacuo* to afford the product as a white crystalline solid (11 mg, 7 μmol , 78%). D-yield: quantitative.

$R_f = 0.00$ (ammonium hydroxide, ninhydrin).

^1H NMR (400 MHz, CD_3OD) δ : 8.21 (s, triazole CH , 1H); 5.31 (s, (triazole) CH_2O , 2H); 4.96 – 4.27 (br m, (triazole) CH_2CH_2 , 6 \times Fréchet CH_2O , 14H); 4.21 (exp dd, app s, 4 \times

CHNH_3^+ , 4H); 3.01 (t, $4 \times \text{CH}_2\text{NH}_3^+$, $^3\text{J} = 6.4$ Hz, 8H); 2.09 – 1.90 (br m, $\text{CH}_2\text{CH}_2(\text{triazole})$, $4 \times \text{CH}_2\text{CHNH}_3^+$, 10H); 1.78 (br s, $4 \times \text{CH}_2\text{CH}_2\text{NH}_2^+$, 8H); 1.66 – 1.49 (m, $4 \times \text{CH}_2\text{CH}_2\text{CH}_2\text{NH}_3^+$, 8H); 1.35, 1.32 (s, total $3 \times \text{CH}_3\text{C}(\text{CO})$ and $\text{CH}_2\text{CH}_2\text{CH}_2(\text{triazole})$, 11H) 1.29 (s, $18 \times \text{alkylCH}_2$, 36H); 0.90 (t, alkylCH_3 , $^3\text{J} = 7.2$ Hz, 3H).

^{13}C NMR (100 MHz, CD_3OD) δ : Absence of some signals due to large molecular weight / small amount of material in sample. 170.23 (total $7 \times \text{C}=\text{O}$, esters); expt ~145, not seen ($\text{triazoleCCH}_2\text{O}$); 128 (triazoleCH); 67.97, 67.93 (total $6 \times \text{Fréchet-CH}_2\text{O}$); exp ~ 58, not seen ($(\text{triazole})\text{CH}_2\text{O}$) 53.88 ($4 \times \text{CH}_2\text{NH}_3^+$); 51.74 ($(\text{triazole})\text{CH}_2\text{CH}_2$); 47.73 ($\text{Fréchet-C}(\text{CH}_3)$); 40.38 ($4 \times \text{CH}_2\text{NH}_3^+$); 33.12 ($4 \times \text{CH}_2\text{CHNH}_3^+$); 31.00 ($\text{CH}_2\text{CH}_2\text{CH}_3$); 30.81 ($17 \times \text{alkylCH}_2$); 28.06 ($4 \times \text{CH}_2\text{CH}_2\text{NH}_3^+$); 27.64 ($(\text{triazole})\text{CH}_2\text{CH}_2$); 23.78 (CH_2CH_3); 23.31 ($4 \times \text{CH}_2\text{CH}_2\text{CH}_2\text{NH}_3^+$); 18.21 ($3 \times \text{Fréchet-C}(\text{CH}_3)$); 14.50 (alkylCH_3).

ESI-MS: 634.96 $[\text{M}+2\text{H}]^{2+}$ (100%), 570.91 $[\text{M-Lys}+2\text{H}]^{2+}$ (99%) where Lys = $\text{C}_6\text{H}_{13}\text{N}_2\text{O}$ and lysine-loss is a likely mass spectrometric effect.

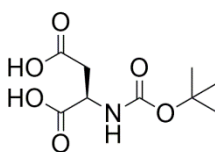
HRMS: Calcd. $[\text{M}+2\text{H}]^{2+}$ ($\text{C}_{64}\text{H}_{123}\text{N}_{11}\text{O}_{14}$) $m/z = 634.9620$, found $[\text{M}+2\text{H}]^{2+}$ $m/z = 634.9585$ (error 5.3 ppm).

IR ν [cm^{-1}]: 3396br w (N–H), 2918s (C–H), 2852s (C–H), 1736s (C=O, esters), 1601w, 1504m, 1470m, 1398w, 1297w, 1212s, 1131s (C–O), 1060m, 997s.

θ_L : + 72.9 mdeg (225 nm, 10 mM, MeOH).

θ_D : – 70.6 mdeg (225 nm, 10 mM, MeOH).

D-Asp-Boc (L: 6.1, D: 6.2)



Chemical Formula: $\text{C}_9\text{H}_{15}\text{NO}_6$

Molecular Weight: 233.22

D-Aspartic acid (1.70 g, 12.75 mmol) and NaOH pellets (1.02 g, 25.50 mmol) were dissolved together in deionised water (20 mL) before the solution was cooled to 0°C . Di-*tert*-butyl dicarbonate (3.06 g, 14.11 mmol) was dissolved separately in dioxane (20 mL) before being added to the reaction mixture dropwise in one portion over 1 hour. The resulting reaction mixture was stirred at 0°C for 2 hours and room temperature for a

further 2 hours. Volatiles were removed *in vacuo*, and the resulting residue was taken up in deionised water and washed with diethyl ether. The aqueous layer was acidified to pH 2 using NaHSO₄ (1.33 M, pH paper) after which the product was extracted into diethyl ether. This organic layer was collected, dried over MgSO₄ and the resulting filtrate concentrated *in vacuo* to afford the product as a white solid (1.48 g, 6.43 mmol, 50%). R_f = 0.26 (9 : 1 DCM : methanol, ninhydrin).

¹H NMR (400 MHz, CD₃OD) δ: 5.04 (br s, NH, 2 × OH, 3H); 4.46 (exp dd, app t, CHNH, ³J = 5.6 Hz, 1H); 2.82 (dd, ²J³J = 16.6 Hz, 5.2 Hz, CH_aH_bCHNH, 1H); 2.77 (dd, ²J³J = 16.6 Hz, 6.4 Hz, CH_aH_bCHNH, 1H); 1.44 (s, C(CH₃)₃, 9H).

¹³C NMR (100 MHz, CD₃OD) δ: 174.66, 174.19 (C=O, acid); 157.76 (C=O, carbamate); 80.78 (C(CH₃)₃); 51.37 (CHNH); 37.27 (CH₂CHN); 28.71 (C(CH₃)₃).

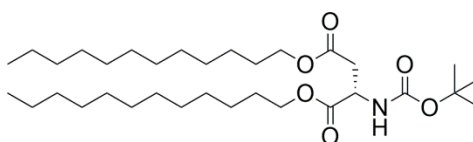
ESI-MS: 256.08 [M+Na]⁺ (100%).

HRMS: Calcd. [M+Na]⁺ (C₉H₁₅NNaO₆) m/z = 256.0792, found [M+Na]⁺ m/z = 256.0795 (error -1.6 ppm).

IR ν [cm⁻¹]: 3354w (N-H), 2978br m (O-H, C-H), 2930br m (O-H, C-H), 1703s (C=O, acid), 1700s (C=O, acid), 1688s (CONH, carbamate I), 1533m, 1514m (CONH, carbamate II), 1409m (C-O), 1393w, 1368w, 1336m (C-H), 1286w, 1250m (C-O), 1157s, 1060m (C-N stretch), 1031w, 1002w, 974m, 860w, 786w, 747w.

α_D: + 4.6 (c. 1.0, CHCl₃).

(C₁₂)₂-L-Asp-Boc (L: 6.3, D: 6.4)



Chemical Formula: C₃₃H₆₃NO₆

Molecular Weight: 569.87

Boc-L-Asp-(OH)₂ (1.00 g, 4.28 mmol, 1 eq.), 1-dodecanol (3.20 g, 17.2 mmol, 4 eq.), DCC (1.77 g, 8.58 mmol, 2 eq.) and DMAP (1.05 g, 8.58 mmol, 2 eq.) were dissolved together in anhydrous DCM (50 mL). The stirred mixture was kept for 10 minutes at 0°C before being allowed to warm to room temperature and left overnight under an N₂ atmosphere. The DCU by-product was removed by filtration through a celite-containing sinter funnel and the filtrate concentrated to a residue *in vacuo*. This residue was taken up in DCM (60 mL) and washed successively with HCl (2 × 30 mL, 0.5 M) and

NaHCO₃ (30 mL, sat.). The organic phase was collected, dried over MgSO₄ and the resulting filtrate concentrated *in vacuo* to afford a clear yellow residue. Purification by flash column chromatography (SiO₂, 95 : 5, DCM : ethyl acetate) afforded pure product as a white powdery solid (877 mg, 1.54 mmol, 36%). D-yield: 45%.

R_f = 0.95 (9 : 1 DCM : methanol, ninhydrin).

¹H NMR (400 MHz, CDCl₃) δ: 5.49 (d, NH, 1H); 4.52 (exp dd, app t, CHNH, ³J = 4.4 Hz, 1H); 4.18 – 4.10 (exp t, app m, CH₂OC(O)CH₂, 2H); 4.05 (t, CH₂OC(O)CH, ³J = 6.8 Hz, 2H); 2.99 (dd, CH_aH_bCHNH, ²J³J = 17.2 Hz, 4.4 Hz, 1H); 2.77 (dd, CH_aH_bCHNH, ²J³J = 17.2 Hz, 4.4 Hz, 1H); 1.65 – 1.59 (m, CH₂CH₂O, 4H); 1.44 (s, C(CH₃)₃, 9H); 1.23 (br s, 18 × alkylCH₂, 36H); 0.88 (t, 2 × alkylCH₃, ³J = 6.4 Hz, 6H).

¹³C NMR (100 MHz, CDCl₃) δ: 171.14, 171.03 (C=O, ester); 155.43 (C=O, carbamate); 80.00 (C(CH₃)₃); 65.88, 65.19 (CH₂O); 49.84 (CHNH); 36.80 (CH₂CHNH); 31.90, 29.62, 29.57, 29.51, 29.34, 29.23, 28.50, 28.45, 28.28 (alkylCH₂); 25.84, 25.79 (CH₂CH₂O); 22.67 (C(CH₃)₃); 14.11 (alkylCH₃).

ESI-MS: 592.45 [M+Na]⁺ (100%), 570.47 [M+H]⁺ (44%).

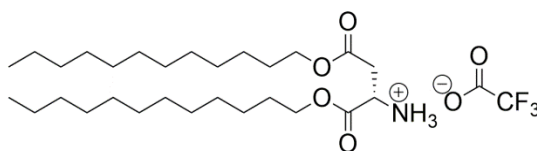
HRMS: Calcd. [M+Na]⁺ (C₃₃H₆₃NNaO₆) m/z = 592.4548, found [M+Na]⁺ m/z = 592.4520 (error 3.9 ppm).

IR ν [cm⁻¹]: 3403_w (N–H stretch), 2955_w, 2918_s (C–H), 2851_m (C–H), 1733_s (C=O, esters), 1709_s (CONH, carbamate I), 1506_m (CONH, carbamate II), 1467_m, 1456_w, 1420_w, 1393_w (C–H), 1342_m, 1209_m, 1165_s (C–N stretch), 1073_w, 1055_w, 1041_w, 781_w, 721_m.

θ_L: + 33.6 mdeg (223 nm, 10 mM, MeOH).

θ_D: – 25.0 mdeg (223 nm, 10 mM, MeOH).

(C₁₂)₂-L-Asp.TFA (L: 6.5, D: 6.6)



Chemical Formula: C₃₀H₅₆F₃NO₆

Molecular Weight: 583.77

(C₁₂)₂-L-Asp-Boc (200 mg, 3.51 mmol) was dissolved in a mixture of trifluoroacetic acid, triisopropylsilane and deionised water (500 μL, 95 : 2.5 : 2.5 v/v) before being shaken until TLC indicated reaction to be complete (3.5 h). Following careful addition

of deionised water (1.5 mL), the reaction mixture was washed with chloroform (3 × 4 mL) to extract non polar by-products. The aqueous layer was then evaporated to dryness *in vacuo* to afford the product as a white powdery solid (186 mg, 3.19 mmol, 91%). D-yield: 90%.

$R_f = 0.76$ (9 : 1 DCM : methanol, ninhydrin).

^1H NMR (400 MHz, CDCl_3) δ : 4.36 (exp dd, app t, CHNH_3^+ , $^3J = 4.8$ Hz, 1H); 4.26 – 4.15 (exp t, app m, $\text{CH}_2\text{OC}(\text{O})\text{CH}_2$, 2H); 4.10 (t, $\text{CH}_2\text{OC}(\text{O})\text{CH}$, $^3J = 6.8$ Hz, 2H); 3.12 (d, CH_2CHNH , $^3J = 4.8$ Hz, 2H); 1.65 – 1.58 (m, $\text{CH}_2\text{CH}_2\text{O}$, 4H); 1.25 (br s, 18 × alkyl CH_2 , 36H); 0.88 (t, 2 × alkyl CH_3 , $^3J = 6.8$ Hz, 6H).

^{13}C NMR (100 MHz, CDCl_3) δ : 171.74, 167.92 (C=O, ester); 161.60 (C=O, acid); 67.57, 66.39 (CH_2O); 49.73 (CHNH); 33.13 (CH_2CHNH); 31.91, 29.65, 29.62, 29.58, 29.49, 29.47, 29.34, 29.22, 29.15, 28.28, 28.17, 25.72, 25.59 (alkyl CH_2); 14.11 (alkyl CH_3).

ESI-MS: 470.42 $[\text{M}-\text{TFA}+\text{H}]^+$ (100%).

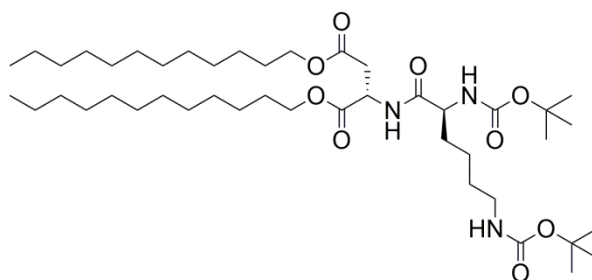
HRMS: Calcd. $[\text{M}+\text{H}]^+$ ($\text{C}_{28}\text{H}_{56}\text{NO}_4$) $m/z = 470.4204$, found $[\text{M}+\text{H}]^+ = 470.4190$ (error 2.5 ppm).

IR ν [cm^{-1}]: 2955 w , 2918 s (N–H), 2850 m (C–H), 1752 m (C=O, ester), 1736 m (C=O, acid) 1665 s , 1593 w , 1466 w , 1431 w , 1399 w , 1371 w (C–H), 1245 m (C–O), 1186 s (C–N), 1141 m , 1125 m , 1092 w , 803 m , 766 w .

θ_L : + 26.7 mdeg (210 nm, 10 mM, MeOH).

θ_D : – 27.6 mdeg (210 nm, 10 mM, MeOH).

(C_{12}) $_2$ -L-Asp-L-Lys(Boc) $_2$ (L: 6.7, D: 6.8)



Chemical Formula: $\text{C}_{44}\text{H}_{83}\text{N}_3\text{O}_9$

Molecular Weight: 798.16

L-Lys(Boc) $_2$ (76 mg, 0.22 mmol, 1.1 eq.) was dissolved in DCM (13 mL) at 0°C and stirred for 10 minutes before TBTU (63 mg, 0.20 mmol, 1 eq.) was added. After a

further 10 minutes, (C₁₂)₂-L-Asp.TFA (100 mg, 0.21 mmol, 1 eq., pre-dissolved in DCM (4 mL)) and DIPEA (52 mg, 0.40 mmol, 2 eq.) were added. The resulting reaction mixture was stirred at 0°C for 20 minutes before being warmed to room temperature and left to stir overnight. The volatiles were removed *in vacuo* and the resulting residue taken up in DCM (10 mL) and washed successively with NaHSO₄ (2 × 15 mL, 1.33 M), NaHCO₃ (2 × 10 mL, sat.), deionised water (3 × 15 mL) and brine (15 mL, sat.). The organic phase was collected, dried over MgSO₄ and the resulting filtrate concentrated *in vacuo* to afford a white powdery solid, which was purified by flash column chromatography (SiO₂, 1 : 1 cyclohexane : ethyl acetate) to afford the product as a white powdery solid (75 mg, 94 μmol, 44%). D-yield: 42%.

R_f = 0.85 (9 : 1 DCM : methanol, ninhydrin).

¹H NMR (400 MHz, CDCl₃) δ: 6.89 (d, AspNH, ³J = 8.0 Hz, 1H); 5.16 (br s, LysCH₂NH, 1H); 4.81 (exp dd, app dt, AspCHNH, ³J³J = 8.0 Hz, 4.4 Hz, 1H); 4.67 (exp dd, app br s, LysCHNH, 1H); 4.17 – 4.06 (exp dd, app m, LysCHNH, 2 × CH₂O, 5H); 3.11 (exp t, app s, CH₂NH, 2H); 3.02 (dd, CH_aH_bCHNHAsp, ²J³J = 17.2 Hz, 4.4 Hz, 1H); 2.80 (dd, CH_aH_bCHNHAsp, ²J³J = 17.2 Hz, 4.4 Hz, 1H); 1.81 – 1.71 (m, CH₂CH₂NH, 2H); 1.67 – 1.58 (m, 2 × CH₂CH₂O, LysCH₂CHNH, 6H); 1.43 (s, (CH₃)₃, 18H); 1.25 (s, 18 × alkylCH₂, CH₂CH₂CHNH, 38H); 0.87 (t, 2 × alkylCH₃, ³J = 7.2 Hz, 6H).

¹³C NMR (100 MHz, CDCl₃) δ: 171.78, 170.97 (C=O, ester); 170.44 (C=O, amide); 156.08 (2 × C=O, carbamate); 79.94, 79.93 (C(CH₃)₃); 66.03, 65.31 (CH₂O); 48.45 (AspCHNH); 36.17 (AspCH₂CHNH, AspCH₂CHNH); 31.88 (CH₂CH₂NH); 29.62, 29.60, 29.56, 29.50, 29.32, 29.23, 29.19 (alkylCH₂); 28.34, 28.21 (C(CH₃)₃); 25.76, 25.68 (alkylCH₂); 22.59 (LysCH₂CHNH); 14.02 (2 × alkylCH₃).

ESI-MS: 820.60 [M+Na]⁺ (100%).

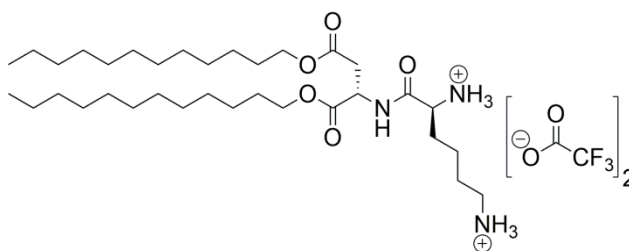
HRMS: Calcd. [M+Na]⁺ (C₄₄H₈₃N₃NaO₉) m/z = 820.6022, found [M+Na]⁺ = 820.5995 (error 2.8 ppm).

IR ν [cm⁻¹]: 3356w (N–H), 3331w (N–H), 2918s (C–H), 2850m (C–H), 1746m (C=O, ester), 1730m (C=O, ester), 1682s (CONH, amide I), 1656s (CONH, carbamates I), 1528s (CONH, amide II), 1471w, 1403w, 1392w, 1365w, 1301m, 1275m, 1247m (C–O), 1170s (C–N), 1087w, 1053w, 1019w, 783w, 766w, 732w, 719w.

Lα_D: + 13.5 (c. 1.0, CHCl₃).

Dα_D: – 11.2 (c. 1.0, CHCl₃).

(C₁₂)₂-L-Asp-L-Lys.2TFA (L: 6.9, D: 6.10)



Chemical Formula: C₃₈H₆₉F₆N₃O₉

Molecular Weight: 825.97

(C₁₂)₂-L-Asp-L-Lys(Boc)₂ (49 mg, 61 μmol) was dissolved in a mixture of trifluoroacetic acid, triisopropylsilane and deionised water (500 μL, 95 : 2.5 : 2.5 v/v) before being shaken until TLC indicated reaction to be complete (2.5 h). Following careful addition of deionised water (1.5 mL), the reaction mixture was washed with chloroform (3 × 4 mL). The combined organic layers were dried over MgSO₄ and resulting filtrate concentrated *in vacuo* to afford the product as a white powdery solid (36 mg, 60 μmol, 98%). D-yield: 97%.

R_f = 0.07 (9 : 1 DCM : methanol, ninhydrin).

¹H NMR (400 MHz, CDCl₃) δ: 7.82 – 7.75 (br m, CHNH₃⁺, 3H); 7.34 (s, CH₂NH₃⁺, 2H); 4.89 – 4.84 (exp dd, app m, AspCHNH, 1H); 4.20 (br s, AspCHNH, 1H); 4.16 – 4.07 (exp dd, app m, CHNH₃⁺, 1H); 4.07 – 4.00 (m, 2 × CH₂O, 4H); 3.08 (exp t, app s, CH₂NH₃⁺, 2H); 2.97 (dd, CH_aH_bCHNHAsp, ²J³J = 17.4 Hz, 5.6 Hz, 1H); 2.80 (dd, CH_aH_bCHNHAsp, ²J³J = 17.4 Hz, 3.2 Hz, 1H); 1.96 (br s, CH₂CHNH₃⁺, 2H); 1.74 (s, CH₂CH₂NH₃⁺, 2H); 1.58 (br s, 2 × CH₂CH₂O, CH₂CH₂CHNH₃⁺, 6H); 1.25 (s, 18 × alkylCH₂, 36H); 0.88 (t, 2 × alkylCH₃, ³J = 6.8 Hz, 6H).

¹³C NMR (100 MHz, CDCl₃) δ: 171.80, 171.16 (C=O, esters); 170.51 (C=O, amide); 161.04 (C=O, acid); 66.86, 66.11 (CH₂O); 61.09 (CHNH₃⁺); 60.51 (CH₂NH₃⁺); 48.10 (CHNHAsp); 39.61 (CH₂CHNH₃⁺); 34.00 (AspCH₂CHNH); 31.89, 29.64, 29.62, 29.58, 29.49, 29.34, 29.24, 29.18, 28.24 (alkylCH₂); 28.20 (CH₂CH₂NH₃⁺); 25.71, 25.66 (alkylCH₂); 14.04 (2 × alkylCH₃).

ESI-MS: 598.51 [M+H]⁺ (100%).

HRMS: Calcd. [M+H]⁺ (C₃₄H₆₈N₃O₅) m/z = 598.5153, found [M+H]⁺ = 598.5139 (error 2.6 ppm).

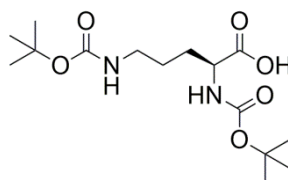
IR ν [cm⁻¹]: 3330_w (N–H), 2917_s (C–H), 2850_m (C–H), 1751_m (C=O, ester), 1725_m (C=O, ester), 1668_s (CONH, amide I), 1539_m (CONH, amide II), 1469_w, 1430_w,

1417w, 1401w, 1362w (C–H), 1345w, 1303w, 1271w, 1201s (C–O), 1178s (C–N), 1128s, 1078w, 1064w, 1003w, 739w, 721s.

θ_L : + 94.4 mdeg (215 nm, 10 mM, MeOH).

θ_D : – 105.3 mdeg (215 nm, 10 mM, MeOH).

***L*-Orn(Boc)₂ (L: 6.11, D: 6.12)**



Chemical Formula: C₁₅H₂₈N₂O₆

Molecular Weight: 332.40

L-Ornithine (2.00 g, 11.86 mmol) and NaOH pellets (1.10 g, 27.50 mmol) were dissolved together in deionised water (30 mL). Di-*tert*-butyl dicarbonate (6.25 g, 28.60 mmol) was dissolved separately in THF (30 mL) before being added to the reaction mixture dropwise in one portion over 30 minutes. The resulting reaction mixture was warmed to 45°C and stirred under an N₂ atmosphere for 4.5 hours. Following the removal of volatiles *in vacuo*, the residue was taken up in deionised water (100 mL) and washed with cyclohexane (50 mL). The aqueous layer was acidified to pH 3 using NaHSO₄ (1.33 M, pH paper) before the product was extracted into ethyl acetate (75 mL) and washed successively with deionised water (50 mL) and brine (50 mL, sat.). The organic phase was dried over MgSO₄ and the resulting filtrate concentrated *in vacuo* to afford the product as a foamy white solid (3.25 g, 9.77 mmol, 65%). D-yield: 75%.

R_f = 0.44 (9 : 1 DCM : methanol, ninhydrin).

¹H NMR (400 MHz, CDCl₃) δ : 10.10 (br s, OH, 1H); 6.19 (s, NH, 1H); 4.85 (s, NH, 1H); 4.34 – 4.26 (exp dd, app m, CHNH, 1H); 3.12 (exp t, app s, CH₂NH, 2H); 1.90 – 1.81 (m, CH_aH_bCHNH, 1H); 1.71 – 1.62 (m, CH_aH_bCHNH, 1H); 1.60 – 1.52 (m, CH₂CH₂NH, 2H); 1.43 (s, 2 × C(CH₃)₃, 18H).

¹³C NMR (100 MHz, CDCl₃) δ : 175.84 (C=O, acid); 156.35, 155.62 (C=O, carbamate); 80.00, 79.99 (C(CH₃)₃); 52.92 (CHNH); 39.90 (CH₂NH); 30.95 (CH₂CHNH); 28.33, 28.27 (C(CH₃)₃); 25.87 (CH₂CH₂NH).

ESI-MS: 355.18 [M+Na]⁺ (100%).

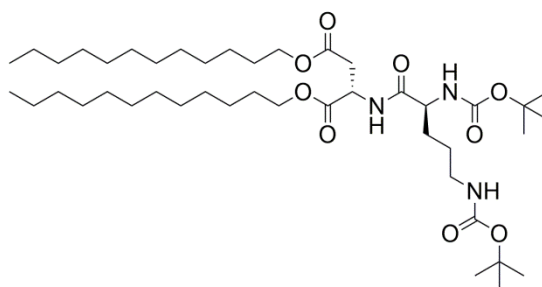
HRMS: Calcd. $[M+Na]^+$ ($C_{15}H_{28}N_2NaO_6$) $m/z = 355.1840$, found $[M+Na]^+ = 355.1822$ (error 4.3 ppm).

IR ν [cm^{-1}]: 3336 w (N–H), 2977 m (O–H), 2934 w (C–H), 1702 s (C=O, acid), 1689 s (CONH, carbamates I), 1516 m (CONH, carbamates II), 1454 w , 1393 m , 1366 s (C–H), 1248 m (C–O) 1158 s , 1050 w (C–N), 1050 w , 1020 w , 856 w , 778 w .

$L\alpha_D$: + 14.2 (c. 1.0, $CHCl_3$).

$D\alpha_D$: – 17.2 (c. 1.0, $CHCl_3$).

(C₁₂)₂-L-Asp-L-Orn(Boc)₂ (L: 6.13, D: 6.14)



Chemical Formula: $C_{43}H_{81}N_3O_9$

Molecular Weight: 784.13

L-Orn(Boc)₂ (296 mg, 0.89 mmol, 1.3 eq.) was dissolved in DCM (15 mL) and cooled to 0°C. After 10 minutes, TBTU (252 mg, 0.78 mmol, 1.1 eq.) was added. After a further 10 minutes, (C₁₂)₂-L-Asp.TFA (400 mg, 0.69 mmol, 1 eq., pre-dissolved in DCM (5 mL)) and DIPEA (281 μ L, 1.61 mmol, 2.3 eq.) were added. The reaction mixture was stirred for 20 minutes at 0°C before being warmed to room temperature and left to stir for 18 hours. The reaction mixture was then concentrated *in vacuo* before the resulting residue was taken up in DCM (10 mL) and washed with NaHSO₄ (2 \times 15 mL, 1.33 M), NaHCO₃ (2 \times 10 mL, sat.), deionised water (3 \times 15 mL) and brine (15 mL, sat.). The organic phase was collected, dried over MgSO₄ and the resulting filtrate concentrated *in vacuo* to afford a white powdery solid. The solid was purified by flash column chromatography (SiO₂, 50 : 50 cyclohexane : ethyl acetate) to afford a white powdery product (246 mg, 0.31 μ mol, 35%). D-yield: 46%.

$R_f = 0.93$ (9 : 1 DCM : methanol, ninhydrin).

¹H NMR (400 MHz, $CDCl_3$) δ : 7.00 (d, AspNH, $J = 8.0$ Hz, 1H); 5.18 (d, OrnNH, $J = 7.6$ Hz, 1H); 4.85 – 4.81 (exp dd, app m, AspCHNH, 1H); 4.70 (br s, OrnNH, 1H); 4.21 – 4.16 (exp dd, app m, CHNHBoc, 1H); 4.14 – 4.04 (m, 2 \times CH₂O, 4H); 3.16 (br s,

CH_aH_bNHBoc , 1H); 3.10 (br s, CH_aH_bNHBoc , 1H); 2.97 (dd, $AspCH_aH_bCHNHOrn$, $^2J^3J = 17.2$ Hz, 4.8 Hz, 1H); 2.79 (dd, $AspCH_aH_bCHNHOrn$, $^2J^3J = 17.2$ Hz, 4.8 Hz, 1H); 1.90 – 1.76 (m, $CH_aH_bCHNHBoc$, 1H); 1.61 – 1.56 (m, $2 \times CH_2CH_2O$, CH_2CH_2NHBoc , $CH_aH_bCHNHBoc$, $J = 6.8$ Hz, 7H); 1.41 (s, $2 \times C(CH_3)_3$, 9H); 1.23 (s, $18 \times alkylCH_2$, 36H); 0.86 (t, $2 \times alkylCH_3$, $^3J = 6.8$ Hz, 6H).

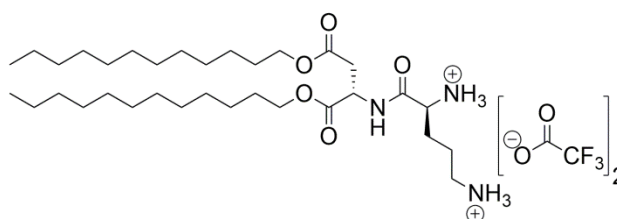
^{13}C NMR (100 MHz, $CDCl_3$) δ : 171.73, 170.79 (C=O, ester); 170.40 (C=O, amide); 156.09, 155.44 (C=O, carbamate); 79.84, 79.13 ($C(CH_3)_3$); 65.96, 65.26 (CH_2O); 53.70 ($CHNHBoc$); 48.47 ($AspCHNHOrn$); 36.13 ($AspCH_2CHNH$); 31.85 ($CH_2CHNHBoc$); 30.15, 29.60, 29.57, 29.53, 29.47, 29.30, 29.20, 29.16 ($alkylCH_2$); 28.35, 28.23 ($C(CH_3)_3$); 25.97 (CH_2CH_2NHBoc); 25.79, 25.71 ($alkylCH_2$); 14.06 ($2 \times alkylCH_3$).

ESI-MS: 806.58 $[M+Na]^+$ (100%), 784.60 $[M+H]^+$ (19%).

HRMS: Calcd. $[M+Na]^+$ ($C_{43}H_{81}N_3NaO_9$) $m/z = 806.5865$, found $[M+Na]^+$ 806.5848 (error 1.9 ppm).

IR ν [cm^{-1}]: 3302 m (N–H), 2918 s (C–H), 2850 m (C–H), 1740 m (C=O, esters), 1670 s (CONH, amide I), 1656 s (CONH, carbamates I), 1538 m (CONH, amide II), 1471 w , 1429 w , 1401 w , 1343 w , 1295 w , 1202 s (C–O), 1179 s (C–N), 1133 m , 1057 w , 985 w , 801 m , 721 w .

(C₁₂)₂-L-Asp-L-Orn.2TFA (L: 6.15, D: 6.16)



Chemical Formula: $C_{37}H_{67}F_6N_3O_9$

Molecular Weight: 811.95

$(C_{12})_2$ -L-Asp-L-Orn(Boc)₂ (40 mg, 51 μ mol) was dissolved in a mixture of trifluoroacetic acid, deionised water and triisopropylsilane (500 μ L, 95 : 2.5 : 2.5 v/v) and shaken until TLC indicated the reaction to be complete (3.5 h). Deionised water (1.5 mL) was carefully added before the reaction mixture was washed with chloroform (2×4 mL). The combined organic layers were concentrated *in vacuo* to afford a white solid (41 mg, 50 μ mol, 99%). D-yield: 98%.

$R_f = 0.29$ (9 : 1 DCM : methanol, ninhydrin).

^1H NMR (400 MHz, CDCl_3) δ : 8.42 (d, AspNH , $J = 8.0$ Hz, 1H); 8.20 (br s, OrnNH_3^+ , 2H); 7.70 (s, OrnNH_3^+ , 2H); 4.83 – 4.79 (exp dd, app m, AspCHNH , 1H); 4.15 – 4.08 (exp dd, app m, CHNH_3^+ , 1H); 4.03 – 3.94 (m, $2 \times \text{CH}_2\text{O}$, 4H); 3.05 – 2.97 (m, CH_2NH_3^+ , 2H); 2.91 (dd, $\text{AspCH}_a\text{H}_b\text{CHNH}$, $^2J^3J = 17.2$ Hz, 5.4 Hz, 1H); 2.79 (dd, $\text{AspCH}_a\text{H}_b\text{CHNH}$, $^2J^3J = 17.2$ Hz, 4.0 Hz, 1H); 2.02 – 1.94 (m, $\text{CH}_2\text{CHNH}_3^+$, 2H); 1.86 – 1.78 (m, $\text{CH}_2\text{CH}_2\text{NH}_3^+$, 2H); 1.56 (exp m, app s, $2 \times \text{CH}_2\text{CH}_2\text{O}$, 4H); 1.25 (s, $18 \times \text{alkylCH}_2$, 36H); 0.87 (t, $2 \times \text{alkylCH}_3$, $^3J = 7.0$ Hz, 6H).

^{13}C NMR (100 MHz, CDCl_3) δ : 171.47, 170.68 (C=O, ester); 168.86 (C=O, amide); 161.72 (q, $^{\text{C-F}}J = 36.7$ Hz, C=O, acid); 66.49, 65.70 (CH_2O); 52.75 (CHNH_3^+); 48.90 (AspCHNH); 39.08 (CH_2NH_3^+); 35.41 ($\text{AspCH}_2\text{CHNH}$); 31.93, 29.74, 29.72, 29.63, 29.43, 29.39, 28.37 (alkyl CH_2); 28.26 ($\text{CH}_2\text{CHNH}_3^+$); 25.86, 25.82, 22.67 (alkyl CH_2); 22.39 ($\text{CH}_2\text{CH}_2\text{NH}_2$); 14.04 ($2 \times \text{alkylCH}_3$).

ESI-MS: 292.75 $[\text{M}+2\text{H}]^{2+}$ (100%), 584.50 $[\text{M}+\text{H}]^+$ (84%).

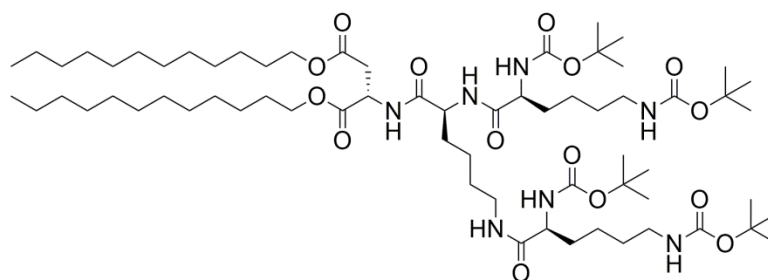
HRMS: Calcd. $[\text{M}+\text{H}]^+$ ($\text{C}_{33}\text{H}_{66}\text{N}_3\text{O}_5$) $m/z = 584.4997$, found $[\text{M}+\text{H}]^+ = 584.4989$ (error 1.0 ppm).

IR ν [cm^{-1}]: 3250 m (N–H), 2918 s (C–H), 2850 m (C–H), 1739 m (C=O, esters), 1659 s (CONH, amide I), 1539 m (CONH, amide II), 1471 w , 1430 w , 1401 w , 1343 w , 1295 w , 1225 w , 1200 s (C–O), 1180 s (C–N), 1133 m , 1058 w , 985 w , 800 m , 721 s .

θ_L : + 48.0 mdeg (216 nm, 10 mM, MeOH).

θ_D : – 48.7 mdeg (216 nm, 10 mM, MeOH).

$(\text{C}_{12})_2\text{-L-Asp-L-Lys(L-Lys(Boc)}_2)_2$ (L: 6.17, D: 6.18)



Chemical Formula: $\text{C}_{66}\text{H}_{123}\text{N}_7\text{O}_{15}$

Molecular Weight: 1254.74

L-Lys(Boc) $_2$ (185 mg, 530 μmol , 2.2 eq) was dissolved in DCM (10 mL) at 0°C and TBTU (171 mg, 530 μmol , 2.2 eq) was added. After stirring for 10 minutes, $(\text{C}_{12})_2\text{-L-Asp-L-Lys.TFA}$ (200 mg, 240 μmol , 1 eq) and DIPEA (169 μL , 970 μmol , 4 eq) were

added along with more cold DCM (10 mL). After 20 minutes, the reaction mixture was allowed to warm to room temperature, and stirred for 40 hours. The volatiles were removed *in vacuo* and resulting residue taken up in DCM (20 mL) before being washed successively with NaHSO₄ (2 × 10 mL, 1.33 M), NaHCO₃ (2 × 10 mL, sat.), deionised water (3 × 10 mL) and brine (10 mL, sat.). The organic phase was collected, dried over MgSO₄ and the resulting filtrate concentrated *in vacuo* to afford a golden solid. This solid was purified by flash column chromatography (SiO₂, 8 : 2, ethyl acetate : cyclohexane) to afford the product as a sticky white solid (31 mg, 25 μmol, 10%). D-yield: 33%.

R_f = 0.69 (8 : 2 ethyl acetate : cyclohexane, ninhydrin).

¹H NMR (400 MHz, CDCl₃) δ: 7.09 (d, AspNH, J = 7.6 Hz, 1H); 6.92 (s, LysNH, 1H); 5.95 (s, LysNH, 1H); 5.50 (s, LysNH, 1H); 4.85 – 4.77 (exp dd, app m, AspCHNH, 1H); 4.29 (exp dd, br s, 2 × CHNHBoc, 2H); 4.13 – 3.95 (m, 2 × CH₂O, LysCHNHLys 5H); 3.10 (exp m, app s, 2 × CH₂NHBoc, CH₂NHLys, 6H); 3.01 (dd, AspCH_aH_bCHNH, ²J³J = 17.4 Hz, 4.6 Hz, 1H); 2.77 (dd, AspCH_aH_bCHNH, ²J³J = 17.4 Hz, 4.6 Hz, 1H); 1.77 – 1.70 (m, 2 × CH₂CHNHBoc, LysCH₂CHNHLys, 6H); 1.68 – 1.62 (m, 2 × CH₂CH₂O, 4H); 1.58 – 1.46 (m, 2 × CH₂CH₂NHBoc, LysCH₂CH₂NHLys, 6H); 1.42 (s, 2 × C(CH₃)₃, 3 × CH₂CH₂CHNH, 24H); 1.41 (s, C(CH₃)₃, 9H) 1.40 (s, C(CH₃)₃, 9H); 1.25 (app s, 18 × alkylCH₂, 36H); 0.87 (t, 2 × alkylCH₃, ³J = 7.0 Hz, 6H).

¹³C NMR (100 MHz, CDCl₃) δ: 173.41 (2 × C=O, ester); 171.02 (3 × C=O, amide); 156.12, 156.05 (2 × C=O, carbamate); 80.69, 79.81 (2 × C(CH₃)₃); 66.08, 65.33 (CH₂O); 54.42, 54.02 (CH₂NHBoc); 53.91, 53.86 (CHNHBoc); 48.41 (AspCHNHLys); 40.33, 40.09, 40.03 (LysCH₂CHNH); 36.18 (AspCH₂CHNH); 31.88 (2 × CH₂CH₂NHBoc, CH₂CH₂NHLys); 29.64, 29.61, 29.52, 29.41, 29.33, 29.26, 29.28, 28.49 (alkylCH₂); 28.43, 28.36 (2 × C(CH₃)₃); 25.86, 25.79 (alkylCH₂); 22.66 (2 × CH₂CH₂CHNHBoc, CH₂CH₂CHNHLys); 14.09 (2 × alkylCH₃).

ESI-MS: 1276.89 [M+Na]⁺ (100%).

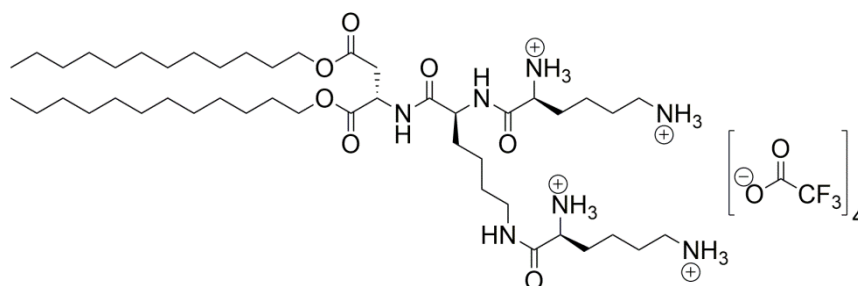
HRMS: Calcd. [M+Na]⁺ (C₆₆H₁₂₃N₇NaO₁₅) m/z = 1276.8969, found [M+Na]⁺ = 1276.8930 (error 3.0 ppm).

IR ν [cm⁻¹]: 3301_m (N–H), 2925_s (C–H), 2855_m (C–H), 1739_m (C=O, esters), 1688_s (CONH, amide I), 1644_s (CONH, carbamates I), 1520_s (CONH, amide II), 1456_m, 1391_m, 1365_s, 1272_w, 1247_s (C–N), 1168_s (C–N), 1091_w, 1046_w, 1017_w, 867_w, 782_w.

Lα_D: + 18.4 (c. 1.0, CHCl₃).

Dα_D: – 22.2 (c. 1.0, CHCl₃).

(C₁₂)₂-L-Asp-L-Lys(L-Lys)₂.4TFA (L: 6.19, D: 6.20)



Chemical Formula: C₅₄H₉₅F₁₂N₇O₁₅

Molecular Weight: 1310.37

(C₁₂)₂-L-Asp-L-Lys(L-Lys(Boc)₂)₂ (28 mg, 22 μmol) was dissolved in a mixture of trifluoroacetic acid, triisopropylsilane and deionised water (500 μL, 95 : 2.5 : 2.5 v/v) before being shaken until TLC indicated reaction to be complete (2 h). Following careful addition of deionised water (1.5 mL), the reaction mixture was washed with chloroform (3 × 4 mL). The combined organic layers were dried over MgSO₄ and the resulting filtrate concentrated *in vacuo* to afford the product as a white powdery solid (25 mg, 19 μmol, 87%). D-yield: 90%.

R_f = 0.00 (9 : 1 DCM : methanol, ninhydrin).

¹H NMR (400 MHz, CD₃OD) δ: 4.82 (exp dd, app t, AspCHNH, ³J = 6.4 Hz, 1H); 4.38 (exp dd, app t, LysCHNH, ³J = 5.6 Hz, 1H); 4.19 – 4.05 (m, 2 × CH₂O, 4H); 3.95 (t, CHNH₃⁺, ³J = 5.4 Hz, 1H); 3.85 (t, CHNH₃⁺, ³J = 6.0 Hz, 1H); 3.29 – 3.18 (m, CH₂NH, 2H); 3.00 – 2.92 (m, 2 × CH₂NH₃⁺, 4H); 2.87 (d, AspCH₂CHNH, ³J = 6.4 Hz, 2H); 1.94 – 1.82 (m, 2 × CH₂CHNH₃⁺, CH₂CHNH, 6H); 1.74 – 1.69 (m, 2 × CH₂CH₂NH₃⁺, CH₂CH₂NH, 6H); 1.64 (exp m, app s, 2 × CH₂CH₂O, 4H); 1.52 – 1.43 (m, 2 × CH₂CH₂CHNH₃⁺, CH₂CH₂CHNH, 6H); 1.30 (s, 18 × alkylCH₂, 36H); 0.90 (t, 2 × alkylCH₃, ³J = 6.8 Hz, 6H).

¹³C NMR (100 MHz, CD₃OD) δ: 173.87, 172.12 (C=O, esters); 172.05, 170.09, 170.00 (C=O, amide); 77.66 (2 × CH₂NH₃⁺); 66.95, 66.42 (CH₂O); 54.87 (CH₂NH, LysCHNHLys); 54.31, 53.93 (CHNH₃⁺); 49.05 (AspCHNH); 40.48, 40.30, 40.26 (LysCH₂CHN); 37.03 (AspCH₂CHNH); 33.14, 32.73, 32.17 (CH₂CH₂N); 30.82, 30.78, 30.55, 30.50, 30.47, 29.96, 29.74, 29.71, 27.12, 27.09 (alkylCH₂); 23.80, 23.02, 22.41 (CH₂CH₂CHN); 14.50 (2 × alkylCH₃).

ESI-MS: 427.85 [M+2H]²⁺ (100%), 854.71 [M+H]⁺ (13%).

HRMS: Calcd. $[M+2H]^{2+}$ ($C_{46}H_{93}N_7NaO_7$) $m/z = 427.8563$, found $[M+H]^+ = 427.8545$ (error 4.4 ppm).

IR ν [cm^{-1}]: 3305 m (N–H), 2930 s (C–H), 2855 m (C–H), 1739 m (C=O, esters), 1689 s (CONH, amide I), 1524 s (CONH, amide II), 1455 m , 1390 m , 1364 s , 1248 s (C–N), 1168 s (C–N), 1091 w , 1046 w , 1017 w , 868 w .

$L\alpha_D$: + 8.0 (c. 1.0, $CHCl_3$).

$D\alpha_D$: – 6.5 (c. 1.0, $CHCl_3$).

7.2 Assay Materials and Methods

Assay Materials

All materials, except novel compounds, employed in spectroscopic assays were obtained from commercial sources and used without further purification unless stated. Sodium salt heparin from porcine intestinal mucosa with a molecular weight between 15,000 \pm 2,000 Da (1 KU = 1000 units) was obtained from Calbiochem®. Ammonium carbonate, deoxyribonucleic acid sodium salt from calf thymus (DNA), ethylenediaminetetraacetic acid trisodium salt hydrate (EDTA), ethidium bromide (EthBr), Gly-Ala, *N*-(2-Hydroxyethyl)piperazine-*N'*-(2-ethanesulfonic acid) (HEPES), human serum (from human male AB plasma), Nile red, PAMAM dendrimers, phosphate buffered saline (PBS), protamine sulfate salt from salmon (Grade X, amorphous powder) and Trizma® hydrochloride (Tris HCl) were obtained from Sigma Aldrich.

UV/Vis absorbance was measured on a Shimadzu UV-2401PC spectrophotometer and fluorescence on a Hitachi F-4500 spectrofluorimeter. All MalB solutions were incubated at 50°C for 24 hours prior to use and stored in the dark. Unless stated, all experiments were performed in triplicate and data is reported as a mean value plus or minus one standard deviation.

Binding of Heparin (or other GAGs) to MalB

A cuvette was charged with 2 mL of a stock solution of MalB (25 μ M) in NaCl (150 mM) and Tris HCl (10 mM). This solution was titrated with a stock solution of heparin (or other GAG) (811 μ M) in MalB (25 μ M), NaCl (150 mM) and Tris HCl (10 mM) to a final cuvette volume of 3 mL. The absorbance at 615 nm was recorded after each addition.

Interference to the MalB-Heparin Interaction By Electrolyte/Buffer

A cuvette was charged with 2 mL of a stock solution of MalB (30 μM MalB) and heparin (27 μM) in Tris HCl (1 mM). For the electrolyte titration, the cuvette was titrated with aliquots of the same stock solution additionally containing a concentration of a NaCl (3 M) to a final cuvette volume of 3 mL. For the buffer titration, stock solutions containing MalB (30 μM), heparin (27 μM) and NaCl (150 mM) were prepared in clean water and Tris HCl (1 M). Titrating different amounts of each stock solution into the other effected the buffer concentration in the cuvette. The absorbance at 615 nm was recorded after each addition.

Determination of Heparin Concentration with MalB

A range of heparin stock solutions (0 U mL⁻¹ – 10 U mL⁻¹) were made up in 100% Human Serum. 0.5 mL of each heparin-in-serum stock was titrated into a cuvette containing 1.5 mL MalB (25 μM) in Tris HCl (20 mM). The absorbance at 615 nm was recorded.

Heparin Displacement Assay In Buffer

A cuvette containing 2 mL of MalB (25 μM), heparin (27 μM) and NaCl (150 mM) in Tris HCl (10 mM) was titrated with binder stock solution to give the cuvette a suitable binder-heparin charge ratio. The binder stock solution was composed of the original MalB/heparin/NaCl/Tris HCl stock solution endowed additionally with a concentration of binder such that, after addition of 10 μL binder stock, the cuvette charge ratio (+ : -) is 0.037. After each addition, the cuvette was inverted to ensure good mixing and the absorbance at 615 nm was recorded against a Tris HCl (10 mM) baseline. Absorbance was normalised between a solution of MalB (25 μM), NaCl (150 mM) in Tris HCl (10 mM) and one containing MalB (25 μM), heparin (27 μM), NaCl (150 mM) in Tris HCl (10 mM).

Heparin Displacement Assay In Serum

Fourteen cuvettes were charged with 1.75 mL of MalB (28.53 μM) in Tris HCl (10 mM) and a volume of binder stock solution to give the cuvette a suitable binder-heparin charge ratio. The binder stock solution was additionally endowed with its own MalB (25 μM), heparin (27 μM) and Tris HCl (10 mM) concentrations. The concentration of binder in the binder stock was determined in the same manner described for the heparin

displacement assay in buffer. Separately, a heparin (216 μM) solution was made in 100% human serum. Sequentially, each cuvette was titrated with 0.25 mL of the heparin-in-serum solution and inverted to ensure thorough mixing. The absorbance was recorded at 615 nm against a baseline of (1.75 mL 10 mM Tris HCl, 0.25 mL 100% Human Serum) and normalised between a solution containing exclusively MalB (25 μM) and one containing MalB (25 μM) and heparin (27 μM).

Transgeden Heparin Binding Fluorescence Study

A cuvette was charged with 1 mL TGD-dendrimer (1 μM) in NaCl (150 mM) and Tris HCl (10 mM) before being titrated with the same solution additionally endowed with heparin (24 μM) up to a total cuvette volume of 2 mL. Following each addition, a fluorescence spectrum was recorded following irradiation at 318 nm. All data obtained from a single run only.

Dynamic Light Scattering (DLS)

Aggregate characteristics were determined using a Zetasizer Nano (Malvern Instruments Ltd., Worcestershire, UK). The principle is based on the measurement of the backscattered light fluctuations at an angle of 173° and the calculation of an autocorrelation function. Data were recorded from 15–20 runs per single measurement, each of which was carried out at 25°C using folded capillary cells (DTS 1060). Monomer solutions were freshly prepared by dissolving an appropriate amount of dry compound in filtered aqueous media (e.g. Tris HCl). All samples were agitated and incubated at 25°C for 10 minutes prior to measurement. These studies were carried out in the laboratory of Dr Marcelo Calderon at Freie Universität Berlin, Germany with assistance from Dr Shashwat Malhotra.

Plasma Clotting Assays

Clotting studies employed an Axis Shield Thrombotrack coagulation analyser in conjunction with Behnk Elektronik cuvettes and ball bearings. Technoclone normal citrated plasma (re-suspended in HPLC grade water), Acros Organics calcium chloride (50 mM in HPLC grade water), Celsus porcine mucosal heparin (201 IU mg^{-1}), Siemens Thromborel® S (re-suspended in HPLC grade water at double the manufacturers recommended concentration) and Siemens Pathromtin SL (inverted 8 times prior to use).

Prothrombin (PT) Assay

A cylindrical cuvette, pre-warmed to 37°C on a heating block, was placed in the coagulation analyser and charged with a ball bearing and normal citrated plasma (50 µL). Following incubation for at least 1 minute, pre-warmed (37°C) test sample (50 µL) was added along with Thromborel® S reagent (50 µL). Upon addition of the final reagent, the coagulation analyser was initiated. Clotting times are reported as the time at which the coagulometer was no longer able to stir the sample. Samples remaining unclotted after 120 seconds were recorded as ‘no clot.’ All measurements were carried out in triplicate with error values reported as one standard deviation.

Activated Partial Thromboplastin (aPTT) Assay

A cylindrical cuvette, pre-warmed to 37°C on a heating block, was placed in the coagulation analyser and charged with a ball bearing, normal citrated plasma (50 µL), Pathromtin SL (50 µL) and test sample (25 µL). Following incubation for at least 2 minutes, pre-warmed (37°C) calcium chloride (25 µL) was added and the coagulation analyser was initiated. Clotting times are reported as the time at which the coagulometer was no longer able to stir the sample. Samples remaining unclotted after 120 seconds were recorded as ‘no clot.’ All measurements were carried out in triplicate with error values reported as one standard deviation.

These studies were carried out in the laboratory of Professor Jeremy Turnbull at University of Liverpool, UK.

Nile Red Release Assay

The binder (25 µM) was dissolved in phosphate buffered saline (PBS, 0.01 M, endowed with NaCl (138 µM) and KCl (2.7 µM)). In a cuvette, an aliquot (1 mL) of this solution was mixed with a small amount of Nile red (1 µL, 2.5 mM in ethanol). Following inversion to ensure mixing, fluorescence intensity at 635 nm was recorded using a 550 nm excitation wavelength. The binder stock solution was incubated at 37°C for 24 hours before another aliquot (1 mL) was taken for fluorescence measurement as before. In the time-resolved study, the initial solution was left in the fluorimeter and the emission was monitored at regular time periods. For the degradation experiment in the presence of heparin, the binder stock solution was additionally endowed with a heparin concentration corresponding to a dosage of 0.79 mg / 100IU.

Mass Spectrometric Degradation Assay

The binder was dissolved (200 μM) in ammonium carbonate (10 mM, pH 7.5). 250 μL of this binder solution was combined with 250 μL of a Gly-Ala standard (1 mM, in 10 mM ammonium carbonate) for mass spectrometric analysis. Following incubation of the binder solution for 24 hours at 37°C, the same analysis was repeated.

Nile Red Encapsulation Assay³²⁶

A dendron stock solution was prepared at a suitable concentration in PBS buffer (0.01 M, endowed with NaCl (138 μM) and KCl (2.7 μM)). In a cuvette, the dendron stock solution was diluted to 1 mL final volume with PBS buffer to afford the required concentration. To the cuvette was added 1 μL Nile Red (2.5 mM, prepared in ethanol). Following inversion to ensure mixing, fluorescence intensity at 635 nm was recorded using a 550 nm excitation wavelength.

TEM Imaging

Monomer solutions were prepared in clean water at concentrations above previously-calculated CAC values to ensure compounds were present in their assembled form. For samples imaged in the presence of heparin, the polysaccharide was introduced at a charge ratio (+ : -) under which the binder had previously exhibited significant interaction with it. Once prepared, aliquots of each solution were loaded on a formvar grid, negatively stained with uranyl acetate and allowed to dry before imaging.

DNA Binding Assay^{356,373}

A cuvette containing 2 mL of EthBr (5.07 μM) and DNA (4 μM with respect to each base (assumed RMM: 330 g mol^{-1})) in SHE Buffer (HEPES (2 mM), EDTA (0.05 mM) and NaCl (150 mM)) was titrated with binder stock solution to give the cuvette a suitable binder-heparin charge ratio. The binder stock solution was composed of the original EthBr/DNA/SHE Buffer stock solution endowed additionally with a concentration of binder such that, after addition of 10 μL binder stock, the cuvette charge ratio (+ : -) is 0.1. After each addition, the cuvette was inverted to ensure good mixing and the fluorescence at 595 nm was recorded using a 540 nm excitation wavelength. Fluorescence was normalised between a solution of EthBr (5.07 μM) and DNA (4 μM) in SHE Buffer and one containing EthBr (5.07 μM) alone in SHE Buffer (0.01 M).

Abbreviations

AA	Azure A
AB	Alcian Blue
ACQ	Aggregation-caused quenching
AIE	Aggregation-induced emission
app	Apparent (NMR)
aPTT	Activated partial thromboplastin time
ATIII	Antithrombin III
bis-MPA	2,2-bis(hydroxymethyl)propionic acid
Boc	<i>tert</i> -butyloxycarbonyl
CAC	Critical Aggregation Concentration
CD	Circular dichroism or Cyclodextrin
CE ₅₀	Charge excess or charge efficiency at 50% binding
C _{eff}	Effective concentration
CMC	Critical Micelle Concentration
CNT	Carbon nanotubes
Con A	Concanavalin A
CS	Chondroitin sulfate
<i>d</i>	doublet (NMR)
DAPMA	<i>N,N</i> -di-(3-aminopropyl)- <i>N</i> -methylamine
DCC	<i>N,N'</i> -dicyclohexylcarbodiimide
DCM	Dichloromethane
Deg	Degradation peak (Mass Spectrometry)
DLS	Dynamic light scattering
DMF	Dimethylformamide
DNA	Deoxyribose nucleic acid
DOFLA	Diversity-oriented fluorescent library approach
DPD	Dissipative particle dynamics
EC ₅₀	Effective concentration at 50% binding
EDTA	Ethylenediaminetetraacetic acid
EM	Effective molarity
EthBr	Ethidium bromide
FRET	Fluorescence resonance electron transfer
GAG	Glycosaminoglycan
GO	Graphene oxide
G _x	Generation x
HA	Hyaluronic acid
HEPES	<i>N</i> -(2-hydroxyethyl)piperazine- <i>N'</i> -(2-ethanesulfonic acid)
HS	Heparan sulfate
IC ₅₀	Concentration at 50% inhibition
IDA	Indicator displacement assay
IHS	International heparin standard
ITC	Isothermal titration calorimetry
LMWH	Low molecular weight heparin
LMWP	Low molecular weight protamine
<i>m</i>	medium (IR)
m	multiplet (NMR)
MalB	Mallard blue

MB	Methylene blue
MD	Molecular dynamics
MG	Methyl green
M_r	Relative molecular mass
MRI	Magnetic resonance imaging
NIR	Near infrared
NMR	Nuclear magnetic resonance
NP	Nanoparticles
NR	Nile red
PAH	Poly(allylaminehydrochloride)
PAMAM	Poly(amidoamine)
PBS	Phosphate buffered saline
PCPE	Phosphorescent conjugated polyelectrolyte
PDI	Polydispersity index (DLS)
PEG	Poly(ethyleneglycol)
PEI	Poly(ethyleneimine)
PNA	Peptide nucleic acid
PPB	Plasma-protein binding
PPV	Poly(phenylenevinylidene)
PT	Prothrombin
PVC	Polyvinyl chloride
q	quartet (NMR)
RGD	Arginine-glycine-aspartic acid tripeptide
RNA	Ribose nucleic acid
s	strong (IR)
s	singlet (NMR)
SAMul	Self-assembled multivalency
siRNA	Small interfering RNA
Std	Standard peak (MS)
t	triplet (NMR)
TA	Thionine acetate
TBTU	<i>O</i> -(Benzotriazol-1-yl)- <i>N,N,N',N'</i> -tetramethyluronium tetrafluoroborate
TEM	Transmission electron microscopy
TGD	Transgeden
THF	Tetrahydrofuran
TPE	Tetraphenylethene
UFH	Unfractionated heparin
UV	Ultra-violet
w	weak (IR)

References

1. J. Huskens, *Curr. Opin. Chem. Biol.*, 2006, **10**, 537-543.
2. R. W. Saalfrank, H. Maid and A. Scheurer, *Angew. Chem. Int. Edit.*, 2008, **47**, 8794-8824.
3. K. Bowman-James, *Accounts Chem. Res.*, 2005, **38**, 671-678.
4. M. Mammen, S. K. Choi and G. M. Whitesides, *Angew. Chem. Int. Edit.*, 1998, **37**, 2755-2794.
5. G. Ercolani, *J. Am. Chem. Soc.*, 2003, **125**, 16097-16103.
6. S. W. Benson, *J. Am. Chem. Soc.*, 1958, **80**, 5151-5154.
7. A. Mulder, J. Huskens and D. N. Reinhoudt, *Org. Biomol. Chem.*, 2004, **2**, 3409-3424.
8. B. Perlmutter-Hayman, *Accounts Chem. Res.*, 1986, **19**, 90-96.
9. G. Ercolani and L. Schiaffino, *Angew. Chem. Int. Edit.*, 2011, **50**, 1762-1768.
10. A. Whitty, *Nat. Chem. Biol.*, 2008, **4**, 435-439.
11. C. A. Hunter and H. L. Anderson, *Angew. Chem. Int. Edit.*, 2009, **48**, 7488-7499.
12. W. A. Eaton, E. R. Henry, J. Hofrichter and A. Mozzarelli, *Nat. Struct. Biol.*, 1999, **6**, 351-358.
13. M. F. Perutz, *Q. Rev. Biophys.*, 1989, **22**, 139-236.
14. M. Takeuchi, M. Ikeda, A. Sugasaki and S. Shinkai, *Accounts Chem. Res.*, 2001, **34**, 865-873.
15. J. J. Lundquist and E. J. Toone, *Chem. Rev.*, 2002, **102**, 555-578.
16. M. I. Page and W. P. Jencks, *P. Natl. Acad. Sci. USA*, 1971, **68**, 1678-&.
17. M. Mammen, E. I. Shakhnovich and G. M. Whitesides, *J. Org. Chem.*, 1998, **63**, 3168-3175.
18. G. Ercolani, *J. Org. Chem.*, 1999, **64**, 3350-3353.
19. C. Galli and L. Mandolini, *Eur. J. Org. Chem.*, 2000, 3117-3125.
20. H. L. Anderson, S. Anderson and J. K. M. Sanders, *J. Chem. Soc. Perk. T. 1*, 1995, 2231-2245.
21. F. Felluga, P. Tecilla, L. Hillier, C. A. Hunter, G. Licini and P. Scrimin, *Chem. Commun.*, 2000, 1087-1088.
22. J. H. Rao, I. J. Colton and G. M. Whitesides, *J. Am. Chem. Soc.*, 1997, **119**, 9336-9340.
23. J. H. Rao and G. M. Whitesides, *J. Am. Chem. Soc.*, 1997, **119**, 10286-10290.

24. J. H. Rao, L. Yan, J. Lahiri, G. M. Whitesides, R. M. Weis and H. S. Warren, *Chem. Biol.*, 1999, **6**, 353-359.
25. J. H. Rao, J. Lahiri, L. Isaacs, R. M. Weis and G. M. Whitesides, *Science*, 1998, **280**, 708-711.
26. J. H. Rao, J. Lahiri, R. M. Weis and G. M. Whitesides, *J. Am. Chem. Soc.*, 2000, **122**, 2698-2710.
27. P. R. Ashton, P. J. Campbell, E. J. T. Chrystal, P. T. Glink, S. Menzer, D. Philp, N. Spencer, J. F. Stoddart, P. A. Tasker and D. J. Williams, *Angew. Chem. Int. Edit.*, 1995, **34**, 1865-1869.
28. T. Chang, A. M. Heiss, S. J. Cantrill, M. C. T. Fyfe, A. R. Pease, S. J. Rowan, J. F. Stoddart and D. J. Williams, *Org. Lett.*, 2000, **2**, 2943-2946.
29. H. W. Gibson, N. Yamaguchi, L. Hamilton and J. W. Jones, *J. Am. Chem. Soc.*, 2002, **124**, 4653-4665.
30. V. Balzani, M. Clemente-Leon, A. Credi, J. N. Lowe, J. D. Badjić, J. F. Stoddart and D. J. Williams, *Chem-Eur. J.*, 2003, **9**, 5348-5360.
31. A. H. Flood, R. J. A. Ramirez, W. Q. Deng, R. P. Muller, W. A. Goddard and J. F. Stoddart, *Aust. J. Chem.*, 2004, **57**, 301-322.
32. J. D. Badjić, A. Nelson, S. J. Cantrill, W. B. Turnbull and J. F. Stoddart, *Accounts Chem. Res.*, 2005, **38**, 723-732.
33. M. C. Misuraca, T. Grecu, Z. Freixa, V. Garavini, C. A. Hunter, P. van Leeuwen, M. D. Segarra-Maset and S. M. Turegat, *J. Org. Chem.*, 2011, **76**, 2723-2732.
34. W. Jiang, K. Nowosinski, N. L. Low, E. V. Dzyuba, F. Klautzsch, A. Schäfer, J. Huuskonen, K. Rissanen and C. A. Schalley, *J. Am. Chem. Soc.*, 2012, **134**, 1860-1868.
35. C. A. Hunter, M. C. Misuraca and S. M. Turega, *J. Am. Chem. Soc.*, 2011, **133**, 582-594.
36. H. J. Hogben, J. K. Sprafke, M. Hoffmann, M. Pawlicki and H. L. Anderson, *J. Am. Chem. Soc.*, 2011, **133**, 20962-20969.
37. C. Fasting, C. A. Schalley, M. Weber, O. Seitz, S. Hecht, B. Kokschi, J. Dervede, C. Graf, E. W. Knapp and R. Haag, *Angew. Chem. Int. Edit.*, 2012, **51**, 10472-10498.
38. G. M. Whitesides, J. P. Mathias and C. T. Seto, *Science*, 1991, **254**, 1312-1319.
39. A. Klug, *Angew. Chem. Int. Edit.*, 1983, **22**, 565-582.
40. D. Philp and J. F. Stoddart, *Angew. Chem. Int. Edit.*, 1996, **35**, 1155-1196.
41. J. M. Lehn, *Science*, 1993, **260**, 1762-1763.
42. J. P. Mathias and J. F. Stoddart, *Chem. Soc. Rev.*, 1992, **21**, 215-225.
43. D. Chandler, *Nature*, 2005, **437**, 640-647.

44. X. L. Chi, A. J. Guerin, R. A. Haycock, C. A. Hunter and L. D. Sarson, *J. Chem. Soc. Chem. Comm.*, 1995, 2563-2565.
45. J. N. Israelachvili, D. J. Mitchell and B. W. Ninham, *J. Chem. Soc. Farad. T. 1*, 1976, **72**, 1525-1568.
46. A. Barnard and D. K. Smith, *Angew. Chem. Int. Edit.*, 2012, **51**, 6572-6581.
47. J. E. Kingery-Wood, K. W. Williams, G. B. Sigal and G. M. Whitesides, *J. Am. Chem. Soc.*, 1992, **114**, 7303-7305.
48. J. Voskuhl, M. C. A. Stuart and B. J. Ravoo, *Chem-Eur. J.*, 2010, **16**, 2790-2796.
49. R. V. Vico, J. Voskuhl and B. J. Ravoo, *Langmuir*, 2011, **27**, 1391-1397.
50. H. K. Lee, K. M. Park, Y. J. Jeon, D. Kim, D. H. Oh, H. S. Kim, C. K. Park and K. Kim, *J. Am. Chem. Soc.*, 2005, **127**, 5006-5007.
51. X. Chen, U. C. Tam, J. L. Czapinski, G. S. Lee, D. Rabuka, A. Zettl and C. R. Bertozzi, *J. Am. Chem. Soc.*, 2006, **128**, 6292-6293.
52. K. Petkau-Milroy and L. Brunsveld, *Eur. J. Org. Chem.*, 2013, 3470-3476.
53. S. Laschat, A. Baro, N. Steinke, F. Giesselmann, C. Haegele, G. Scalia, R. Judele, E. Kapatsina, S. Sauer, A. Schreivogel and M. Tosoni, *Angew. Chem. Int. Edit.*, 2007, **46**, 4832-4887.
54. A. R. A. Palmans, J. Vekemans, H. Fischer, R. A. Hikmet and E. W. Meijer, *Chem-Eur. J.*, 1997, **3**, 300-307.
55. K. Petkau-Milroy, M. H. Sonntag, A. Colditz and L. Brunsveld, *Int. J. Mol. Sci.*, 2013, **14**, 21189-21201.
56. D. J. Welsh and D. K. Smith, *Org. Biomol. Chem.*, 2011, **9**, 4795-4801.
57. D. Deniaud, K. Julienne and S. G. Gouin, *Org. Biomol. Chem.*, 2011, **9**, 966-979.
58. J. J. Reczek, A. A. Kennedy, B. T. Halbert and A. R. Urbach, *J. Am. Chem. Soc.*, 2009, **131**, 2408-2415.
59. S. W. A. Reulen, P. Y. W. Dankers, P. H. H. Bomans, E. W. Meijer and M. Merkx, *J. Am. Chem. Soc.*, 2009, **131**, 7304-7312.
60. E. L. Doyle, C. A. Hunter, H. C. Phillips, S. J. Webb and N. H. Williams, *J. Am. Chem. Soc.*, 2003, **125**, 4593-4599.
61. D. J. Welsh, P. Posocco, S. Pricl and D. K. Smith, *Org. Biomol. Chem.*, 2013, **11**, 3177-3186.
62. U. Griesenbach, D. M. Geddes, E. Alton and U. K. C. F. G. T. Co, *Gene Ther.*, 2006, **13**, 1061-1067.
63. B. L. Fang and J. A. Roth, *Cancer Biol. Ther.*, 2003, **2**, S115-S121.
64. N. P. Gabrielson and J. Cheng, *Biomaterials*, 2010, **31**, 9117-9127.

65. S. P. Jones, N. P. Gabrielson, D. W. Pack and D. K. Smith, *Chem. Commun.*, 2008, 4700-4702.
66. S. K. M. Nalluri, J. Voskuhl, J. B. Bultema, E. J. Boekema and B. J. Ravoo, *Angew. Chem. Int. Edit.*, 2011, **50**, 9747-9751.
67. S. P. Jones, G. M. Pavan, A. Danani, S. Pricl and D. K. Smith, *Chem-Eur. J.*, 2010, **16**, 4519-4532.
68. D. J. Welsh, S. P. Jones and D. K. Smith, *Angew. Chem. Int. Edit.*, 2009, **48**, 4047-4051.
69. A. Barnard, P. Posocco, S. Pricl, M. Calderon, R. Haag, M. E. Hwang, V. W. T. Shum, D. W. Pack and D. K. Smith, *J. Am. Chem. Soc.*, 2011, **133**, 20288-20300.
70. A. Barnard, P. Posocco, M. Fermeglia, A. Tschiche, M. Calderon, S. Pricl and D. K. Smith, *Org. Biomol. Chem.*, 2014, **12**, 446-455.
71. A. Barnard, M. Calderon, A. Tschiche, R. Haag and D. K. Smith, *Org. Biomol. Chem.*, 2012, **10**, 8403-8409.
72. A. Tschiche, A. M. Staedtler, S. Malhotra, H. Bauer, C. Bottcher, S. Sharbati, M. Calderon, M. Koch, T. M. Zollner, A. Barnard, D. K. Smith, R. Einspanier, N. Schmidt and R. Haag, *J. Mater. Chem. B*, 2014, **2**, 2153-2167.
73. Y. Zhang, J. Chen, C. S. Xiao, M. Q. Li, H. Y. Tian and X. S. Chen, *Biomacromolecules*, 2013, **14**, 4289-4300.
74. P. M. Levine, T. P. Carberry, J. M. Holub and K. Kirshenbaum, *Med. Chem.*, 2013, **4**, 493-509.
75. S. Middeldorp, *Thromb. Res.*, 2008, **122**, 753-762.
76. J. McLean, *Am. J. Physiol.*, 1916, **41**, 250-257.
77. J. McLean, *Circulation*, 1959, **19**, 75-78.
78. W. H. Howell, *Am. J. Physiol.*, 1925, **71**, 553-562.
79. R. D. Rosenberg and P. S. Damus, *J. Biol. Chem.*, 1973, **248**, 6490-6505.
80. D. L. Rabenstein, *Nat. Prod. Rep.*, 2002, **19**, 312-331.
81. T. R. Rudd, M. A. Skidmore, M. Guerrini, M. Hricovini, A. K. Powell, G. Siligardi and E. A. Yates, *Curr. Opin. Struc. Biol.*, 2010, **20**, 567-574.
82. I. Capila and R. J. Linhardt, *Angew. Chem. Int. Edit.*, 2002, **41**, 390-412.
83. R. Sasisekharan and G. Venkataraman, *Curr. Opin. Chem. Biol.*, 2000, **4**, 626-631.
84. R. Raman, V. Sasisekharan and R. Sasisekharan, *Chem. Biol.*, 2005, **12**, 267-277.
85. J. Hirsh and R. Raschke, *Chest*, 2004, **126**, 188S-203S.

86. J. Hirsh, R. Raschke, T. E. Warkentin, J. E. Dalen, D. Deykin and L. Poller, *Chest*, 1995, **108**, S258-S275.
87. R. J. Kandrotas, *Clin. Pharmacokinet.*, 1992, **22**, 359-374.
88. P. Brunet, N. Simon, A. Opris, V. Faure, A. M. Lorec-Penet, H. Portugal, B. Dussol and Y. Berland, *Am. J. Kidney Dis.*, 2008, **51**, 789-795.
89. E. W. Davie and O. D. Ratnoff, *Science*, 1964, **145**, 1310-1312.
90. R. G. Macfarlane, *Nature*, 1964, **202**, 498-&.
91. E. W. Davie, K. Fujikawa and W. Kisiel, *Biochemistry*, 1991, **30**, 10363-10370.
92. J. Hirsh, T. E. Warkentin, S. G. Shaughnessy, S. S. Anand, J. L. Halperin, R. Raschke, C. Granger, E. M. Ohman and J. E. Dalen, *Chest*, 2001, **119**, 64S-94S.
93. M. Petitou, B. Casu and U. Lindahl, *Biochimie*, 2003, **85**, 83-89.
94. H. C. Hemker and S. Beguin, *Thromb. Haemostasis*, 1993, **70**, 724-728.
95. W. H. Howell, *Am. J. Physiol.*, 1923, **63**, 434.
96. S. Wessler and S. N. Gitel, *Blood*, 1979, **53**, 525-544.
97. D. R. Bangham and M. V. Mussett, *B. World Health Organ.*, 1959, **20**, 1201-1208.
98. D. Basu, J. Cade, A. Gallus and J. Hirsh, *New Engl. J. Med.*, 1972, **287**, 324-327.
99. V. Ignjatovic, R. Summerhayes, A. Gan, J. Than, A. Chan, A. Cochrane, M. Bennett, S. Horton, F. Shann, G. Lane, M. Ross-Smith and P. Monagle, *Thromb. Res.*, 2007, **120**, 347-351.
100. R. Balhorn, *Genome Biol.*, 2007, **8**, 227.
101. F. P. Ottensmeyer, R. F. Whiting and A. P. Korn, *P. Natl. Acad. Sci. USA*, 1975, **72**, 4953-4955.
102. S. M. Bromfield, P. Posocco, M. Fermeiglia, S. Pricl, J. Rodríguez-López and D. K. Smith, *Chem. Commun.*, 2013, **49**, 4830-4832.
103. J. Butterworth, Y. A. Lin, R. C. Prielipp, J. Bennett, J. W. Hammon and R. L. James, *Ann. Thorac. Surg.*, 2002, **74**, 1589-1595.
104. J. Butterworth, Y. A. Lin, R. Prielipp, J. Bennett and R. James, *Anesth. Analg.*, 2002, **94**, 514-522.
105. K. H. Teoh, E. Young, C. A. Bradley and J. Hirsh, *Circulation*, 1993, **88**, Ii420-425.
106. A. Galeone, C. Rotunno, P. Guida, B. Assunta, G. Rubino, L. d. L. T. Schinosa and D. Paparella, *J. Cardiothor. Vasc. An.*, 2013, **27**, 853-858.
107. C. Hermans and D. Claeys, *Curr. Med. Res. Opin.*, 2006, **22**, 471-481.

108. P. Martin, F. Horkay, N. K. Gupta, C. Gebitekin and D. R. Walker, *Blood Coagul. Fibrin.*, 1992, **3**, 187-191.
109. K. H. T. Teoh, E. Young, M. H. Blackall, R. S. Roberts and J. Hirsh, *J. Thorac. Cardiovasc. Surg.*, 2004, **128**, 211-219.
110. M. Stafford-Smith, E. A. Lefrak, A. G. Qazi, I. J. Welsby, L. Barber, A. Hoeft, A. Dorenbaum, J. Mathias, J. J. Rochon and M. F. Newman, *Anesthesiology*, 2005, **103**, 229-240.
111. R. Porsche and Z. R. Brenner, *Heart Lung*, 1999, **28**, 418-428.
112. Y. Q. Chu, L. J. Cai, D. C. Jiang, D. Jia, S. Y. Yan and Y. Q. Wang, *Clin. Ther.*, 2010, **32**, 1729-1732.
113. M. Nybo and J. S. Madsen, *Basic & Clinical Pharmacology & Toxicology*, 2008, **103**, 192-196.
114. S. E. Kimmel, M. A. Sekeres, J. A. Berlin, L. R. Goldberg and B. L. Strom, *J. Clin. Epidemiol.*, 1998, **51**, 1-10.
115. J. J. van Veen, R. M. Maclean, K. K. Hampton, S. Laidlaw, S. Kitchen, P. Toth and M. Makris, *Blood Coagul. Fibrin.*, 2011, **22**, 565-570.
116. M. A. Crowther, L. R. Berry, P. T. Monagle and A. K. C. Chan, *Br. J. Haematol.*, 2002, **116**, 178-186.
117. G. J. Despotis, G. Gravlee, K. Filos and J. Levy, *Anesthesiology*, 1999, **91**, 1122-1151.
118. P. D. Raymond, M. J. Ray, S. N. Callen and N. A. Marsh, *Perfusion-UK*, 2003, **18**, 269-276.
119. D. J. Murray, W. J. Brosnahan, B. Pennell, D. Kapalanski, J. M. Weiler and J. Olson, *J. Cardiothor. Vasc. An.*, 1997, **11**, 24-28.
120. D. P. Prisco, R, *Thromb. J.*, 2003, **1**, 1 - 10
121. A. F. Rosenberg, M. Zumberg, L. Taylor, A. LeClaire and N. Harris, *J. Pharm. Pract.*, 2010, **23**, 210-216.
122. P. D. Raymond, M. J. Ray, S. N. Callen and N. A. Marsh, *Perfusion-UK*, 2003, **18**, 277-281.
123. J. C. Horrow, *Anesth. Analg.*, 1985, **64**, 348-361.
124. N. Sadeghi, D. Hoppensteadt, O. Iqbal, W. Jeske, J. M. Walenga and J. Fareed, *Faseb J.*, 2010, **24**, 1.
125. T. D. James and S. Shinkai, in *Host-Guest Chemistry: Mimetic Approaches to Study Carbohydrate Recognition*, ed. S. Penades, Springer-Verlag Berlin, Berlin, 2002, vol. 218, pp. 159-200.
126. K. Sandanayake and S. Shinkai, *J. Chem. Soc. Chem. Comm.*, 1994, 1083-1084.
127. R. Nishiyabu, Y. Kubo, T. D. James and J. S. Fossey, *Chem. Commun.*, 2011, **47**, 1106-1123.

128. S. D. Bull, M. G. Davidson, J. M. H. Van den Elsen, J. S. Fossey, A. T. A. Jenkins, Y. B. Jiang, Y. Kubo, F. Marken, K. Sakurai, J. Z. Zhao and T. D. James, *Accounts Chem. Res.*, 2013, **46**, 312-326.
129. Y. J. Huang, W. J. Ouyang, X. Wu, Z. Li, J. S. Fossey, T. D. James and Y. B. Jiang, *J. Am. Chem. Soc.*, 2013, **135**, 1700-1703.
130. J. P. Lorand and J. O. Edwards, *J. Org. Chem.*, 1959, **24**, 769-774.
131. J. Yoon and A. W. Czarnik, *J. Am. Chem. Soc.*, 1992, **114**, 5874-5875.
132. J. Yan, G. Springsteen, S. Deeter and B. H. Wang, *Tetrahedron*, 2004, **60**, 11205-11209.
133. S. C. Ma, V. C. Yang and M. E. Meyerhoff, *Anal. Chem.*, 1992, **64**, 694-697.
134. J. A. Wahr, J. H. Yun, V. C. Yang, L. M. Lee and M. E. Meyerhoff, *J. Cardiothor. Vasc. An.*, 1996, **10**, 447-450.
135. S. C. Ma, V. C. Yang, B. Fu and M. E. Meyerhoff, *Anal. Chem.*, 1993, **65**, 2078-2084.
136. S. Amemiya, Y. Kim, R. Ishimatsu and B. Kabagambe, *Anal. Bioanal. Chem.*, 2011, **399**, 571-579.
137. H. Qi, L. Zhang, L. Yang, P. Yu and L. Mao, *Anal. Chem.*, 2013, **85**, 3439-3445.
138. Y. Chen, R. N. Liang and W. Qin, *Chinese Chem. Lett.*, 2012, **23**, 233-236.
139. J. Umlas, R. H. Taff, G. Gauvin and P. Swierk, *Anesth. Analg.*, 1983, **62**, 1095-1099.
140. G. Gauvin, J. Umlas and N. Chin, *Med. Instrum.*, 1983, **17**, 165-168.
141. M. D. Klein, R. A. Drongowski, R. J. Linhardt and R. S. Langer, *Anal. Biochem.*, 1982, **124**, 59-64.
142. Q. C. Jiao, Q. Liu, C. Sun and H. He, *Talanta*, 1999, **48**, 1095-1101.
143. Q. C. Jiao and Q. Liu, *Anal. Lett.*, 1998, **31**, 1311-1323.
144. Z. L. Zhong and E. V. Anslyn, *J. Am. Chem. Soc.*, 2002, **124**, 9014-9015.
145. A. T. Wright, Z. L. Zhong and E. V. Anslyn, *Angew. Chem. Int. Edit.*, 2005, **44**, 5679-5682.
146. Y. Egawa, R. Hayashida, T. Seki and J.-i. Anzai, *Talanta*, 2008, **76**, 736-741.
147. Q. Chen, Y. Cui, J. Cao and B.-H. Han, *Polymer*, 2011, **52**, 383-390.
148. S. V. Nalage, S. V. Bhosale and S. K. Bhargava, *Tetrahedron Lett.*, 2012, **53**, 2864-2867.
149. W. Sun, H. Bandmann and T. Schrader, *Chem-Eur. J.*, 2007, **13**, 7701-7707.
150. M. Wang, D. Q. Zhang, G. X. Zhang and D. B. Zhu, *Chem. Commun.*, 2008, 4469-4471.

151. L. T. Zeng, P. F. Wang, H. Y. Zhang, X. Q. Zhuang, Q. Dai and W. M. Liu, *Org. Lett.*, 2009, **11**, 4294-4297.
152. K. Y. Pu and B. Liu, *Macromolecules*, 2008, **41**, 6636-6640.
153. K.-Y. Pu and B. Liu, *Adv. Funct. Mater.*, 2009, **19**, 277-284.
154. K. Pu, R. Zhan, J. Liang and B. Liu, *Science China-Chemistry*, 2011, **54**, 567-574.
155. B. Xu, X. Wu, H. Li, H. Tong and L. Wang, *Polymer*, 2012, **53**, 490-494.
156. T. Bříza, Z. Kejík, I. Císařová, J. Králová, P. Martásek and V. Král, *Chem. Commun.*, 2008, 1901-1903.
157. J. C. Saucedo, R. M. Duke and M. Nitz, *ChemBioChem*, 2007, **8**, 391-394.
158. H. Szelke, S. Schübel, J. Harenberg and R. Krämer, *Chem. Commun.*, 2010, **46**, 1667-1669.
159. M. C.-L. Yeung and V. W.-W. Yam, *Chem-Eur. J.*, 2011, **17**, 11987-11990.
160. S. L. Wang and Y. T. Chang, *Chem. Commun.*, 2008, 1173-1175.
161. X. Gu, G. Zhang and D. Zhang, *Analyst*, 2012, **137**, 365-369.
162. J. D. Luo, Z. L. Xie, J. W. Y. Lam, L. Cheng, H. Y. Chen, C. F. Qiu, H. S. Kwok, X. W. Zhan, Y. Q. Liu, D. B. Zhu and B. Z. Tang, *Chem. Commun.*, 2001, 1740-1741.
163. N. B. Shustova, T. C. Ong, A. F. Cozzolino, V. K. Michaelis, R. G. Griffin and M. Dinca, *J. Am. Chem. Soc.*, 2012, **134**, 15061-15070.
164. R. T. K. Kwok, J. L. Geng, J. W. Y. Lam, E. G. Zhao, G. Wang, R. Y. Zhan, B. Liu and B. Tang, *J. Mater. Chem. B*, 2014, **2**, 4134-4141.
165. H. L. Liu, P. S. Song, R. R. Wei, K. Li and A. J. Tong, *Talanta*, 2014, **118**, 348-352.
166. H. Szelke, J. Harenberg and R. Krämer, *Thromb. Haemostasis*, 2009, **102**, 859-864.
167. H. F. Shi, H. B. Sun, H. R. Yang, S. J. Liu, G. Jenkins, W. Feng, F. Y. Li, Q. Zhao, B. Liu and W. Huang, *Adv. Funct. Mater.*, 2013, **23**, 3268-3276.
168. D. H. Kim, Y. J. Park, K. H. Jung and K. H. Lee, *Anal. Chem.*, 2014, **86**, 6580-6586.
169. E. Climent, P. Calero, M. D. Marcos, R. Martínez-Mañez, F. Sancenon and J. Soto, *Chem-Eur. J.*, 2009, **15**, 1816-1820.
170. B. K. Jena and C. R. Raj, *Biosens. Bioelectron.*, 2008, **23**, 1285-1290.
171. R. Cao and B. X. Li, *Chem. Commun.*, 2011, **47**, 2865-2867.
172. X. L. Fu, L. X. Chen and J. H. Li, *Analyst*, 2012, **137**, 3653-3658.

173. X. L. Fu, L. X. Chen, J. H. Li, M. Lin, H. Y. You and W. H. Wang, *Biosens. Bioelectron.*, 2012, **34**, 227-231.
174. R. Godavarti and R. Sasisekharan, *J. Biol. Chem.*, 1998, **273**, 248-255.
175. T. Ammar and C. F. Fisher, *Anesthesiology*, 1997, **86**, 1382-1386.
176. H. F. Wu, R. L. Lundblad and F. C. Church, *Blood*, 1995, **85**, 421-428.
177. A. K. Udit, C. Everett, A. J. Gale, J. R. Kyle, M. Ozkan and M. G. Finn, *ChemBioChem*, 2009, **10**, 503-510.
178. A. Luganini, A. Giuliani, G. Pirri, L. Pizzuto, S. Landolfo and G. Gribaudo, *Antivir. Res.*, 2010, **85**, 532-540.
179. Y. Byun, V. K. Singh and V. C. Yang, *Thromb. Res.*, 1999, **94**, 53-61.
180. L. C. Chang, H. F. Lee, Z. Q. Yang and V. C. Yang, *AAPS Pharmsci*, 2001, **3**, art. no.-17.
181. L. C. Chang, J. F. Liang, H. F. Lee, L. M. Lee and V. C. Yang, *AAPS Pharmsci*, 2001, **3**, art. no.-18.
182. L. M. Lee, L. C. Chang, S. Wroblewski, T. W. Wakefield and V. C. Yang, *AAPS Pharmsci*, 2001, **3**, art. no.-19.
183. T. W. Wakefield, P. C. Andrews, S. K. Wroblewski, A. M. Kadell, A. Fazzalari, B. J. Nichol, T. Vanderkooi and J. C. Stanley, *J. Surg. Res.*, 1994, **56**, 586-593.
184. M. J. Hernaiz, L. A. LeBrun, Y. Wu, J. W. Sen, R. J. Linhardt and N. H. H. Heegaard, *Eur. J. Biochem.*, 2002, **269**, 2860-2867.
185. W. A. Weiss, J. S. Gilman, A. J. Catenacci and A. E. Osterberg, *JAMA-J. Am. Med. Assoc.*, 1958, **166**, 603-607.
186. M. Kikura, M. K. Lee and J. H. Levy, *Anesth. Analg.*, 1996, **83**, 223-227.
187. G. Montalescot, W. M. Zapol, A. Carvalho, D. R. Robinson, A. Torres and E. Lowenstein, *Circulation*, 1990, **82**, 1754-1764.
188. C. W. Lillehei, L. P. Sterns, D. M. Long and D. Lepley, *Ann. Surg.*, 1960, **151**, 11-16.
189. K. Kamiński, M. Płonka, J. Ciejka, K. Szczubiałka, M. Nowakowska, B. Lorkowska, R. Korbut and R. Lach, *J. Med. Chem.*, 2011, **54**, 6586-6596.
190. B. Kałaska, E. Sokolowska, K. Kaminski, K. Szczubiałka, K. Kramkowski, A. Mogielnicki, M. Nowakowska and W. Buczko, *Eur. J. Pharmacol.*, 2012, **686**, 81-89.
191. K. Kamiński, B. Kałaska, P. Koczurkiewicz, M. Michalik, K. Szczubiałka, A. Mogielnicki, W. Buczko and M. Nowakowska, *Med. Chem.*, 2014, **5**, 489-495.
192. S. H. Bai, C. Thomas and F. Ahsan, *J. Pharm. Sci.*, 2007, **96**, 2090-2106.
193. X. Y. Feng, Y. Y. Cheng, K. Yang, J. H. Zhang, Q. L. Wu and T. W. Xu, *J. Phys. Chem. B*, 2010, **114**, 11017-11026.

194. S. Bai and F. Ahsan, *Pharm. Res.*, 2009, **26**, 539-548.
195. S. Metz, J. C. Horrow, I. P. Goel, M. L. R. Kuretu and C. Bellwoar, *J. Cardiothor. Vasc. An.*, 1996, **10**, 474-476.
196. R. E. McAllister, *Circulation*, 2010, **122**.
197. J. Kuziej, E. Litinas, D. A. Hoppensteadt, D. H. Liu, J. M. Walenga, J. Fareed and W. Jeske, *Clin. Appl. Thromb.-Hem.*, 2010, **16**, 377-386.
198. C. E. Mahan, *J. Thromb. Thrombolys.*, 2014, **37**, 271-278.
199. F. Cunsolo, G. M. L. Consoli, C. Geraci and T. Mecca, *Abiotic Heparin Antagonists*, 2005, **WO/2005/028422**.
200. T. Mecca, G. M. L. Consoli, C. Geraci, R. La Spina and F. Cunsolo, *Org. Biomol. Chem.*, 2006, **4**, 3763-3768.
201. T. Mecca and F. Cunsolo, *Polym. Advan. Technol.*, 2010, **21**, 752-757.
202. S. Choi, D. J. Clements, V. Pophristic, I. Ivanov, S. Vemparala, J. S. Bennett, M. L. Klein, J. D. Winkler and W. E. DeGrado, *Angew. Chem. Int. Edit.*, 2005, **44**, 6685-6689.
203. C. Kelly, S. Khaja, A. Vena, A. Yu and J. M. Esson, *Anal. Chim. Acta*, 2010, **681**, 1-7.
204. G. L. Montalvo, Y. Zhang, T. M. Young, M. J. Costanzo, K. B. Freeman, J. Wang, D. J. Clements, E. Magavern, R. W. Kavash, R. W. Scott, D. H. Liu and W. F. DeGrado, *ACS Chem. Biol.*, 2014, **9**, 967-975.
205. M. Schuksz, M. M. Fuster, J. R. Brown, B. E. Crawford, D. P. Ditto, R. Lawrence, C. A. Glass, L. C. Wang, Y. Tor and J. D. Esko, *P. Natl. Acad. Sci. USA*, 2008, **105**, 13075-13080.
206. D. T. Hunter and J. M. Hill, *Nature*, 1961, **191**, 1378-1379.
207. K. Rajangam, H. A. Behanna, M. J. Hui, X. Q. Han, J. F. Hulvat, J. W. Lomasney and S. I. Stupp, *Nano Lett.*, 2006, **6**, 2086-2090.
208. H. A. Behanna, K. Rajangam and S. I. Stupp, *J. Am. Chem. Soc.*, 2007, **129**, 321-327.
209. K. Rajangam, M. S. Arnold, M. A. Rocco and S. I. Stupp, *Biomaterials*, 2008, **29**, 3298-3305.
210. A. D. Cardin and H. J. R. Weintraub, *Arteriosclerosis*, 1989, **9**, 21-32.
211. A. C. Rodrigo, A. Barnard, J. Cooper and D. K. Smith, *Angew. Chem. Int. Edit.*, 2011, **50**, 4675-4679.
212. S. M. Bromfield, E. Wilde and D. K. Smith, *Chem. Soc. Rev.*, 2013, **42**, 9184-9195.
213. G. R. Jones, R. Hashim and D. M. Power, *Biochim. Biophys. Acta.*, 1986, **883**, 69-76.

214. J. H. Stebbins, *J. Am. Chem. Soc.*, 1884, **6**, 304-305.
215. P. N. Marshall, *Histochem. J.*, 1979, **11**, 489-493.
216. P. N. Marshall and S. M. Lewis, *Stain Technol.*, 1975, **50**, 375-381.
217. R. W. Mowry and F. H. Kasten, *Biotech. Histochem.*, 1975, **50**, 65-81.
218. W. Löhr, I. Sohmer and D. Wittekind, *Stain Technol.*, 1974, **49**, 359-366.
219. E. Tuite and J. M. Kelly, *Biopolymers*, 1995, **35**, 419-433.
220. E. M. Sloand, C. M. Kessler, C. L. McIntosh and H. G. Klein, *Thromb. Res.*, 1989, **54**, 677-686.
221. E. H. Flewellen, *Tex. Med.*, 1980, **76**, 49-51.
222. J. G. Whitwam, A. R. Taylor and J. M. White, *Anaesthesia*, 1979, **34**, 181-182.
223. N. Blass and D. Fung, *Anesthesiology*, 1976, **45**, 458-459.
224. V. C. Yang, Y. Y. Fu, C. L. C. Teng, S. C. Ma and J. N. Shanberge, *Thromb. Res.*, 1994, **74**, 427-434.
225. V. E. Nicotra, M. F. Mora, R. A. Iglesias and A. M. Baruzzi, *Dyes Pigments*, 2008, **76**, 315-318.
226. M. Havelcová, P. Kubát and I. Němcová, *Dyes Pigments*, 1999, **44**, 49-54.
227. K. Ahmed, R. Azmat, F. Uddin and M. Q. Fatmi, *Chinese J. Chem.*, 2011, **29**, 643-649.
228. R. Nothelfer, J. Ruprecht, Heyl and H. Baumgärtel, *Biopolymers*, 1986, **25**, 1273-1281.
229. W. C. Lai, N. S. Dixit and R. A. Mackay, *J. Phys. Chem.*, 1984, **88**, 5364-5368.
230. R. A. Rhoades and D. R. Bell, *Medical Physiology: Principles for Clinical Medicine*, Lippincott, Williams and Wilkins, Philadelphia, PA, 2008.
231. A. K. Krey and F. E. Hahn, *Biochemistry*, 1975, **14**, 5061-5067.
232. J. E. Scott, *Histochemistry*, 1967, **9**, 30-47.
233. J. E. Scott, G. Quintarelli and M. C. Dellovo, *Histochemistry*, 1964, **4**, 73-85.
234. J. E. Scott, *Eur. J. Oral Sci.*, 1996, **104**, 2-9.
235. P. Whiteman, *Biochem. J.*, 1973, **131**, 343-350.
236. J. E. Scott and I. H. Willett, *Nature*, 1966, **209**, 985-&.
237. S. Bjornsson, *Anal. Biochem.*, 1993, **210**, 282-291.
238. T. T. Williams, C. Dohno, E. D. A. Stemp and J. K. Barton, *J. Am. Chem. Soc.*, 2004, **126**, 8148-8158.
239. R. E. Hileman, J. R. Fromm, J. M. Weiler and R. J. Linhardt, *Bioessays*, 1998, **20**, 156-167.

240. A. Isidro-Llobet, M. Álvarez and F. Albericio, *Chem. Rev.*, 2009, **109**, 2455-2504.
241. P. A. Wender, T. C. Jessop, K. Pattabiraman, E. T. Pelkey and C. L. VanDeusen, *Org. Lett.*, 2001, **3**, 3229-3232.
242. S. M. Bromfield, A. Barnard, P. Posocco, M. Fermeglia, S. Priel and D. K. Smith, *J. Am. Chem. Soc.*, 2013, **135**, 2911-2914.
243. J. C. van Kerkhof, P. Bergveld and R. B. M. Schasfoort, *Biosens. Bioelectron.*, 1995, **10**, 269-282.
244. K. Gaus and E. A. H. Hall, *Biosens. Bioelectron.*, 1998, **13**, 1307-1315.
245. J. F. Callan, A. P. de Silva and D. C. Magri, *Tetrahedron*, 2005, **61**, 8551-8588.
246. Z. Shriver and R. Sasisekharan, *Nat. Chem.*, 2013, **5**, 644-646.
247. L. Zhang and G. Q. Tang, *J. Fluoresc.*, 2013, **23**, 303-310.
248. B. S. Fujimoto, J. B. Clendenning, J. J. Delrow, P. J. Heath and M. Schurr, *J. Phys. Chem.*, 1994, **98**, 6633-6643.
249. G. Somer and A. Temizer, *Photochem. Photobiol.*, 1984, **40**, 575-580.
250. A. Mills and J. Wang, *J. Photoch. Photobio. A*, 1999, **127**, 123-134.
251. A. H. Gemeay, I. A. Mansour, R. G. El-Sharkawy and A. B. Zaki, *J. Chem. Technol. Biot.*, 2004, **79**, 85-96.
252. Y. Usui and M. Koizumi, *B. Chem. Soc. Jpn.*, 1961, **34**, 1651-1658.
253. A. Chakraborty, M. Ali and S. K. Saha, *Spectrochim. Acta A*, 2010, **75**, 1577-1583.
254. A. Czímerová, J. Bujdák and A. Gáplovský, *Colloid Surface A*, 2004, **243**, 89-96.
255. D. K. Smith, *Chem. Commun.*, 1999, 1685-1686.
256. G. M. Dykes, L. J. Brierley, D. K. Smith, P. T. McGrail and G. J. Seeley, *Chem-Eur. J.*, 2001, **7**, 4730-4739.
257. G. J. Despotis, J. H. Joist, C. W. Hogue, A. Alsoufiev, D. JoinerMaier, S. A. Santoro, E. Spitznagel, J. I. Weitz and L. T. Goodnough, *Thromb. Haemostasis*, 1996, **76**, 902-908.
258. B. P. Schick, D. Maslow, A. Moshinski and J. D. San Antonio, *Blood*, 2004, **103**, 1356-1363.
259. J. D. Zhang, G. Rivers, Y. Y. Zhu, A. Jacobsen, J. Peyers, G. Grundstrom, P. Burch, S. Hussein, A. Marolewski, W. Herlihy and J. Rusche, *Bioorg. Med. Chem.*, 2001, **9**, 825-836.
260. A. Sekiya, S. Oishi, N. Fujii and T. Koide, *Chem. Pharm. Bull.*, 2012, **60**, 371-376.

261. S. L. Wiskur, H. Ait-Haddou, J. J. Lavigne and E. V. Anslyn, *Accounts Chem. Res.*, 2001, **34**, 963-972.
262. B. T. Nguyen and E. V. Anslyn, *Coordin. Chem. Rev.*, 2006, **250**, 3118-3127.
263. N. Y. Kang, H. H. Ha, S. W. Yun, Y. H. Yu and Y. T. Chang, *Chem. Soc. Rev.*, 2011, **40**, 3613-3626.
264. P. Rossmann, K. Matoušovic and V. Horáček, *Virchows Arch. B*, 1982, **40**, 81-98.
265. J. Maurer, S. Haselbach, O. Klein, D. Baykut, V. Vogel and W. Mäntele, *J. Am. Chem. Soc.*, 2011, **133**, 1134-1140.
266. D. A. Tomalia, H. Baker, J. Dewald, M. Hall, G. Kallos, S. Martin, J. Roeck, J. Ryder and P. Smith, *Polym. J.*, 1985, **17**, 117-132.
267. D. A. Tomalia, A. M. Naylor and W. A. Goddard, *Angew. Chem. Int. Edit.*, 1990, **29**, 138-175.
268. D. K. Smith and F. Diederich, *Chem-Eur. J.*, 1998, **4**, 1353-1361.
269. C. Liang and J. M. J. Frechet, *Prog. Polym. Sci.*, 2005, **30**, 385-402.
270. R. Esfand and D. A. Tomalia, *Drug Discov. Today*, 2001, **6**, 427-436.
271. W. D. Jang, K. M. K. Selim, C. H. Lee and I. K. Kang, *Prog. Polym. Sci.*, 2009, **34**, 1-23.
272. N. T. Pourianazar, P. Mutlu and U. Gunduz, *J. Nanopart. Res.*, 2014, **16**, 38.
273. A. E. Beezer, A. S. H. King, I. K. Martin, J. C. Mitchell, L. J. Twyman and C. F. Wain, *Tetrahedron*, 2003, **59**, 3873-3880.
274. R. Z. Xu, Y. L. Wang, X. L. Wang, E. K. Jeong, D. L. Parker and Z. R. Lu, *Exp. Biol. Med.*, 2007, **232**, 1081-1089.
275. B. Klajnert, M. Cangiotti, S. Calici, M. Ionov, J. P. Majoral, A. M. Caminade, J. Cladera, M. Bryszewska and M. F. Ottaviani, *New J. Chem.*, 2009, **33**, 1087-1093.
276. R. Duncan and L. Izzo, *Adv. Drug Deliv. Rev.*, 2005, **57**, 2215-2237.
277. N. Malik, R. Wiwattanapatapee, R. Klopsch, K. Lorenz, H. Frey, J. W. Weener, E. W. Meijer, W. Paulus and R. Duncan, *J. Control. Release*, 2000, **65**, 133-148.
278. P. K. Maiti, T. Cagin, S. T. Lin and W. A. Goddard, *Macromolecules*, 2005, **38**, 979-991.
279. Y. Liu, V. S. Bryantsev, M. S. Diallo and W. A. Goddard, *J. Am. Chem. Soc.*, 2009, **131**, 2798-2799.
280. H. Szelke, S. Schübel, J. Harenberg and R. Krämer, *Bioorg. Med. Chem. Lett.*, 2010, **20**, 1445-1447.
281. P. Posocco, S. Pricl, S. Jones, A. Barnard and D. K. Smith, *Chem. Sci.*, 2010, **1**, 393-404.

282. E. Díez-Barra, J. C. García-Martínez and J. Rodríguez-López, *J. Org. Chem.*, 2003, **68**, 832-838.
283. A. R. Cano-Marín, E. Díez-Barra and J. Rodríguez-López, *Tetrahedron*, 2005, **61**, 395-400.
284. C. Hadad, J. C. García-Martínez and J. Rodríguez-López, *J. Org. Chem.*, 2012, **77**, 6223-6230.
285. E. Díez-Barra, J. C. García-Martínez, R. del Rey, J. Rodríguez-López, F. Giacalone, J. L. Segura and N. Martín, *J. Org. Chem.*, 2003, **68**, 3178-3183.
286. J. C. García-Martínez, E. Díez-Barra and J. Rodríguez-López, *Curr. Org. Synth.*, 2008, **5**, 267-290.
287. J. C. García-Martínez, C. Atienza, M. de la Peña, A. C. Rodrigo, J. Tejada and J. Rodríguez-López, *J. Mass Spectrom.*, 2009, **44**, 613-620.
288. J. Tolosa, C. Romero-Nieto, E. Díez-Barra, P. Sánchez-Verdú and J. Rodríguez-López, *J. Org. Chem.*, 2007, **72**, 3847-3852.
289. E. Díez-Barra, J. C. García-Martínez, S. Merino, R. del Rey, J. Rodríguez-López, P. Sánchez-Verdú and J. Tejada, *J. Org. Chem.*, 2001, **66**, 5664-5670.
290. M. Martín-Zarco, S. Toribio, J. C. García-Martínez and J. Rodríguez-López, *J. Polym. Sci. A1*, 2009, **47**, 6409-6419.
291. A. C. Rodrigo, I. Rivilla, F. C. Pérez-Martínez, S. Monteagudo, V. Ocaña, J. Guerra, J. C. García-Martínez, S. Merino, P. Sánchez-Verdú, V. Ceña and J. Rodríguez-López, *Biomacromolecules*, 2011, **12**, 1205-1213.
292. G. M. Pavan, S. Monteagudo, J. Guerra, B. Carrion, V. Ocana, J. Rodríguez-López, A. Danani, F. C. Pérez-Martínez and V. Cena, *Curr. Med. Chem.*, 2012, **19**, 4929-4941.
293. J. Guerra, A. C. Rodrigo, S. Merino, J. Tejada, J. C. García-Martínez, P. Sánchez-Verdú, V. Ceña and J. Rodríguez-López, *Macromolecules*, 2013, **46**, 7316-7324.
294. S. M. Bromfield, P. Posocco, M. Fermeglia, J. Tolosa, A. Herreros-López, S. Pricl, J. Rodríguez-López and D. K. Smith, *Chem-Eur. J.*, 2014, **20**, 9666-9674.
295. G. M. Pavan, A. Danani, S. Pricl and D. K. Smith, *J. Am. Chem. Soc.*, 2009, **131**, 9686-9694.
296. G. M. Pavan, L. Albertazzi and A. Danani, *J. Phys. Chem. B*, 2010, **114**, 2667-2675.
297. C. B. Sun, T. Tang and H. Uludag, *J. Phys. Chem. B*, 2012, **116**, 2405-2413.
298. E. Chargaff and K. B. Olson, *J. Biol. Chem.*, 1937, **122**, 153-167.
299. M. Schapira and B. W. Christman, *Circulation*, 1990, **82**, 1877-1879.
300. C. A. Palma, M. Cecchini and P. Samori, *Chem. Soc. Rev.*, 2012, **41**, 3713-3730.

301. L. Brunsveld, B. G. G. Lohmeijer, J. A. J. M. Vekemans and E. W. Meijer, *Chem. Commun.*, 2000, 2305-2306.
302. M. K. Müller and L. Brunsveld, *Angew. Chem. Int. Edit.*, 2009, **48**, 2921-2924.
303. D. K. Smith, *Chem. Commun.*, 2006, 34-44.
304. M. A. Kostiainen, C. Pietsch, R. Hoogenboom, R. J. M. Nolte and J. Cornelissen, *Adv. Funct. Mater.*, 2011, **21**, 2012-2019.
305. J. Mikkilä, H. Rosilo, S. Nummelin, J. Seitsonen, J. Ruokolainen and M. A. Kostiainen, *ACS Macro Lett.*, 2013, **2**, 720-724.
306. J. M. Chen, T. M. Su and C. Y. Mou, *J. Phys. Chem.*, 1986, **90**, 2418-2421.
307. V. K. Aswal and P. S. Goyal, *Chem. Phys. Lett.*, 2002, **364**, 44-50.
308. J. Lu, S. C. Owen and M. S. Shoichet, *Macromolecules*, 2011, **44**, 6002-6008.
309. T. Miller, A. Hill, S. Uezguen, M. Weigandt and A. Goepferich, *Biomacromolecules*, 2012, **13**, 1707-1718.
310. S. Kim, Y. Z. Shi, J. Y. Kim, K. Park and J. X. Cheng, *Expert Opin. Drug Del.*, 2010, **7**, 49-62.
311. J. K. Choi, J. Ho, S. Curry, D. H. Qin, R. Bittman and J. A. Hamilton, *J. Lipid Res.*, 2002, **43**, 1000-1010.
312. S. M. Bates and J. I. Weitz, *Circulation*, 2005, **112**, E53-E60.
313. E. R. Gillies and J. M. J. Fréchet, *J. Am. Chem. Soc.*, 2002, **124**, 14137-14146.
314. E. R. Gillies, E. Dy, J. M. J. Fréchet and F. C. Szoka, *Mol. Pharm.*, 2005, **2**, 129-138.
315. C. C. Lee, E. R. Gillies, M. E. Fox, S. J. Guillaudeu, J. M. J. Fréchet, E. E. Dy and F. C. Szoka, *P. Natl. Acad. Sci. USA*, 2006, **103**, 16649-16654.
316. G. Stehle, A. Wunder, H. Sinn, H. H. Schrenk, E. A. Friedrich, C. E. Dempfle, W. Maierborst and D. L. Heene, *J. Surg. Res.*, 1995, **58**, 197-204.
317. R. J. Linhardt, *J. Med. Chem.*, 2003, **46**, 2551-2564.
318. R. M. C. Sutton, K. L. Sutton and A. M. Stalcup, *Electrophoresis*, 1997, **18**, 2297-2304.
319. H. Nishi and Y. Kuwahara, *J. Biochem. Biophys. Meth.*, 2001, **48**, 89-102.
320. A. M. Stalcup and N. M. Agyei, *Anal. Chem.*, 1994, **66**, 3054-3059.
321. J. Wang and D. L. Rabenstein, *Biochemistry*, 2006, **45**, 15740-15747.
322. J. Wang and D. L. Rabenstein, *Biochim. Biophys. Acta.*, 2009, **1790**, 1689-1697.
323. K. S. Partridge, D. K. Smith, G. M. Dykes and P. T. McGrail, *Chem. Commun.*, 2001, 319-320.
324. W. Edwards and D. K. Smith, *J. Am. Chem. Soc.*, 2013, **135**, 5911-5920.

325. P. Wu, M. Malkoch, J. N. Hunt, R. Vestberg, E. Kaltgrad, M. G. Finn, V. V. Fokin, K. B. Sharpless and C. J. Hawker, *Chem. Commun.*, 2005, 5775-5777.
326. M. C. A. Stuart, J. C. van de Pas and J. Engberts, *J. Phys. Org. Chem.*, 2005, **18**, 929-934.
327. Y. B. Lim, E. Lee and M. Lee, *Angew. Chem. Int. Edit.*, 2007, **46**, 9011-9014.
328. S. M. Bromfield, P. Posocco, C. W. Chan, M. Calderon, S. E. Guimond, J. E. Turnbull, S. Pricl and D. K. Smith, *Chem. Sci.*, 2014, **5**, 1484-1492.
329. M. Friedman, *J. Agr. Food Chem.*, 1999, **47**, 3457-3479.
330. M. Friedman and C. E. Levin, *Amino Acids*, 2012, **42**, 1553-1582.
331. J. D. Watson and F. H. C. Crick, *Nature*, 1953, **171**, 737-738.
332. R. Srinivas, S. Samanta and A. Chaudhuri, *Chem. Soc. Rev.*, 2009, **38**, 3326-3338.
333. X. Guo and L. Huang, *Accounts Chem. Res.*, 2012, **45**, 971-979.
334. M. A. Mintzer and E. E. Simanek, *Chem. Rev.*, 2009, **109**, 259-302.
335. S. Y. Wong, J. M. Pelet and D. Putnam, *Prog. Polym. Sci.*, 2007, **32**, 799-837.
336. P. P. Karmali and A. Chaudhuri, *Med. Res. Rev.*, 2007, **27**, 696-722.
337. S. C. De Smedt, J. Demeester and W. E. Hennink, *Pharm. Res.*, 2000, **17**, 113-126.
338. D. K. Smith, *Curr. Top. Med. Chem.*, 2008, **8**, 1187-1203.
339. J. G. Hardy, M. A. Kostianen, D. K. Smith, N. P. Gabrielson and D. W. Pack, *Bioconjugate Chem.*, 2006, **17**, 172-178.
340. S. P. Jones, N. P. Gabrielson, C. H. Wong, H. F. Chow, D. W. Pack, P. Posocco, M. Fermeglia, S. Pricl and D. K. Smith, *Mol. Pharm.*, 2011, **8**, 416-429.
341. M. Michaud, E. Jourdan, A. Villet, A. Ravel, C. Grosset and E. Peyrin, *J. Am. Chem. Soc.*, 2003, **125**, 8672-8679.
342. M. A. Rehder-Silinski and L. B. McGown, *J. Chromatogr. A*, 2003, **1008**, 233-245.
343. X. G. Qu, J. O. Trent, I. Fokt, W. Priebe and J. B. Chaires, *P. Natl. Acad. Sci. USA*, 2000, **97**, 12032-12037.
344. S. Sforza, G. Haaima, R. Marchelli and P. E. Nielsen, *Eur. J. Org. Chem.*, 1999, 197-204.
345. S. Sforza, T. Tedeschi, R. Corradini and R. Marchelli, *Eur. J. Org. Chem.*, 2007, 5879-5885.
346. S. Sforza, R. Corradini, S. Ghirardi, A. Dossena and R. Marchelli, *Eur. J. Org. Chem.*, 2000, 2905-2913.

347. A. Calabretta, T. Tedeschi, R. Corradini, R. Marchelli and S. Sforza, *Tetrahedron Lett.*, 2011, **52**, 300-304.
348. V. Menchise, G. De Simone, T. Tedeschi, R. Corradini, S. Sforza, R. Marchelli, D. Capasso, M. Saviano and C. Pedone, *P. Natl. Acad. Sci. USA*, 2003, **100**, 12021-12026.
349. G. Roelfes, *Mol. Biosyst.*, 2007, **3**, 126-135.
350. A. J. Boersma, R. P. Megens, B. L. Feringa and G. Roelfes, *Chem. Soc. Rev.*, 2010, **39**, 2083-2092.
351. G. Roelfes, A. J. Boersma and B. L. Feringa, *Chem. Commun.*, 2006, 635-637.
352. S. Park and H. Sugiyama, *Molecules*, 2012, **17**, 12792-12803.
353. A. J. Boersma, B. L. Feringa and G. Roelfes, *Org. Lett.*, 2007, **9**, 3647-3650.
354. D. Coquière, B. L. Feringa and G. Roelfes, *Angew. Chem. Int. Edit.*, 2007, **46**, 9308-9311.
355. A. J. Boersma, B. L. Feringa and G. Roelfes, *Angew. Chem. Int. Edit.*, 2009, **48**, 3346-3348.
356. B. F. Cain, B. C. Baguley and W. A. Denny, *J. Med. Chem.*, 1978, **21**, 658-668.
357. H. Ihre, A. Hult, J. M. J. Fréchet and I. Gitsov, *Macromolecules*, 1998, **31**, 4061-4068.
358. B. Trappmann, K. Ludwig, M. R. Radowski, A. Shukla, A. Mohr, H. Rehage, C. Böttcher and R. Haag, *J. Am. Chem. Soc.*, 2010, **132**, 11119-11124.
359. B. J. Boyd, L. M. Kaminskas, P. Karellas, G. Krippner, R. Lessene and C. J. H. Porter, *Mol. Pharm.*, 2006, **3**, 614-627.
360. S. E. Stiriba, H. Frey and R. Haag, *Angew. Chem. Int. Edit.*, 2002, **41**, 1329-1334.
361. K. T. Al-Jamal, W. T. Al-Jamal, S. Akerman, J. E. Podesta, A. Yilmazer, J. A. Turton, A. Bianco, N. Vargesson, C. Kanthou, A. T. Florence, G. M. Tozer and K. Kostarelos, *P. Natl. Acad. Sci. USA*, 2010, **107**, 3966-3971.
362. K. T. Al-Jamal, W. T. Al-Jamal, J. T. W. Wang, N. Rubio, J. Buddle, D. Gathercole, M. Zloh and K. Kostarelos, *ACS Nano*, 2013, **7**, 1905-1917.
363. M. Ohsaki, T. Okuda, A. Wada, T. Hirayama, T. Niidome and H. Aoyagi, *Bioconjugate Chem.*, 2002, **13**, 510-517.
364. C. S. Love, A. R. Hirst, V. Chechik, D. K. Smith, I. Ashworth and C. Brennan, *Langmuir*, 2004, **20**, 6580-6585.
365. A. R. Hirst, J. E. Miravet, B. Escuder, L. Noirez, V. Castelletto, I. W. Hamley and D. K. Smith, *Chem-Eur. J.*, 2009, **15**, 372-379.
366. J. G. Hardy, A. R. Hirst and D. K. Smith, *Soft Matter*, 2012, **8**, 3399-3406.

367. E. Durán-Lara, L. Guzmán, A. John, E. Fuentes, M. Alarcón, I. Palomo and L. S. Santos, *Eur. J. Med. Chem.*, 2013, **69**, 601-608.
368. S. Boye, D. Appelhans, V. Boyko, S. Zschoche, H. Komber, P. Friedel, P. Formanek, A. Janke, B. I. Voit and A. Lederer, *Biomacromolecules*, 2012, **13**, 4222-4235.
369. T. Okuda, S. Kawakami, N. Akimoto, T. Niidome, F. Yamashita and M. Hashida, *J. Control. Release*, 2006, **116**, 330-336.
370. M. Driffield, D. M. Goodall and D. K. Smith, *Org. Biomol. Chem.*, 2003, **1**, 2612-2620.
371. O. Freund, J. Amédee, D. Roux and R. Laversanne, *Life Sci.*, 2000, **67**, 411-419.
372. M. Pittelkow, R. Lewinsky and J. B. Christensen, *Synthesis-Stuttgart*, 2002, 2195-2202.
373. H. Gershon, R. Ghirlando, S. B. Guttman and A. Minsky, *Biochemistry*, 1993, **32**, 7143-7151.